UNIVERSITÉ LAVAL

New magnetic stimulation routes with magnetic nanoparticles from process intensification in chemical engineering

Thèse

Pouya Hajiani

Doctorat en génie chimique
Philosophiae Doctor (Ph.D.)

Québec, Canada

I will prepare, and some day my chance will come.

Abraham Lincoln

Nothing is more common than unfulfilled potential.

Howard Hendricks

Résumé

Les **n**ano**p**articules **m**agnétiques (NPM) suscitent un vif intérêt dans plusieurs branches de l'ingénierie et de la recherche. En effet, la taille de ces dernières ainsi que leur propriétés magnétiques lorsqu'en suspension permettent leur manipulation à distance en utilisant des champs magnétiques externes appropriés. Cela ouvre la voie à l'activation de fonctionnalités supplémentaires lorsqu'ancrées à des catalyseurs métalliques, des enzymes ou des agents thérapeutiques. Conséquemment, les NPM ont été impliquées au sein de plusieurs applications dans lesquelles le mélange à l'échelle microscopique est une problématique importante, par exemple dans les réactions catalytiques, la séparation et l'administration de médicaments.

Le présent travail de thèse explore l'utilisation de NPM en tant que dispositifs nanométriques pour manipuler le mélange à l'échelle microscopique lorsque le système complet est soumis à des champs magnétiques. Toutes les expérimentations ont été menées à l'intérieur d'un électro-aimant à bobines tubulaire statique possédant deux pôles et trois phases. Ce dernier génère des champs magnétiques rotatifs uniformes (CMR), des champs magnétiques oscillatoires (CMO) ainsi que des champs magnétiques stationnaires (CMS).

En premier lieu, une technique de mélange dans laquelle un CMR transforme des NPM en agitateurs nanométriques créant de petits tourbillons dans la phase liquide est présentée. L'utilisation de cette technique permet l'augmentation du coefficient de diffusion de l'eau quiescente dans une cellule de diffusion statique jusqu'à 200 fois. Les études systématiques des paramètres d'opération révèlent que l'ampleur de l'augmentation dépend de la fraction volumique en NPM ainsi que de la force et de la fréquence du champ magnétique.

En second lieu, un écoulement convectif est utilisé afin de comprendre l'effet du couple hydrodynamique sur le comportement des NPM en champs magnétiques. Des tests de distribution de temps de séjour par impulsion sont effectués avec et sans champ magnétique dans le but d'examiner la dispersion axiale d'un écoulement laminaire de Poiseuille à l'intérieur d'un tube capillaire (Tests de dispersion de Taylor). Les résultats obtenus démontrent que le mélange latéral au long du tube est favorisé en présence de NPM et d'un champ magnétique. De plus, l'effet hydrodynamique observé de ce mélange latéral sur le

profil de vitesse laminaire est interprété comme provenant d'une approche d'un profil de vitesse plat similaire à celui d'un écoulement piston. À l'aide de la même technique, l'effet des CMO et des CMS sur la dispersion de Taylor et sur le profil de vitesse laminaire est aussi examiné en écoulement capillaire. Alors que les CMO n'induisent pas de mélange nano-convectif dans le capillaire et ont un impact négligeable sur la dispersion axiale, les CMS pour leur part, détériorent le mélange latéral du traceur et créent des profils de vitesse déviant de la forme parabolique vers une forme plus saillie. Une discussion détaillée de la vorticité du fluide en fonction de l'orientation du champ magnétique est aussi présentée.

Finalement, un écoulement multiphasique est étudié en ciblant le transfert de matière gaz-liquide entre des bulles de Taylor d'oxygène et la phase liquide, composée d'une solution diluée de NPM, à l'intérieur de tubes capillaires soumis à des CMR, des CMO et des CMS. Les résultats indiquent que les NPM qui tournent sous l'action d'un CMR améliorent le mélange dans le film lubrificateur qui entoure les bulles de Taylor comme cela est révélé par une augmentation mesurable du k_La. À l'opposé, les CMS immobilisent les NPM, menant à des taux de transfert de matière systématiquement plus faibles alors que les CMO n'ont pas d'effet détectable sur le coefficient de transfert de matière. Par ailleurs, l'interaction entre le couple magnétique et le couple hydrodynamique nécessaire pour dominer la direction de rotation des NPM est tirée de ces résultats.

Abstract

Magnetic **n**ano**p**articles (MNPs) have attracted significant interest in diverse areas of engineering and research. Particle size and magnetic properties of suspended MNPs in a suspension allow their manipulation at a distance using appropriate external magnetic fields. In particular by enabling additional functionality in forms anchored to metal catalysts, enzymes or therapeutic drug agents. Owing to this feature, MNPs have been involved in many applications where mixing in micro-scale is also a critical issue, e.g., catalytic reaction, separation and drug delivery.

This thesis explores MNPs as nano-scale devices to manipulate mixing in micro-scale when the whole system is subject to magnetic fields. All the experiments were performed in tubular two-pole, three-phase stator winding magnet, generating uniform rotating magnetic field (RMF), oscillating magnetic field (OMF) and stationary magnetic field (SMF).

Initially, we present a mixing technique in which a RMF converts MNPs into nano-stirrers generating small vortices in liquid phase. Using this technique, self-diffusion coefficient of motionless water in a static diffusion cell was intensified up to 200 folds. Systematic studies of operating parameters revealed that the extent of enhancement depends on MNP volume fraction, and strength and frequency in magnetic field.

In order to understand the effect of hydrodynamic torque on the MNPs behavior under magnetic fields, convective flow was also included. As such, axial dispersion of pressure-driven laminar Poiseuille flows in a capillary tube (Taylor dispersion test) was examined through a series of impulse (residence time distribution) RTD tests with and without RMF. This resulted in lateral mixing along the channel that was promoted relative to that in absence of MNPs or magnetic field. Moreover, we interpreted the observed hydrodynamic effects of such lateral mixing on laminar velocity profile as resulting from an approach to plug flow-like flat velocity profile. Using the same technique, the effect of OMF and SMF on Taylor dispersion and laminar velocity profile was examined in capillary flows. OMF did not induce nano-convective mixing in the capillary and had negligible impact on axial dispersion. On the contrary, SMF deteriorated lateral mixing of solute tracer and led to

velocity profiles deviating from parabolic shape towards more protruded ones. A detailed discussion of magnetic field orientation versus fluid vorticity vector was presented.

Finally a multiphase flow case concerned gas-liquid mass transfer from oxygen Taylor bubbles to the liquid in capillaries which was studied using dilute concentration of MNPs as the liquid phase under RMF, OMF and SMF. Experimental results implied that spinning MNPs under RMF improved mixing in the lubricating film that surrounds Taylor bubbles which reflected in a measurable enhancement of $k_L a$. On the contrary, SMF pinned MNPs leading to systematically degraded gas-liquid mass transfer rates whereas axial oscillating magnetic field had no detectable effects on the mass transfer coefficient. Moreover, interaction between magnetic torque and hydrodynamic torque to dominate MNP spin direction was conceived from these results.

Acknowledgements

I would like to thank my advisor, Prof. Faical Larachi, for being a superior mentor to me who generously shared his knowledge, experience, and time with me. He has helped me become a better researcher and technical writer. I am grateful for the amount of time he spent reading and discussing the material of this thesis. His level of rigor and care in research, writing and teaching are something I will never forget and will always aspire towards in my life.

I would like to thank Dr. Hamidipour, former student of our group, for showing me the door through which I walked in and was admitted in this group. He was always being concerned about my progress.

I would like to thank Mugurel Munteanu for teaching me how to use the Vibrating Sample Magnetometer and Rodica Plesu from CERMA group who helped me to figure out how to perform particle size analysis with Zetasizer for my specific application. I also appreciate Olivier Gravel's contribution in the lab during last four semesters. We had a lot of fun and I learned from his diverse area of interests in science and philosophy. I would like to thank Ali Faridkhou for helpful editing assistance of last two chapters of the thesis.

The help of the chemical engineering department technical staff (in Pavillon Adrien Pouliot), Jerome Noel, Marc Lavoie, and Claude Carrier during this research project is also appreciated.

I acknowledge the financial support of Natural Sciences and Engineering Research Council of Canada (NSERC) and the Canada Research Chair "Green processes for cleaner and sustainable energy".

I would also like to thank my office colleagues for their support. To all my friends who have always been there for me as my family through all these years. The list is a long one but I would like to thank Hamidreza Radfarnia and Sanaz Mossadegh Sedghi in particular. We shared great times with each other that I will always remain in the lanes of my memory.

I would like to thank my parents, Fatemeh Shapouri and Hamidreza Hajiani, and my brother Payam. If it were not by your support over these years, I would have not made it. Thank you for giving me everything I ever wanted in life and supporting me in every endeavor I have undertaken.

My deep and sincere gratitude goes to my loving wife, Elahe, for her constant support and apprehension in this long way. During the darkest days and nights of graduate life here, I was still happy because of her even though around me there was very little reason to be so.

Foreword

This PhD thesis comprises five chapters. Each chapter represents an article published, accepted or submitted in the scientific journals. These articles are listed below.

P. Hajiani, F. Larachi, Ferrofluid applications in chemical engineering, *International Review of Chemical Engineering*, 1 (2009) 221-237.

P. Hajiani, F. Larachi, Reducing Taylor dispersion in capillary laminar flows using magnetically excited nanoparticles: Nano-mixing mechanism for micro/nanoscale applications, *Chemical Engineering Journal*, 203 (2012) 492-498.

P. Hajiani, F. Larachi, Giant liquid-self diffusion in stagnant liquids by magnetic nano-mixing, *Chemical Engineering and Processing*, Accepted.

P. Hajiani, F. Larachi, Remotely excited magnetic nanoparticles and gas-liquid mass transfer in Taylor flow regime, *Chemical Engineering Science*, Accepted.

P. Hajiani, F. Larachi, Controlling lateral mixing and velocity profile of dilute ferrofluid in capillary in uniform DC, AC and rotating magnetic fields, *Chemical Engineering Journal*, Submitted.

Some results of these studies were presented in the following conferences:

P. Hajiani, F. Larachi, Lateral nano-mixing and velocity profile of dilute ferrofluid capillary flows in uniform DC, AC and rotating magnetic fields: Single- and multiphase flow cases, *IMFT*, 2012, Toulouse, France.

P. Hajiani, F. Larachi, Lateral nano-mixing in micro-channel, *GLS-F6*, 2012, Marrakech, Morocco.

P. Hajiani, O. Gravel, F. Larachi, Augmentation de la diffusion en mililеu liquide par rotation de nanoparticules magnétiques (npm) en champs magnétiques rotatifs, *ACFAS 80*, 2012, Montreal, Canada.

P. Hajiani, F. Larachi, Nano-mixing: A technique to overcome intrinsic liquid phase self-diffusion barrier via spinning magnetic nanoparticles, *NanoQuebec*, 2012, Quebec, Canada.

P. Hajiani, F. Larachi, Ferrofluid applications in chemical engineering, *CCEC 61*, 2011, London, Canada.

P. Hajiani, F. Larachi, Spin-up flows: Application in transport phenomena intensification, *CERPIC*, 2011, Quebec, Canada.

Table of contents

Résumé v
Abstract vii
Acknowledgements ix
Foreword xi
Table of contents xiii
List of Figures xvii
List of Tables xxii
1 Introduction 1
1.1 Ferrofluids 1
1.2 Background 2
1.2.1 Response to magnetic field 2
1.2.2 Equilibrium magnetization 3
1.2.3 Relaxation time 3
1.2.4 Magnetization relaxation equation 5
1.2.5 Magnetoviscosity 7
1.2.6 Ferrohydrodynamic transport equations 13
1.3 Application 16
1.3.1 Pipe flow momentum transfer 16
1.3.2 Ferrohydrodynamic laminar model 18
1.3.3 Ferrohydrodynamic turbulent model 24
1.3.4 Porous media momentum transfer 31
1.3.5 Mass transfer enhancement 33
1.4 Scope of thesis 43
1.5 Nomenclature 44
1.6 References 50
2 Giant liquid-self diffusion in stagnant liquids by magnetic nano-mixing 55
2.1 Abstract 55
2.2 Introduction 56
2.3 Experimental 57
2.3.1 Colloidal suspension 57
2.3.2 Magnet 58
2.3.3 Diffusion measurement 59

2.4 Result and discussion 62
2.5 Conclusion 65
2.6 References 67
3 Reducing Taylor dispersion in capillary laminar flows using magnetically excited nanoparticles: *Nano-mixing mechanism for micro/nanoscale applications* 71
3.1 Abstract 71
3.2 Introduction 71
3.3 Experimental section 72
3.3.1 MNP suspension 72
3.3.2 Magnet 73
3.3.3 RTD test 73
3.4 Results and discussion 74
3.4.1 Taylor dispersion test 74
3.4.2 MNPs alter laminar velocity profile in capillary tube 81
3.5 Conclusion 84
3.6 References 85
4 Controlling lateral nano-mixing and velocity profile of dilute ferrofluid capillary flows in uniform DC, AC and rotating magnetic fields 91
4.1 Abstract 91
4.2 Introduction 91
4.3 Experimental section 94
4.3.1 Magnet 94
4.3.2 Taylor dispersion in capillary 98
4.3.3 Impulse RTD test 98
4.3.4 Capillary tube and magnetic field relative alignment 100
4.3.5 Colloidal suspension 101
4.4 Results and discussion 101
4.4.1 Taylor dispersion under ^{T}RMF and ^{T}OMF 101
4.4.2 Taylor dispersion under SMF 108
4.4.3 Excited MNPs alter laminar velocity profile in capillary flow 114
4.5 Conclusion 119
4.6 Nomenclature 120
4.7 References 123

5 Remotely excited magnetic nanoparticles promote gas-liquid mass transfer in capillary Taylor flow regime 129
5.1 Abstract 129
5.2 Introduction 129
5.3 Experimental 132
5.3.1 Magnet 132
5.3.2 Colloidal suspension 134
5.3.3 Capillary tube and magnetic field relative alignment 134
5.3.4 Experimental setup 135
5.4 Results and discussion 137
5.4.1 Mass transfer enhancement in rotating magnetic field 138
5.4.2 Mass transfer enhancement in oscillating magnetic field 141
5.4.3 Mass transfer enhancement in static magnetic field 143
5.5 Conclusion 144
5.6 Nomenclature 145
5.7 References 147
6 Conclusion and future work 151
6.1 Key contributions 151
6.2 Suggested future work 152
7 Appendix A 155
7.1 Properties of magnetic nanoparticles (MNP) 155
7.2 Section II: magnet 157
7.3 Section III: RTD test & data reduction 158
7.4 References 162

List of Figures

FIGURE 1-1 : STEADY-STATE ILLUSTRATION OF TYPICAL RDMNPS SUBJECT TO DC MAGNETIC FIELD IN PLANAR COUETTE OR POISEUILLE FLOW. DEVIATION OF MAGNETIZATION FROM X DIRECTION IS DUE TO FLUID VORTICITY [2], [10] 8
FIGURE 1-2 : ONE CYCLE OF AC-FIELD OSCILLATION 9
FIGURE 1-3 : SCHEMATIC OF MNPS EXPOSED TO AC MAGNETIC FIELD IN PLANE COUETTE OR POISEUILLE FLOW IN RISING ART OF THE CYCLE. DEVIATION OF MAGNETIZATION FROM X DIRECTION IS CAUSED BY FLUID VORTICITY [4] 10
FIGURE 1-4 : SCHEMATIC OF MNPS EXPOSED TO AC MAGNETIC FIELD IN PLANE COUETTE OR POISEUILLE FLOW IN DIVING PART OF THE CYCLE. DEVIATION OF MAGNETIZATION FROM X DIRECTION IS CAUSED BY FLUID VORTICITY [4] 11
FIGURE 1-5 : IMPACT ON AC-FIELD MAGNETOVISCOSITY PHENOMENA WITH RESPECT TO THE RELATIVE ORDER OF BROWNIAN, HYDRODYNAMIC AND AC CHARACTERISTIC TIMES: A) $T_B > T_H > T_{AC}$, $\Delta H>0$; B) $T_B > T_{AC} > T_H$, $\Delta H>0$; C) $T_{AC} > T_B > T_H$, $\Delta H<0$ 12
FIGURE 1-6 : OSCILLATING MAGNETIC FIELD CAUSES SYNCHRONIZED ROTATION OF RDMNPS WHEN $T_{AC} > T_B > T_H$ 12
FIGURE 1-7 : COUETTE FLOWS OF FERROFLUID CONFINED BETWEEN TWO PARALLEL PLATES SUBJECT TO MAGNETIC FIELD. ADAPTED FROM [22] 15
FIGURE 1-8 : FRACTIONAL PRESSURE DROP VERSUS FERROFLUID REYNOLDS NUMBER MEASURED AT DIFFERENT STRENGTHS OF 400 HZ AC MAGNETIC FIELD. ADAPTED FROM [25] 17
FIGURE 1-9 : SIMULATED PROFILES OF NORMALIZED VELOCITY U, SPIN VELOCITY Ω AND AVERAGED MAGNETIC BODY TORQUE T0 FOR FERROFLUID LAMINAR PIPE FLOW EXPOSED TO OSCILLATING MAGNETIC FIELD (948 OE, 60 HZ) IN COMPARISON WITH ZERO FIELD PROFILES. ADAPTED FROM [25]. 21
FIGURE 1-10 : FITTED BROWNIAN TIME CONSTANT VERSUS FERROFLUID REYNOLDS NUMBER AT DIFFERENT AC-FIELD FREQUENCIES. ADAPTED FROM [25]) 21
FIGURE 1-11 : SIMULATED PROFILES OF NORMALIZED VELOCITY U, SPIN VELOCITY Ω AND AVERAGED MAGNETIC BODY TORQUE T0, TURBULENT KINETIC ENERGY K AND TURBULENT DISSIPATION RATE E FOR FERROFLUID TURBULENT PIPE FLOWS EXPOSED TO OSCILLATING MAGNETIC FIELD (948 OE, 60 HZ). ADAPTED FROM [25]. 22
FIGURE 1-12 : COMPARISON OF SIMULATED RE-DEPENDENT FRACTIONAL PRESSURE DROP WITH EXPERIMENTAL DATA FOR DIFFERENT OSCILLATING MAGNETIC FIELD STRENGTH. MAGNETIC FIELD FREQUENCY (A) 60 HZ, (B) 400 HZ, (C) 1000 HZ. ADAPTED FROM [25]. 24
FIGURE 1-13 : EFFECT OF MAGNETIC FIELD STRENGTH (EMBEDDED IN DIMENSIONLESS MAGNETIC FIELD, □) ON (A) RMS SPIN VELOCITY, (B) RMS LINEAR VELOCITY, (C) ON AVERAGED ENERGY TERMS: ◊ FOR Φ_B; ○ FOR E_V; □ FOR Ψ$_S$; + FOR E_C; Δ FOR E_A, IN TURBULENT MODEL. ADAPTED FROM [15] 29
FIGURE 1-14 : POROUS MEDIUM AND FLOW DETAILS: PACKED BED AND MAGNETIC FIELD PROGRAMMING [30] 32
FIGURE 1-15 : SPIN VELOCITY PROFILES AND POSITIVE/NEGATIVE GRADIENT MAGNETIC FIELD AT (A) BED EXIT Z = L, RE = 2110. BOX LEGEND SYNTAX: A (+) □ H0Z = A Z/L OE; A (-) □ H0Z = A (1 - Z/L) OE, [30] 32
FIGURE 1-16 : AXIAL VELOCITY COMPONENT RADIAL PROFILES AND POSITIVE/NEGATIVE GRADIENT MAGNETIC FIELD AT BED EXIT Z = L AND FERROFLUID REYNOLDS NUMBERS RE = 21.1. BOX LEGEND SYNTAX: A (+) □ H_{0Z} = A Z/L OE; A (-) □ H_{0Z} = A (1 - Z/L) OE, [30] 33
FIGURE 1-17 : ENHANCEMENT FACTOR VS. MNP MASS FRACTION AT 300 AND 500 STIRRER SPEED, PHYSICAL ABSORPTION TESTS. ADAPTED FROM [34] 36
FIGURE 1-18 : ENHANCEMENT VS. DISSIPATED ENERGY AT THREE DIFFERENT MNP CONCENTRATIONS IN CHEMICAL ABSORPTION TESTS AT VS = 14.5 CM/MIN. ADAPTED FROM [34] 36
FIGURE 1-19 : ENHANCEMENT VS. SUPERFICIAL VELOCITY AT THREE MNP MASS CONCENTRATIONS IN CHEMICAL ABSORPTION TESTS AT POWER P.U.V = 2.1 KW/M3. ADAPTED FROM [34] 37

FIGURE 1-20 : KLA, A, KL ENHANCEMENT VS. DISSIPATED ENERGY AT THREE DIFFERENT MNP CONCENTRATIONS IN CHEMICAL ABSORPTION TESTS AT VS = 14.5 CM/MIN. ADAPTED FROM [34] 37
FIGURE 1-21 : KLA, A, KL ENHANCEMENT VS. SPECIAL VELOCITY AT THREE DIFFERENT MNP CONCENTRATIONS IN CHEMICAL ABSORPTION TESTS AT POWER P.U.V = 2.1 KW/M3. ADAPTED FROM [34] 38
FIGURE 1-22 : STABILITY OF MAGNETIC NANOPARTICLE SIZES AT DIFFERENT CONCENTRATIONS OF MDEA VS. TIME. ADAPTED FROM [36] 39
FIGURE 1-23 : PARTICLE SIZE DISTRIBUTION OF SILICA AGGREGATES (VOLUME FRACTION SCALE), FLUID AT REST (BLACK LINE), AFTER 1 H, RE = 26 000 IN ABSENCE (RED LINE), AND IN PRESENCE (BLUE LINE) OF EXTERNAL MAGNETIC FIELD. ADAPTED FROM [37] 41
FIGURE 1-24 : PARTICLE SIZE EVOLUTION OF SILICA AGGREGATES IN PRESENCE (BLUE LINE) AND ABSENCE (RED LINE) OF EXTERNAL MAGNETIC FIELD, RE = 8 000. ADAPTED FROM [37] 42
FIGURE 1-25 : MEAN DIAMETER OF Γ-ALUMINA CLUSTERS FORMED IN PRESENCE OF MAGNETIC FIELD (BLUE LINE) AND IN ABSENCE OF MAGNETIC FIELD (RED LINE) VERSUS REYNOLDS NUMBER. ADAPTED FROM [37] 42
FIGURE 2-1 : A) TOP AND SIDE VIEW OF THE MAGNET WITH DIFFUSION CELL EMBEDDED INSIDE WITH CELL CONTAINING MNP SUSPENSION. B) DIFFUSION CELL SUBJECT TO URMF GENERATED BY TWO-POLE THREE-PHASE MAGNET ENERGIZED BY A THREE-PHASE POWER SUPPLY. C) DIFFUSION CELL WITH TWO SETS OF ELECTRICAL CONDUCTIVITY SENSORS. 59
FIGURE 2-2 : ELECTRODE RESPONSES OF A CONDUCTIVITY CELL, WITH AND WITHOUT URMF NANO-MIXING STIMULATION. MINUTE VOLUME OF TRACER IS INJECTED UPSTREAM INTO THE CAPILLARY TUBE (D = 1 MM) AND TRACKED AT TWO POSITIONS, FIVE AND THIRTY-FIVE MM DOWN THE INJECTION POINT BY TWO SETS OF ELECTRODES MEASURING CROSS-SECTIONAL AVERAGE ELECTRICAL CONDUCTIVITY. TRENDS REPRESENT THE TIME EVOLUTION OF TRACER CONDUCTIVITY AS DETECTED BY UPSTREAM AND DOWNSTREAM ELECTRODES A) MAGNETIC FIELD DISABLED, $\phi = 0.004$ AND B) MAGNETIC FIELD ENABLED UNDER URMF, $\phi = 0.01$, $H_0 = 31.4$ KA/M, $f = 100$ HZ 61
FIGURE 2-3 : SCHEMATIC DIAGRAM OF MNPS SPIN IN HYDROSTATIC CONDITIONS WITH AND WITHOUT URMF (A) IN ABSENCE OF MAGNETIC FIELD, MNPS GYRATION AND TRANSLATION IS SOLELY DUE TO BROWNIAN THERMAL AGITATION; MNP TIME-AVERAGE SPIN VECTOR (ω) IS EQUAL TO ZERO SINCE MNP MAGNETIC MOMENTS (M) ARE RANDOMIZED IN ALL DIRECTIONS; (B) IN PRESENCE OF URMF (H_0), MNP SPIN VECTOR (ω) TURNS NORMAL TO H_0 AND HENCE LATERAL MIXING OCCURS IN ALL DIRECTIONS ALONG CAPILLARY. 63
FIGURE 2-4 : DIFFUSION ENHANCEMENT FACTOR UNDER URMF VERSUS A) MAGNETIC FIELD STRENGTH, B) MAGNETIC FIELD FREQUENCY AND C) MNP CONCENTRATION. D_0 IS LIQUID SELF-DIFFUSION COEFFICIENT WITHOUT MAGNETIC FIELD 65
FIGURE 3-1 : TAYLOR DISPERSION IN CAPILLARY TUBE EXPOSED TO A ROTATING MAGNETIC FIELD (A) DISPERSION OF A TRACER PLUG IN POISEUILLE FLOW; (B) EXPERIMENTAL SETUP CONSISTS OF A TWO-POLE THREE-PHASE TUBULAR MAGNET (6 CM LONG, 4.5 CM I.D.) POWERED BY A THREE-PHASE POWERSUPPLY TO GENERATE A TRANSVERSE ROTATING MAGNETIC FIELD (WITH VARIABLE FREQUENCY AND STRENGTH) ACROSS A COAXIALLY ALIGNED GLASS CAPILLARY (10 CM LONG, 1 MM I.D.) (C) MAGNET UPPER VIEW SHOWING A UNIFORM HORIZONTAL ROTATING MAGNETIC FIELD OVER A CAPILLARY FLOW OF A DILUTE SUSPENSION OF MAGNETIC NANOPARTICLES 75
FIGURE 3-2 : SCHEMATIC DIAGRAM OF MNPS SPIN IN SHEAR FLOW WITH AND WITHOUT ^{T}RMF (A) IN THE ABSENCE OF MAGNETIC FIELD, MNPS GYRATE SYNCHRONOUSLY WITH FLUID VORTICITY; MNP SPIN VECTOR (ω) IS EQUAL HALF FLUID VORTICITY ($1/2\nabla\times v$) AND MNP MAGNETIC MOMENTS (M) ARE RANDOMIZED IN ALL DIRECTIONS; (B) IN PRESENCE OF ^{T}RMF (H_0), MNP SPIN VECTOR (ω) TURNS NORMAL TO AZIMUTHAL FLUID VORTICITY VECTOR AND HENCE MIXING IS LATERAL. MIXED SPHEROID ZONES FORM AROUND MNPS WHEN MAGNETIC TORQUE ($\mu_0 M\times H$, M IS MNP MAGNETIC MOMENT, H IS MAGNETIC FIELD AND μ_0 IS VACUUM PERMEABILITY) OVERCOMES BROWNIAN AGITATION AND FRICTIONAL TORQUE

$(2\zeta(\nabla\times u-2\omega)$, u is linear fluid velocity, ω is local MNP spin, ζ is spin viscosity). The distance between stirred spheroids is affected by MNP concentration and TRMF frequency. Significant mixing occurs when most of the stirred zones overlap to assist material exchange amongst them. 76

Figure 3-3 : Impulse response of a Taylor dispersion capillary with and without nano-mixing (a) Schematic of Taylor dispersion capillary tube with two sets of detectors inside magnet bore; (b,c) Laminar Poiseuille flow in a capillary tube: $D = 1$ mm, $Pe \sim 10^3$, $Re \sim 1$. A plug of tracer is injected upstream into the capillary tube and tracked at two positions, five and eight cm down the injection point by two sets of electrodes measuring cross-sectional average electrical conductivity. Trends represent the time evolution of tracer conductivity as detected by upstream and downstream electrodes (■,□) for unstirred Poiseuille flow, (▲,Δ) nano-mixing for laterally stirred MNPs $\phi = 0.0025$, $H_0 = 10.4$ kA/m, $F = 50$ Hz, (●,○) nano-mixing for laterally stirred MNPs $\phi = 0.0025$, $H_0 = 36.5$ kA/m, $F = 50$ Hz. Peak narrowing indicates axial dispersion is reduced under nano-mixing. 77

Figure 3-4 : The effect of convective flow on axial dispersion attenuation Axial dispersion coefficient, presented as dimensionless number D/UL, and estimated from moment analysis of convoluted data from impulse tests (such as in Figure 3-3). Experiments performed with $\phi = 0.001$, $H_0 = 31.4$ kA/m. Milder slopes imply strong nano-mixing counteracting convective stretching. Error bars indicate standard deviation (number of repeat runs = 3) 78

Figure 3-5 : Axial dispersion attenuation is dependent on TRMF strength and frequency, and MNP concentration and core diameter. Experiments carried out at $\phi = 0.001$ and MNP median diameter $D_C = 16.0$ nm unless otherwise stated. (a) D/D_0 versus F (▲) at $H_0 = 31.4$ kA/m plateaus at about 50 Hz. D/D_0 versus H_0 (●) at $F = 50$ Hz. (b) D/D_0 versus ϕ (♦) at $H_0 = 31.4$ kA/m plateaus at about 0.0012. D/D_0 versus D_C (■)at $H_0 = 36.5$ kA/m and $F = 50$ Hz. Error bars indicate standard deviation (number of repeat runs = 12). 80

Figure 3-6 : Mixing effect on laminar velocity profile. Power-law index N and τ/τ_{MIN} ratio as a function of (a) magnetic field strength, (b) magnetic field frequency, (c) MNP volume fraction. Error bars indicate standard deviation (number of repeat runs = 6), (d) Simulated laminar flow velocity profile for different lateral mixing intensities in a capillary as a function of power-law index. 83

Figure 4-1 : Taylor dispersion in capillary tube exposed to magnetic field. a) Schematic drawing depicts dispersion of a tracer blob in Poiseuille flow with parabolic laminar velocity profile. b) Schematic of the experimental setup including two-pole three-phase magnet and glass-made capillary tube at the center. c) Upfront view of magnet with a capillary set vertically and coaxially with magnet bore, a uniform *horizontal* magnetic field imposed across capillary tube hosting a flow of MNP-laden suspension. 96

Figure 4-2 : Taylor dispersion capillary tube submitted to three magnetic field scenarios. Two-pole three-phase magnet generates a) uniform rotating magnetic field (RMF) when energized by a three-phase power supply, b) oscillating magnetic field (OMF) when energized by a single-phase power supply, c) uniform static magnetic field (SMF) when energized by a DC current. Perpendicular to (y,x) plane is z-direction. 97

Figure 4-3 : Impulse test of a Taylor dispersion capillary with and without RMF. a) Schematic drawing of Taylor dispersion capillary tube with two sets of detectors five and eight cm down the injection point. b) RTD responses from first (full marks) and second (empty marks) electrode. Trends represent time evolution of tracer impulse responses, respectively, of first and second electrodes (intensity in arbitrary units): (■,□) for magnetic-field-free Poiseuille flow, (▲,Δ) for Poiseuille flow laterally stirred by nano-mixing ($\phi = 0.0025$, $H_0 = 10.4$ kA/m, $F = 50$ Hz), (●,○)for Poiseuille flow laterally stirred by nano-mixing ($\phi = 0.0025$,

H_0 = 36.5 kA/m, F = 50 Hz). Peak narrowing indicates lateral mixing under rotating magnetic field. c, d) Schematic diagram of MNPs spin in shear flow with and without RMF. c) In the absence of magnetic field, MNP spins, ω, gyrate collinear to fluid vorticity and MNP magnetic moments (m) are randomized in all directions. d) Under transverse RMF (H_0), ω becomes perpendicular to azimuthal fluid vorticity and hence, mixing is lateral. It is expected that a mixed zone forms around MNP when magnetic torque, m×H overcomes Brownian thermal agitation and viscous shear forces. 100

Figure 4-4 : Axial dispersion coefficient in capillary with low Re number subjected to transverse OMF and RMF. Axial dispersion coefficient, compacted in dimensionless number UL/D, estimated from impulse RTD tests. Experiments performed at ϕ = 0.001, D/ν = 1.0, H_0 = 31.4 kA/m for ^{T}RMF and H_{0RMS} = 31.4 kA/m for ^{T}OMF. Axial dispersion attenuation under ^{T}RMF implies that it changes orientation of MNP spin vectors thus inducing lateral mixing in capillary whilst under ^{T}OMF, MNP behavior does not show significant change relative to no magnetic field tests. Error bars indicate standard deviation (triplicate tests). 104

Figure 4-5 : Relative axial dispersion coefficient in capillary under ^{T}OMF and ^{T}RMF. $K_0 = 3.47\times10^{-6}$ m^2/s is axial dispersion coefficient of dilute ferrofluid (ϕ = 0.001) without magnetic field excitation. Moderate-strength ^{T}OMF at low frequency cannot excite MNPs to reflect in notable effects on axial dispersion. Axial dispersion attenuation under ^{T}RMF occurs and reaches a plateau after a certain frequency. Error bars indicate standard deviation (n = 12). 104

Figure 4-6 : MNP response to ^{T}OMF in a position where magnetic field direction is perpendicular to fluid vorticity, a) Magnetic field is strong enough to orient MNPs to its dominant direction, b) ^{T}OMF passes briefly through zero while changing direction leaving MNP magnetic moments shortly unassisted to lose, due to randomization effect of Brownian collisions, their coherent direction, c) Magnetic field on the rise until peak and MNP magnetic moments to resume orientational coherence. Synchronous particle rotation driven by ^{T}OMF is prohibited by midway Brownian reshuffling of MNPs. 106

Figure 4-7 : MNP response to OMF in a position where magnetic field direction is parallel to fluid vorticity. MNP gyration under shear flow is not opposed by magnetic torque. As a result, there is no momentum transfer between MNP and fluid due to OMF-nanoparticle interactions. 108

Figure 4-8 : Impulse test of a Taylor dispersion capillary with and without SMF. a) Schematic drawing of Taylor dispersion capillary tube with two sets of detectors one and four cm down the injection point, b) RTD responses from first (full marks) and second electrode (empty marks). Trends represent the time evolution of tracer intensity from first and second electrodes, respectively, (▲,Δ) with unexcited MNPs flowing in laminar Poiseuille flow, (●,○) with excited MNPs (ϕ = 0.0025, H_0 = 31.4 kA/m). Axial dispersion increases in capillary when magnetic torque prevents MNPs gyration under shear flow. 110

Figure 4-9 : Schematic of MNPs motion under shear flow in capillary tube. a) Magnetic field free, particles gyrate by friction torque and their magnetic moments directions are randomized. b) Under ^{A}SMF, hard dipoles are locked by the coaxially applied external magnetic field. Nanometrically, the velocity gradient has been removed in some regions (where highlighted) and augmented in the rest to satisfy continuity (black dotted line). That may result in mimetic shear thickening behaviour of liquid under ^{A}SMF. The brown dash-dotted line represents the original parabolic velocity profile as it occurs in a). 111

Figure 4-10 : Axial dispersion perturbations under ^{T}RMF and ^{A}SMF versus a) magnetic field strength and b) MNP concentration. a, b) ^{A}SMF promotes axial dispersion (●,♦) whilst ^{T}RMF attenuates K/K_0 (♦,▲). Error bars indicate standard deviation (number of repeat runs = 6). Magnetically locked MNPs under ^{A}SMF reduce lateral mass transfer rate in capillary

WHEREAS MAGNETICALLY SPINNING MNPS UNDER ^{T}RMF PROMOTE LATERAL MASS TRANSFER THROUGH NANOCONVECTIVE MIXING. IN A) $K_0(\phi=0.001, {}^{T}\text{RMF}) = 3.47\times10^{-6}$ M^2/S AND $K_0(\phi=0.005, {}^{A}\text{SMF}) = 1.13\times10^{-6}$ M^2/S. IN B) $K_0(\phi=0, {}^{T}\text{RMF}) = 5.08\times10^{-6}$ M^2/S AND $K_0(\phi=0, {}^{A}\text{SMF}) = 1.11\times10^{-6}$ M^2/S. 113
FIGURE 4-11 : EXCITED MNPS EFFECT ON LAMINAR VELOCITY PROFILE UNDER ^{T}RMF AND ^{A}SMF. POWER-LAW INDEX N AND $\bar{t}/T_{MIN}$ RATIO AS A FUNCTION OF A) MAGNETIC FIELD STRENGTH, B) MNP VOLUME FRACTION. ERROR BARS INDICATE STANDARD DEVIATION (NUMBER OF REPEAT RUNS = 6). C) EXPECTED LAMINAR FLOW VELOCITY PROFILE IN A CAPILLARY AS A FUNCTION OF POWER-LAW INDEX. 116
FIGURE 4-12 : EFFECTIVE DIFFUSIVITY IN LAMINAR FLOW UNDER ^{T}RMF AND ^{A}SMF. D_{EFF}/D RATIO AS A FUNCTION OF A) MAGNETIC FIELD STRENGTH, B) MNP VOLUME FRACTION. 119
FIGURE 5-1 : TAYLOR BUBBLES IN CAPILLARY TUBE EXPOSED TO MAGNETIC FIELD: A) EXPERIMENTAL SET-UP INCLUDING TWO-POLE THREE-PHASE MAGNET AND GLASS-MADE CAPILLARY TUBE AT THE CENTER; B) UPFRONT VIEW OF MAGNET WITH CAPILLARY SET VERTICALLY AND COAXIALLY WITH MAGNET BORE, AND UNIFORM *HORIZONTAL* MAGNETIC FIELD IMPOSED ACROSS CAPILLARY TUBE HOSTING A FLOW OF MNP-LADEN SUSPENSION; C) RISING TAYLOR BUBBLES IN CAPILLARY; D) EXPANDED AREA OF LUBRICATING FILM WHERE MNP SPIN PLANE IS PERPENDICULAR TO CAPILLARY WALL. 133
FIGURE 5-2 : A) EXPERIMENTAL SET-UP FOR GAS-LIQUID MASS TRANSFER STUDY IN CAPILLARY; B) SINGLE TAYLOR BUBBLE SURROUNDED BY SPINNING MNPS IN A ^{T}RMF 137
FIGURE 5-3 : A) CAPILLARY TUBE LOCATED COAXIALLY IN THE BORE OF A TWO-POLE THREE-PHASE MAGNET (TOP VIEW). MAGNET GENERATES A UNIFORM ROTATING MAGNETIC FIELD (RMF) WHEN ENERGIZED BY A THREE-PHASE POWER SUPPLY; B) K_LA ENHANCEMENT FACTOR AS A FUNCTION OF ^{T}RMF FREQUENCY: FOR EXPERIMENTS UNDER MAGNETIC FIELD (♦, ▲, ●), ENHANCEMENT WAS DUE TO ^{T}RMF AND K_LA_0 IS MASS TRANSFER COEFFICIENT IN ABSENCE OF MAGNETIC FIELD FOR EACH PARTICLE CONCENTRATION, $U_L = 0.1$ CM/S, $U_G = 0.3$ CM/S AND $H_0 = 31.4$ KA/M. FOR K_LA VERSUS GAS FLOW RATE WITHOUT MAGNETIC FIELD (■), ENHANCEMENT ORIGINATED FROM GAS FLOW AUGMENTATION AND K_LA_0 CORRESPONDS TO $U_G = 0.3$ CM/S. OTHER PARAMETERS ARE THE SAME (I.E., $\phi = 0$ AND $U_L = 0.1$ CM/S); C) K_LA ENHANCEMENT FACTOR UNDER ^{T}RMF AS A FUNCTION OF U_G FOR TWO MNP CONCENTRATIONS WHILE U_L, H_0 AND Ω WERE KEPT CONSTANT. 140
FIGURE 5-4 : A) SIDE VIEW OF THE MAGNET WITH A CAPILLARY TUBE WHICH WAS SET VERTICALLY AND TRANSVERSE WITH MAGNET BORE, A UNIFORM *VERTICAL* MAGNETIC FIELD IMPOSED ALONG CAPILLARY TUBE; B) RISING TAYLOR BUBBLES SURROUNDED WITH AZIMUTHALLY SPINNING MNPS ARE SHOWN. FLUID VORTICITY AND CONSEQUENTLY, PARTICLE SPIN VECTOR INVERTED OVER FILM THICKNESS; C) THE MAGNET GENERATES A UNIFORM OSCILLATING MAGNETIC FIELD (OMF) WHEN ENERGIZED BY AN AC POWER SUPPLY; D) K_LA ENHANCEMENT FACTOR VERSUS FIELD FREQUENCY FOR THREE PARTICLE CONCENTRATIONS EXPOSED TO $H_{0\,RMS} = 31.4$ KA/M. K_LA_0 IS MASS TRANSFER COEFFICIENT FOR EACH PARTICLE CONCENTRATION WITHOUT MAGNETIC FIELD EFFECT. 143
FIGURE 5-5 : A) CAPILLARY TUBE WAS LOCATED VERTICALLY IN HORIZONTAL MAGNET (SIDE VIEW). THE MAGNET GENERATES A UNIFORM STATIONARY MAGNETIC FIELD (SMF) WHEN ENERGIZED BY A DC POWER SUPPLY; B) K_LA ENHANCEMENT FACTOR VERSUS FIELD INTENSITY FOR THREE PARTICLE CONCENTRATIONS. K_LA_0 IS SUSPENSION MASS TRANSFER COEFFICIENT FOR EACH PARTICLE CONCENTRATION WITHOUT MAGNETIC FIELD EFFECT. 144
FIGURE 7-1: MAGNETIZATION CURVE OF EMG705 WATER-BASED FERROFLUID ($M_S = 18.7$ KA/M) 156
FIGURE 7-2 : MAGNETIZATION LINEAR REGION FOR EMG705 WATER-BASED FERROFLUID ($\chi_0 = 2.94$) 156
FIGURE 7-3 : PARTICLE SIZE DISTRIBUTION MEASUREMENT FOR EMG705 BY DLS TECHNIQUE (NUMBER AVERAGE DIAMETER = 24.8 NM), ERROR BARS INDICATE STANDARD DEVIATION WITH 3 RUNS. 157
FIGURE 7-4 : GOODNESS OF FIT BETWEEN MEASURED I_{II} AND SIMULATED I_2 OUTLET SIGNALS USING AXIAL DISPERSION MODEL. 160

List of Tables

TABLE 1-1 : PARAMETERS USED IN FERROFLUID LAMINAR AND TURBULENT SIMULATIONS [25] 17
TABLE 1-2 : MAGNETIC AND HYDRODYNAMIC PARAMETERS USED IN FERROFLUID TURBULENT SIMULATIONS [15] 30
TABLE 1-3 : TIME-AVERAGED 3-D SPIN VELOCITY, FERROFLUID VELOCITY, INDUCED MAGNETIC FIELD AND MAGNETIZATION RMS COMPONENTS OF TURBULENT FLOW AS SIMULATED IN [15] 30
TABLE 2-1 : MAGNETIC PROPERTIES OF EMG 705 FROM MAGNETOMETRY MEASUREMENT 57
TABLE 4-1 : MAGNETIC PROPERTIES OF EMG 705 FROM MAGNETOMETRY MEASUREMENT 101
TABLE 5-1 : MAGNETIC PROPERTIES OF EMG 705 FROM MAGNETOMETRY MEASUREMENT 134
TABLE 7-1 : RMF STRENGTH GENERATED BY 3-PHASE CURRENT INTENSITY AT CENTER OF MAGNET BORE 158

1 Introduction

Ferrofluids have been vastly persuaded in diverse areas of engineering and research. This introduction briefly exposes some concepts specific to ferrofluids and how they relate to recent applications emerging in chemical engineering, including mass transfer enhancement, momentum transfer in laminar and turbulent pipe flows and in porous media flows, and the motion of magnetic nanoparticles in gas-liquid mass transfer mechanisms with/without external magnetic fields. The noticeable effects of magnetic fields on ferrofluid flow behavior will be surveyed as well as a discussion about common assumptions to simplify and solve some ferrohydrodynamic models. As the core concept involved in this report, magnetoviscosity was explained phenomenologically and some contradictions in literature addressed as well. With respect to the intriguing features caused by dispersed magnetic nanoparticles on ferrofluid behavior, considerable theoretical and experimental work is left for mining new opportunities in chemical engineering on the subject of ferrofluid interactions between magnetic fields, mass, heat, and momentum transfer phenomena.

1.1 Ferrofluids

Ferrofluids are man-made magnetic colloidal dispersions involving aqueous or organic non-magnetic liquid carriers wherein a large number (*ca*. 10^{17} particles per cubic centimeter) of magnetic nanoparticles (MNP), *ca*. 10 to 15 nm in magnetic core size, are seeded and maintained afloat thanks to thermal agitation and *ad hoc* grafted surfacting moieties [1, 2]. While Brownian agitation prevents MNP sedimentation and, to some extent, magnetic dipole-dipole induced agglomeration, it is insufficient to undo agglomeration by the short-range van der Waals attraction, thus requiring surfactant agents and/or the nanoparticles to be electrically charged to achieve stability of the colloidal system. The giant magnetic moment borne in those MNP inclusions typically ranges between 10^3 and 10^5 Bohr magneton units depending on the (ferri)/ferromagnetic material and particle size [1]. The magnetization of ferrofluids in response to a moderate external magnetic field (about a few tenths of Tesla) is reminiscent of materials endowed with simple paramagnetism; though ferrofluids, in comparison, possess a colossal magnetic susceptibility which is to be linked to the super-paramagnetism stemming from the single-domain feature of their MNPs.

Application of an external magnetic field bestows on ferrofluids unique and intriguing characteristics owing to which they are increasingly scrutinized in the scientific and technical literatures. Shifting from the traditional realm of physics to that of engineering at large, ferrofluid applications, in chemical engineering in particular, are perhaps lagging behind those in other engineering areas, as few applications have hitherto been dubbed to chemical engineering. This brief review will be devoted to a discussion of some nascent and potentially relevant applications of ferrofluids to chemical engineering. We will briefly remind some fundamental concepts of ferrofluids before summarizing the experimental and theoretical studies about mass transfer enhancement, and momentum transfer in laminar/turbulent pipe flows as well as flow through porous media.

1.2 Background

1.2.1 Response to magnetic field

There are two types of MNPs as regards freedom of rotation of the magnetic moment vector inside their solid crystal structures. In particles with 'rigid dipoles magnetic nanoparticle' (rdMNP) [3], or synonymously 'freezing-in magnetic moment' [4], the strong anisotropic energy locks the magnetic moment inside the solid crystal. Conversely, 'soft dipoles' particles (sdMNP) enable the magnetic moment to twist freely inside the solid crystal due to thermal agitation perturbations, and therefore exhibit super-paramagnetism [5]. The magnetic dipole moment for each nanoparticle experiences a torque from the magnetic field prevailing inside the ferrofluid which tends to align the magnetic moment to the field direction. In the case of rdMNP, the torque is also felt through the solid body and may result in an "asynchronous" angular motion vis-à-vis the surrounding fluid. Whereas in the case of sdMNP, alignment of the magnetic moment does not require an exerting torque on the particle's body. The rdMNP spin can even be blocked, regardless of fluid flow vorticity, if a sufficiently strong *stationary* magnetic field is applied; whilst, in the same conditions, the sdMNP spin would match flow vorticity [3]. Magnetic dipole rigidity or softness is characterized by a relaxation time constant, τ, to be explained later after introducing the magnetization phenomenon.

1.2.2 Equilibrium magnetization

Magnetization is the macroscopic magnetic response of a (magnetic or non-magnetic) material to an external magnetic field. In (motionless) magnetohydrostatic context, the magnetization of ferrofluids is described by means of the same Langevin magnetization equation originally proposed for non-magnetic materials featuring simple paramagnetism [1],[2]:

$$\mathbf{M}_0 = M_s L(\alpha)\frac{\mathbf{H}}{H}, \quad L(\alpha) = \coth(\alpha) - \alpha^{-1}, \quad \alpha = \mu_0 m_p H / k_B T, \quad H = |\mathbf{H}| \tag{1}$$

In equation 1, m_p is the magnetic dipole moment of one single MNP with magnetic core diameter d_p; M_s stands for the saturation magnetization which occurs when all the MNP magnetic moment vectors are aligned with the external vector field, $\mathbf{H}$; μ_0 and k_B are the vacuum permeability and the Boltzmann constant, respectively; and T is the absolute temperature.

1.2.3 Relaxation time

Consider an external magnetic field is applied on a collection of MNPs, seeded in a ferrofluid at rest, such that saturation magnetization, M_s, is achieved. After this magnetic field is suddenly disabled, magnetization will decay according to [5]:

$$\mathbf{M} = \mathbf{M}_s e^{-t/\tau} \qquad 0 < t < \tau_m \tag{2}$$

where τ_m is the observational time scale of the experiment and τ is a relaxation time constant. For $\tau_m << \tau$, the instantaneous magnetization remains stable near M_s over τ_m. For small τ ($\tau_m >> \tau$), the instantaneous magnetization decays to zero as time evolves because of the randomizing effect by thermal agitation on the magnetic moments [5]. Thermal agitation in ferrofluids shuffles the magnetic moments following two different mechanisms depending on whether MNPs are rigid or soft dipoles. rdMNPs are randomly, but "bodily", rotated as a result of Brownian collisions. Such a Brownian relaxation mechanism, stemming from a hydrodynamically-driven Brownian rotational diffusion, is characterized by a time constant τ_B [2]:

$$\tau_B = 3V_h \mu / k_B T \tag{3}$$

Martsenyuk et al. [6] attempted to quantify the effect of magnetic field on τ_B using an effective-field theory and the Fokker-Planck equation. They assumed small deviations of magnetization from equilibrium-state magnetization (equation 1) and derived two time constants for relaxation of the parallel and perpendicular (with respect to external magnetic field) magnetization vector components. They finally concluded that the effect of magnetic field on parallel Brownian relaxation time constant is insignificant, unlike the perpendicular one which is field dependent:

$$\tau_{B\parallel} = \tau_B \qquad \tau_{B\perp} = \frac{2\tau_B}{2 + \alpha L(\alpha)} \tag{4}$$

However, a field-invariant τ_B, as calculated from equation 3, has been indistinguishably employed in the literature for any magnetic field changes and without verifying Martsenyuk et al. [6] assumptions.

The second thermal agitation mechanism of magnetization relaxation manifests due to rotation of the magnetic moment inside the crystal lattice of the particle and does not necessitate "bodily" rotation of the MNP, *per se*. This mechanism applies to sdMNP and is characterized by a Néelian relaxation time constant, τ_N [1],[2].

$$\tau_N = \frac{1}{f_0} \exp\left(\frac{KV_p}{k_B T}\right) \tag{5}$$

MNP size distributions in commercial ferrofluids present some polydispersity so that soft and rigid dipoles may coexist within the same fluid sample with a threshold size demarcating the finer sdMNP, which relax according to a Néelian mechanism, and coarser rdMNP which swerve following a Brownian mechanism. In this case, Martsenyuk et al. [6] proposed to use an effective relaxation time constant defined as a harmonic mean between τ_B or τ_N [1] to reflect more weight by the smaller of the two relaxation times:

$$\tau = \frac{\tau_N \tau_B}{\tau_N + \tau_B} \tag{6}$$

1.2.4 Magnetization relaxation equation

Different dynamic circumstances may arise in practice in which the magnetization vector cannot catch up instantaneously with the equilibrium magnetization vector. These comprise, for instance, ferrofluids subject to time-varying magnetic fields such as rotating or alternating current (AC) magnetic field. In motionless ferrofluids under rotating magnetic fields, the magnetization vector, **M**, lags behind the magnetic field vector, **H**, due to the relaxation time. In AC magnetic fields, despite **M** is all the time collinear with **H**, relaxation is also in action due to the distribution in magnetic dipoles misalignments. Another example resulting in a lack of collinearity between **M** and **H** can also be due to local flow vorticity when a ferrofluid is set to motion in a magnetic field featuring a normal component with respect to the vorticity axis. These cases, or variants thereof, require establishment of a constitutive equation for non-equilibrium magnetization to account for the relaxation phenomenon. Since an accurate and comprehensive kinetic theory to describe MNP relaxation at the microscopic level has yet to be developed, ersatz phenomenological approaches have been considered [7]. Mathematical model proposed for all magnetization equations has a similar frame work. An infinitesimal small volume (i.s.v.) respect to hydrodynamic dimensions is considered containing large number of MNPs. A local frame coordinate at the center of the i.s.v. rotates in average spin velocity of MNPs (**ω**) presenting them immobilized in local reference view (zero mean spin velocity). Magnetization of MNPs in this element is treated like equilibrium magnetization following Langevin equation (equation 1) locally. Authors proposed different deviation terms representing magnetization variation from local equilibrium. From dynamic of a vector in rotating coordinate, term (**ω**×**M**) is added to magnetization equilibrium deviation term as a coupling of local magnetization vector and locally averaged spin velocity. This term quantifies the abovementioned assumption implying that local magnetization vector of a i.s.v. rotates in **ω** providing the synchronized rotation of all MNPs inside the i.s.v. regardless of other intervening factors like fluid vorticity or relaxation time constants. As it will be discussed later, there are circumstances in which this assumption becomes reasonable, (i.e. rotating magnetic field or high frequency AC-field) providing satisfying prediction of the experimental results [11], [8]. In other cases, model predictions deviate from experimental

results due to the dramatic violation of this assumption [9]. Three major magnetization equations have been proposed in the literature which shall be recalled briefly.

Shliomis [10] pioneered the contributions regarding the magnetization relaxation constitutive equations. In his approach, the magnetization relaxation equation treats a ferrofluid as a homogeneous fluid. A slight deviation from equilibrium magnetization of the locally-averaged magnetization, i.e., $1/\tau(\mathbf{M}\text{-}\mathbf{M}_0)$, was assumed along with considering the rotation of local magnetization vector coupled to the locally-averaged spin velocity of MNP, $\boldsymbol{\omega}$, i.e., $\boldsymbol{\omega}\times\mathbf{M}$, to account for the exchange to external-observer referential:

$$\frac{\partial \mathbf{M}}{\partial t} = -\mathbf{u}\cdot\nabla\mathbf{M} + \boldsymbol{\omega}\times\mathbf{M} - \frac{1}{\tau}\left(\mathbf{M}-\mathbf{M}_0\right) \tag{7}$$

where $\mathbf{u}$ is the ferrofluid linear velocity and τ is as defined in equation 6.

However, the predictive capability of equation 7 was challenged by Bacri et al. [11] as it was found unsuccessful in predictions of experimental results especially for hydrodynamic time scales ($1/|\nabla\times\mathbf{v}|$) smaller than the relaxation time.

In a second approach, Martsenyuk et al. [6] improved the former magnetization relaxation equation by defining a local *effective* magnetic field, $\mathbf{H}_e$, under which magnetization would follow Langevin equilibrium equation [6]. In doing so, they solved the Fokker-Planck equation on locally averaged (macroscopic) MNP dipole moment vector distribution, obtaining a dynamic magnetization equation with a set of two time constants [6],[12]:

$$\frac{\partial \mathbf{M}}{\partial t} = -\mathbf{u}\cdot\nabla\mathbf{M} + \left(\frac{1}{2}\nabla\times\mathbf{u}\right)\times\mathbf{M} - \frac{1}{\tau}\left(1-\frac{\left(\boldsymbol{\xi}\cdot\boldsymbol{\xi}_e\right)}{\xi_e^2}\right)\mathbf{M} - \frac{1}{6\mu\varphi}\left(\frac{\xi_e - L\left(\xi_e\right)}{\xi_e L^2\left(\xi_e\right)}\right)\mathbf{M}\times\left(\mathbf{M}\times\mathbf{H}\right)$$

$$\boldsymbol{\xi} = \frac{\mu_0 m_p \mathbf{H}}{k_B T} \qquad \boldsymbol{\xi}_e = \frac{\mu_0 m_p \mathbf{H}_e}{k_B T} \qquad \mathbf{M} = M_s L\left(\xi_e\right)\frac{\boldsymbol{\xi}_e}{\xi_e} \tag{8}$$

where $\mathbf{M}$ is a non-equilibrium magnetization which is in equilibrium with (dimensionless) effective magnetic field $\boldsymbol{\xi}_e$.

Felderhof and Kroh [13] proposed a phenomenological magnetization relaxation equation in the framework of irreversible thermodynamics by deriving an expression for entropy production during dynamic magnetization [13],[14]:

$$\frac{\partial \mathbf{M}}{\partial t} = -\mathbf{u}\cdot\nabla\mathbf{M} + \boldsymbol{\omega}\times\mathbf{M} - \frac{\chi_0}{\tau}\left(\mathbf{H}-\mathbf{H}_{\mathrm{eq}}\right) \tag{9}$$

where χ_0 given as $\lim_{H\to 0}(M_0/\mathrm{H})=(\mu_0 m_\mathrm{p}\mathrm{M_s})/(3k_\mathrm{B}T)$ is the initial susceptibility of the ferrofluid obtained in the linear-limit of Langevin function (equation 1). Furthermore, $\mathbf{H}_{\mathrm{eq}}$ represents the local equilibrium magnetic field calculated using $\mathbf{H}_{\mathrm{eq}} = \mathbf{M}C(|\mathbf{M}|)$. A form of C as used by Schumacher et al. [25] is given as follows:

$$|\mathbf{M}| = M_S\left\{\left(\tanh\left(\frac{3\chi_0}{M_\mathrm{S}}|\mathbf{M}|C\right)\right)^{-1} - \left(\frac{3\chi_0}{M_\mathrm{S}}|\mathbf{M}|C\right)^{-1}\right\},\ |\mathbf{M}| = \sqrt{M_\mathrm{x}^2 + M_\mathrm{y}^2 + M_\mathrm{z}^2} \tag{10}$$

1.2.5 Magnetoviscosity

One of the most fascinating attributes of ferrofluids is their ability to exhibit anisotropic apparent viscosity when subject to magnetic fields. In essence, this anisotropy stems from the rdMNPs being pinned by the magnetic field forcing them to spin asynchronously relative to the contiguous fluid. This leads the wall shear stress a ferrofluid exerts on a wall to change in the presence of a magnetic field [2]. The physical manifestations of this *magnetoviscosity* can be categorized into three classes depending on the nature of the applied magnetic field, *i.e.* static (or DC) field magnetoviscosity, AC field magnetoviscosity, and rotating field magnetoviscosity.

DC-field magnetoviscosity arises when the external field exhibits a perpendicular projection with respect to the fluid vorticity vector, which we refer to as the normal-to-vorticity magnetic field component ($H_{\perp(\nabla\times\mathbf{v})}\neq 0$). This magnetoviscous behavior was first observed by Rosensweig et al. [26] and McTague [27], and a theoretical framework to explain it was elaborated by Shliomis [10]. While rdMNPs tend to be rotated by fluid vorticity under viscid-flow shear forcing, the normal-to-vorticity magnetic field component hinders the dipoles free rotation. This results in an inflated apparent viscosity. A directional mismatch between **M** and **H** occurs in response to an ensemble-average effect of the local

fluid's frictional torques exerting on each MNP. This causes inflation in the measured viscosity denoted, in the literature, as rotational viscosity, $\Delta\eta$ [1], [4]. Figure 1-1 depicts a representative rdMNP in planar (Couette or Poiseuille) flow subject to (+ *x* oriented) static magnetic field as explained by Shliomis [10] and Rosensweig [2]. It can be seen that the resulting (+ *z* oriented) magnetic torque acts in opposition to the (– *z* oriented) vorticity torque (*i.e.*, mechanical torque). Obviously, magnetoviscosity would not manifest in (± *z* oriented) magnetic fields as **M** would be able to align with **H** without being bothered by vorticity.

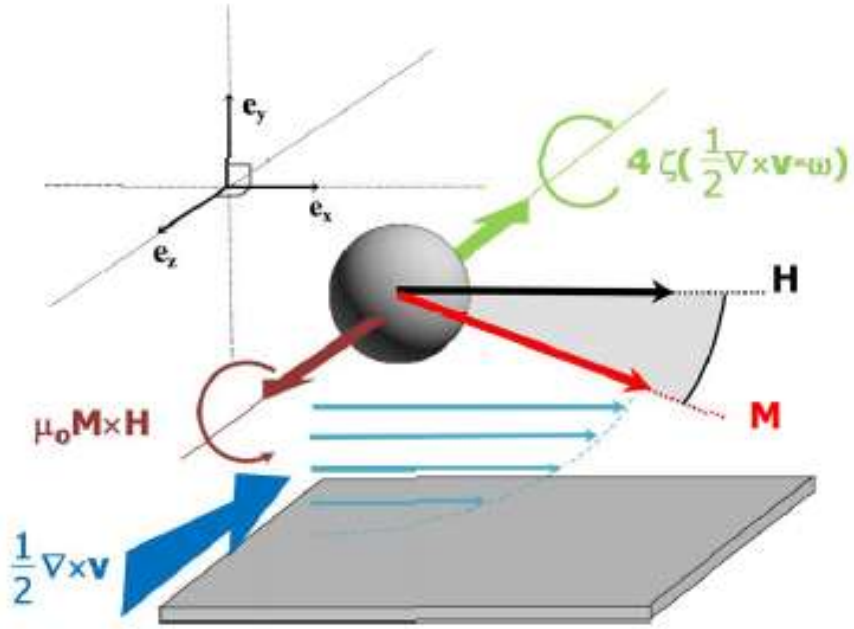

Figure 1-1 : Steady-state illustration of typical rdMNPs subject to DC magnetic field in planar Couette or Poiseuille flow. Deviation of magnetization from x direction is due to fluid vorticity [2], [10]

AC-field magnetoviscosity was first theoretically conceived by Shliomis and Morozov [4] and then experimentally investigated by Bacri et al. [11] and Zeuner et al. [28]. Ferrofluids are polarized linearly (i.e., with invariant direction) with an alternating magnetic field (figure 1-2) so that their rdMNPs would try to imitate the **H** pattern via gyration. In the motionless case, gyration transitions are racemic in the sense that the rdMNPs have two equiprobable choices to swing, either clockwise or anticlockwise, in a manner reminiscent of a metronome rhythm imposed by the alternating magnetic field. This entrains the average spin angular velocity per unit volume (p.u.v.) of ferrofluid to be in permanence zero, i.e., **ω**

= **0**, with **M** being forced to transition across **0** in its quest in tracking **H**. In shear flows and provided ($H_{\perp(\nabla\times\mathbf{v})}\neq 0$), the rdMNP spin is partly orchestrated by the fluid vorticity which imposes its rotational direction, $\nabla\times\mathbf{v}$, as the preferential direction. This biasing direction destroys symmetry between the two aforementioned equiprobable swing directions by privileging the one as illustrated in figure 1-3 and 1-4. Figure 1-3 depicts the rdMNP behavior of a Couette-Poiseuille flow in an AC magnetic field while the field is rising to maximum amplitude, and conversely figure 1-4, while the field is decreasing to zero [4].

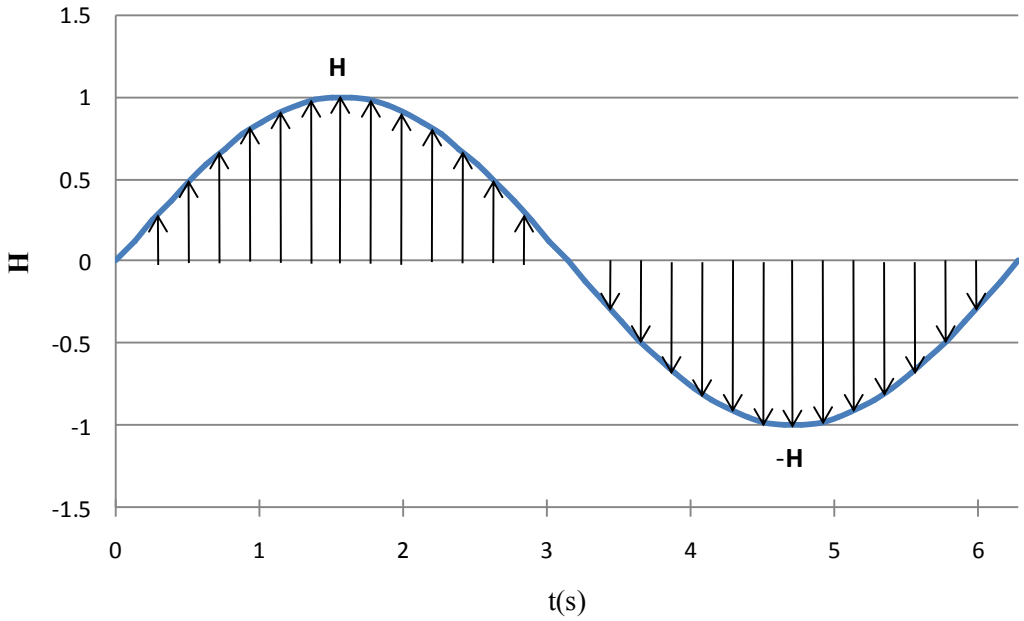

Figure 1-2 : One cycle of AC-field oscillation

Shliomis and Morozov [4] view the "vorticity" slap on the rdMNP as the determining event for the initialization of rotation of the magnetization vector [in its quest for catching up the varying magnetic field]. We will denote the fluid vorticity (hydrodynamic) time scale as τ_h. They also view the characteristic time scale of AC magnetic field as equal to the Brownian relaxation time τ_B that is the characteristic time for which the magnetization vector is locked to the changing magnetic field. Assuming $Re \approx 1$, they arrived at $\tau_B << \tau_h$ which implies that the rotation of **M**, after its initiation by the vorticity slap, is relayed by the AC magnetic field. This nuances the role of fluid vorticity in the rotation of the rdMNPs as it only comes into play as a starter, each time **H** transitions through 0 (figure 1-2).

It has been shown theoretically [4] and later proven experimentally [11],[18] that low frequency (Ω_{AC}, $\Omega_{AC}\tau_B < 1$) AC field inflates ferrofluid apparent viscosity, that is $\Delta\eta > 0$ and $\omega < \frac{1}{2}|\nabla\times\mathbf{v}|$. When $\Omega_{AC}\tau_B = 1$, the magnetoviscous effect is nullified ($\Delta\eta = 0$) which is tantamount to $\boldsymbol{\omega} = \frac{1}{2}\nabla\times\mathbf{v}$ or to cancelled friction torque between rdMNP and fluid mixture. High frequency magnetic fields ($\Omega_{AC}\tau_B > 1$) occasion energy transfers from the AC field to the fluid flow *via* rdMNP kinetic energy. It is this "oriented" energy transfer that decreases the apparent viscosity ($\Delta\eta < 0$; $\omega > \frac{1}{2}|\nabla\times\mathbf{v}|$). Unlike what is shown in Figure 1-3 and 1-4, the mechanical torque exerted on the rdMNP is in opposite direction [4]. It is this phenomenon which is referred to as negative rotational viscosity in the literature.

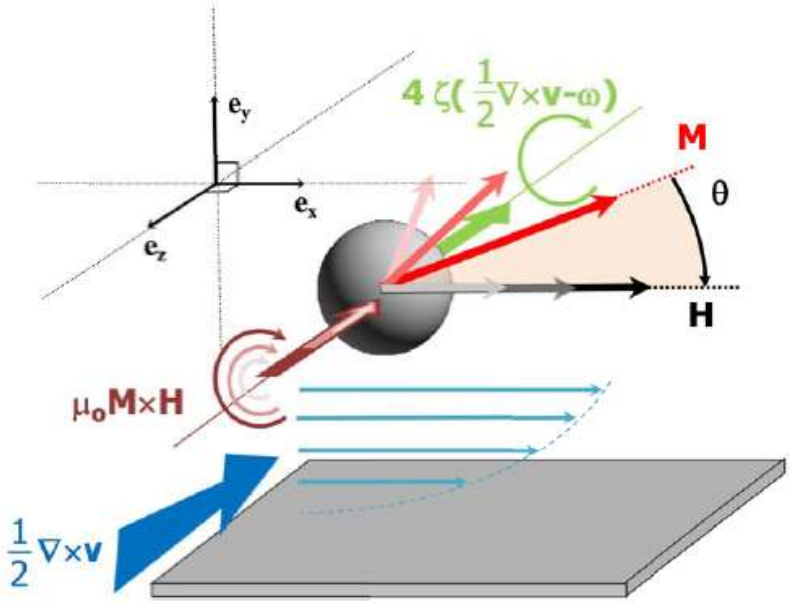

Figure 1-3 : Schematic of MNPs exposed to AC magnetic field in plane Couette or Poiseuille flow in rising art of the cycle. Deviation of magnetization from x direction is caused by fluid vorticity [4]

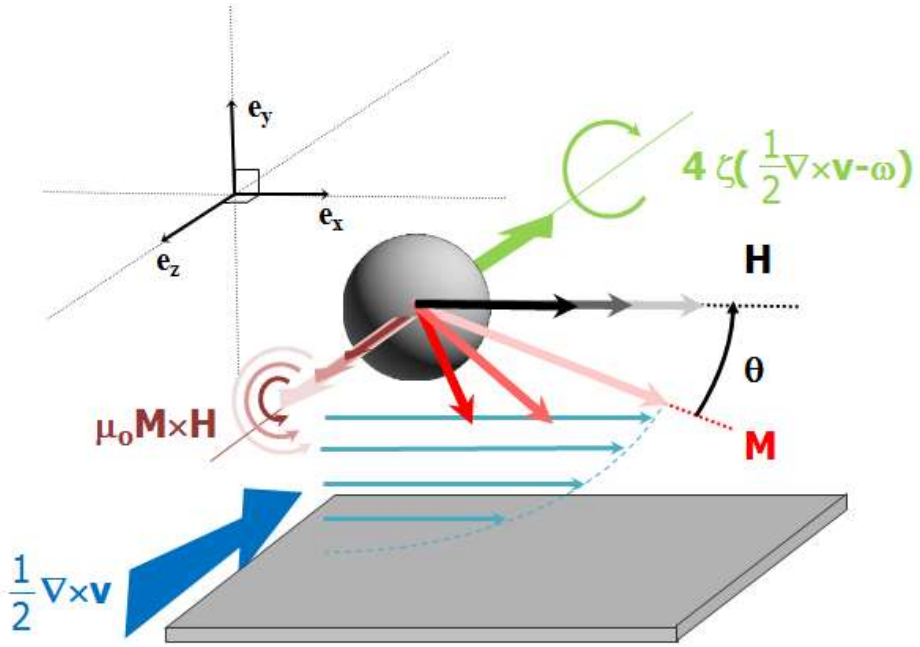

Figure 1-4 : Schematic of MNPs exposed to AC magnetic field in plane Couette or Poiseuille flow in diving part of the cycle. Deviation of magnetization from x direction is caused by fluid vorticity [4]

We have just seen that three characteristic times come into play in ferrofluid AC-field magnetoviscosity. Figure 1-5a-c highlight the three possible scenarios that might occur depending on the values of τ_B, τ_{AC} (= $1/\Omega_{AC}$), and τ_h (= $1/|\nabla\times\mathbf{v}|\approx R/u_{RMS}$). Let us analyze the "rotational" fate of the rdMNP within one AC-field cycle. For case I ($\tau_B < \tau_h < \tau_{AC}$, figure 1-5a), when **H** transitions across zero, Brownian agitation is capable of quickly randomizing the rdMNPs orientations because such reshuffling requires less time than the AC-field period. In addition, since $\tau_h < \tau_{AC}$, the breakage (with respect to fluid vorticity) is the most acutely felt by the rotating rdMNP when **H** is about to peak twice within each cycle, i.e., at its maximum and minimum values (figure 1-2). This breakage gives rise to positive rotational viscosity ($\Delta\eta > 0$). In case II ($\tau_B < \tau_{AC} < \tau_h$, see figure 1-5b), Brownian agitation entails the same effect as in case I. However, remagnetization of the ferrofluid after it is Brownianly reshuffled (near $\mathbf{H} \approx \mathbf{0}$) follows a path similar to the one depicted above in the motionless situation, that is $\omega \approx 0$ when H is decreasing towards –H. This explains in part the occurrence in case II of $\omega < \frac{1}{2}|\nabla\times\mathbf{v}|$ and of the positive rotational viscosity effect. In case III ($\tau_{AC} < \tau_B < \tau_h$, see figure 1-5c), and unlike cases I and II, ferrofluid magnetization survives when **H** comes across **0** because Brownian agitation is too

slow to disorganize the rdMNPs. In addition and unlike in the motionless situation, the vorticity slap is crucial at enabling all the rdMNPs to rotate at diapason to allow a *gyrating* magnetization vector to catch the oscillating magnetic field (figure 1-6). Since rdMNP rotation is locked to the frequency of the magnetic field, and this frequency being faster than fluid vorticity, therefore $\omega > \frac{1}{2}|\nabla \times \mathbf{v}|$ yielding negative rotational viscosity ($\Delta\eta < 0$).

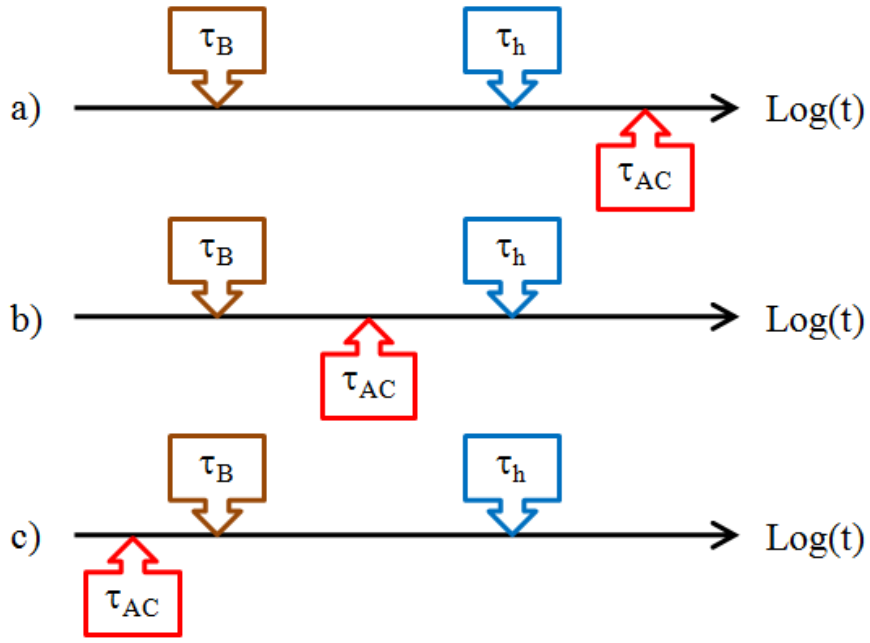

Figure 1-5 : Impact on AC-field magnetoviscosity phenomena with respect to the relative order of Brownian, hydrodynamic and AC characteristic times: a) $\tau_B > \tau_h > \tau_{AC}$, $\Delta\eta>0$; b) $\tau_B > \tau_{AC} > \tau_h$, $\Delta\eta>0$; c) $\tau_{AC} > \tau_B > \tau_h$, $\Delta\eta<0$

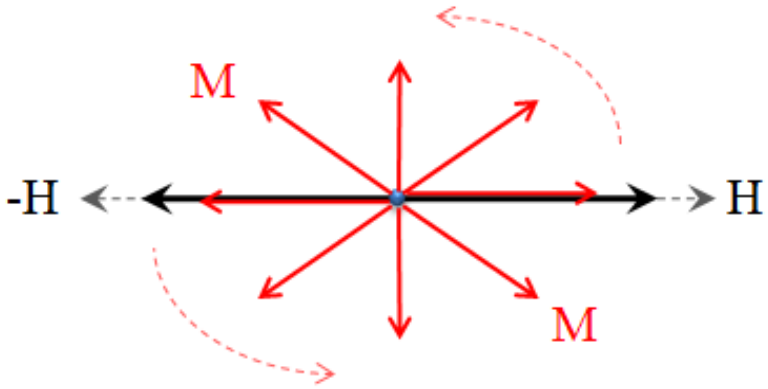

Figure 1-6 : Oscillating magnetic field causes synchronized rotation of rdMNPs when $\tau_{AC} > \tau_B > \tau_h$

The rotating magnetic field (RMF) is generated using a two-pole three phase stator. The major character makes rotating-field magnetoviscosity distinguishable from AC-field

magnetoviscosity is the fact that in former case, neither magnetic field nor magnetization vector pass *via* zero point during a cycle. Thus, Ferrofluid magnetization vector (**M**) tracks **H** regardless of the field frequency. Since there is no off-field moment, thermal agitation mechanism not allowed destroying **M** by shuffling MNPs. As a result, synchronized rotation of rdMNPs is attainable even in low field frequencies. Following all given reasoning, one expects negative rotational viscosity in much lower frequencies rather than AC-field magnetoviscosity. Torque measurement experiments of ferrofluid exposed to RMF performed by MIT group (Rosenthal et al. [8], Rinaldi et al. [19], and He et al. [20]) declare that considerable negative rotational viscosity is achievable. These experiments show even *negative apparent viscosity* $(\eta+\Delta\eta) < 0$ at 50 Hz (96 Gauss field), 100 Hz (60 Gauss), 500 Hz (41 Gauss) using the same size of MNPs as used by Bacri et al. [11]. In literature, RMF magnetoviscosity modeled and treated exactly similar to AC-field magnetoviscosity following Shliomis and Morozov [4] approach. An argument on the puzzling huge frequency difference in negative rotational viscosity manifestation arises using AC-field or RMF is still lacking.

1.2.6 Ferrohydrodynamic transport equations

Solving the ferrohydrodynamic transport equations require embedding the physical concepts relating to Brownian relaxation, magnetization relaxation, and chiefly, magnetoviscosity, into conventional Newtonian non-magnetic fluid transport equations. This was accomplished by Shliomis [10] as explained in details by Rosensweig [2]. Magnetoviscosity entails the formulation of an internal angular momentum balance equation for the magnetic nanoparticles.

The conservation equation of ferrofluid linear momentum writes as:

$$\rho\left(\frac{\partial \mathbf{u}}{\partial t}+\mathbf{u}\cdot\nabla\mathbf{u}\right)=-\nabla p+(\mu+\zeta)\nabla^2\mathbf{u}+2\zeta\nabla\times\boldsymbol{\omega}+\mu_0\mathbf{M}\cdot\nabla\mathbf{H}+(\lambda+\mu-\zeta)\nabla(\nabla\cdot\mathbf{u}) \tag{11}$$

Similarly, the conservation equation of ferrofluid internal angular momentum is:

$$\rho I\left(\frac{\partial \boldsymbol{\omega}}{\partial t}+\mathbf{u}\cdot\nabla\boldsymbol{\omega}\right)=\eta'\nabla^2\boldsymbol{\omega}+2\zeta(\nabla\times\mathbf{u}-2\boldsymbol{\omega})+\mu_0\mathbf{M}\times\mathbf{H}+(\lambda'+\eta')\nabla(\nabla\cdot\boldsymbol{\omega}) \tag{12}$$

where ρ is the fluid density, I is the moment of inertia per unit mass of MNPs, **u** is the linear flow velocity vector, **ω** is the spin velocity vector (i.e., average spin rate of all MNPs p.u.v. of ferrofluid [**Erreur ! Signet non défini.**]), p is hydrodynamic pressure, μ is the ynamic shear viscosity, λ is the dilatational viscosity, η′ is the shear spin viscosity, λ′ is the bulk spin viscosity, ζ is the vortex viscosity, and μ_0 is the vacuum permeability. To get a better grasp on understanding equation 11 and 12, it is convenient to recall the physical meaning of each term.

Equation 11 RHS aggregates all the terms contributing to the production or consumption of linear momentum for polar fluid endowed with internal angular momentum. The vortex viscosity increment, ζ, represents the effect of nanoparticles on mixture viscosity, in Newtonian suspension flows, regardless of their magnetic character or application of magnetic field [1],[2]. The next term in equation 11 points out that non-uniform spin velocity may induce linear momentum through vortex viscosity. The Kelvin body force term, $\mu_0\mathbf{M}\cdot\nabla\mathbf{H}$, stems in situations where a spatially inhomogeneous magnetic field is exerted on incompressible ferrofluids. The last term in equation 11 is often dropped for incompressible ferrofluids, which is a common assumption.

The RHS first term in equation 12 derived from the divergence of spin gradient tensor stands for spin viscous diffusion between rotating MNP clumps (in the volume average sense) laying in the same neighborhood. The second term represents inter-conversion between internal and external angular momenta. Fluid vorticity represents the flow tendency to rotate free infinitesimal elements, such as MNP, while **ω**, the actual MNP spin rate, arises from the magnetic torque felt by the MNP. As a result, this coupling transfers angular momenta between MNP and ferrofluid. The magnetic body couple density, $\mu_0\mathbf{M}\times\mathbf{H}$, stands for the magnetic torque exerted on the magnetic particles and driving their rotation. In some specified flow geometries, the MNP spin velocity vector field, appearing in the last term of equation 12, is assumed solenoidal [2],[21]. One such a geometry in which $\nabla\cdot\boldsymbol{\omega} = 0$ occurs when the 2nd and 3rd terms of equation 12 RHS are collinear with fluid vorticity $\frac{1}{2}\nabla\times\mathbf{u}$ vector as exemplified in figure 1-7 [22-24]. Fluid vorticity is parallel to y-direction before applying magnetic field as is also the case with $\mu_0\mathbf{M}\times\mathbf{H}$ when the field is enabled. As a result, $\omega_x = \omega_z = 0$ and ω_y is only x dependent.

The ferrofluid continuity and conservation equations of the linear and internal angular momenta combined with one of the magnetization relaxation equations discussed in section *II.5*, are in principle closed by adjoining the Maxwell equations. Maxwell's equations consist of the Gauß's law for magnetic flux density and the (zero free-current density) Ampere's law for magnetic field intensity, respectively:

$$\nabla \cdot \mathbf{B} = 0, \quad \nabla \times \mathbf{H} = \mathbf{0} \tag{13}$$

Vector fields **B, H** and **M** are related through the well-known **BHM** constitutive equation:

$$\mathbf{B} = \mu_0 (\mathbf{M} + \mathbf{H}) \tag{14}$$

In equation 14, **B** and **H** are, respectively, *total* magnetic flux density and *total* magnetic field intensity in which both external field and induced field generated by (and felt within) ferrofluid are summed-up. Outside the ferrofluid domain, for instance in the non-magnetic surrounding material, the contribution of magnetization *via* BHM constitutive equation is marginal ($\chi \approx 0$) with **B** and **H** only generated by the sources external to the non-magnetic material (i.e., including the ferrofluid magnetization contribution).

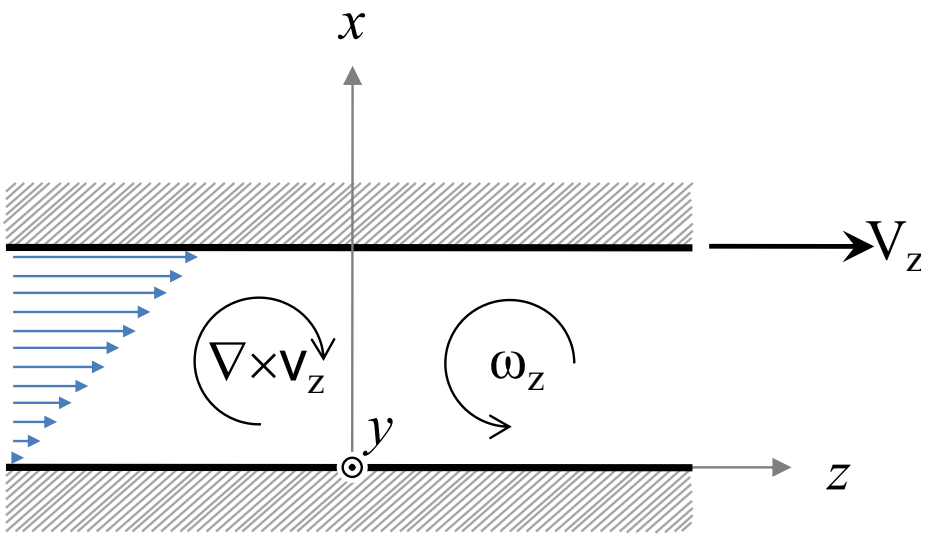

Figure 1-7 : Couette flows of ferrofluid confined between two parallel plates subject to magnetic field. Adapted from [22]

1.3 Application

1.3.1 Pipe flow momentum transfer

Further than the experiments performed in AC fields by Bacri et al. [11] and Zeuner et al. [18] to validate the magnetoviscosity theory, Schumacher et al. [25] aimed at investigating the effect of AC fields on pressure drop of ferrofluid pipe flow in laminar and turbulent regime. They also proposed a computational model based on ferrohydrodynamic theory and accompanied it with experimental data. Schumacher et al. [25] tested AC (in the [0-1] kHz range) magnetic field in the range [0 - 1264] Oe with a ferrofluid passing through 3 mm inner diameter tube. They defined the fractional pressure drop ($fPd = \Delta P(H)/\Delta P(H = 0) - 1$) merely as the relative variation of (downstream) pressure drop subject to H (inside solenoid) with respect to (upstream) pressure drop (outside solenoid, i.e., $H = 0$) over equal tube lengths and fully developed flows. As illustrated in figure 1-8, *fPd* was obtained for a range of Reynolds numbers covering laminar and transitional flow regimes. This figure highlights a strong dependence of *fPd* to flow rate. Based on the arguments discussed above regarding AC-field magnetoviscosity, *fPd* can take negative values (i.e., negative pressure drop) only if $\Omega_{AC}\tau_B > 1$. The maximum $\Omega_{AC}\tau_B$ reached by Schumacher et al. [25] was 0.061 thus explaining why only $fPd > 0$ were reported coherent with expectation from theory. In the two sub-sections below we will try to summarize the modeling efforts by these authors regarding the ferrohydrodynamic models in laminar and turbulent pipe flows.

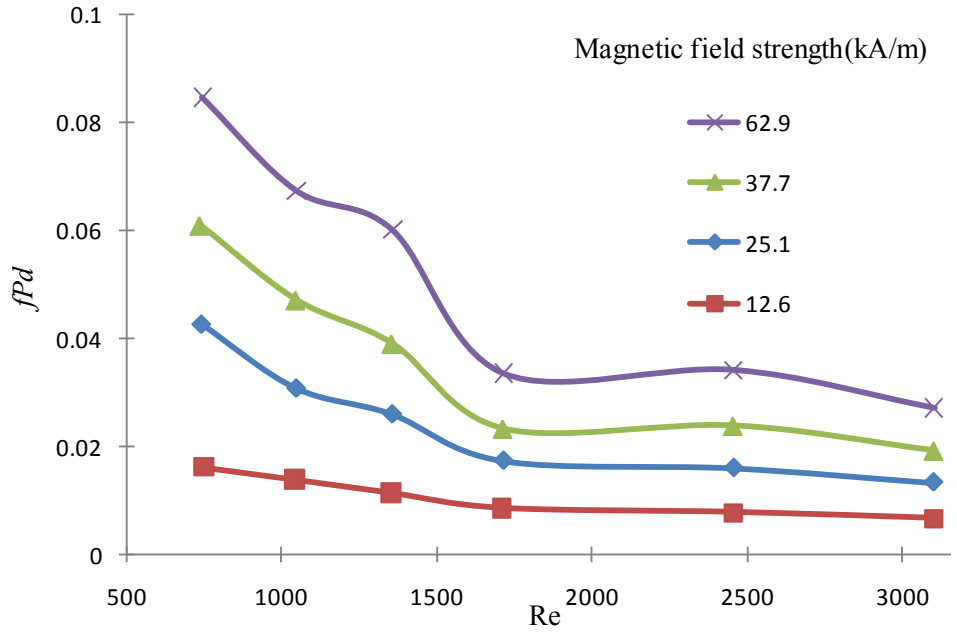

Figure 1-8 : Fractional pressure drop versus ferrofluid Reynolds number measured at different strengths of 400 Hz AC magnetic field. Adapted from [25]

Table 1 lists the parameters used by Schumacher et al. [25] in their ferrofluid flow simulations.

Table 1-1 : Parameters used in ferrofluid laminar and turbulent simulations [25]

	Laminar Flow Model	Turbulent Flow Model
μ (Pa s)	3.85×10^{-3}	3.85×10^{-3}
ρ (kg m^{-3})	1187.4	1187.4
ζ (Pa·s)	1.93×10^{-3}	1.93×10^{-3}
η' (kg·m·s^{-1})	6.40×10^{-20}	6.40×10^{-20}
$C_1 = \zeta/\mu$	0.5	0.5
$C_3 = \eta'/R^2\zeta$	1.5×10^{-11}	1.5×10^{-11}
Q (mL·min^{-1})	500	1400
H (Oe)	948	948
Ω (Hz)	60	60
τ_B (μs)	1.5	1.5
χ_0	0.04	0.04
φ	0.025	0.025

1.3.2 Ferrohydrodynamic laminar model

Schumacher et al. [25] solved the one-dimensional axisymmetrical laminar version of pipe flow ferrohydrodynamic model in which the continuity, the linear momentum (equation 11), the angular momentum (equation 12), and the magnetization relaxation (equation 7) equations were simplified into a set of four algebraic 2nd-order differential equations for solving the axial ferrofluid velocity component (u), the MNP spin rate ($\omega = \omega_\theta$), the axial pressure gradient ($-dp/dz$) and the magnetic torque density $(\mathbf{M}\times\mathbf{H})_\theta$ as a function of pipe radial coordinate, r. The following assumptions were made:

* (Pseudo)-steady-state flow, $\partial/\partial t = 0$;

* Axisymmetry, $\partial/\partial\theta = 0$;

* Fully developed flow for ferrofluid velocity and MNP spin rate, $\partial u/\partial z = 0$, $\partial\omega/\partial z = 0$;

* Ferrofluid flow is incompressible, i.e., $\nabla\cdot\mathbf{u} = 0$, which is also supported by the fully developed flow assumption;

* In the absence of magnetic field, the spin rate vector $\boldsymbol{\omega}$ is in θ direction. According to AC magnetoviscosity theory [4] summarized above, streamwise $\mathbf{H}$ oscillations constrain $\boldsymbol{\omega}$ to keep along θ direction yielding $\nabla\cdot\boldsymbol{\omega} = 0$ (i.e., $\partial\omega/\partial\theta = 0$). This supports the above axisymmetry assumption;

* The spatially uniform magnetic field entrains that $\mathbf{M}\cdot\nabla\mathbf{H} = \mathbf{0}$ in equation 11;

* Viscous forces are dominant so that inertial effects in equation 11 are negligible as well as in equation 12 so that $\rho I(\mathbf{u}\cdot\nabla\boldsymbol{\omega}) = \mathbf{0}$;

* By extension, inertial effects on transporting magnetization are also neglected in equation (7), $\mathbf{u}\cdot\nabla\mathbf{M} = \mathbf{0}$. This is justified by the fact that in uniform magnetic field, magnetization spatial dependency is only due to velocity field gradient $\nabla\mathbf{u}$ which is perpendicular to $\mathbf{u}$ in the studied geometry.

Therefore, the linear and internal angular momentum balance equations simplify to:

$$\frac{(\mu+\zeta)}{r}\frac{\mathrm{d}}{\mathrm{d}r}r\frac{\mathrm{d}u}{\mathrm{d}r}+\frac{2\zeta}{r}\frac{\mathrm{d}(\omega r)}{\mathrm{d}r}-\frac{\mathrm{d}p}{\mathrm{d}z}=0 \tag{15}$$

$$\eta'\left(\frac{\mathrm{d}^2\omega}{\mathrm{d}r^2}+\frac{1}{r}\frac{\mathrm{d}\omega}{\mathrm{d}r}+\frac{\omega}{r^2}\right)-2\zeta\left(\frac{\mathrm{d}u}{\mathrm{d}r}+2\omega\right)+\left\langle\mu_0\left(\mathbf{M}\times\mathbf{H}\right)_\theta\right\rangle_{1/\Omega_{AC}}=0 \tag{16}$$

Regarding description of the hydrodynamic effects on the magnetization relaxation phenomenon, Schumacher et al. [25] bypassed the necessity to solve the magnetization relaxation equation by averaging the magnetic body couple density over one cycle of the AC field and by including it in the pseudo steady-state angular momentum balance equation 16. Following the same assumption, Zahn and Pioch [23] derived an expression for the time-averaged magnetic body couple density for planar Couette flow subject to a rotating magnetic field.

$$\begin{aligned}
&T_0\equiv\frac{\left\langle\mu_0\left(\mathbf{M}\times\mathbf{H}\right)_\theta\right\rangle_{1/\Omega_{AC}}}{\mu_0 H_0^2}=\frac{0.5}{a^2+b^2}\chi_0\left[a\left(e-c\right)-\chi_0\left(ce+df\right)\right]\\
&a=\left(\omega\tau\right)^2-\left(\Omega_{AC}\tau\right)^2+1+\chi_0\,,\quad b=\Omega_{AC}\tau\left(2+\chi_0\right),\\
&c=\omega\tau+1\,,\quad d=f=\Omega_{AC}\tau\,,\quad e=\left(1+\chi_0\right)-\omega\tau
\end{aligned} \tag{17}$$

Schumacher et al. [25] assumed this expression also valid in his AC field Poiseuille flow experiments and used it in equation 16. Schumacher et al. [25] assumed also a rotation of the magnetization vector, in flow conditions, to track the AC magnetic field. Let us evaluate the likelihood of this assumption in the light of the Shliomis and Morozov [4] AC-field magnetoviscosity theory explained in section *II.5*. In laminar flow for *Re* = 1090, the hydrodynamic time scale is estimated to be τ_h = 1.3 ms, whereas in the transitional flow region for *Re* = 4160 (the highest *Re* value hit in the authors' tests) τ_h = 0.3 ms. The Brownian time scale estimated by Schumacher et al. [25] was τ_B = 1.5 µs. For an AC field, τ_{AC} = 8.3 ms, 1.2 ms, 0.5 ms, respectively, for 60 Hz, 400 Hz and 1000 Hz frequencies. According to figure 1-5 taxonomy, a positive rotational magnetoviscosity prevails in Schumacher et al. [25] tests regardless of AC field frequency. In our opinion, this might affect the hypothesis regarding rotation of the magnetization vector because the magnetization vector may decay twice towards zero during one cycle due to Brownian relaxation in the laminar case, and Brownian and fluid vorticity mechanisms in the transitional case. *Stricto sensu*, this entrains that the magnetization vector keeps nearly

parallel to the magnetic field thus yielding on the contrary a nearly zero time-averaged magnetic body couple density instead of what is suggested by equation 17. A *post facto* justification of this interpretation indeed comes out from the authors' own simulations. For example in figure 1-9 (adapted from figure 1-9 in [25]), it is suggested that MNP spin velocity take the same values as (no-magnetic-field) fluid vorticity. However, the radial velocity profiles with and without magnetic field are virtually identical suggesting that fluid vorticity remains nearly indifferent to magnetic field.

To improve model representation of pressure drop experiments, the authors also assumed an *ad hoc* empirical correction of initial magnetic susceptibility vis-à-vis the applied magnetic field intensity. They also found that τ_B needed to be readjusted in laminar flow regime for each of the AC-field frequencies (Ω_{AC}) and for each flow rate. This further assumption was justified by the authors as due to the possibility of MNPs agglomeration to form clusters in laminar flow which would imply larger Brownian relaxation time constants instead of the theoretical single MNP equation 6. Figure 1-10 illustrates the fitted cluster Brownian relaxation times normalized by the single MNP τ_B as a function of *Re* and parameterized by AC field frequency. It can be seen that the higher the *Re* (similarly, the higher the Ω_{AC}), the lower the τ_B. In the transitional flow regime, the higher shear stresses involved would likely go against cluster formation whereby single MNP τ_B value is sufficient to describe the *Re* and AC field frequency changes. Figure 1-12a-c gather the simulated *fPD* as a function of *Re* and parameterized with different magnetic field intensities for three different AC field frequencies. The simulated *fPD* measurements in laminar flow concern the left portion of these figures. It is worthy of notice that the good match between model and measurements is the resultant of the above mentioned two fitted parameters, which indicates that there is still room for developing fully predictive Poiseuille flow models Krekhov et al. [26].

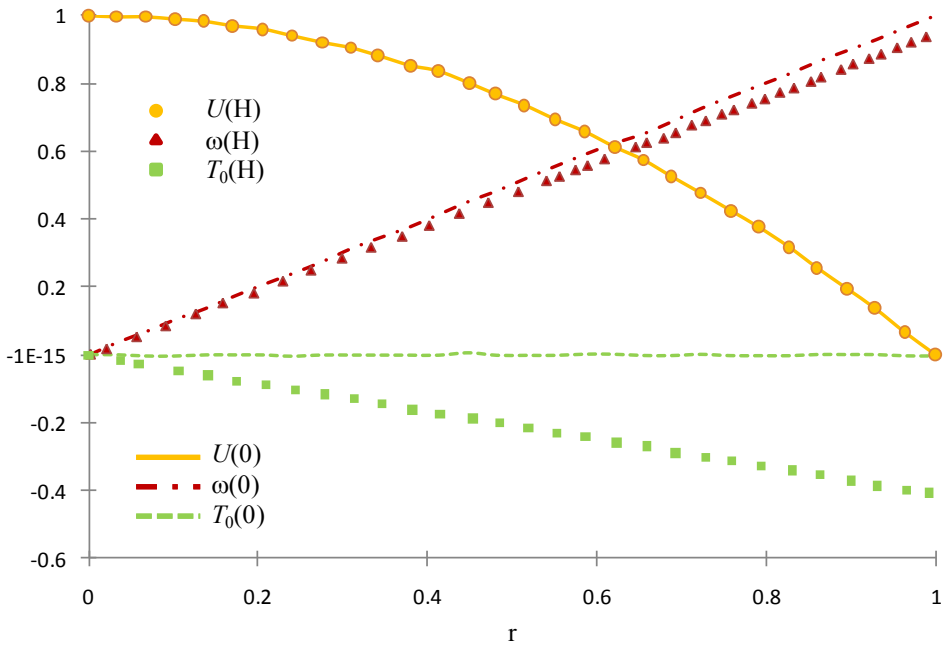

Figure 1-9 : Simulated profiles of normalized velocity U, spin velocity ω and averaged magnetic body torque T0 for ferrofluid laminar pipe flow exposed to oscillating magnetic field (948 Oe, 60 Hz) in comparison with zero field profiles. Adapted from [25].

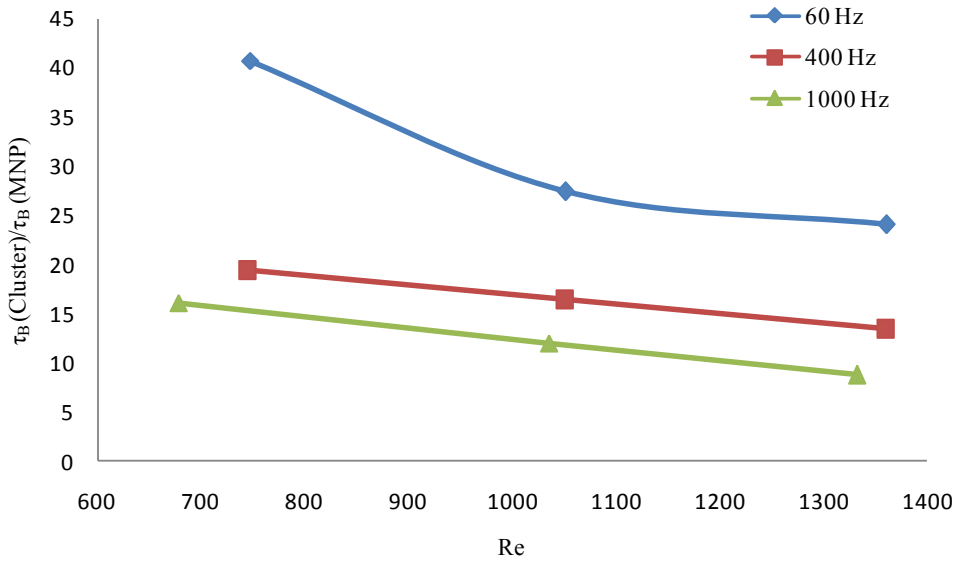

Figure 1-10 : Fitted Brownian time constant versus ferrofluid Reynolds number at different AC-field frequencies. Adapted from [25])

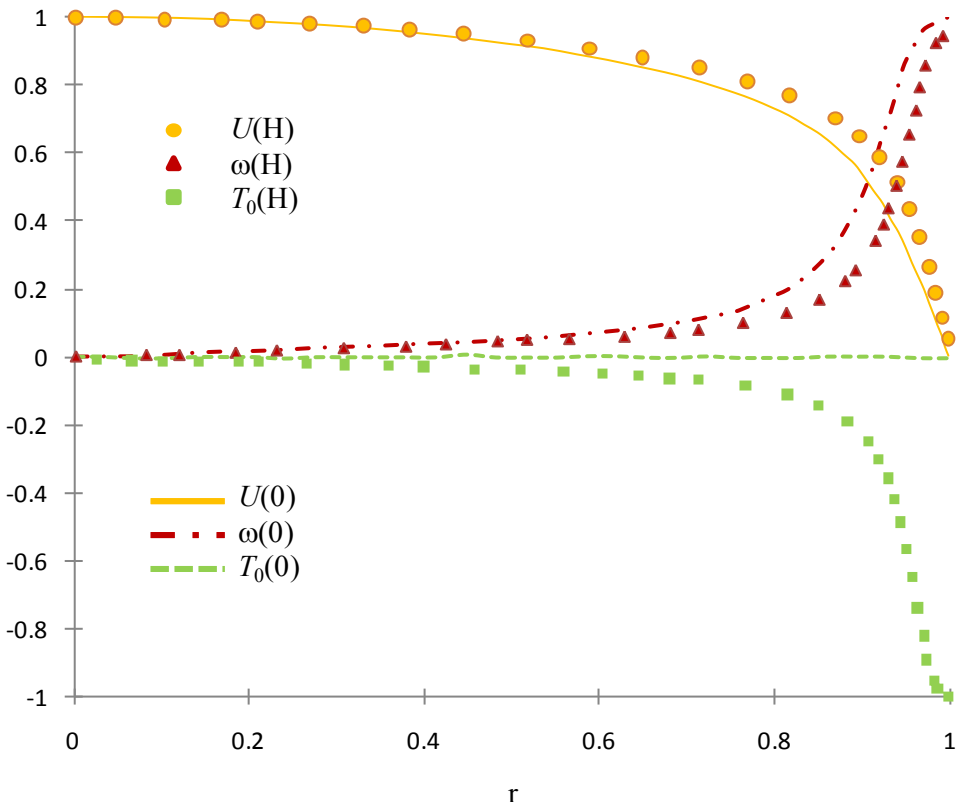

Figure 1-11 : Simulated profiles of normalized velocity U, spin velocity ω and averaged magnetic body torque T0, turbulent kinetic energy k and turbulent dissipation rate ε for ferrofluid turbulent pipe flows exposed to oscillating magnetic field (948 Oe, 60 Hz). Adapted from [25].

a

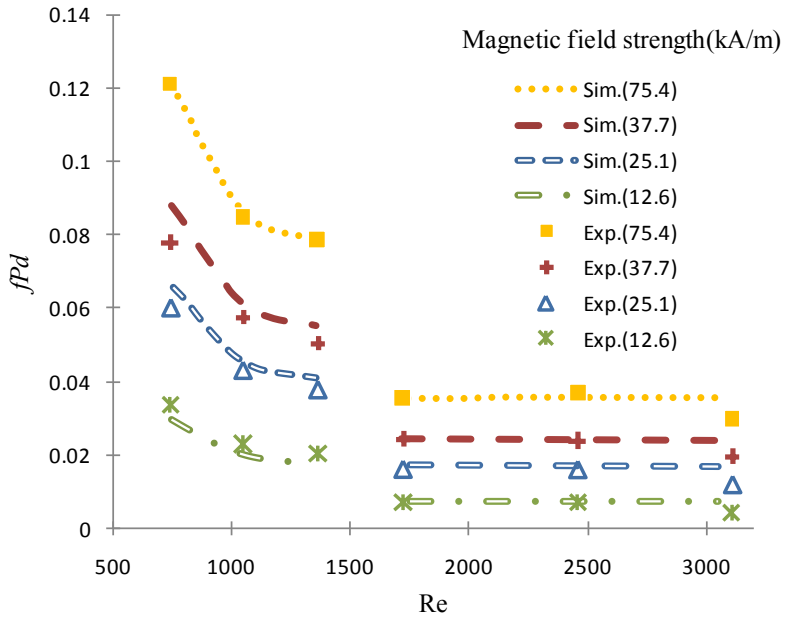
Magnetic field strength(kA/m)
Sim.(75.4)
Sim.(37.7)
Sim.(25.1)
Sim.(12.6)
Exp.(75.4)
Exp.(37.7)
Exp.(25.1)
Exp.(12.6)
fPd
Re
0.14
0.12
0.1
0.08
0.06
0.04
0.02
0
500
1000
1500
2000
2500
3000

b

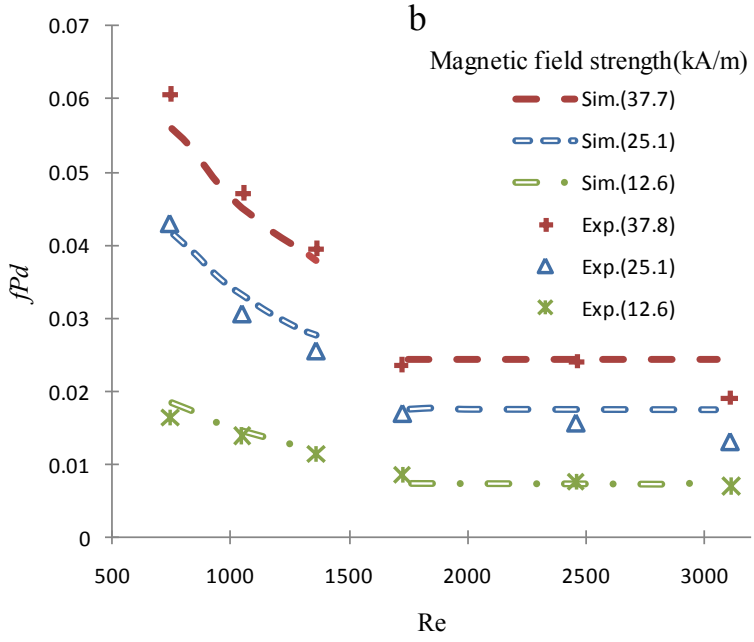
Magnetic field strength(kA/m)
Sim.(37.7)
Sim.(25.1)
Sim.(12.6)
Exp.(37.8)
Exp.(25.1)
Exp.(12.6)
fPd
Re
0.07
0.06
0.05
0.04
0.03
0.02
0.01
0
500
1000
1500
2000
2500
3000

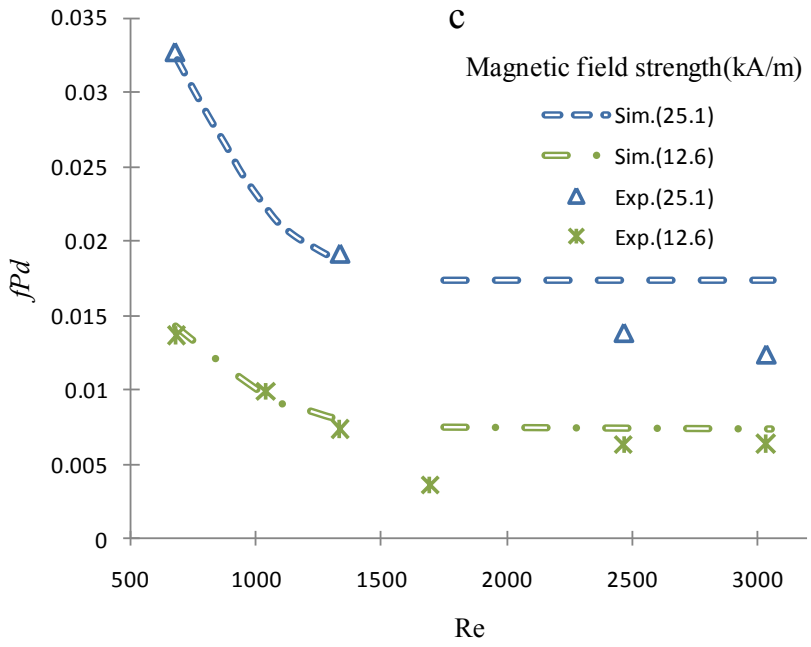

Figure 1-12 : Comparison of simulated Re-dependent fractional pressure drop with experimental data for different oscillating magnetic field strength. Magnetic field frequency (a) 60 Hz, (b) 400 Hz, (c) 1000 Hz. Adapted from [25].

1.3.3 Ferrohydrodynamic turbulent model

The main assumption made by Schumacher et al. [25] is to analogize ferrofluid turbulent behavior to that of a Newtonian fluid suspension with inflated dynamic viscosity, $(\mu + \zeta)$. In their proposed framework, the range of the eddy sizes, from the Kolmogorov length microscale (i.e., smallest eddy size) to the system's integral length scale [27], is not overlapping with the much smaller MNP length scale. Derivation of time-averaged (turbulent flow) forms of ferrofluid linear and angular momentum balance equation 15 and 16 was attempted. A low Reynolds number k-ε model was applied to close the Reynolds turbulence stress tensor in the time-averaged linear momentum balance. An important assumption was that magnetoviscosity does not affect turbulent kinetic energy and turbulent kinetic energy dissipation rate [25]. Since time averaging of the angular momentum was taken over one cycle of the AC magnetic field, the averaged angular equation ignored turbulence connection to spin velocity as if the remote action of magnetic fields on the rotation of the MNPs would remains unfelt at the eddy scale. This is perhaps a gross approximation as is evident from the RHS second term of equation 12 after introducing the Reynolds decomposition on velocity field, $u = \langle u \rangle + u^*$. In $2\zeta(\nabla \times \mathbf{u} - 2\boldsymbol{\omega})$, MNP spin

perturbation originates from two vorticity sources out of the time-average velocity component (<u>) and the fluctuating velocity component (u*).

Simulations using the low-Reynolds k-ε turbulence model of the time-average radial profiles of axial velocity component, MNP spin velocity and cycle-averaged magnetic torque density are shown in figure 1-11 for a magnetic field intensity of 948 Oe and AC-field frequency of 60 Hz. Simulations with disabling the magnetic field are also shown for the similar hydrodynamic variables. Figure 1-12a-c gather the simulated *fPd* data in the non-laminar region (Figure 1-12 right portion) for the same magnetic field features given in the previous section *III.1.1*. These figures suggest that the simulated *fPd* are fairly well in agreement in comparison to their measured counterparts. The proposed k-ε turbulent model represented the *fPd* experimental data successfully in AC-magnetic fields.

Very recently, Schumacher et al. [15] provided a rigorous homogeneous turbulent model for ferrofluid flow subject to steady spatially uniform magnetic field in which flow is simulated in a cube with periodic boundary conditions. An important innovation in their work is the additive inter-conversion of three energy terms representing different forms of energies in ferrofluid including translational kinetic energy $(\rho/2)u_i^2$, rotational kinetic energy $(\rho I/2)\omega_i^2$, and internal energy U. Time averaging after Reynolds decomposition of the dependent variables, the Reynolds-averaged forms of linear and internal angular momentum and continuity equations were arrived at. In addition to the classical Reynolds turbulence stress tensor, the averaging procedure brings out three additional nonlinear fluctuating tensors through decomposition of the magnetic field intensity, magnetic flux density and magnetization fields into fluctuating and time average contributions. These terms are namely the turbulent transport flux of fluctuating spin velocity, the fluctuating Kelvin body force, and the fluctuating body couple density, all of which requiring closures. By assuming zero mean velocity and zero spin gradients as well as homogeneous turbulence, to turn to zero all the spatial gradients of averaged quantities, Schumacher et al. [15] proposed expressions for the mean kinetic (translational and rotational) energies and mean internal energy:

$$\frac{dE_t}{dt} = -\varepsilon_V - \varepsilon_A - \Phi_b + \Psi$$
$$\frac{dE_r}{dt} = -\varepsilon_C + \Phi_b + \Psi_S$$
$$\frac{dU_{int}}{dt} = \varepsilon_V + \varepsilon_A + \varepsilon_C \tag{18}$$

where, $E_t = \frac{1}{2}\rho\overline{u_i'^2}$, $E_r = \frac{1}{2}\rho I\overline{\omega_i'^2}$, $U_{int} = \rho\hat{\bar{U}}_{int}$, $\varepsilon_V = 2\mu\overline{e_{ij}'e_{ij}'}$, $\varepsilon_A = \frac{1}{4\zeta}\overline{A_i'A_i'}$, $\varepsilon_C = 2\eta'\overline{s_{ij}'s_{ij}'}$, $\Psi = \overline{u_i'S_i'}$,

$\Phi_b = \overline{\omega_i'A_i'}$, $\Psi_s = \overline{\omega_i'Q_i'}$

where ε_V is the viscous dissipation rate of translational turbulent kinetic energy due to viscous shear stresses, ε_C is the dissipation rate depicting the loss of rotational kinetic energy due to the couple stresses, Φ_b is the rate of work done on the spin by the asymmetric stresses, and results in the transfer of translational kinetic energy to (or from) rotational kinetic energy, ε_A is the dissipation rate of translational kinetic energy due to antisymmetric part of the stress, Ψ is the rate of work done on the turbulent flow by the magnetic body forces, and Ψ_s is the rate of work done on the turbulent flow by the magnetic body couples [15]. These five terms are novelties introduced in this turbulent ferrofluid model. Omitting those degenerates the energy conservation equation to the one as derived for Newtonian fluids.

In their numerical simulations, Schumacher et al. [15] expanded the fluctuating variables as finite three-dimensional Fourier series before performing direct numerical simulation of a ferrohydrodynamic turbulent flow. In the absence of magnetic field, Schumacher et al. [15] showed that ferrofluids behave similarly to a Newtonian fluid. Table 2 lists the magnetic and hydrodynamic properties used in turbulent simulations. Time-average root mean square components of spin velocity and linear velocity are listed in Table 2. This table indicates that uniform magnetic fields do not affect the RMS fluctuating velocities in turbulent flow simulations. However, there are indications that magnetic fields bring considerable anisotropic dampening in the fluctuations for the two spin velocity components normal to the magnetic field. Induced magnetic field fluctuations and magnetization fluctuations due to turbulence were also estimated by Schumacher et al. [15] for their particular cubic ferrofluid element. Table 3 illustrates the marginal contributions of the simulated RMS

fluctuating magnetic field and resulting fluctuating magnetization to the applied magnetic field $H = 251$ A·cm^{-1} and mean magnetization $M = 68.3$ A·cm^{-1}. It is worth mentioning that although these fluctuations remain very small in comparison to the mean values, one should be alert that these fluctuations may exhibit non-negligible spatial gradients that could cause significant magnetic body force (via $\nabla \mathbf{H}'$) or magnetic convection (via $\nabla \mathbf{M}'$) terms.

The effect of magnetic field intensity on spin velocity fluctuation and velocity fluctuation is illustrated in figure 1-13a, b as a function of the dimensionless magnetic field (ξ) and using the various most popular magnetization relaxation equations. The damping effect of magnetic field on spin velocity fluctuation is remarkable whereas the velocity fluctuations are barely influenced as already discussed from table 3 data. The effect of magnetic field strength on energetic terms in equation 18 is illustrated in figure 1-13 using the Shliomis [10] and Martsenyuk et al. [6] magnetization relaxation equations. An instructive display is shown on how energy dissipation terms are mutually involved in converting energy due to an interacting external magnetic field. The slight decrease of ε_V is very well understood by the fact that the decrease of u_{RMS} versus magnetic field is marginal. The blocking effect of magnetic field on spin velocity fluctuations (Table 3, Figure1-13a) is mirrored by a reduction in energy dissipation via ε_C. The increasing trend of ε_A as magnetic field is increased can be understood as a hindrance effect by the decreasing spin velocity fluctuations (Figure 1-13b) on ferrofluid vorticity.

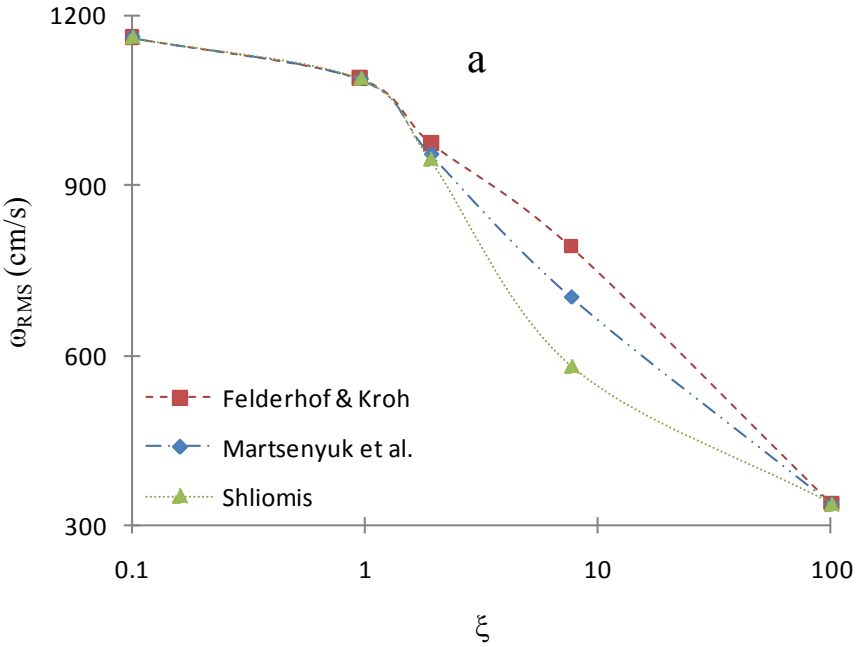
a
1200
900
600
300
ω_{RMS} (cm/s)
Felderhof & Kroh
Martsenyuk et al.
Shliomis
0.1
1
10
100
ξ

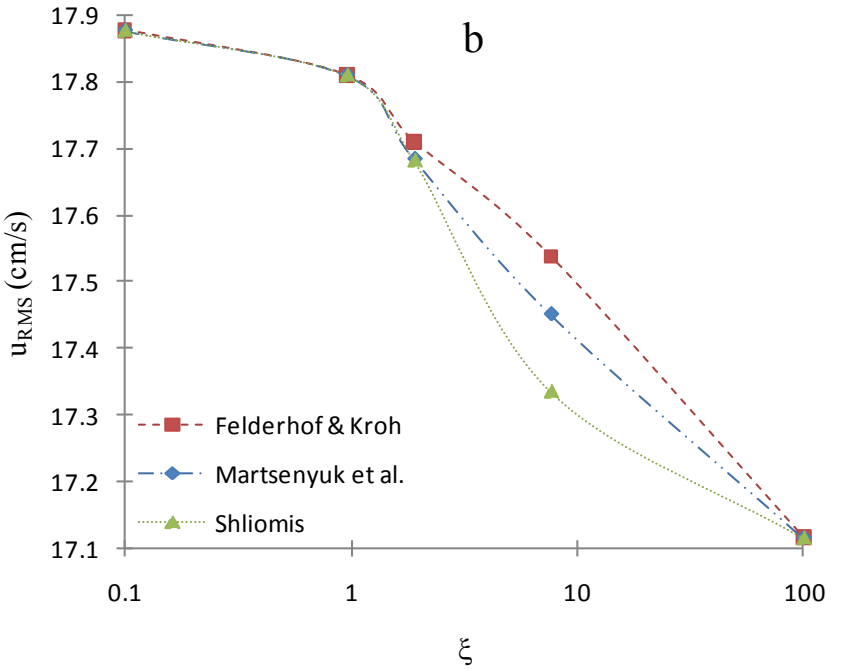
b
17.9
17.8
17.7
17.6
17.5
17.4
17.3
17.2
17.1
u_{RMS} (cm/s)
Felderhof & Kroh
Martsenyuk et al.
Shliomis
0.1
1
10
100
ξ

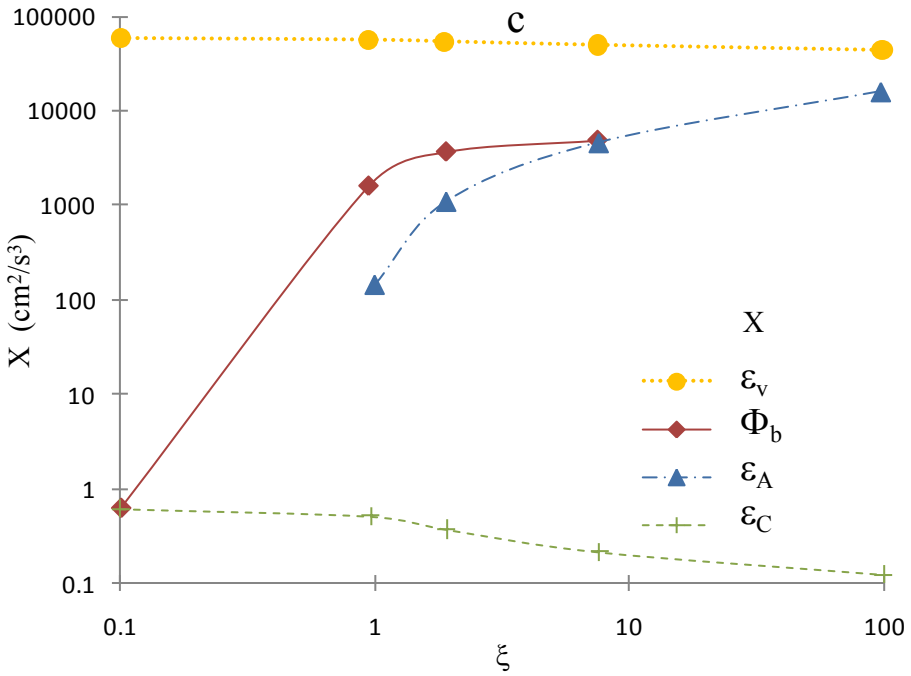

Figure 1-13 : Effect of magnetic field strength (embedded in dimensionless magnetic field, □) on (a) RMS spin velocity, (b) RMS linear velocity, (c) on averaged energy terms: ◊ for Φ_b; ○ for ε_v; □ for Ψs; + for ε_C; Δ for ε_A, in turbulent model. Adapted from [15]

Table 1-2 : Magnetic and hydrodynamic parameters used in ferrofluid turbulent simulations [15]

d_p (nm)	10
d_h (nm)	29.5
μ (Pa.s)	3.85×10^{-3}
ρ (kg·m^{-3})	1187.4
m_p (A·m^2)	2.5×10^{-19}
M_s (Oe)	164
ζ/μ	0.5
η' (kg·m·s^{-1})	2×10^{-15}
τ_B (μs)	10
H (Oe)	158, 316, 1264
χ_0	0.332
T (K)	298.15
d_{tube} (mm)	3
Re	3100
u_{RMS} (cm·s^{-1})	20.9

Table 1-3 : Time-averaged 3-D spin velocity, ferrofluid velocity, induced magnetic field and magnetization RMS components of turbulent flow as simulated in [15]

H (Oe)	0	158	316	1264
$\sqrt{\overline{\omega_x'^2}}$ (s^{-1})	379	375	368	355
$\sqrt{\overline{\omega_y'^2}}$ (s^{-1})	401	364	295	178
$\sqrt{\overline{\omega_z'^2}}$ (s^{-1})	381	345	280	169
$\sqrt{\overline{u_x'^2}}$ (cm s^{-1})	19.8	-	19.5	-
$\sqrt{\overline{u_y'^2}}$ (cm s^{-1})	22.2	-	22.1	-
$\sqrt{\overline{u_z'^2}}$ (cm s^{-1})	19.6	-	19.4	-
$H = 251$ A·cm^{-1}				
	$\sqrt{\overline{H_x'^2}}$ (A·cm^{-1})	0.049	$\sqrt{\overline{M_x'^2}}$ (A·cm^{-1})	0.009
	$\sqrt{\overline{H_y'^2}}$ (A·cm^{-1})	0.062	$\sqrt{\overline{M_y'^2}}$ (A·cm^{-1})	0.120
	$\sqrt{\overline{H_z'^2}}$ (A·cm^{-1})	0.069	$\sqrt{\overline{M_z'^2}}$ (A·cm^{-1})	0.125

1.3.4 Porous media momentum transfer

Taktarov [28, 29] was the first author who considered the motion of magnetizable fluids in porous media. In his study, volume-average formulations of the equations of motion were derived for magnetizable non-electroconductive liquids in nonmagnetic porous media subject to external non-uniform magnetic fields. Spatial averaging was applied for the linear momentum conservation equation (equation 11) assuming zero vortex viscosity ($\zeta = 0$). This led to the neglect in his analysis of formulating an internal angular momentum conservation equation.

More recently, Larachi and coworker, [30-33] developed a model of ferrofluid flow through porous media in presence of steady non-uniform magnetic field. The effect of static field magnetoviscosity and magnetic body force on flow behavior was numerically investigated. The starting point of the approach was the microscale ferrohydrodynamic set of ferrofluid phasic equations as depicted in section *II.6*. Employing spatial averaging theorems, the microscale formulation was muted into macroscale ferrohydrodynamic model equations which led to numerous additional closure terms. Spatially-averaged continuity, linear momentum balance, internal angular momentum balance, and magnetization relaxation equations plus Gauß's law and Ampere's law were obtained for 3-D axisymmetrical cylindrical geometry. The system of partial differential equations was solved for a ferrofluid flow inside packed bed porous media subject to a linearly increasing (or decreasing) external magnetic field in direction of bulk flow (figure 1-14). One application sought out of this work was a magnetic remote control of fluid velocity patterns aimed at overcoming wall channeling and flow short-circuiting in packed beds with low column to particle diameter ratios. As many of the 15 closure terms arouse through volume averaging, some assumptions were made to decouple the ferrohydrodynamic model into a hydrodynamic sub-model and a magnetostatic sub-model. This decoupling was mainly motivated by convergence difficulties associated with induced magnetic field effects. An important result stemming from their simulations was a dramatic reduction of spin velocity due to the external magnetic field close to the packed bed wall (figure 1-15), together with better approach to plug-flow radial velocity profile despite the large permeability contrasts between bed core and wall (figure 1-16). Magnetoviscosity effect was found to prevail mostly close to the wall (figure 1-15).

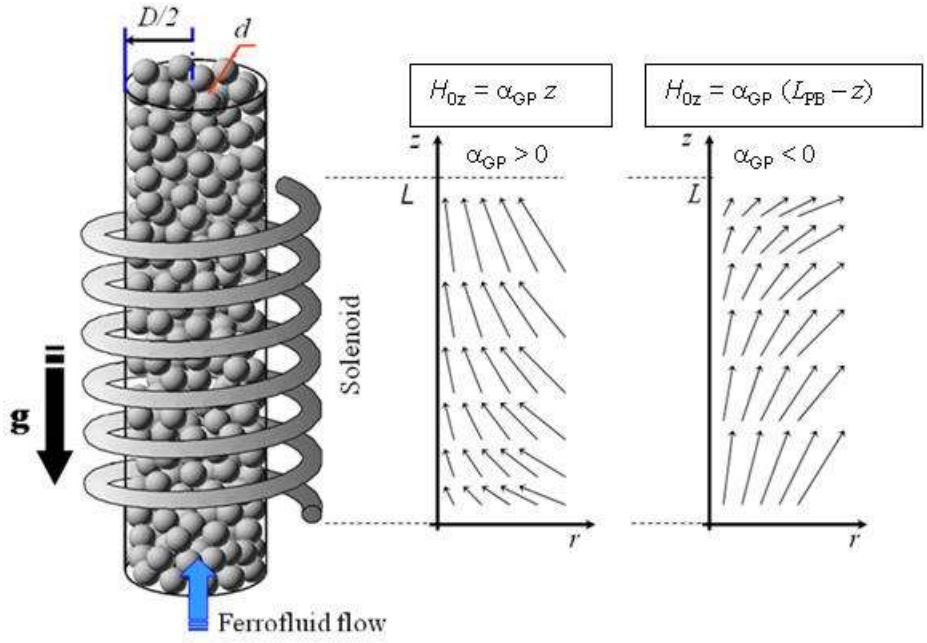

Figure 1-14 : Porous medium and flow details: Packed bed and magnetic field programming [30]

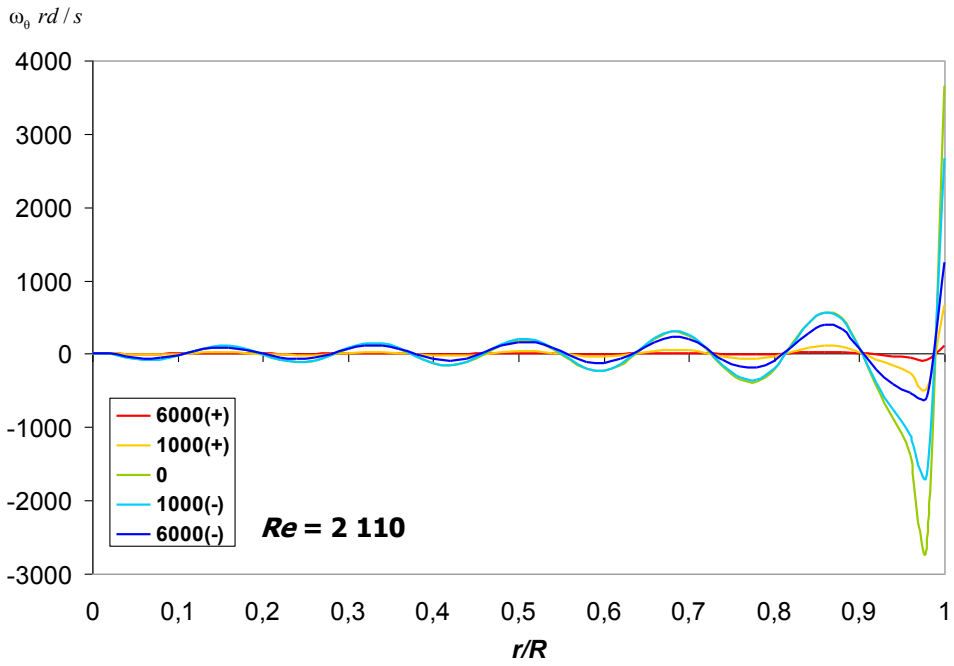

Figure 1-15 : Spin velocity profiles and positive/negative gradient magnetic field at (a) bed exit z = L, Re = 2110. Box legend syntax: A (+) □ H0z = A z/L Oe; A (-) □ H0z = A (1 - z/L) Oe, [30]

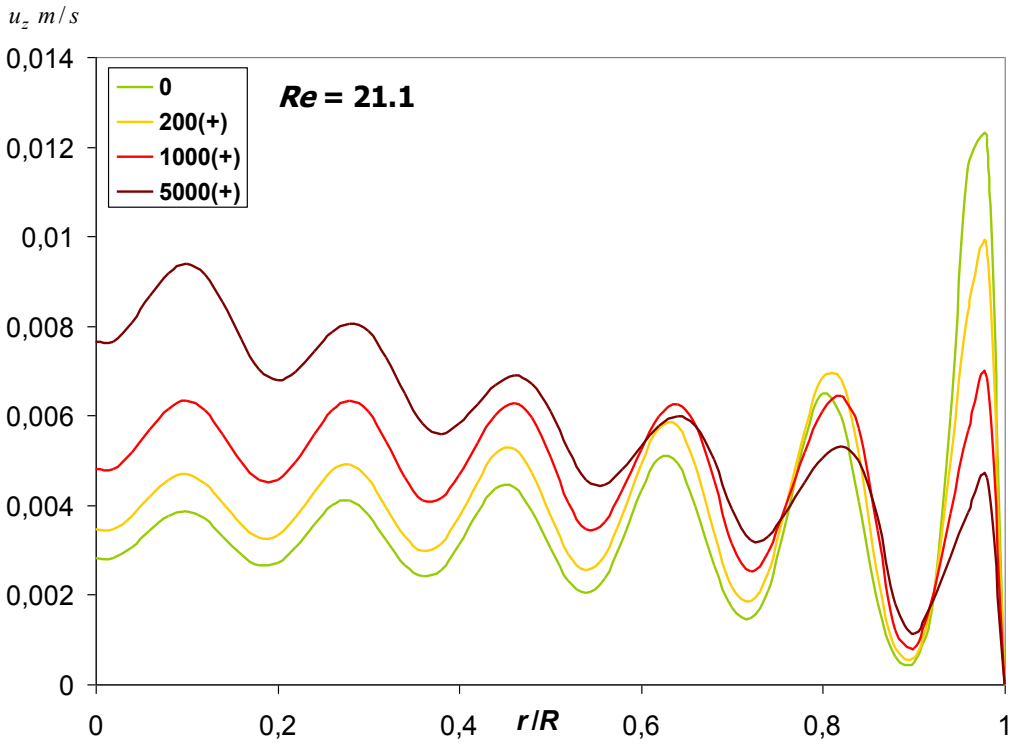

Figure 1-16 : Axial velocity component radial profiles and positive/negative gradient magnetic field at bed exit z = L and ferrofluid Reynolds numbers Re = 21.1. Box legend syntax: A (+) □ H_{0z} = A z/L Oe; A (-) □ H_{0z} = A (1 - z/L) Oe, [30]

1.3.5 Mass transfer enhancement

Quite recently an emerging trend in chemical engineering concerns attempts to enhance transport operations beyond what can be accomplished in the classical paradigm. For example, it has been stated that the presence of MNPs may enhance gas-liquid mass transfer both in presence and in absence of an external magnetic field.

1.3.5.1 MNP Suspensions & No Magnetic Field

Olle et al. [34] dispersed MNPs in liquid phase with the objective to enhance gas-liquid mass transfer. The MNPs consisted of oleic-acid grafted surfactant as an internal layer, and (Hitenol-BC) grafted as second-layer polymerizable surfactant. Synthesis, purification and pH stability issues were resolved during the preparation of these MNPs with large hydrodynamic diameter due to the double-surfactant layer. Stability against agglomeration over a wide pH range was also examined. The volumetric gas-liquid mass transfer coefficient $k_L a$ was determined according to physical and chemical absorption protocols.

During physical absorption, dissolved oxygen absorption dynamic tests were carried out in a flat-surface mechanically-stirred cell. The $k_L a$ values were obtained in the absence of an external magnetic field with and without introducing MNP in the aqueous medium. The MNP mass fractions ranged from zero (control test) to 4%, and an enhancement factor due to the presence of MNPs, was defined as $E_{H=0} = k_{L\oplus MNP}/k_L$. Up to 70% amelioration of $E_{H=0}$ is shown in figure 1-17 as a function of stirrer speed and MNP mass fraction. It can be seen that in presence of up to 1% w/w of MNP in liquid, an enhancement of gas-liquid mass transfer takes place. Although the enhancement mechanism is still not elucidated, improvements are more visible at lower agitation rates.

Chemical absorption experiments were also carried out using copper (or cobalt) homogeneously catalyzed oxidation of sulfite into sulfate with dissolved oxygen in aqueous phase.

Copper-catalyzed reaction gave access to the pure physical mass transfer coefficients in the so-called slow-reaction in diffusion film and rapid reaction in liquid bulk (chemical enhancement factor ≈ 1, O_2 dissolved concentration in liquid bulk ≈ 0). An MNP enhancement factor similar to the one defined in the case of physical absorption was defined while considering that the gas-liquid contacting area is no longer a flat interface:

$$E' = \frac{(k_L a)_{L\oplus MNP}}{k_L a} \tag{19}$$

The cobalt-catalyzed reaction gave access to the gas-liquid interfacial area in the so-called fast-reaction diffusional film (Hatta number > 3, chemical enhancement factor ≈ Hatta number, O_2 dissolved concentration in liquid bulk ≈ 0). An interfacial area MNP enhancement factor in this absorption regime can be defined as:

$$E_a = \frac{a_{MNP}}{a} = \frac{(N a)_{L\oplus MNP}}{(N a)_L} \frac{\left(C^*_{O_2}\sqrt{C^{*\,n-1}_{O_2}}\right)_L}{\left(C^*_{O_2}\sqrt{C^{*\,n-1}_{O_2}}\right)_{L\oplus MNP}} \tag{20}$$

Mass transfer coefficient enhancement E′ (equation 19) increases with increasing MNP concentration as shown as a function of specific power dissipation and sparging superficial

gas velocity and illustrated in figure 1-18 and 1-19, respectively. The absorption process can be enhanced up to five times due to the presence of MNPs (Figure 1-18). However, as power dissipation increases after a certain limit, the enhancement factor decreases, regardless of MNP concentration. Figure 1-19 shows that gas superficial velocity is not a determining operating variable in the enhancement of mass transfer, equation 20.

E_a enhancement factor along with E′ enhancement factor and the enhancement brought about only on the pure mass transfer coefficient k_L are illustrated in figure 1-20 and 1-21. From figure 1-20 it may be seen that most of volumetric mass transfer enhancement is due to the interfacial area growth (more than 80% of 600% total enhancement) over the total range of power draw. The k_L slight enhancement seen at low power input and superficial velocity collapses afterwards when these variables keep increasing. Such effects are coherent with reduction in surface tension with up to 0.1% MNP concentration, as seen commonly during gas sparging in mechanically agitated systems with coalescence inhibiting liquids. However, increasing further MNPs concentration had no major effect on surface tension reduction. These results purport evidence of the presence of MNPs near the gas-liquid interface to explain these enhancement factors. However, no mechanism can be ruled out for explaining the enhancement on k_L and a [34]. The question as to whether this phenomenon is related in any sort to the magnetic nature of nanoparticles has to be elucidated.

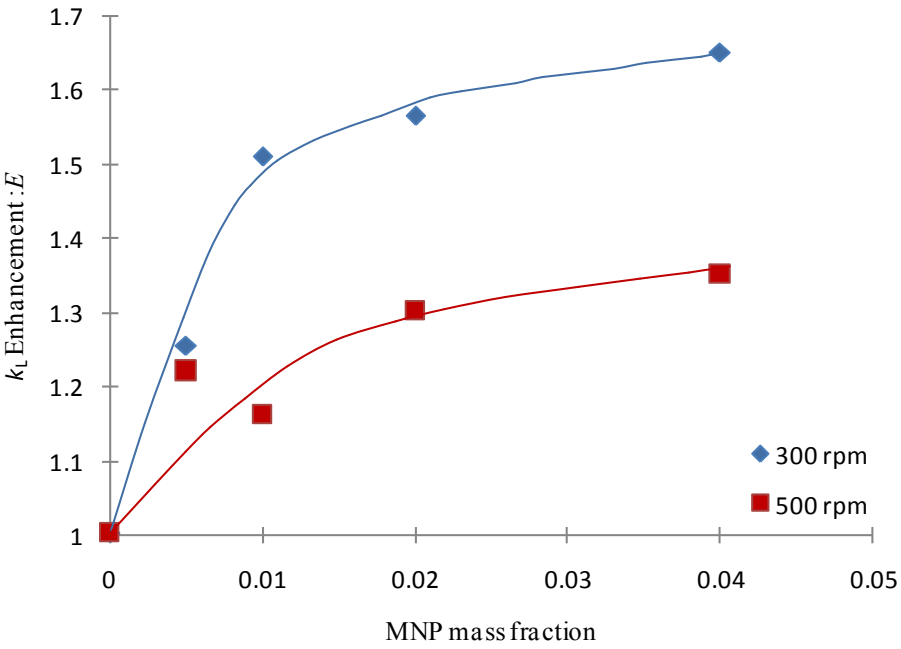

Figure 1-17 : Enhancement factor vs. MNP mass fraction at 300 and 500 stirrer speed, physical absorption tests. Adapted from [34]

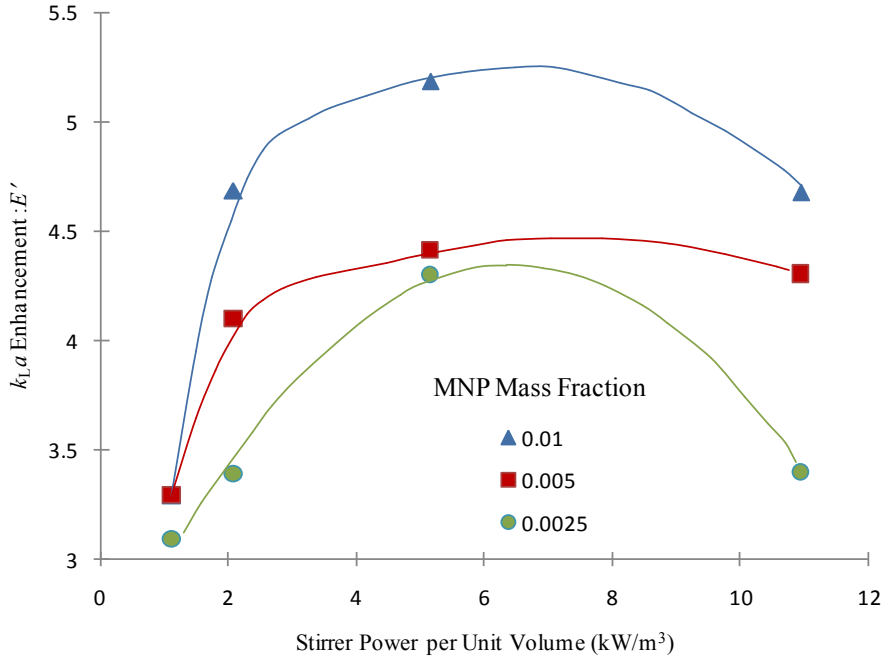

Figure 1-18 : Enhancement vs. dissipated energy at three different MNP concentrations in chemical absorption tests at Vs = 14.5 cm/min. Adapted from [34]

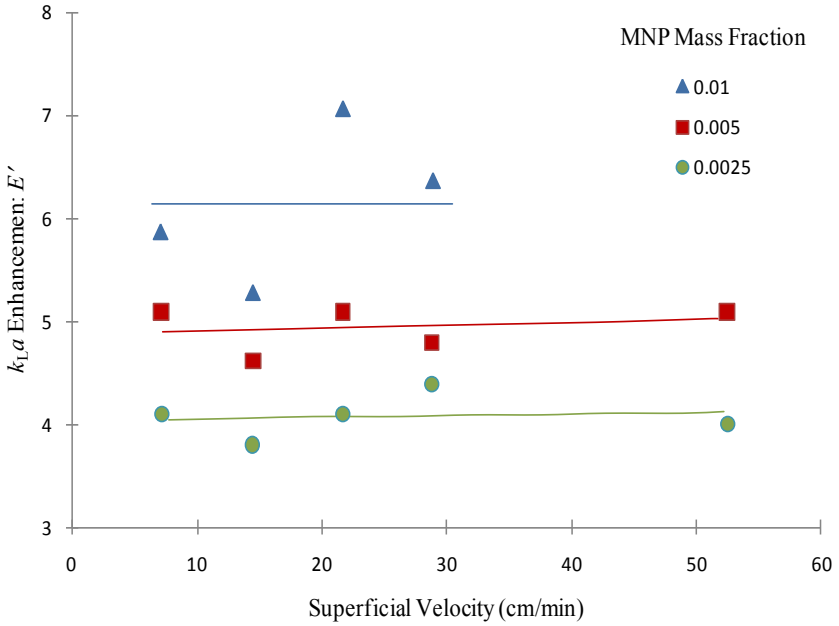

Figure 1-19 : Enhancement vs. superficial velocity at three MNP mass concentrations in chemical absorption tests at power p.u.v = 2.1 kW/m3. Adapted from [34]

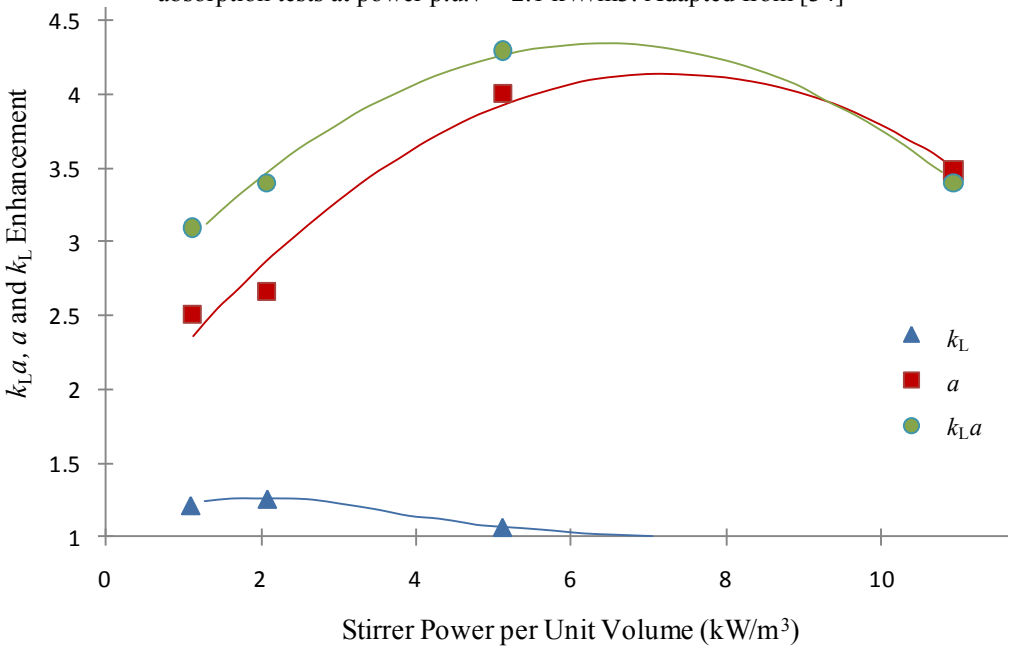

Figure 1-20 : KLa, a, KL enhancement vs. dissipated energy at three different MNP concentrations in chemical absorption tests at Vs = 14.5 cm/min. Adapted from [34]

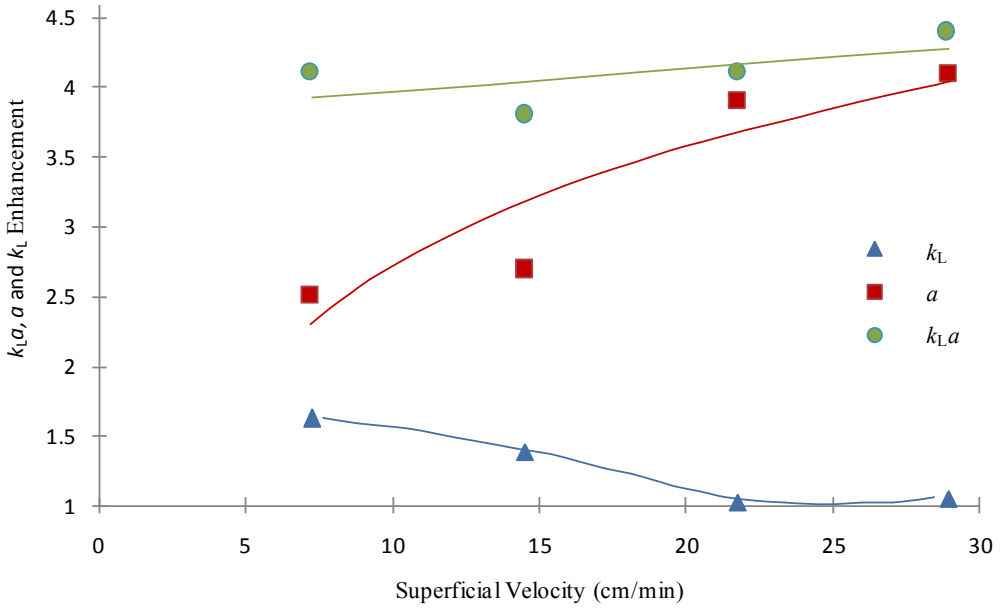

Figure 1-21 : KLa, a, KL enhancement vs. special velocity at three different MNP concentrations in chemical absorption tests at power p.u.v = 2.1 kW/m3. Adapted from [34]

1.3.5.2 MNP Suspensions & Magnetic Field

In this approach, first proposed by Suresh and Bhalerao [35], a ferrofluid volume was added to alkaline aqueous solution in a wetted-wall falling-film column and bubble column to monitor effects from MNP in carbon dioxide absorption using an AC magnetic field to enhance gas-liquid interfacial mass transfer. The Olle et al. [34] measured diminution of surface tension through addition of minute MNP concentration levels indicates that MNP are enough small to protrude through, and populate, the liquid diffusional boundary layer. MNP stimulations by an external magnetic field makes them reminiscent of microscale stirrers in the liquid diffusional boundary layer and thus are foreseen to decrease interfacial mass transfer resistance.

A 50-Hz AC magnetic field was generated by two coils one mounted on top of the other. Instantaneous diffusion-limited absorption reactions (CO_2 absorption in carbonate-bicarbonate buffers and in sodium hydroxide solutions) were selected for rate measurements in presence and in absence of AC magnetic field. The saturation magnetization of the ferrofluid used was M_s = 100 Gauß before dilution and M_s = 2 Gauß after fifty-fold dilution in the alkaline aqueous solutions. Similarly to Olle al. [34], they reported a slight mass transfer enhancement of ca 5% in the absence of magnetic field and

26% with the magnetic field ON. Since these two studies concerned three different reactor types (falling film, bubble column, stirred tank), apart from the consensual qualitative enhancement in mass transfer, it is difficult to drive the comparisons to a farther level.

Mass transfer improvements plateaued after 2.3% v/v MNP ferrofluid was added into the alkaline solutions. Maximum enhancement achieved was 50% on $k_L a$ which is lower than what Olle et al. [34] reported. Possible MNP agglomeration, driven by ionic strength and pH effects, was advanced by the authors as a reason for the lesser improvements arrived at.

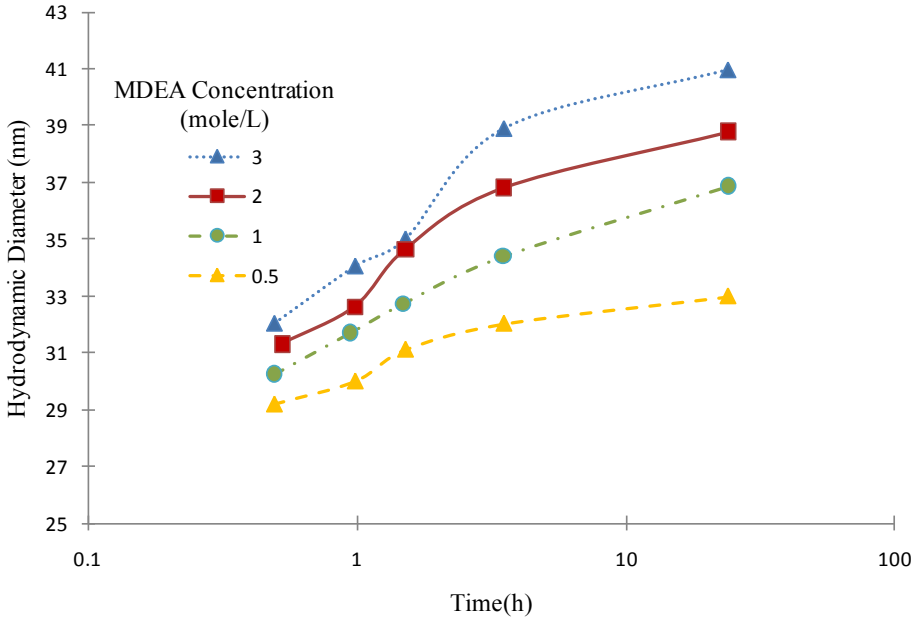

Figure 1-22 : Stability of magnetic nanoparticle sizes at different concentrations of MDEA vs. time. Adapted from [36]

More recently, CO_2 absorption was implemented by in methyl-diethanolamine (MDEA) aqueous solutions using a falling-film device [35]. The amine, being tertiary and thus little reactive one, shifts the absorption regime to intermediate between diffusion control and chemical control. A 50% v/v blend of ferrofluid (0.4% solid volume fraction, M_s = 35 Gauß) and MDEA solution was used. AC magnetic fields from 100 to 300 Gauß and 500Hz to 100 kHz were tested. Another coil generating up to 1000 Gauß AC field was used to investigate mass transfer enhancement in much stronger fields. Komati and Suresh [36] selected the matrix liquid solution based on MNP size stability. Using a dynamic light scattering technique, ferrofluid colloids were indeed found to be more stable in solutions of

tertiary amines, such as triethanolamine and MDEA than ferrofluid in solutions with primary and secondary amines. MNP clusters coarsen in MDEA to a diameter of *ca* 28-38 nm after ca 5 h and then nearly stabilize in size. Figure 1-22 shows the growth of MNP clusters as a function of MDEA concentration and time. The same enhancement definition (equation 19) proposed by Olle et al. [34] was used by Komati and Suresh [36] and found that the volumetric mass transfer coefficient can be almost doubled. According to the authors, the flow regime of the falling film precluding ripples' formation on the free surface led them to ascribe the enhancement only to the k_L factor.

Most recently, Stuyven et al. [37] devised a clever experiment in which a steady-state homogeneous magnetic field was applied to promote dispersion and disaggregation of non-magnetic nanoclusters in high ionic strength solutions. This approach was dubbed as a new energy process intensification method compared to more conventional disaggregation techniques relying on microwaves, ultrasounds, and jet and ball mills. A mild static magnetic field (0.31 T) was generated by two permanent magnets which set a transverse magnetic field with respect to the flow of silica nanoparticle suspension.

The size of the agglomerated nanoparticles was observed for different Reynolds numbers with and without applied magnetic field. Figure 1-23 shows three different particle fraction distributions -PSD- (based on volume). The black line represents PSD in a fluid at rest without external magnetic field. The red line stands for the PSD after 1 h turbulent flow at Re = 26 000 without external magnetic field. In this case, the shear forces arising in turbulent flow were able to disaggregate nanoclusters from 1400 nm to 261 nm in size. Applying an external magnetic field at the same Re value reduced further the mean particle diameter to 169 nm (blue line). The narrower PSD shape in this last case indicates that most of the clusters are broken when the Lorentz force come to into play along with the hydrodynamic forces.

Figure 1-24 illustrates another experiment by Stuyven et al. [37] in which nanoparticles size stabilized (red portion of the curve on the left) around 390 nm at Re =8 000 without magnetic field. Enabling the magnetic field caused a reduction of the mean diameter to 310 nm (blue middle portion) then disabling the magnetic field (red portion of the curve on the right) resumed nearly reversibly re-agglomeration of particles.

Another set of experiments was aimed to the study of the effect of *Re* on the magnetic field-agglomeration interaction. It can be seen that magnetic fields enhance agglomeration in laminar flow regime (figure 1-25) and cluster disaggregation in transitional and turbulent flows. The stable aggregation was interpreted by Stuyven et al. [37] as resulting from a balance between attractive and repulsive forces between initially charged nanoparticles. In laminar flow, collision frequency is promoted by the magnetic field while hydrodynamic strain on cluster due to velocity gradient is weak. In this regime the Lorentz force acting on the *differently* charged nanoparticles, being part and parcel of a given nanoclusters, cannot split them apart, thus agglomeration prevails. Conversely, in turbulent flow regime, the random shear stress fluctuations and strong strain, especially near the wall, promote small size clusters. In this case, the Lorentz force drags the charged clusters towards the wall hence enhancing their disaggregation.

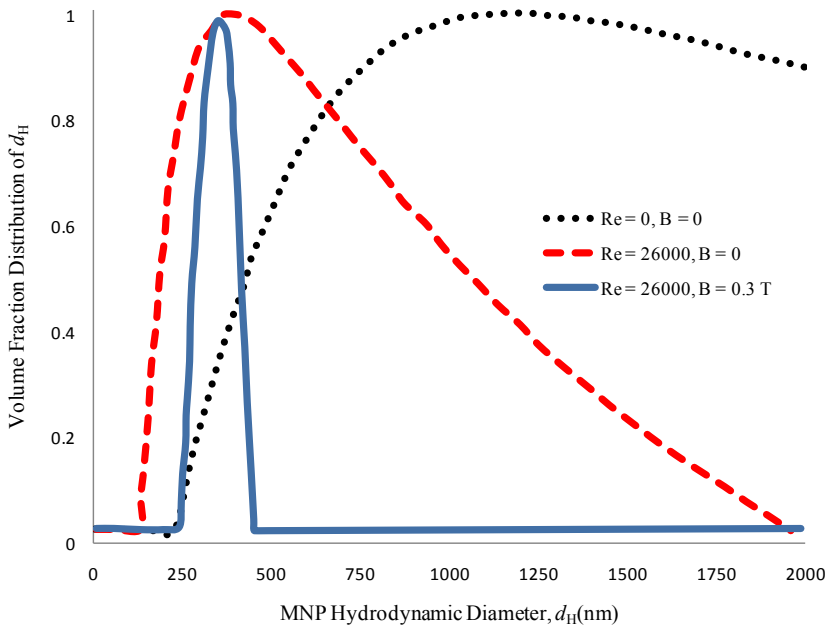

Figure 1-23 : Particle size distribution of silica aggregates (volume fraction scale), fluid at rest (Black line), after 1 h, Re = 26 000 in absence (Red line), and in presence (Blue line) of external magnetic field. Adapted from [37]

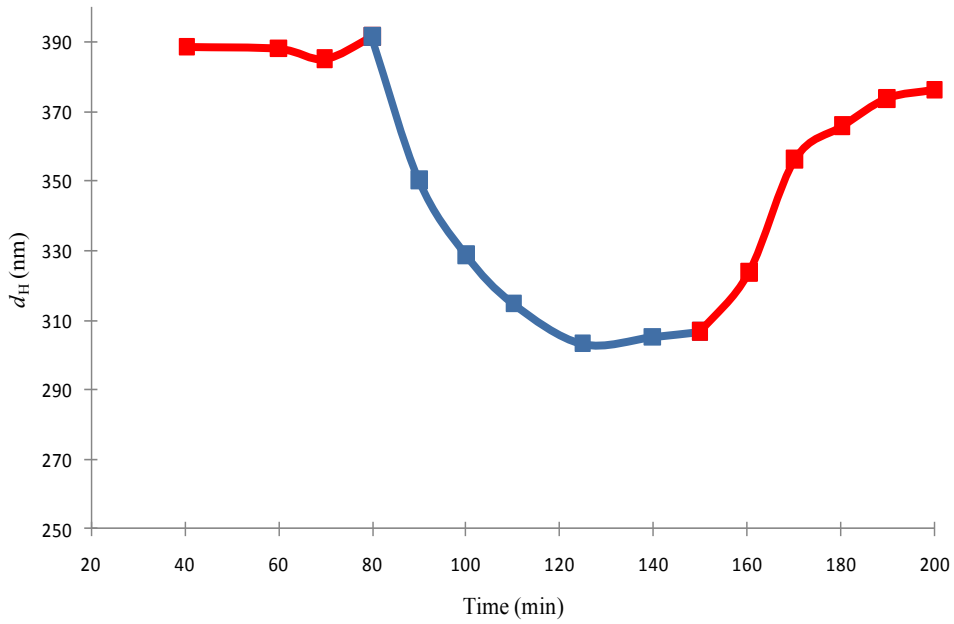

Figure 1-24 : Particle size evolution of silica aggregates in presence (Blue line) and absence (Red line) of external magnetic field, Re = 8 000. Adapted from [37]

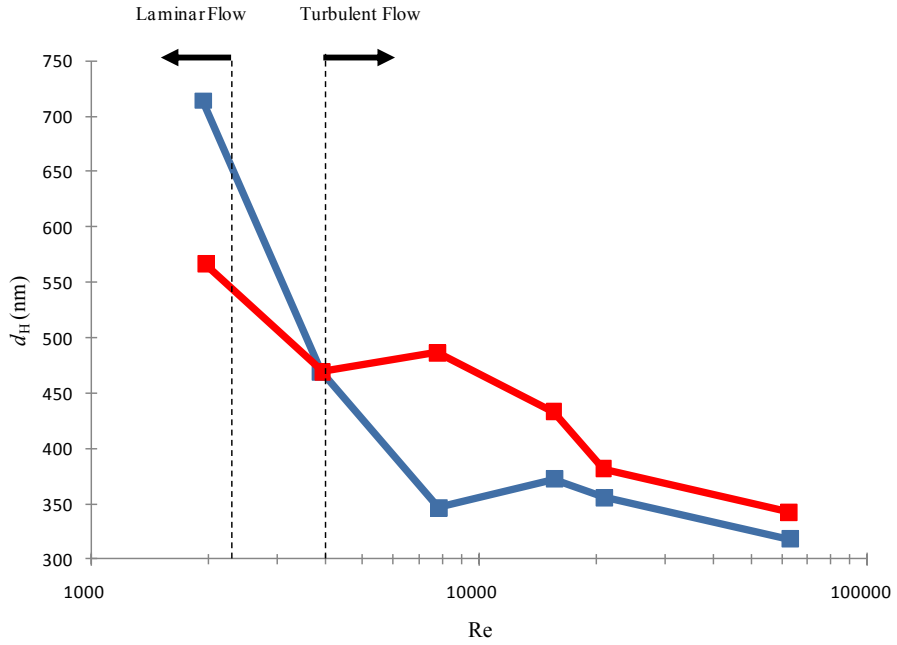

Figure 1-25 : Mean diameter of γ-alumina clusters formed in presence of magnetic field (Blue line) and in absence of magnetic field (Red line) versus Reynolds number. Adapted from [37]

1.4 Scope of thesis

Although ferrofluids are applied widely across many disciplines and industrial sectors, they have not received sufficient coverage in the realm of chemical engineering. In this introduction, the most potentially relevant theoretical concepts and practical applications of ferrofluid to chemical engineering have been summarized and discussed.

The purpose of this research is to provide experimental data on transport phenomenon in the presence of magnetically excited MNPs suspended in liquid. In particular, this thesis is focused on mass transfer enhancement in the presence of MNPs and magnetic field to unveil new mechanisms and discoveries of fluid-fluid enhancement processes which are relevant to chemical reaction engineering.

In the presence of rotating magnetic fields (RMF), MNPs will rotate with an attempt to align their magnetic moment with the field. Also, stationary magnetic field (SMF) locks MNP and prohibits the gyration under shear forces. Because of the viscous fluid, spinning or pinned particle delivers a magnetic torque to the adjacent liquid around it. This torque may induce nano-convective mixing under RMF or create a nano-stagnant zone. Therefore, mixing properties of the liquid which is dominated by molecular diffusion in nano-scale, is affected by the mechanism. This effect is measured and described in the thesis using several experimental scenarios. The sensitivity of this effect is analyzed as a function of magnetic field amplitude, frequency and MNP concentration. The first set of experiments in chapter 2, measure the nano-convective mixing effect on self-diffusion coefficient of a suspension in a capillary. The diffusion cell is centered inside the two-pole three-phase magnet horizontally. Significant mass transfer enhancement observed and discussed. The experiments in chapter 3 and 4 consist of axial dispersion coefficient measurement in the capillary to identify the effect of magnetically excited MNPs on Taylor dispersion and on laminar velocity profile under RMF, OMF and SMF. Chapter 5 studies gas-liquid mass transfer coefficient ($k_L a$) when the Taylor flow regime in conducted in the tube, passing through the magnet. Gas-liquid mass transfer was measured in the presence (absence) of magnetic field (under RMF and SMF) and the results were compared.

1.5 Nomenclature

a	Specific interfacial area, 1/m
$\mathbf{B}$	Magnetic induction vector, T, N/Am
C_i^*	Concentration of component i in saturated liquid, mol/m^3
D	Column diameter, m
d	Grain diameter, m
d_H	Nanocluster hydrodynamic diameter, m
d_h	MNP hydrodynamic diameter, m
d_p	MNP core diameter, m
d_{tube}	Tube diameter, m
E	Absolute enhancement in k_L
E_a	Absolute enhancement in interfacial area,
E_r	Turbulent rotational kinetic energy, J
E_t	Turbulent translational kinetic energy, J
E'	Absolute enhancement in $k_L a$
f_0	Larmor frequency of magnetization vector in the anisotropy field of the particle, 1/s
$\mathbf{g}$	Gravity vector, m/s^2
$\mathbf{H}$	Total magnetic field vector, A/m
$\mathbf{H}_e$, $\mathbf{H}_{eq}$	Effect magnetic field in equilibrium with dynamic magnetization, A/m

$\mathbf{H}'$	Fluctuating component of magnetic field caused by turbulence, A/m
I	Moment of inertia per unit mass of MNPs, m^2
K	Anisotropic constant of material, J/m^3
k	Turbulent kinetic energy, kg m^2/s^2 = J
k_B	Boltzmann's constant, J/K
k_L	Liquid phase mass transfer coefficient, m/s
$k_L a$	Volumetric mass transfer coefficient, 1/s
k_n	Rate constant of nth-order reaction, $m^3/(mol\ s)$ for $n = 2$
L	Langevin magnetization function operator,
L_{PB}	Column length, m
L_{tube}	Tube length, m
$\mathbf{M}$	Magnetization vector, A/m
M_s	Ferrofluid saturation magnetization of the liquid, A/m or Oe
$\mathbf{M}_0$	Equilibrium magnetization, A/m
M'	Magnetization fluctuating component, A/m
$\sqrt{\overline{M_i'^2}}$	Magnetization x-component RMS, A/m
m_p	Magnetic dipole moment of single domain nanoparticles, Am^2
n	Reaction order,
Na	Absorption rate, $mol/(m^2 s)$
p	Hydrodynamic pressure, Psi

Q	Liquid volumetric flow rate, mL/min
r	Radial coordinate in cylindrical coordinate, m
R	Tube diameter, m
Re	Reynolds number,
rd	Radian
T	Absolute temperature, K
T_0	Time-averaged magnetic body couple density, dimensionless
t	time, s
U	Normalized linear velocity, m/s
U_{int}	Internal energy, J
$\mathbf{u}$	Ferrofluid linear velocity, m/s
u_{RMS}	Root-mean-square translational velocity, m/s
u'	Linear velocity fluctuating component, m/s
$\langle u \rangle$	Time averaged linear velocity, m/s
$\sqrt{\overline{u_{\text{i}}'^2}}$	Linear velocity x-component RMS, m/s
V_{h}	MNP hydrodynamic volume, m^3
V_{p}	MNP core volume, m^3
V_{s}	Superficial velocity, cm/min

Greek letters

α	Dimensionless Langevin module
α_{GP}	Gradient programming of the applied magnetic field, A/m^2
ΔP	Pressure drop, Psi
$\Delta\eta$	Rotational viscosity, Pa s
ε	Turbulent kinetic energy dissipation rate, kg m^2/s^3 = J/s
ε_A	Vortex viscose dissipation rate, cm^2/s^3
ε_C	Rotational kinetic dissipation rate, cm^2/s^3
ε_v	Classical viscous dissipation rate, cm^2/s^3
ζ	Vortex viscosity, Pa s
η'	Shear spin viscosity, kg m/s
θ	The angle between **M** and **H**, rad
λ	Dilatational viscosity, Pa s
λ'	Bulk spin viscosity, kg m/s
μ	Dynamic viscosity (shear viscosity), Pa s
μ_0	Vacuum permeability $4\pi\times10^{-7}$, N/A^2, Tm/A, J/A^2m
ξ	Dimensionless magnetic field
ξ_e	Dimensionless effective magnetic field
ρ	Fluid density, kg/m^3
τ	(Effective) magnetization relaxation time constant, s
τ_{AC}	AC magnetic field oscillation time scale = $1/\Omega_{AC}$, s

τ_B	Brownian relaxation time constant, s
τ_m	Experiment time scale, s
τ_N	Néelian relaxation time constant, s
φ	MNPs' grains volume fraction in colloidal fluid
Φ_b	Energy transfers between translational and rotational kinetic energy, cm^2/s^3
χ_0	Initial magnetic susceptibility,
Ψ	Energy transfers to translational kinetic energy by magnetic field, cm^2/s^3
Ψ_s	Energy transfers to rotational kinetic energy by magnetic field, cm^2/s^3
Ω_{AC}	Oscillating field frequency, Hz
$\boldsymbol{\omega}$	Spin velocity per unit volume of ferrofluid, rad/s 0r cm/s
ω'	Linear velocity fluctuating component, m/s
$\sqrt{\overline{\omega_i'^2}}$	Spin velocity *x*-component RMS, rad/s

Subscripts

i	i direction component of a vectorial field, i = (x,y,z) or (r,θ,z)
L	Liquid phase
MNP	In presence of MNPs,

Acronyms

DLS	Dynamic Light Scattering

fPd	Fractional Pressure Drop,
MNP	Magnetic Nanoparticle
PSD	Particle Size Distribution
p.u.v.	Per unit volume
RHS	Right hand side
RMF	Rotating magnetic field
RMS	Root mean square
rdMNP	Rigid Dipole Magnetic Nanoparticle
sdMNP	Soft Dipole Magnetic Nanoparticle

1.6 References

[1] S. Odenbach, Magnetoviscous Effects in Ferrofluids (Springer, 2002).

[2] R. E. Rosensweig, Ferrohydrodynamics (Dover Publications, 1997).

[3] K. Morozov, M. I. Shliomis, M. Zahn, Magnetoviscosity in suspensions of grains with finite magnetic anisotropy, *Phys*. *Rev*. *E*. 73 (2006) 066312.

[4] M. I. Shliomis, K. I. Morozov, Negative viscosity of ferrofluid under alternating magnetic field, *Phys*. *Fluids* 6 (1994) 2855-2861.

[5] A. H. Morrish, Physical Principles of Magnetism (Wiley Press, 2001).

[6] M. Martsenyuk, Y. Raikher, M. I. Shliomis, On the kinetics of magnetization of suspensions of ferromagnetic particles, *Sov*. *Phys*. *JETP* 38 (1974) 413-416.

[7] B. U. Felderhof, Flow of a ferrofluid down a tube in an oscillating magnetic field, *Phys*. *Rev*. *E* 64 (2001) 021508.

[8] A. D. Rosenthal, C. Rinaldi, T. Franklin, M. Zahn, Torque measurements in spin-up flow of ferrofluids, *J*. *Fluids Eng*. 126 (2004) 198-205.

[9] J. P. Embs, S. May, C. Wagner, A. V. Kityk, A. Leschhorn, M. Lücke, Measuring the transverse magnetization of rotating ferrofluids, *Phys*. *Rev*. *E*. 73 (2006) 036302.

[10] M. I. Shliomis, Effective viscosity of magnetic suspentions, *Sov*. *Phys*. *JETP* 34 (1972) 11291-1294.

[11] J. -C. Bacri, R. Perzynski, M. I. Shliomis, G. I. Burde, Negative-Viscosity effect in a magnetic field, *Phys*. *Rev*. *Lett*. 75 (1995) 2128-2131.

[12] M. I. Shliomis, Ferrohydrodynamics Testing a third magnetization equation, *Phys*. *Rev*. *E*. 64 (2001) 060501.

[13] B. U. Felderhof, H. J. Kroh, Hydrodynamics of magnetic and dielectric fluids in interaction with the electromagnetic field, *J*. *Chem*. *Phys*. 110 (1999) 7403-7411.

[14] B. U. Felderhof, Magnetoviscosity and relaxation in ferrofluids, *Phys*. *Rev*. *E* 62 (2000) 3848-3854.

[15] K. R. Schumacher, J. J. Riley, B. A. Finlayson, Homogeneous turbulence in ferrofluids with a steady magnetic field, *J*. *Fluid Mech*. 599 (2008) 1-28.

[16] R. E. Rosensweig, R. Kaiser, G. Miskolczy, Viscosity of magnetic fluid in a magnetic field, *J*. *Colloid Interface Sci*. 29 (1969) 680-686.

[17] J. P. McTague, Magnetoviscosity of magnetic colloids *J*. *Chem*. *Phys*. 51 (1969) 133-136.

[18] A. Zeuner, R. Richter, I. Rehberg, Experiments on negative and positive magnetoviscosity in an alternating magnetic field, *Phys*. *Rev*. *E* 58 (1998) 9287-8293.

[19] C. Rinaldi, F. Gutman, X. He, A. D. Rosenthal, M. Zahn, Torque measurements on ferrofluid cylinders in rotating magnetic fields, *J*. *Magn*. *Magn*. *Mater*. 298 (2005) 307–310.

[20] X. He, S. Elborai, D. Kim, S. H. Lee, M. Zahn, Effective magnetoviscosity of planar-Couette magnetic fluid flow, *J*. *Appl*. *Phys*. 97 (2005) 10Q302.

[21] C. Rinaldi, A. Chaves, S. Elboria, X. He, M. Zahn, Magnetic fluid rheology and flows, *Curr*. *Opin*. *Colloid Interface Sci*. 10 (2005) 141-157.

[22] M. Zahn, D. R. Greer, Ferrohydrodynamic pumping in spatially uniform sinusoidally time varying magnetic fields, *J*. *Magn*. *Magn*. *Mater*. 149 (1995) 165-173.

[23] M. Zahn, L. L. Pioch, Magnetizable fluid behaviour with effective positive, zero or negative dynamic viscosity, *Indian J*. *Eng*. *Mater*. *Sci*. 5 (1998) 400-410.

[24] C. Rinaldi, M. Zahn, Effects of spin viscosity on ferrofluid flow profiles in alternating and rotating magnetic fields, *Phys*. *Fluids* 14 (2002) 2847-2870.

[25] K. R. Schumacher, I. Sellien, G. S. Knoke, T. Cader, B. A. Finlayson, Experiment and simulation of laminar and turbulent ferrofluid pipe flow in an oscillating magnetic field, *Phys*. *Rev*. *E* 67 (2003) 026308.

[26] A. P. Krekhov, M. I. Shliomis, S. Kamiyama, Ferrofluid pipe flow in an oscillating magnetic field, *Phys*. *Fluids* 17 (2005) 033105.

[27] H. Tennekes, J. L. Lumley, A First Course in Turbulence (MIT Press, 1972).

[28] N. G. Taktarov, Motion of magnetizable liquids in porous media, *Magnetohydrodynamics* 16, (1980) 251-255.

[29] N. G. Taktarov, Convection of magnetizable fluids in porous media, *Magnetohydrodynamics* 17, (1981) 333-335.

[30] F. Larachi, D. Desvigne, Magnetoviscous control ofwall channeling in packed beds using magnetic nanoparticles—Volume-average ferrohydrodynamic model and numerical simulations, *Chem*. *Eng*. *Sci*. 61 (2006) 1627 – 1657.

[31] F. Larachi, D. Desvigne, Ferrofluid induced-field effects in inhomogeneous porous media under linear-gradient d.c. magnetic fields, *Chem*. *Eng*. *Process*. 46 (2007) 729-735.

[32] F. Larachi, D. Desvigne, Ferrofluid magnetoviscous control of wall channeling in porous media, *China Particuol.* 5 (2007) 50 – 60.

[33] F. Larachi, Experimental and theoretical explorations of weak and strong gradient magnetic fields in chemical multiphase processes, Chap. 11 in Modeling of Process Intensification, F. J. Keil, (Wiley–VCH, 2007, pp. 365-399).

[34] B. Olle, S. Bucak, T. C. Holmes, L. Bromberg, T. A. Hatton, D. I. C. Wang, Enhancement of oxygen mass transfer using functionalized magnetic nanoparticle, *Ind*. *Eng*. *Chem*. *Res*. 45 (2006) 4355-4363.

[35] A. K. Suresh, S. Bhalerao, Rate intensification of mass transfer process using ferrofluids, *Indian J. Pure Appl*. *Phys*. 40 (2001) 172-184.

[36] S. Komati, A. K. Suresh, CO2 absorption into amine solutions a novel strategy for intensification based on the addition of ferrofluids, *J. Chem. Techno. Biotechnol*. 83 (2008) 1094-1100.

[37] B. Stuyven, Q. Chen, W. V. d. Moortel, H. Lipkens, B. Caerts, A. Aerts, L. Giebeler, B. V. Eerdenbrugh, P. Augustijns, G. V. d. Mooter, J. V. Humbeeck, J. Vanacken, V. V. Moshchalkov, J. Vermantc, J. A. Martens, Magnetic field assisted nanoparticle dispersion, *Chem. Commun*. 1 (2009) 47-49.

2 Giant liquid-self diffusion in stagnant liquids by magnetic nano-mixing

2.1 Abstract

Many chemical engineering applications require tools to intensify processes in regions where Fickian molecular diffusion is the dominant mechanism, such as in boundary layers, microporous catalysts or microfluidics. We demonstrate in this study that spinning **m**agnetic **n**ano**p**articles (MNP) by means of rotating magnetic fields (RMF) gives rise to an intriguing nanomotion mechanism capable of triggering *giant* diffusion in stagnant liquids and thus able to stimulate transport beyond the molecular diffusion barrier especially in *stagnant* liquids. To evidence this mechanism, we report original water self-diffusion coefficients measured in aqueous media containing very low concentrations of ferrite MNPs that can be rotated in uniform RMF. The self-diffusion coefficient of distilled water (i.e., $D_0 \approx 3.5\times10^{-9}$ m^2/s) was enhanced up to 200 times by application of a rotating magnetic field in stagnant-liquid conditions. It was concluded that in absence of macroscopic convective flows, MNPs may prove to be efficient nanostirrers to enhance liquid transport properties at nanoscale. By delivering giant diffusion around them, rotating MNPs can constitute an appealing nano-mixing process intensification tool.

2.2 Introduction

Molecular transport and diffusion in liquids play a key role in many different contexts of physics, chemistry, biology and chemical engineering [1,2]. Quite recently, an emerging trend in science and engineering attempts to enhance liquid phase transport operations using seeded nanoparticles, beyond what can be accomplished in the classical diffusion paradigm [2]. For example, it has been stated that the presence of nanoparticles in liquids (so-called nanofluids) may modify heat [3-5] and mass transport [6-14] properties of the medium. Most prominently, **m**agnetic **n**ano**p**articles (MNP) have been applied in a few studies to direct mass transfer, both in absence [8,15] and in presence [7,16] of an external magnetic field. Although, the general effect of nanoparticles on liquid transport properties is still anomalous [17], the method of exciting MNPs seeding liquids with a time-varying external magnetic field seems to be a promising approach to achieve process intensification. A related magnetic field assisted nano-mixing is the basis of the present work as a stable suspension of single-domain MNPs are externally modulated by means of a uniform rotating magnetic field (uRMF).

Briefly, external magnetic fields exert magnetic torque on the magnetic moment of MNPs suspended in liquids thus forcing MNP to be aligned with magnetic field direction [18]. For those MNPs whose magnetic moment is locked in the solid crystal structure (so-called rigid-dipole MNPs), magnetic torque is felt bodily and associated momentum is transferable to the adjacent liquid phase [18]. In purely hydrostatic conditions, this magnetic body torque is opposed only by Brownian collisions from the solvent molecules as suspensions are at rest [18]. Interestingly, the nature of mechanical interactions between magnetically excited MNPs and the bulk of liquid depends on the characteristics of applied magnetic field. For instance, a time-varying magnetic field such as uRMF exerts an angular torque on MNPs forcing them to gyrate versus the contiguous liquid. Note that, while changing direction continuously at any point of the domain, uRMF has constant field intensity over time. In their quest to catch-up with uRMF direction, the suspended rdMNPs spin in a direction primarily imposed by RMF [18]. The goal of this work is to investigate the effect of these spinning MNPs on liquid self-diffusion coefficient. As the main result, we observed that this technique triggers a giant enhancement of liquid self-diffusion, exceeding its field field-free diffusivity by more than two orders of magnitude. Moreover, magnetic

field intensity (H_0), field frequency (f) and MNP concentration (ϕ) were found to influence the extent of diffusion enhancement.

The current approach stands out from other magnetic mixing processes (which rely on applying magnetic Kelvin force and are restricted to the boundary of magnetic and nonmagnetic fluids [19]) as it is versatile and can be used in magnetically homogenous or inhomogeneous liquid media. Also, those systems that induce magnetic mixing in electrolytic media [20-23] are very different from ours.

2.3 Experimental

2.3.1 Colloidal suspension

Dilute concentrations of ferrite (Fe_3O_4) MNPs (ϕ = 0.001 – 0.01 v/v magnetic content) dispersed in water were prepared from a commercial ferrofluid, EMG705 (FerroTec). The magnetic properties of EMG 705 were measured by an alternating gradient magnetometer, MicroMag model 2900 (Princeton Instrument Co.) at 298 K in low-field (for initial susceptibility, χ_0) and high-field (for saturation magnetization, M_s) asymptote of magnetization curve. Using these values, particle core diameter was estimated following a method proposed by Chantrell [24]. Table 4 summarizes the magnetic properties of EMG-705 ferrofluid. Particle size distribution of dilute ferrofluid with different concentrations was measured *via* magnetometry. The results assured us of no cluster or chain formation during the course of experiments.

Table 2-1 : Magnetic properties of EMG 705 from magnetometry measurement

Saturation magnetization, M_s (kA/m)	18.7
Initial susceptibility, χ_0	2.9
MNP volume fraction, ϕ (v/v)	0.042
Estimated median magnetic core diameter, d_p (nm)	16.0

2.3.2 Magnet

To generate uRMF, a tubular two-pole and three-phase (5.5-cm high and 4.5-cm i.d. cylindrical bore) magnet has been designed and built in collaboration with MotionTech LLC and Winding Inc (figure 2-1a). The magnet has the capacity to provide both uniform and non-uniform magnetic fields at moderate strength (< 50 mT) at the bore center with up to 3 A three-phase currents. Since RMF emerges from superposition of three OMFs that are 120° out of phase, the coils are fed by three balanced AC currents from a variable frequency drive (ABB, ACS150, 2.2kW Variable Frequency Derive) as illustrated in figure 2-1a,b. Both magnetic field strength and frequency can be controlled directly by means of this power supply. The temperature of the magnet solid part is controlled by a water cooling jacket that encompasses the outer shell of the stator and filled with a coolant circulated in and out from a constant-temperature thermostated bath (Lauda, Model RKT20).

a

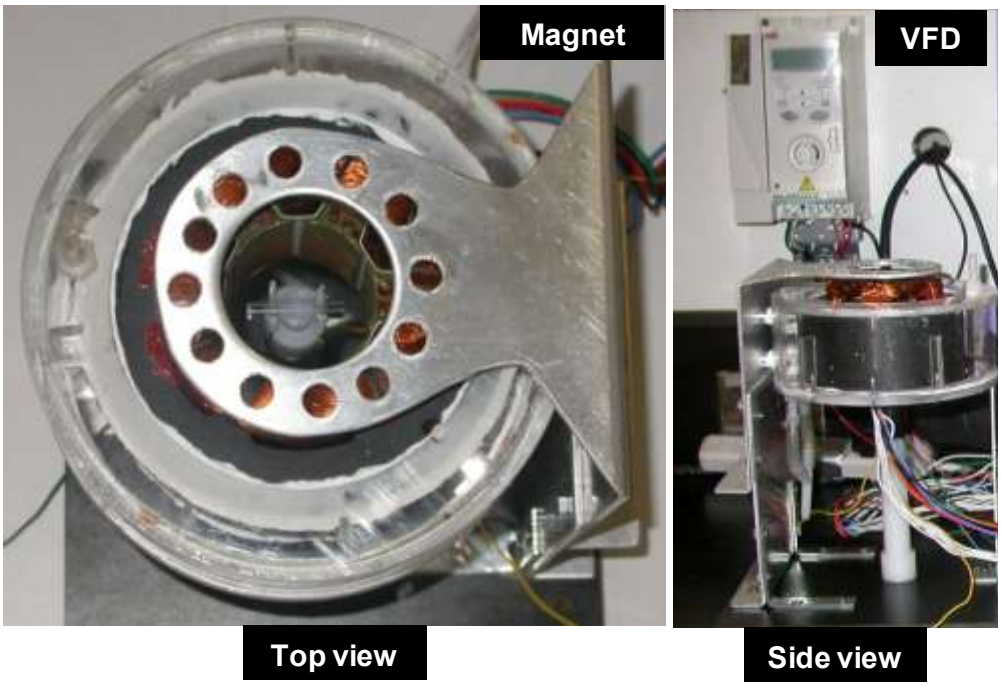

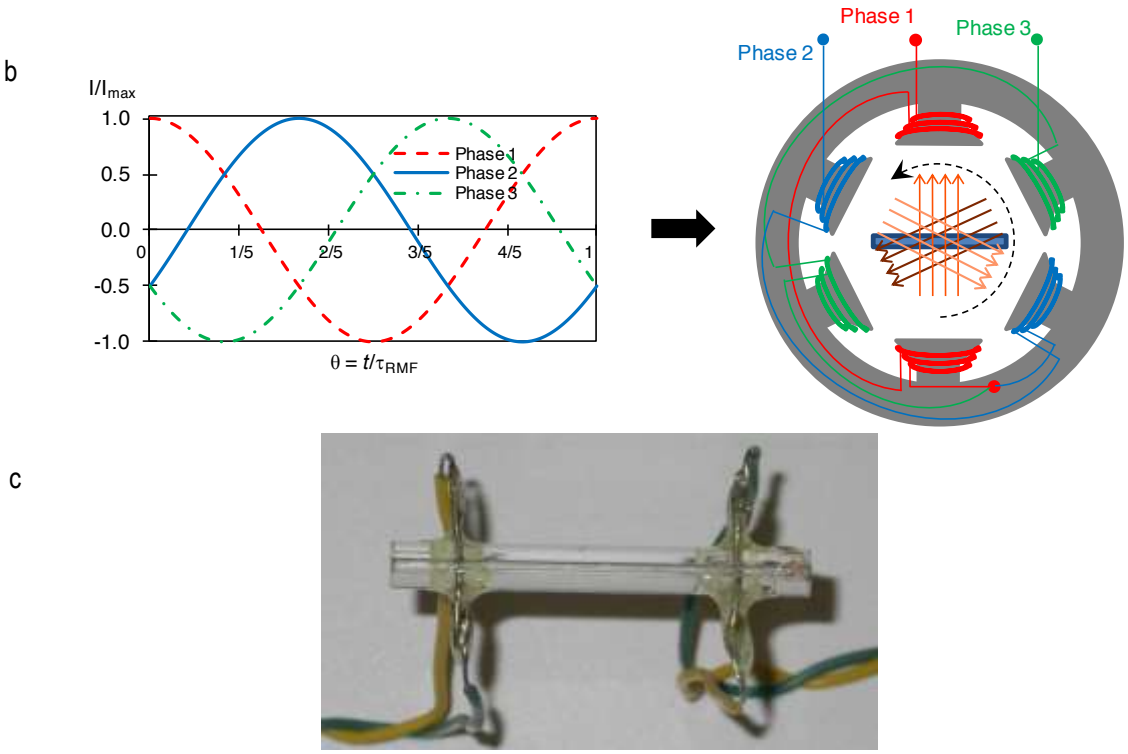

Figure 2-1 : a) Top and side view of the magnet with diffusion cell embedded inside with cell containing MNP suspension. b) Diffusion cell subject to uRMF generated by two-pole three-phase magnet energized by a three-phase power supply. c) Diffusion cell with two sets of electrical conductivity sensors.

2.3.3 Diffusion measurement

A simplified conductimetric method originally proposed by Leaist [25-28] was employed in this study to estimate self-diffusion coefficients of liquids loaded with MNPs with and without uRMF. The conductimetric cell consists of a short capillary tube sealed at both ends and fitted with two pairs of miniature electrodes as shown in figure 2-1c. The glass capillary had 1 mm inner diameter and 40 mm length (L). Platinum wire electrodes, 0.7 mm in diameter were sealed with epoxy glue into horizontal holes drilled at L/6 and 5L/6 accurately from one end [29]. The electrodes were connected to the conductivity meter (Omega CDTX-90) which generates a signal in mV, reflecting the electrical conductivity of the fluid in between each electrode pair. We employed (NaCl solution) electrolyte at low concentration (i.e., 0.05 M) mixed with dilute ferrofluids as a tracer. By virtue of Kohlrausch's law when electric conductances are relatively small, the transient behavior of the signal intensities is a linear function of electrolyte concentration in the liquid (figure 2-

2a,b). Great care was exercised in the preparation of the tracer solutions so that after dilution the MNP concentration in the tracer must be identical to that of the ferrofluids provided in the cell. This manner prevented magnetic Kelvin force [18] interference resulting from magnetic susceptibility discontinuities at the moment of injecting the tracer into the capillary. The applied voltage on the electrodes is tuned to be less than 1 V to avoid heating the suspension.

Before each run, the diffusion chamber was rinsed carefully, soaked and then overfilled with the MNP suspension. A thin film of high-vacuum nonmagnetic grease (silicone grease, Dow Corning #12) was applied around the outer edges of the capillary. The diffusion chamber was then sealed by two microscope slides pressed onto the capillary edges. After filling and sealing the cell, it was set at the middle height of the magnet and the desired magnetic field was applied. Only after reaching thermal equilibrium, which was recognized after detecting a constant conductivity signal, the cell received a tracer injection. A small volume of tracer (i.e., 0.5 μL) was injected into the cell gradually to minimize convection. D can be evaluated by least squares analysis of the slope of the conductance difference between upstream and downstream probe pairs plotted against time according to the expression [30]:

$$D = -\left(\frac{L}{\pi}\right)^2 \frac{d}{dt}\ln\left[C_1 - C_2\right] \tag{1}$$

Where C1 and C2 stand for the first and second conductance measured at time t and corrected by the ratio of cell constant (figure 2-2a, b). This conductimetric cell was used to determine distilled water self-diffusion coefficient in ambient conditions (atmospheric pressure and 298 K). We measured D = 2.1×10^{-9} m2/s which compared within 5 % with the reference self-diffusion coefficient value of water (2.2×10^{-9} m2/s) reported in the literature [31]. Also, the apparent self-diffusivity variations in presence of excited MNPs under different magnetic field intensities and frequencies were examined to assess their influence on liquid molecular transport.

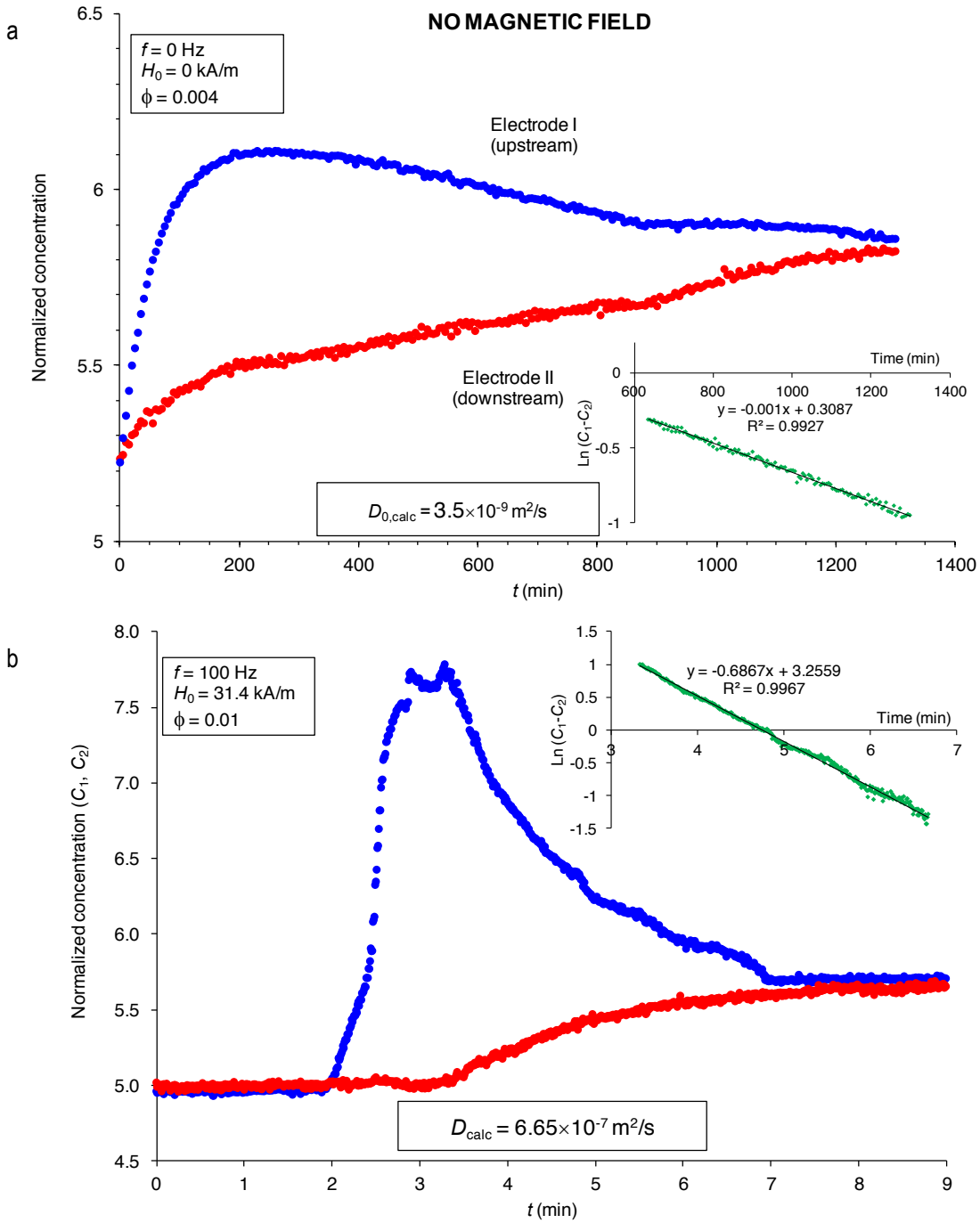

Figure 2-2 : Electrode responses of a conductivity cell, with and without uRMF nano-mixing stimulation. Minute volume of tracer is injected upstream into the capillary tube (d = 1 mm) and tracked at two positions, five and thirty-five mm down the injection point by two sets of electrodes measuring cross-sectional average electrical conductivity. Trends represent the time evolution of tracer conductivity as detected by upstream and downstream electrodes a) magnetic field disabled, $\phi = 0.004$ and b) magnetic field enabled under uRMF, $\phi = 0.01$, $H_0 = 31.4$ kA/m, $f = 100$ Hz

2.4 Result and discussion

Figure 2-2 presents conductimetric responses to the tracer injection with and without rotating magnetic field. It is clearly evident that magnetically-excited spinning of MNPs generate nano-mixing in capillaries as demonstrated by the dramatic attenuation of response time relative to that in magnetic-field-free test.

Since the average MNP particle-particle distance is several times longer than the MNP diameter (e.g., $d_{p\text{-}p} \sim 95$ nm for $\phi = 0.0025$) [18], particle mutual interactions may be neglected [32, 33] and the mixing phenomenon can be interpreted as resulting from the individual particle behavior under magnetic field. Figure 2-3a shows schematically the motion of MNPs in the absence of external magnetic field while their diffusional translation and diffusional rotation is due to random collisions of solvent molecules (i.e., Brownian motion). Accordingly, the particle spin vector ($\boldsymbol{\omega}$, the ensemble-average of single particle spin) is equal to zero and MNP magnetic moments ($\mathbf{m}$) are randomized in all directions due to thermal agitation. Enabling uRMF yields strong enough a magnetic torque, ($\mu_0 \mathbf{m} \times \mathbf{H}$, $\mathbf{H}$ is magnetic field and μ_0 is vacuum permeability) on individual MNPs to overcome Brownian agitation. Thus, MNPs undergo rotational reorientation which forces them to spin perpendicular to H_0 (figure 2-3b). Consequently, spinning MNPs dissipate kinetic energy in the cell prompting effective mixing in the liquid spheroids enclosing each MNP. It is the stimulated motion of liquid molecule in these spheroids that is thought to generate giant self-diffusion in the liquid.

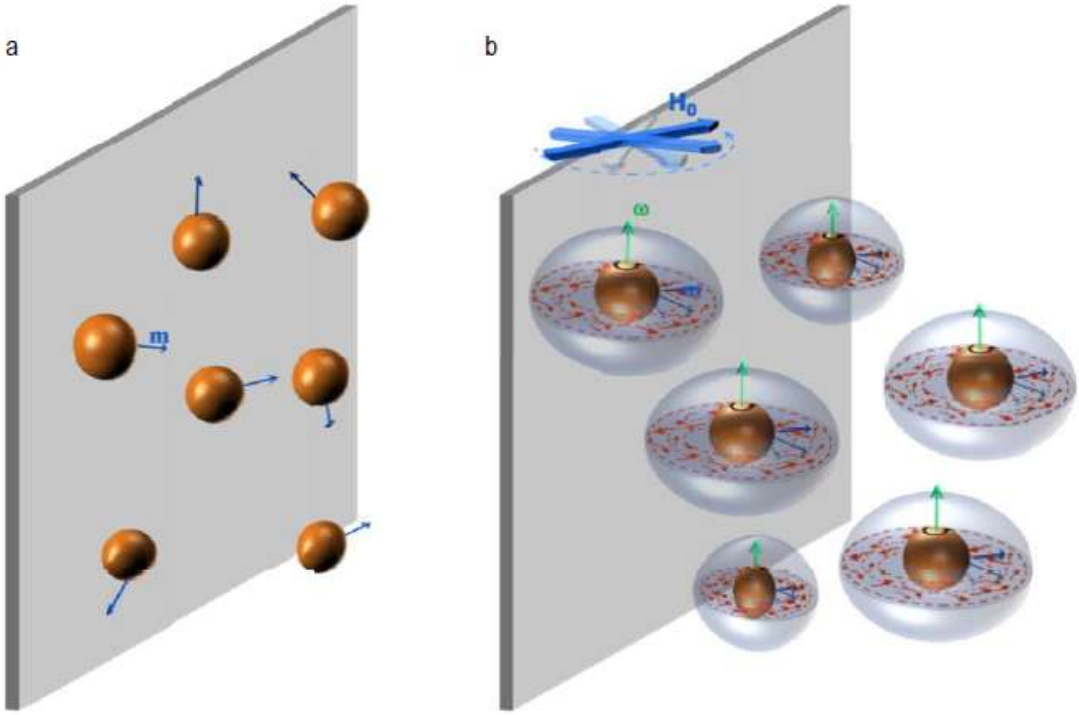

Figure 2-3 : Schematic diagram of MNPs spin in hydrostatic conditions with and without uRMF (a) In absence of magnetic field, MNPs gyration and translation is solely due to Brownian thermal agitation; MNP time-average spin vector (**ω**) is equal to zero since MNP magnetic moments (**m**) are randomized in all directions; (b) In presence of uRMF ($\mathbf{H}_0$), MNP spin vector (**ω**) turns normal to $\mathbf{H}_0$ and hence lateral mixing occurs in all directions along capillary.

To gain more insights into this nano-mixing mechanism, we have further investigated the relationship of D to H_0 (0 to 35 kA/m), ϕ (0 to 0.01) and f (0 to 200 Hz). D/D_0 is plotted as a function of H_0, f and ϕ in figure 2-4 where D_0 refers to suspension self-diffusion coefficient at $H_0 = 0$ (figure 2-4a,b) or $\phi = 0$ in figure 2-4c. In logarithmic scale, D/D_0 increases almost linearly with H_0 (figure 2-4a) echoing sensitivity of effective mixing on magnetic torque. Moreover, D/D_0 increases versus frequency, and then plateaus (figure 2-4b) after nearly all magnetized nanoparticles synchronize with the rotation of a sufficiently strong H_0. One interpretation for the plateauing effect would be that there must be a threshold in rotational speed of MNPs (*ca*. $\boldsymbol{\omega} =$ 50 Hz in figure 2-4b) in which MNP solid-body faster rotation may not proportionally transfer more hydrodynamic torque to the adjacent solvent. Such rupture may occur because at this threshold, the boundary condition on MNP surface may change from no-slip to slip condition [34]. Figure 2-4c illustrates the pronounced effect of concentration of nanostirrers on the enhancement factor. This

observation indicates that at low MNP concentration, at least a part of mass transport over some distance between the spinning MNPs is still dominated by molecular diffusion only. Increasing the MNP concentration shrinks the length scale of the domains where molecular diffusion is the only dominant transport mechanism.

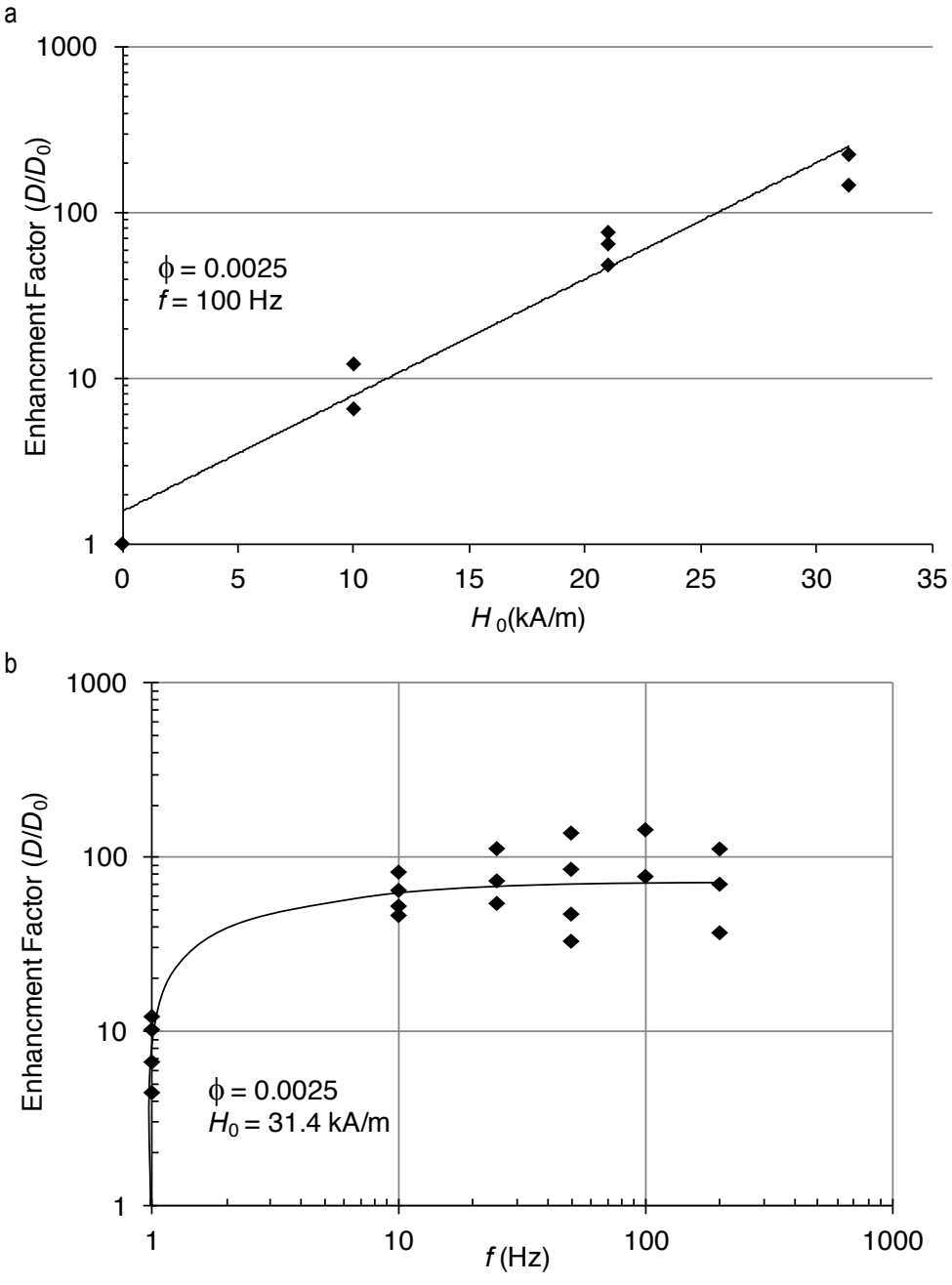

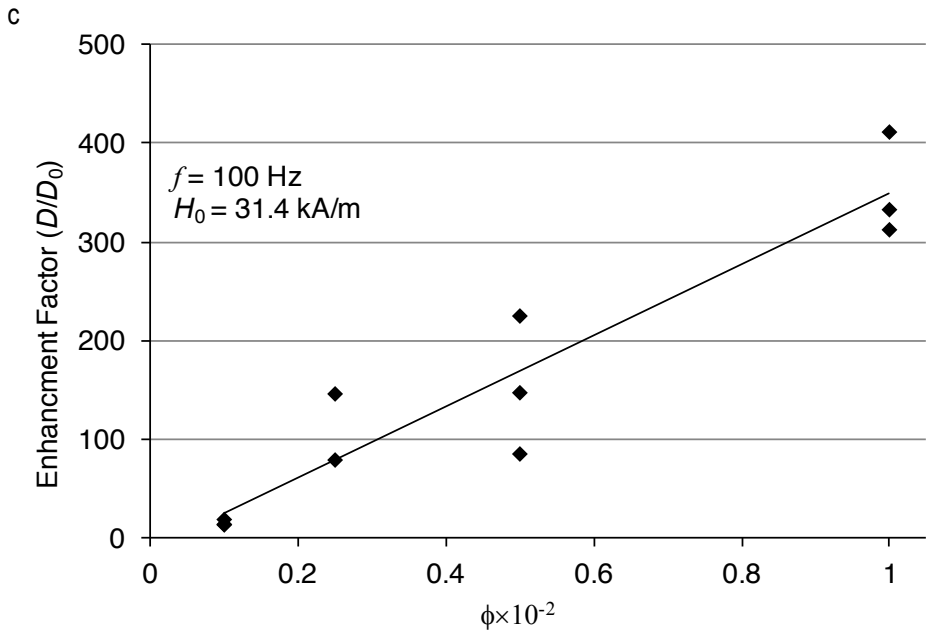

Figure 2-4 : Diffusion enhancement factor under uRMF versus a) magnetic field strength, b) magnetic field frequency and c) MNP concentration. D_0 is liquid self-diffusion coefficient without magnetic field

It is worthy to mention that the mixing mechanism investigated in this study occurs within a single-phase *homogeneous* dilute ferrofluid. As such, it is different from mixing of ferrofluids with nonmagnetic liquids under the effect of a time-varying magnetic field.[19] A distinguishable feature of this latter system is that it is the Kelvin magnetic force that drives mixing due to MNP concentration gradients. Accordingly, the mixing phenomenon *per se* vanishes once uniform MNP concentration throughout the suspension is achieved. In contrast, the nano-mixing mechanism highlighted in our study is not tied to magnetic-force mixing effects and occurs regardless of whether MNP concentration gradients exist or not.

2.5 Conclusion

Although there have been several studies on the effect of nanoparticles on liquid transport properties of nanofluids, the possibility of using magnetically-excited MNPs to stimulated mixing and diffusion in a still-liquid medium that serve as nano-mixing devices has so far not received enough attention. Thus, we performed self-diffusion coefficient measurements in a capillary static cell to identify in which manner interactions between excited MNPs under uRMF and solvent molecules may affect apparent transport properties of the mixture. We note that even at low MNP concentration (*e.g.*, $\phi = 0.0025$), moderate uRMF strength (*e.g.*, $\mu_0 H < 50$ mT) and ultra-low frequency (*e.g.*, $f < 200$ Hz), the liquid self-diffusion

coefficient can be intensified up to two-orders of magnitude. MNP excitation at distance combined with intrinsic magnetic field penetrability into nonmagnetic materials has the potential to open up a range of process intensification strategies where controlled mixing is required in sub-micron thin regions. The fact that suspended functionalized MNPs are finding extensive applications in a variety of disciplines will broaden the scope of this nano-mixing tool beyond that inherent to molecular transport limitation. Hence, uRMF-excited MNPs can easily be converted into catalyst or enzyme supports endowed with magnetic property where nano-stirring enhances the rates of diffusion-limited reactions or of heat transfer from reaction sites toward bulk flows. Finally, the MNPs can then be magnetically separated downstream and used anew.

2.6 References

[1] J.L. Plawsky, Transport Phenomena Fundamentals, Second ed., CRC Press, New York, 2010.

[2] D.D. Devdatta Kulkarni, Nanofluids Properties and Their Applications, First ed., LAP Lambert Academic, New York, 2012.

[3] K.V. Wong, O. De Leon, Applications of nanofluids: current and future, *Adv*. *Mech*. *Eng*. (2010) 1-11.

[4] P.D. Shima, J. Philip, B. Raj, Synthesis of aqueous and nonaqueous iron oxide nanofluids and study of temperature dependence on thermal conductivity and viscosity, *J*. *Phys*. *Chem*. *C* 114 (2010) 18825-33.

[5] K.-F.V. Wong, T. Kurma, Transport properties of alumina nanofluids, *Nanotechnology*, 19 (2008) 345702.

[6] W. Yu, H.Q. Xie, A review on nanofluids: Preparation, stability mechanisms, and applications, *J*. *Nanomater*. (2012) 1-17.

[7] S. Komati, A.K. Suresh, CO2 absorption into amine solutions: a novel strategy for intensification based on the addition of ferrofluids, *J*. *Chem*. *Technol*. *Biotechnol*. 83 (2008) 1094-100.

[8] S. Komati, A.K. Suresh, Anomalous enhancement of interphase transport rates by nanoparticles: Effect of magnetic iron oxide on gas-liquid mass transfer, *Ind*. *Eng*. *Chem*. *Res*. 49 (2010) 390-405.

[9] A.N. Turanov, Y.V. Tolmachev, Heat- and mass-transport in aqueous silica nanofluids, *Heat Mass Transfer* 45 (2009) 1583-1588.

[10] V. Subba-Rao, P.M. Hoffmann, A. Mukhopadhyay, Tracer diffusion in nanofluids measured by fluorescence correlation spectroscopy, *J*. *Nanopart*. *Res*. 13 (2011) 6313-6319.

[11] J. Veilleux, S. Coulombe, A dispersion model of enhanced mass diffusion in nanofluids, *Chem. Eng. Sci.* 66 (2011) 2377-2384.

[12] J. Veilleux, S. Coulombe, A total internal reflection fluorescence microscopy study of mass diffusion enhancement in water-based alumina nanofluids, *J. Appl. Phys.* 108 (2010) 104316.

[13] X.M. Feng, D.W. Johnson, Mass transfer in SiO2 nanofluids: A case against purported nanoparticle convection effects, *Int. J. Heat Mass Transfer* 55 (2012) 3447-3453.

[14] X.P. Fang, Y.M. Xuan, Q. Li, Experimental investigation on enhanced mass transfer in nanofluids, *Appl. Phys. Lett.* 95 (2009) 203108.

[15] B. Olle, S. Bucak, T.C. Holmes, L. Bromberg, T.A. Hatton, D.I.C. Wang, Enhancement of oxygen mass transfer using functionalized magnetic nanoparticles, *Ind. Eng. Chem. Res.* 45 (2006) 4355-4363.

[16] A.K. Suresh, S. Bhalerao, Rate intensification of mass transfer process using ferrofluids, *Indian J. Pure Appl. Phys.* 40 (2001) 172-181.

[17] A. Sergis, Y. Hardalupas, Anomalous heat transfer modes of nanofluids: a review based on statistical analysis, *Nanoscale Res. Lett.* 6 (2011) 1-37.

[18] R.E. Rosensweig, Ferrohydrodynamics, First ed., Dover Publications, New York, 1997.

[19] L.D. Mao, H. Koser, Overcoming the diffusion barrier: Ultra-fast micro-scale mixing via ferrofluids, in: Transducers '07 & Eurosensors Xxi, Digest of Technical Papers, Vols 1 and 2, Ieee, New York, 2007, pp. U923-U24.

[20] R. Rakoczy, S. Masiuk, Influence of transverse rotating magnetic field on enhancement of solid dissolution process, *Aiche J.* 56 (2010) 1416-1433.

[21] R. Rakoczy, S. Masiuk, Studies of a mixing process induced by a transverse rotating magnetic field, *Chem. Eng. Sci.* 66 (2011) 2298-2308.

[22] R. Rakoczy, Study of effect of temperature gradient on solid dissolution process under action of transverse rotating magnetic field, *Aiche J*. 58 (2012) 1030-1039.

[23] B. Stuyven, Q. Chen, W. Van de Moortel, H. Lipkens, B. Caerts, A. Aerts, L. Giebeler, B. Van Eerdenbrugh, P. Augustijns, G. Van den Mooter, J. Van Humbeeck, J. Vanacken, V.V. Moshchalkov, J. Vermant, J.A. Martens, Magnetic field assisted nanoparticle dispersion *Chem*. *Commun*. (2009) 47-49.

[24] R.W. Chantrell, J. Popplewell, S.W. Charles, Measurements of particle-size distribution parameters in ferrofluids, *IEEE Trans*. *Magn*. 14 (1978) 975-977.

[25] D.G. Leaist, P.A. Lyons, Multicomponent diffusion in dilute-solutions of mixed electrolytes, *Aust*. *J*. *Chem*. 33 (1980) 1869-1887.

[26] D.G. Leaist, Diffusion in dilute aqueous-solutions of phosphoric-acid - verification of the limiting law for diffusion of weak electrolytes, *J*. *Chem*. *Soc*. *Farad*. *T*. 1, 80 (1984) 3041-3050.

[27] D.G. Leaist, Diffusion-coefficient of aqueous sulfur-dioxide at 25-degrees-c, *J*. *Chem*. *Eng*. *Data* 29 (1984) 281-282.

[28] D.G. Leaist, P.A. Lyons, Diffusion in dilute aqueous acetic-acid solutions at 25-degrees-C, *J*. *Solution Chem*. 13 (1984) 77-85.

[29] H.S. Harned, D.M. French, A conductance method for the determination of the diffusion coefficients of electrolytes, *Ann*. *N*. *Y*. *Acad*. *Sci*. 46 (1945) 267-283.

[30] T.A. Renner, P.A. Lyons, Electrolyte diffusion in acetonitrile - Harned conductometric technique, *J*. *Phys*. *Chem*. 78 (1974) 1667-1670.

[31] K. Tanaka, Self-diffusion coefficients of water in pure water and in aqueous-solutions of several electrolytes with O-18 and H-2 as tracers, *J*. *Chem*. *Soc*. *Farad*. *T*. 1, 74 (1978) 1879-1881.

[32] S.P. Gubin, Y.A. Koksharov, G.B. Khomutov, G.Y. Yurkov, Magnetic nanoparticles: Preparation methods, structure and properties, *Usp*. *Khim*. 74 (2005) 539-574.

[33] H.T. Yang, H.L. Liu, N.N. Song, H.F. Du, X.Q. Zhang, Z.H. Cheng, J. Shen, L.F. Li, Determination of the critical interspacing for the noninteracting magnetic nanoparticle system, *Appl*. *Phys*. *Lett*. 98 (2011) 153112.

[34] Y.X. Zhu, S. Granick, Limits of the hydrodynamic no-slip boundary condition, *Phys*. *Rev*. *Lett*. 88 (2002) 106102.

3 Reducing Taylor dispersion in capillary laminar flows using magnetically excited nanoparticles:

Nano-mixing mechanism for micro/nanoscale applications

3.1 Abstract

Magnetic nanoparticles (MNP) suspended in liquids lend themselves to manipulation at distance using suitable external magnetic fields to shuttle anchored catalysts, enzymes or drugs. Despite their widespread use in (bio)catalysis/separation or drug delivery – applications where nanoscale mixing can be a substantive issue–, the use of MNPs to promote nano-mixing has not yet been explored. We report a new magnetically-induced nanoconvection mechanism that will enhance transport beyond the limits of molecular diffusion. This mechanism is demonstrated using a Taylor dispersion capillary flow cell where MNPs are excited using low-frequency transverse rotating magnetic fields. Forcing MNP spin direction to align parallel to flow in opposition to fluid vorticity is shown to intensify lateral mixing far more rapidly than molecular diffusion. This nano-mixing mechanism could find applications in (bio)chemical engineering, medical and pharmaceutical areas where transport intensification is crucial.

3.2 Introduction

In recent years, the realm of single-domain superpara**m**agnetic **n**ano**p**articles (MNP) has permeated into a vast range of technical and scientific disciplines. The interest in MNPs stems from the unique ability to maneuver them at otherwise inaccessible spatial scales using suitable external magnetic fields. They provide a technique to induce desirable MNP momentum/heat responses, *e.g*., translation, resonance, hyperthermia, etc. [1-7] remotely and non-invasively. The focus in most current studies has been put on deploying strategies to harness their use as recyclable shuttles in homogeneous-heterogeneous (bio)catalysis and (bio)separations [8-21], as drug vehicles for the delivery of therapeutic payloads or as heating mediators in cancer therapy [7, 22-24].

In this paper we propose to expand the horizon of MNP possibilities by identifying magnetically-induced nanoconvection mechanism to intensify transport beyond the scope of molecular diffusion. A rigid-dipole MNP, by virtue of its Brownian relaxation pattern

[25], spins bodily in a rotating magnetic field as its magnetic moment tries to follow the dynamic magnetic field [25]. Spinning nanoparticles in dilute colloidal suspensions – where magnetic mutual interactions among MNPs are negligible–[26, 27] transfer their momentum to the surrounding liquid molecules and thus entrain them in an angular motion. Hence, nanoscale mixing effects around individual nanoparticles may be expected in so far as each MNP spins as an independent nanostirrer. If this picture proves true, the potential of nano-mixing induced by rotating magnetic fields bears enormous implications in fields where molecular diffusion represents a severe barrier to transport, *e.g.*, mass/heat transfer in laminar-flow fluidics [28], diffusion-limited uptake around high-turnover-frequency catalyst sites in synthetic or physiological fluids [29, 30], etc. For instance, it is vital in several applications in microfluidics to rapidly homogenize microchannel contents transverse to the direction of a main laminar flow [31, 32].

We report that externally excited suspended MNPs are efficient nanotools for generating liquid-phase mixing at submicron levels using low-frequency rotating magnetic fields. Here, we describe a mixing tool to enhance mass transport laterally to streamlined laminar flows through microchannels. To measure the extent of nano-mixing, residence time distribution measurements are performed using a Taylor dispersion capillary cell from which axial dispersion coefficients are obtained. Evidence for a secondary nanoconvective transverse mixing mechanism that is superior to molecular diffusion is obtained by measuring the reduction of axial dispersion even under very low MNP volume fractions ($\sim 0.1\%$). As a second manifestation of nano-mixing, we report that laminar velocity profiles exhibit mimetic shear-thinning behavior that tends to flatten with intensified nano-mixing. From a hydrodynamic perspective, both effects are optimally taken advantage of as the MNP spin vector is set parallel to direction of the flow.

3.3 Experimental section

3.3.1 MNP suspension

Dilute aqueous suspensions of ferrite (Fe_3O_4) MNPs (0.05%vol to 1%vol magnetic content) are prepared from commercial ferrofluids (EMG705, Ferrotec). The magnetic properties of MNP-containing suspensions are measured using an alternating gradient magnetometer (MicroMag model 2900, Princeton Instrument Co.) at 298 K in low- and high-field

asymptotes of the magnetization curve. The magnetic core median diameter, d_c, is estimated to be 16.0 nm. The particle size distribution measured using a dynamic light scattering technique gave a number-average particle hydrodynamic diameter of 24.8 nm (Appendix A). Suspensions with finer MNP d_c are obtained through centrifugation of as-received ferrofluids at 20,000 rpm for 4 h (Beckman model Avanti™ J-30I). After the magnetic properties of the centrifuged product are characterized, the desired particle volume fraction, $\phi = 10^{-3}$, is achieved via dilution. Due to low MNP concentration, particle-particle MNP interactions are negligible with solvent physical properties barely altered. Most experiments are performed for $\phi = 10^{-3}$ where vortex viscosity is zero and relative shear viscosity is one [33-35].

3.3.2 Magnet

To generate ^{T}RMF, a tubular two-pole and three-phase (6-cm high and 4.5-cm i.d. cylindrical bore) magnet has been designed and built in collaboration with MotionTech LLC and Winding Inc. The magnet has the capacity to provide both uniform and gradient magnetic fields at moderate strength (< 50 mT) at the bore center with up to 3 A three-phase currents. Both magnetic field strength and frequency can be controlled directly by means of three-phase power supply (ACS150, 2.2kW Variable Frequency Drive) while the magnet is cooled with a water cooling jacket (Appendix A).

3.3.3 RTD test

The glass capillary tube is equipped with two conductivity electrode sets 3 cm apart as a typical length of microfluidic channels. The dilute aqueous MNP suspension is pumped through the capillary by a syringe pump. The tracer consists of 5.10^{-2} M NaCl dissolved in MNP suspension carefully tuned to yield the same MNP volume fraction as in the main circulating MNP suspension to prevent susceptibility jump (and thus epiphenomenal mixing) at the encounter between the two streams under ^{T}RMF. The axial dispersion coefficient is estimated by means of an open-open boundary dispersion model [36] in laminar flow (Appendix A).

3.4 Results and discussion

3.4.1 Taylor dispersion test

A Poiseuille flow of water sparsely seeded with MNPs is subjected to a uniform transverse rotating magnetic field (^{T}RMF) in a capillary (d = 1 mm, i.d.) aligned coaxially inside a magnet bore (Figure 3-1). Unexcited (magnetic-field free) MNPs whose spins are collinear to fluid vorticity have randomly directed magnetic moments due to the effects of Brownian agitation (Figure 3-2a) [25]. When a magnetic field is applied the nanoparticle magnetic moments are coerced to gyrate transversely to the flow direction in response to the ^{T}RMF. This aligns the spin direction of excited MNPs to nearly parallel to the flow direction while being at odds with fluid vorticity (Figure 3-2b). Viscid shear forces oppose nanoparticle bodily rotation causing MNPs to spin in θ-tilted planes (Figure 3-2b) reflecting shear that is maximum on the wall and fading to zero towards the capillary centerline [37]. A sufficiently strong magnetic torque is required near the capillary wall to enable the MNPs to bodily rotate ($\theta \neq 0$) while close to centerline the viscous torque is easily overcome by the magnetic torque ($\theta \rightarrow 0$). We hypothesize that the excited MNPs possess a hitherto undocumented ability to enhance the diffusive migration across streamlines in laminar flows, beyond the scope of molecular diffusion, and this occurs via a nanoconvection mechanism.

Taylor dispersion [38, 39] measurements are performed both with magnetically-excited and unexcited MNPs to test this hypothesis and to assess the enhancement of lateral mixing in purely linear laminar flows. A thin tracer slice is briefly injected at t = 0 and two electrodes, placed 5 cm and 8 cm downstream of injection, monitor the spreading of concentration signals over a capillary length L = 3 cm (Figure 3-3a). Axial dispersion coefficients (D) are obtained from residence time distribution (RTD) experiments, moment and convolution analyses [36] for a range of rotating magnetic field strengths and frequencies, H_0 and f, MNP magnetic core volume fraction and median diameter, ϕ and d_c, and fluid superficial velocity, U, while ensuring low Reynolds ($Re = Ud/\nu \sim O(1)$) and large Péclet ($Pe = Ud/D \sim O(10^3)$) numbers.

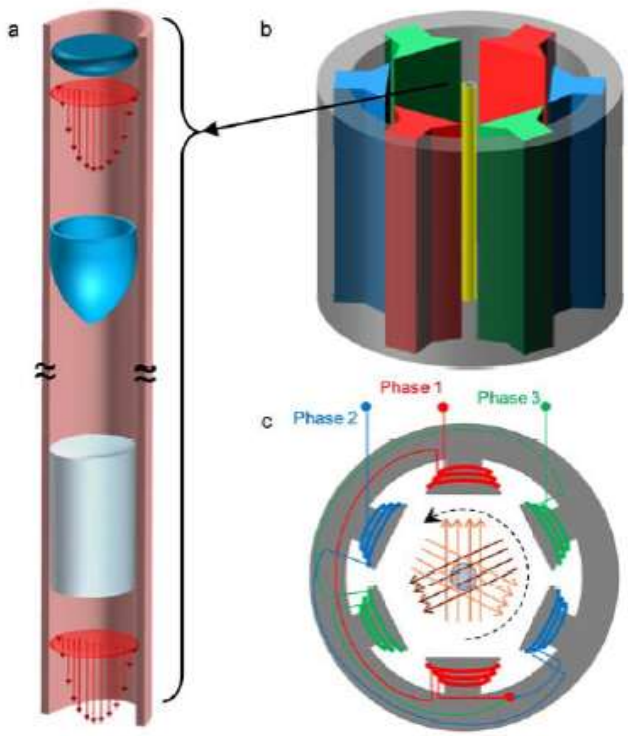

Figure 3-1 : Taylor dispersion in capillary tube exposed to a rotating magnetic field (a) Dispersion of a tracer plug in Poiseuille flow; (b) Experimental setup consists of a two-pole three-phase tubular magnet (6 cm long, 4.5 cm i.d.) powered by a three-phase powersupply to generate a transverse rotating magnetic field (with variable frequency and strength) across a coaxially aligned glass capillary (10 cm long, 1 mm i.d.) (c) Magnet upper view showing a uniform horizontal rotating magnetic field over a capillary flow of a dilute suspension of magnetic nanoparticles

Magnetic field-free convective flow alone would stretch the tracer slice into a paraboloidal shell the vertex of which protrudes a distance $2Ut$ away from tracer incipient point. Tracer lateral leakage by molecular diffusion – outwards from tracer-rich centerline on the front and inwards from the likewise tracer-rich wall on the back – distorts the shell into a quite evenly shaped plug (Figure 3-1a) at sojourn times larger than $d^2/Đ$ (Đ tracer molecular diffusivity). Over short lengths or residence times, Taylor dispersion in laminar flows fails to achieve adequate lateral mixing when relying only on molecular diffusion [40]. Therefore, a reduction of the measured D values should be observed when techniques to enhance lateral spreading by allowing the tracer to mix across the capillary are used [41]. Induced by ^{T}RMF-excited MNPs, this reduction of the D values is used to characterize lateral nano-mixing crosswise to flow direction.

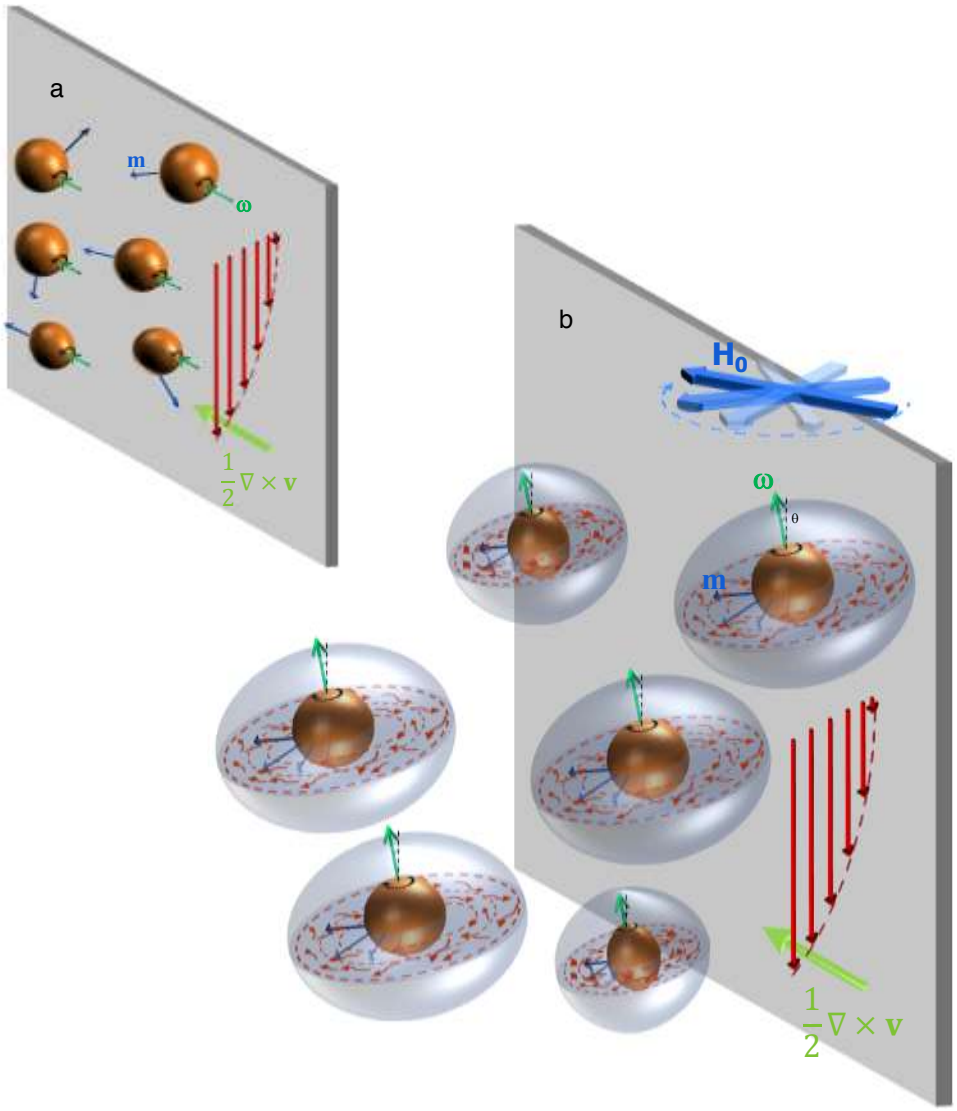

Figure 3-2 : Schematic diagram of MNPs spin in shear flow with and without ^{T}RMF (a) In the absence of magnetic field, MNPs gyrate synchronously with fluid vorticity; MNP spin vector ($\boldsymbol{\omega}$) is equal half fluid vorticity ($1/2\nabla\times\mathbf{v}$) and MNP magnetic moments ($\mathbf{m}$) are randomized in all directions; (b) In presence of ^{T}RMF ($\mathbf{H}_0$), MNP spin vector ($\boldsymbol{\omega}$) turns normal to azimuthal fluid vorticity vector and hence mixing is lateral. Mixed spheroid zones form around MNPs when magnetic torque ($\mu_0\mathbf{m}\times\mathbf{H}$, $\mathbf{m}$ is MNP magnetic moment, $\mathbf{H}$ is magnetic field and μ_0 is vacuum permeability) overcomes Brownian agitation and frictional torque ($2\zeta(\nabla\times\mathbf{u}-2\boldsymbol{\omega})$, $\mathbf{u}$ is linear fluid velocity, $\boldsymbol{\omega}$ is local MNP spin, ζ is spin viscosity). The distance between stirred spheroids is affected by MNP concentration and ^{T}RMF frequency. Significant mixing occurs when most of the stirred zones overlap to assist material exchange amongst them.

Transient impulse responses registered by 1st (■,▲,●) and 2nd (□,△,○) electrodes are shown in Figure 3-3b for identical f, ϕ, d_c and U but increased magnetic field strength: 0(■,□), 10.4 kA/m (▲,△) and 36.5 kA/m (●,○). The breakthrough (Figure 3-3c) and asymmetry (long tail, Figure 3-3b) of (■,□) signals correspond to weakly dispersed centerline tracer

and strongly dispersed tracer originally in the shear-active wall region when passing by the electrodes. Relative to unstirred Poiseuille flow (■,□), the ability of rotating MNPs to induce lateral nano-mixing results in more symmetric peaks featuring significant reduction of peak variance, short tails and slow-paced breakthroughs. These changes imply conclusively that diffusive migration is assisted across streamlines by a secondary mixing mechanism.

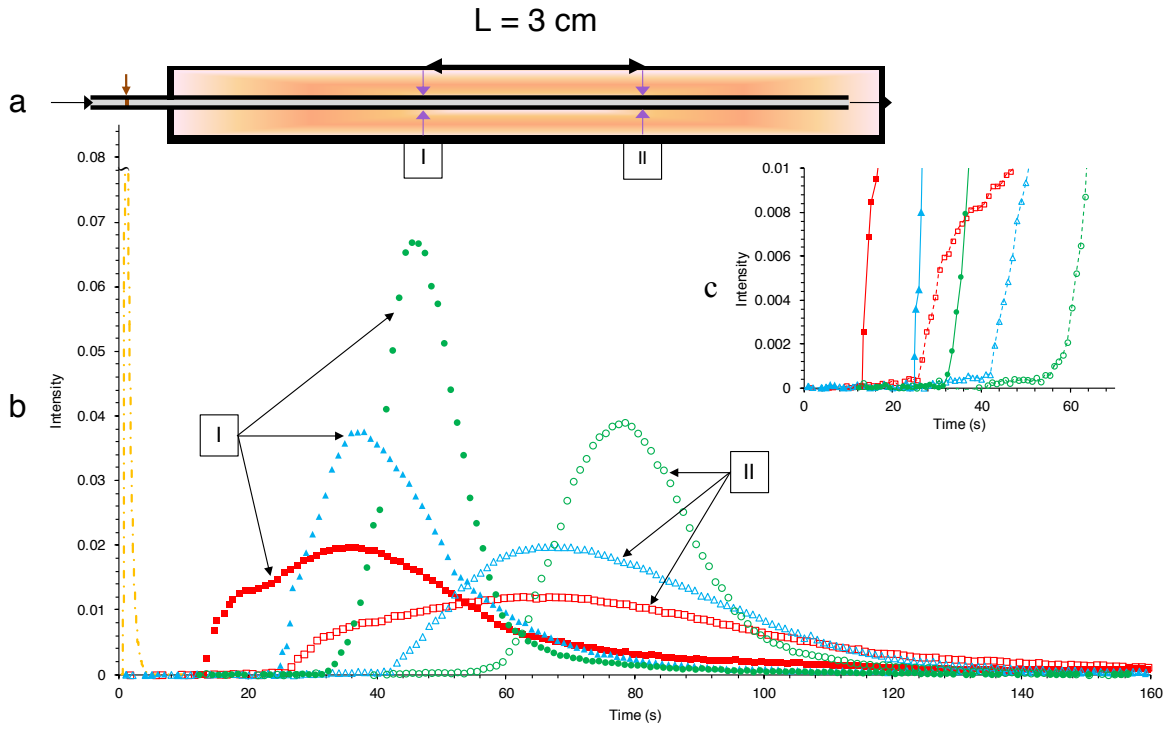

Figure 3-3 : Impulse response of a Taylor dispersion capillary with and without nano-mixing (a) Schematic of Taylor dispersion capillary tube with two sets of detectors inside magnet bore; (b,c) Laminar Poiseuille flow in a capillary tube: d = 1 mm, $Pe \sim 10^3$, $Re \sim 1$. A plug of tracer is injected upstream into the capillary tube and tracked at two positions, five and eight cm down the injection point by two sets of electrodes measuring cross-sectional average electrical conductivity. Trends represent the time evolution of tracer conductivity as detected by upstream and downstream electrodes (■,□) for unstirred Poiseuille flow, (▲,△) nano-mixing for laterally stirred MNPs ϕ = 0.0025, H_0 = 10.4 kA/m, f = 50 Hz, (●,○) nano-mixing for laterally stirred MNPs ϕ = 0.0025, H_0 = 36.5 kA/m, f = 50 Hz. Peak narrowing indicates axial dispersion is reduced under nano-mixing.

Plots of dimensionless D/UL vs. Re are displayed in Figure 3-4 for a range of nano-mixing levels. D/UL is highest for (magnetic-field free) unexcited MNPs while it decreases when excited MNPs generate lateral mixing. As nano-mixing intensifies, D/UL becomes less sensitive to convective flow as reflected in the gentler D/UL vs. Re slopes. This is likely due to laterally magnetized MNPs resisting the fluid viscous tendency to slide telescopic

isovelocity layers over each other (Figure 3-2b). The slopes of trends in Figure 3-4 also suggest that Brownian agitation is more effective in countering magnetic torque compared to the mechanical torque as otherwise there would have been less of a reduction in axial dispersion after a fourfold *Re* increase.

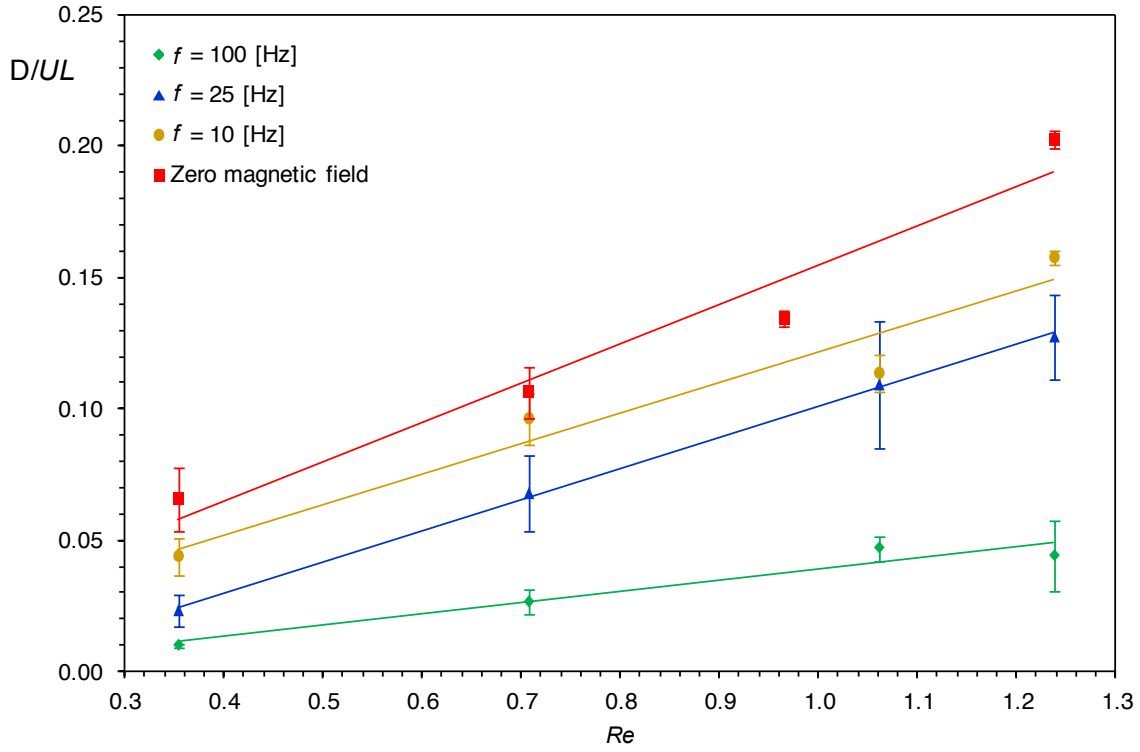

Figure 3-4 : The effect of convective flow on axial dispersion attenuation Axial dispersion coefficient, presented as dimensionless number *D*/*UL*, and estimated from moment analysis of convoluted data from impulse tests (such as in Figure 3-3). Experiments performed with ϕ = 0.001, H_0 = 31.4 kA/m. Milder slopes imply strong nano-mixing counteracting convective stretching. Error bars indicate standard deviation (number of repeat runs = 3)

To gain more insights into the nano-mixing mechanism, we have further investigated the relationship of D to H_0 (0 to 35 kA/m), f (0 to 200 Hz), ϕ (0 to 0.01) and d_c (10.2 and 16.0 nm). D/D_0 is plotted as a function of ^{T}RMF (H_0 and f, Figure 3-5a) and suspension (ϕ and d_c, Figure 3-5b) properties where D_0 refers to axial dispersion at $H_0 = 0$ (Figure 3-5a) or $\phi = 0$ (Figure 3-5b). D/D_0 decreases almost linearly with H_0 (Figure 3-5a) and, echoing size-sensitivity of single-domain magnetic moment (and torque), also with d_c (Figure 3-5b). This latter trend denotes that for invariant ϕ, fewer and larger MNPs (*ca.* 2.3×10^{14} per cm^3, d_c = 16.0 nm, $\phi = 10^{-3}$) absorb magnetic energy and deliver it to the liquid more effectively than more numerous but smaller MNPs (*ca.* 9.0×10^{14} per cm^3, d_c = 10.2 nm, $\phi = 10^{-3}$). As the

frequency increases, D/D_0 decreases and then plateaus (Figure 3-5a) after nearly all magnetized nanoparticles synchronize with the rotation of a sufficiently strong H_0.

For magnetic core volume fractions varying from 10^{-3} to 10^{-2}, the average MNP interparticle distance varies from 129 nm to 60 nm for d_c = 16.0 nm [25]. At such dilution levels, the relative vortex and shear viscosities are, respectively, close to 0 and 1, and magnetic interactions between rigid dipole MNPs may be neglected so that nano-mixing results from the behavior of individual MNPs [26, 27]. Hence, a magnetically-spinning MNP is viewed as an individual nanostirrer encapsulated at the center of a mixed-cup oblate spheroid of solvent molecules. The internally stirred spheroids appear as soon as MNP magnetic torque overcomes Brownian agitation and the mechanical viscous torque. This ensemble of stirred spheroids moves down the capillary following the convective flow (Figure 3-2). It is worth noting that lateral material transport in the complementary inter-spheroid fluid domain occurs via molecular diffusion only.

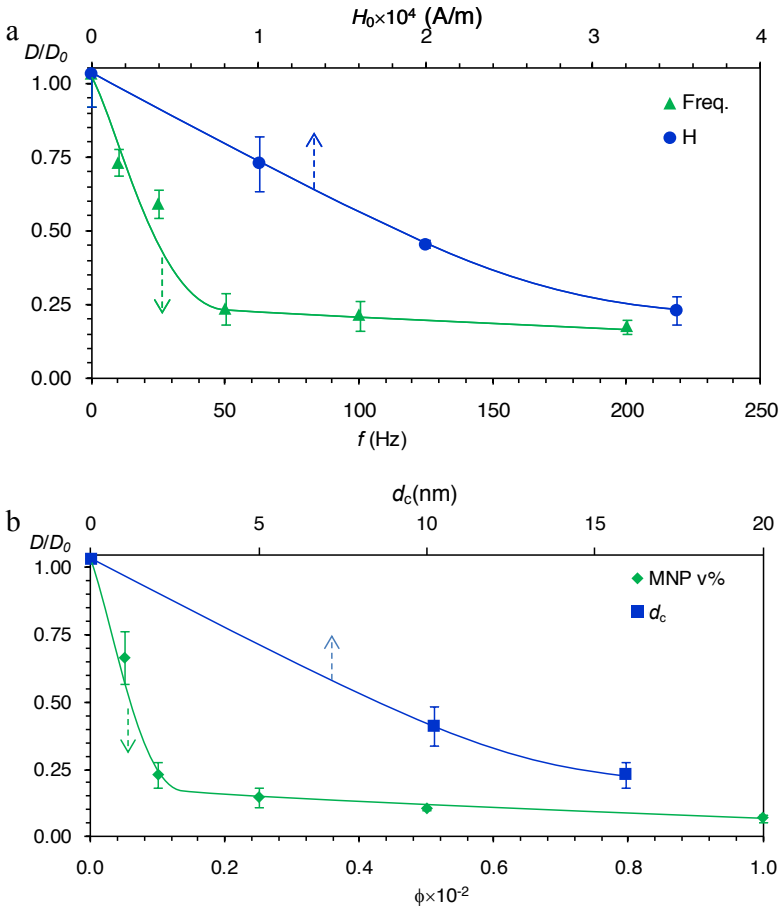

Figure 3-5 : Axial dispersion attenuation is dependent on TRMF strength and frequency, and MNP concentration and core diameter. Experiments carried out at $\phi = 0.001$ and MNP median diameter $d_c = 16.0$ nm unless otherwise stated. (a) D/D_0 versus f (▲) at $H_0 = 31.4$ kA/m plateaus at about 50 Hz. D/D_0 versus H_0 (●) at $f = 50$ Hz. (b) D/D_0 versus ϕ (♦) at $H_0 = 31.4$ kA/m plateaus at about 0.0012. D/D_0 versus d_c (■)at $H_0 = 36.5$ kA/m and $f = 50$ Hz. Error bars indicate standard deviation (number of repeat runs = 12).

The size of the internally-stirred spheroids coarsens with increasing TRMF frequency (and thus MNP spin frequency). This coarsening in combination with MNP spinning in planes almost perpendicular to flow direction (Figure 3-2b) promotes lateral transport as the diffusion length scale is brought down from channel diameter to spheroid length scale. A critical state is reached when adjacent spheroids begin to overlap each other, this accounts for the D/D_0 plateauing trend observed when increasing frequency (Figure 3-5a) or MNP concentration (Figure 3-5b). For instance, this overlap occurs near $f = 50$ Hz at $\phi = 0.001$ for $H_0 = 31.4$ kA/m in Figure 3-5a. Interestingly, a plateau is also reached in Figure 3-5b close to $\phi = 0.0012$ at 50 Hz and $H_0 = 31.4$ kA/m. Exceeding this frequency and volume fraction will not result in improved lateral mixing.

The four variables described above seem to be intrinsically associated in a way to support the nano-mixing mechanism depicted in this study. Since both H_0 and d_c influence MNP magnetic torque in counteracting Brownian agitation and mechanical torque, similar D/D_0 trends are anticipated when increasing either H_0 or d_c. On the other hand, the inter-spheroid distance being controlled by both the MNP volume fraction and ^{T}RMF frequency, analogous D/D_0 trends are likewise expected in their variations with f and ϕ. The experimental results in Figure 3-4 confirm this.

3.4.2 MNPs alter laminar velocity profile in capillary tube

We further investigated how MNP-induced lateral nano-mixing may affect the velocity profile in laminar Poiseuille flows. Spinning MNPs as depicted in Figure 3-2b may attenuate the radial velocity gradients yielding more flattened velocity profiles compared to the usual (unexcited-MNP) parabolic profile. Figure 3-3c provides a crucial clue as the separation between the breakthrough times at the two electrodes amplifies with increased nano-mixing whilst the mean residence time ($\tau = L/U$) is kept identical for all tests. The breakthrough time span features the fastest centerline tracer blob passing by the electrodes with minimum residence time (τ_{min}). The τ/τ_{min} ratio declines from 2 to 1 for a velocity profile evolving from a parabolic to a completely flattened velocity-homogenized one. Assuming no-slip boundary condition on the wall and negligible radial convective effects induced by ^{T}RMF in the capillary, this ratio can be used as a quantitative index to understand how far velocity profiles flatten due to nano-mixing. This can be accomplished by drawing an analogy with non-Newtonian power-law radial velocity profiles, $u(r)$ [37]:

$$u(r) = \frac{3n+1}{1+n} U \left(1 - \left(\frac{r}{a} \right)^{1+1/n} \right) \tag{1}$$

where the power-law index, n, varies between 1 (parabolic profile) and 0 (flat profile) and is expressed as a function of τ_{min}/τ according to [37]:

$$n = \frac{1 - \tau_{min}/\tau}{3\tau_{min}/\tau - 1} \tag{2}$$

Figure 3-6a,b,c plots τ/τ_{min} and n versus H_0, f and ϕ for Figure 3-5a,b (●,▲,♦) experiments. Minimum magnetic field strength (10^4 A/m) and frequency (25 Hz) are required (Figure 3-6a,b) to demonstrate nano-mixing-mediated hydrodynamic effects. Sensitivity of τ/τ_{min} and n to frequency dwindles after 50 Hz (Figure 3-6b) though not reflecting a plateau as in Figure 3-5a (▲). Furthermore, Figure 3-6c shows a minimum at $\phi \sim 0.0025$ exceeding $\phi \sim 0.0012$ in Figure 3-5b (♦). We conclude that unlike concentration homogenization, velocity homogenization (i.e., reduction of n) via nano-mixing is more demanding and requires larger minimal H_0 and ϕ. This is illustrated in Figure 3-6d which shows that the computed velocity profiles flatten as n decreases (from 1 to 10^{-2}) to echo increased nano-mixing intensities.

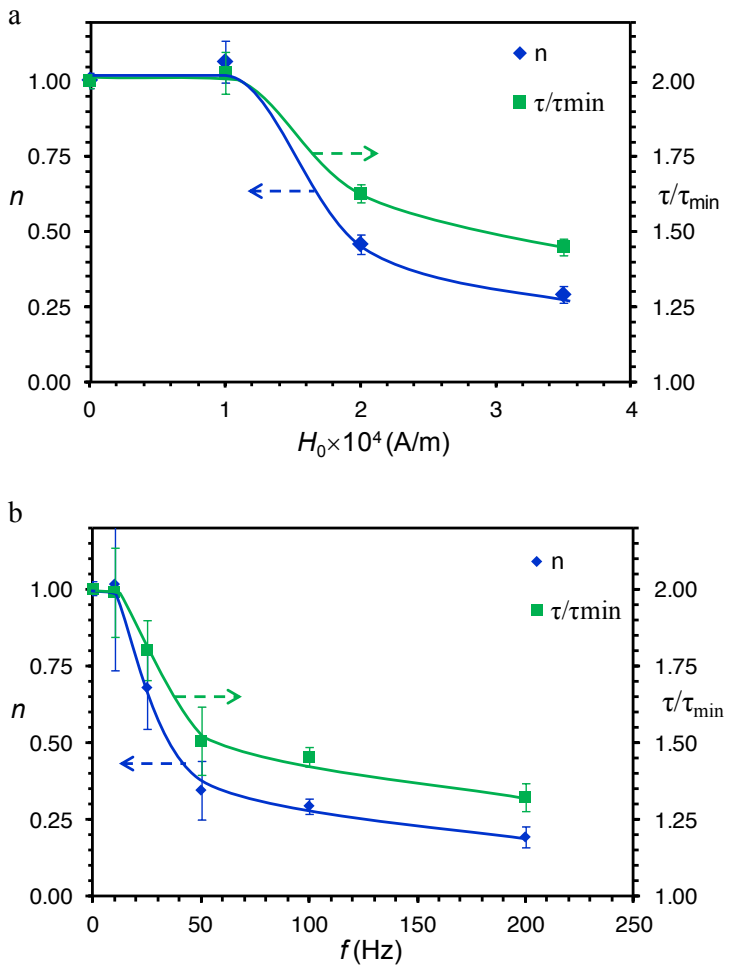

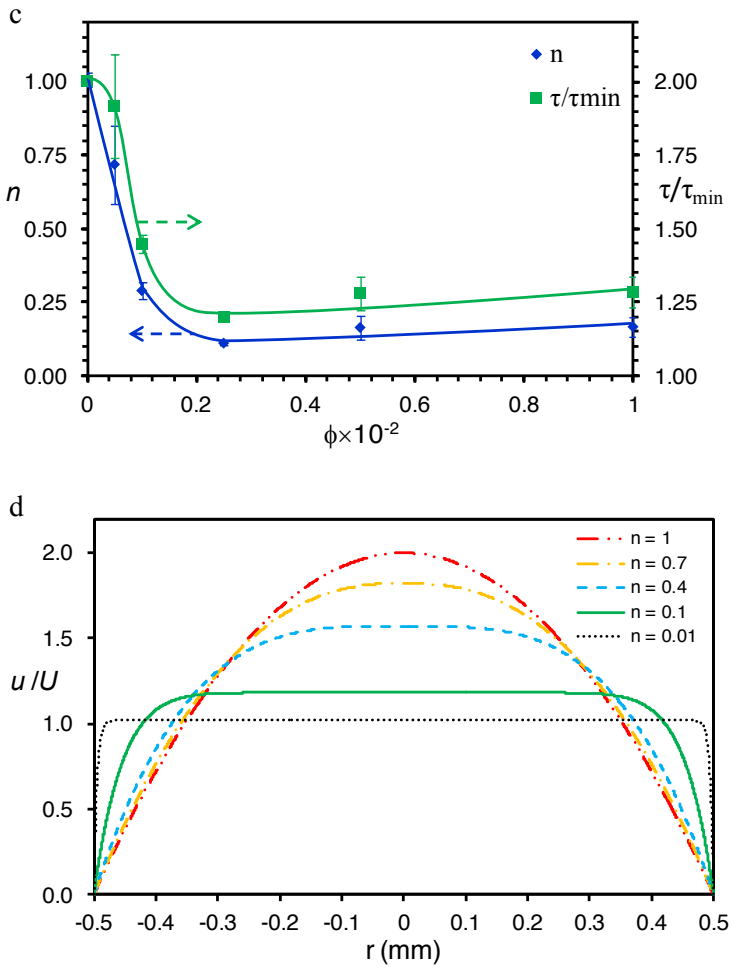

Figure 3-6 : Mixing effect on laminar velocity profile. Power-law index *n* and τ/τ_{min} ratio as a function of (a) magnetic field strength, (b) magnetic field frequency, (c) MNP volume fraction. Error bars indicate standard deviation (number of repeat runs = 6), (d) Simulated laminar flow velocity profile for different lateral mixing intensities in a capillary as a function of power-law index.

There has so far been little awareness of the possibility of using magnetically-excited MNPs as nano-mixing devices. In this study, we implement a remote liquid nano-mixing technique by subjecting MNPs to rotating magnetic fields. Bodily spinning rigid-dipole MNPs are used to deliver electromagnetic energy from an external source to the liquid phase in the desired mixing plane even in small thin regions. To demonstrate its potential, the technique is applied to generate lateral nano-mixing. We note that macroscopic properties in fluidic systems, such as the axial dispersion coefficient and the liquid velocity profile, can be modified via this nano-mixing technique. The experimental results reveal that spinning MNPs stir the liquid within 20-nm length-scale fluid spheroids surpassing the mixing capability of molecular diffusion even at very low MNP concentrations ($\phi < 10^{-2}$).

This also implies that mixing is enhanced on a spatial scale much smaller than the turbulent Kolmogorov scale [42, 43] giving access to mixing scales thus far unreachable even to turbulence. MNP excitation at distance combined with intrinsic magnetic field penetrability into nonmagnetic materials has the potential to open up a range of process intensification and biomedical strategies where controlled mixing is required in sub-micron thin regions. This nano-mixing technique utilizes a low-frequency (f < 200 Hz) moderate strength rotating magnetic field (B < 50 mT) generated by a simply-designed magnet to stimulate MNPs. It worth to mention that Nano-mixing technique is distinguished from magnetohydrodynamic mixing in which Lorentz body force induces disturbance on the interface of an electrically conducting fluid with another miscible liquid [44]. The fact that suspended functionalized MNPs are finding extensive applications in a variety of disciplines will broaden the scope of this nano-mixing tool beyond that inherent to molecular transport limitation. ^{T}RMF-excited MNPs can easily be converted into catalyst or enzyme supports endowed with magnetic property where nanostirring enhances the rates of diffusion-limited reactions or of heat transfer from reaction sites toward bulk flows. Finally, the MNPs can then be magnetically separated downstream and used anew.

3.5 Conclusion

By studying axial dispersion in a dilute liquid suspension containing MNPs and flowing through a Taylor capillary cell under moderate strength low frequency transverse rotating magnetic fields (^{T}RMF), we found that spinning MNPs produce nano-sized vortices that objectively enhance liquid transport properties beyond the capability of molecular diffusion. Systematic study of capillary axial dispersion versus design parameters (i.e., ^{T}RMF strength and frequency, MNP concentration and median particle diameter) with and without excited MNPs enabled understanding of a nano-mixing mechanism. Spinning MNPs was found to induce meaningful nanoconvective mixing levels around nanoparticles; a phenomenon which is especially valuable for applications combining stimulation of lateral mixing in laminar flows and functionalized MNPs utilized as separable agents.

3.6 References

[1] C. Alexiou, W. Arnold, R.J. Klein, F.G. Parak, P. Hulin, C. Bergemann, W. Erhardt, S. Wagenpfeil, A.S. Lubbe, Locoregional cancer treatment with magnetic drug targeting, *Cancer*. *Res*. 60 (2000) 6641-6648.

[2] B. Chertok, B.A. Moffat, A.E. David, F.Q. Yu, C. Bergemann, B.D. Ross, V.C. Yang, Iron oxide nanoparticles as a drug delivery vehicle for MRI monitored magnetic targeting of brain tumors, *Biomaterials* 29 (2008) 487-496.

[3] J. Dobson, Magnetic nanoparticles for drug delivery, *Drug Dev*. *Res*. 67 (2006) 55-60.

[4] N. Kohler, C. Sun, A. Fichtenholtz, J. Gunn, C. Fang, M.Q. Zhang, Methotrexate-immobilized poly(ethylene glycol) magnetic nanoparticles for MR imaging and drug delivery, *Small* 2 (2006) 785-792.

[5] S.C. McBain, H.H.P. Yiu, J. Dobson, Magnetic nanoparticles for gene and drug delivery, Int. *J*. *Nanomed*. 3 (2008) 169-180.

[6] J.-H. Lee, J.-t. Jang, J.-s. Choi, S.H. Moon, S.-h. Noh, J.-w. Kim, J.-G. Kim, I.-S. Kim, K.I. Park, J. Cheon, Exchange-coupled magnetic nanoparticles for efficient heat induction, *Nat*. *Nanotechnol*. 6 (2011) 418-422.

[7] Q.A. Pankhurst, J. Connolly, S.K. Jones, J. Dobson, Applications of magnetic nanoparticles in biomedicine, *J*. *Phys*. *D-Appl*. *Phys*. 36 (2003) R167-R181.

[8] S. Shylesh, V. Schunemann, W.R. Thiel, Magnetically separable nanocatalysts: Bridges between homogeneous and heterogeneous catalysis, *Angew*. *Chem*. *Int*. *Ed*. 49 (2010) 3428-3459.

[9] T.J. Yoon, W. Lee, Y.S. Oh, J.K. Lee, Magnetic nanoparticles as a catalyst vehicle for simple and easy recycling, *New*. *J*. *Chem*. 27 (2003) 227-229.

[10] P.D. Stevens, G.F. Li, J.D. Fan, M. Yen, Y. Gao, Recycling of homogeneous Pd catalysts using superparamagnetic nanoparticles as novel soluble supports for Suzuki, Heck, and Sonogashira cross-coupling reactions, *Chem*. *Commun*. (2005) 4435-4437.

[11] M. Shokouhimehr, Y. Piao, J. Kim, Y. Jang, T. Hyeon, A magnetically recyclable nanocomposite catalyst for olefin epoxidation, *Angew*. *Chem*. *Int*. *Ed*. 46 (2007) 7039-7043.

[12] C. Che, W. Li, S. Lin, J. Chen, J. Zheng, J.-c. Wu, Q. Zheng, G. Zhang, Z. Yang, B. Jiang, Magnetic nanoparticle-supported Hoveyda-Grubbs catalysts for ring-closing metathesis reactions, *Chem*. *Commun*. (2009) 5990-5992.

[13] X.X. Zheng, S.Z. Luo, L. Zhang, J.P. Cheng, Magnetic nanoparticle supported ionic liquid catalysts for $CO_{(2)}$ cycloaddition reactions, *Green Chem*. 11 (2009) 455-458.

[14] T.Q. Zeng, L. Yang, R. Hudson, G.H. Song, A.R. Moores, C.J. Li, $Fe_{(3)}O_{(4)}$ Nanoparticle-supported copper(I) pybox catalyst: Magnetically recoverable catalyst for enantioselective direct-addition of terminal alkynes to imines, *Org*. *Lett*. 13 (2011) 442-445.

[15] V. Polshettiwar, R. Luque, A. Fihri, H. Zhu, M. Bouhrara, J.-M. Bassett, Magnetically recoverable nanocatalysts, *Chem*. *Rev*. 111 (2011) 3036-3075.

[16] L.Z. Gao, J. Zhuang, L. Nie, J.B. Zhang, Y. Zhang, N. Gu, T.H. Wang, J. Feng, D.L. Yang, S. Perrett, X. Yan, Intrinsic peroxidase-like activity of ferromagnetic nanoparticles, *Nat*. *Nanotechnol*. 2 (2007) 577-583.

[17] L. Guo, J. Huang, X. Zhang, Y. Li, L. Zheng, Bacterial magnetic nanoparticles as drug carriers, *J*. *Mater*. *Chem*. 18 (2008) 5993–5997.

[18] H.H. Yang, S.Q. Zhang, X.L. Chen, Z.X. Zhuang, J.G. Xu, X.R. Wang, Magnetite-containing spherical silica nanoparticles for biocatalysis and bioseparations, *Anal*. *Chem*. 76 (2004) 1316-1321.

[19] A. Debrassi, A.F. Correa, T. Baccarin, N. Nedelko, A. Slawska-Waniewska, K. Sobczak, P. Dluzewski, J.-M. Greneche, C.A. Rodrigues, Removal of cationic dyes from

aqueous solutions using N-benzyl-O-carboxymethylchitosan magnetic nanoparticles, *Chem*. *Eng*. *J*. 183 (2012) 284-293.

[20] Y. Pang, G. Zeng, L. Tang, Y. Zhang, Y. Liu, X. Lei, Z. Li, J. Zhang, Z. Liu, Y. Xiong, Preparation and application of stability enhanced magnetic nanoparticles for rapid removal of Cr(VI), *Chem*. *Eng*. *J*. 175 (2011) 222-227.

[21] Z.-p. Yang, X.-y. Gong, C.-j. Zhang, Recyclable Fe(3)O(4)/hydroxyapatite composite nanoparticles for photocatalytic applications, *Chem*. *Eng*. *J*. 165 (2010) 117-121.

[22] A. Ito, M. Shinkai, H. Honda, T. Kobayashi, Medical application of functionalized magnetic nanoparticles, *J*. *Biosci*. *Bioeng*. 100 (2005) 1-11.

[23] Q.A. Pankhurst, N.K.T. Thanh, S.K. Jones, J. Dobson, Progress in applications of magnetic nanoparticles in biomedicine, *J*. *Phys*. *D-Appl*. *Phys*. 42 (2009) 15.

[24] I. Giouroudi, J. Kosel, Recent progress in biomedical applications of magnetic nanoparticles, *Recent Pat*. *Nanotechnol*. 4 (2010) 111-118.

[25] R.E. Rosensweig, Ferrohydrodynamics, Dover Publications, Mineola, 1997.

[26] S.P. Gubin, Y.A. Koksharov, G.B. Khomutov, G.Y. Yurkov, Magnetic nanoparticles: Preparation methods, structure and properties, *Usp*. *Khim*. 74 (2005) 539-574.

[27] H.T. Yang, H.L. Liu, N.N. Song, H.F. Du, X.Q. Zhang, Z.H. Cheng, J. Shen, L.F. Li, Determination of the critical interspacing for the noninteracting magnetic nanoparticle system, *Appl*. *Phys*. *Lett*. 98 (2011) 3.

[28] T.M. Squires, S.R. Quake, Microfluidics: Fluid physics at the nanoliter scale, *Rev*. *Mod*. *Phys*. 77 (2005) 977-1026.

[29] F. Larachi, Kinetic model for the reversible hydration of carbon dioxide catalyzed by human carbonic anhydrase II, *Ind*. *Eng*. *Chem*. *Res*. 49 (2010) 9095-9104.

[30] A. Pohar, P. Žnidaršič-Plazl, I. Plazl, Integrated system of a microbioreactor and a miniaturized continuous separator for enzyme catalyzed reactions, *Chem. Eng. J.* 189-190 (2012) 376-382.

[31] A.J. deMello, Control and detection of chemical reactions in microfluidic systems, *Nature* 442 (2006) 394-402.

[32] V. Kumar, M. Paraschivoiu, K.D.P. Nigam, Single-phase fluid flow and mixing in microchannels, *Chem. Eng. Sci.* 66 (2011) 1329-1373.

[33] H. Brenner, Rheology of a dilute suspension of dipolar spherical particles in an external field, *J. Colloid Interf. Sci.* 32 (1970) 141-158.

[34] H. Brenner, Antisymmetric stresses induced by the rigid-body rotation of dipolar suspensions - vortex flows, *Int. J. Eng. Sci.* 22 (1984) 645-682.

[35] S. Feng, A.L. Graham, J.R. Abbott, H. Brenner, Antisymmetric stresses in suspensions: vortex viscosity and energy dissipation, *J. Fluid Mech.* 563 (2006) 97-122.

[36] O. Levenspiel, Chemical Reaction Engineering, John Wiley & Sons, New York, 1999.

[37] R.B. Bird, W.E. Stewart, E.N. Lightfoot, Transport Phenomena, J. Wiley, New York, 2002.

[38] G. Taylor, Dispersion of soluble matter in solvent flowing slowly through a tube, *Proc. R. Soc. London, Ser. A* 219 (1953) 186-203.

[39] G.I. Taylor, Diffusion and mass transport in tubes, *Proc. Phys. Soc. B*, 67 (1954) 857-869.

[40] H. Brenner, D.A. Edwards, Macrotransport Processes, Butterworth-Heinemann, Boston, 1993.

[41] A.D. Stroock, S.K.W. Dertinger, A. Ajdari, I. Mezic, H.A. Stone, G.M. Whitesides, Chaotic mixer for microchannels, *Science* 295 (2002) 647-651.

[42] H. Tennekes, J.L. Lumley, A First Course in Turbulence, The MIT Press, Massachusetts, 1972.

[43] S.B. Pope, Turbulent Flows, Cambridge University Press, Cambridge, 2000.

[44] S. Qian, H.H. Bau, Magneto-hydrodynamics based microfluidics, *Mech*. *Res*. *Commun*. 36 (2009) 10-21.

4 Controlling lateral nano-mixing and velocity profile of dilute ferrofluid capillary flows in uniform DC, AC and rotating magnetic fields

4.1 Abstract

The influence of magnetic-field dependent viscosity (rotational viscosity) on molecular transport of species in dilute ferrofluids has been studied. For this purpose, a Taylor dispersion test in a capillary tube has been performed while suspended magnetic nanoparticles (MNPs) are subjected to both magnetic field and low Re shear flow field. Axial dispersion has been quantified from residence time distributions (RTD) and tracer injection tests conducted in three distinct situations where the capillary is subjected to a) uniform transverse rotating magnetic field (^{T}RMF), b) uniform transverse oscillating magnetic field (^{T}OMF) and c) uniform axial static magnetic field (ASMF). The various types of magnetic fields have been generated in a specially designed stator energized by three phase, AC and DC currents. Results obtained from the three cases are reported in terms of axial dispersion coefficients. For ^{T}RMF, an increase in lateral mixing is observed whereas no significant effect is detected for ^{T}OMF. In ASMF, the lateral mixing mechanism is retarded by magnetically locked MNPs. Both effects under ^{T}RMF and ASMF reach a plateau as MNP concentration in the liquid is increased. These findings highlight the effect of rotational viscosity on diffusion of other species hosted in dilute ferrofluids and point to attractive applications to engineering fields where transport phenomena are central. Analysis of RTD breakthrough times enabled laminar velocity profile in capillary flow to be reconstructed. It suggests that (magnetic field-free) parabolic velocity profiles evolve towards flattened and protruded shapes, respectively, in TRMF and ASMF. These results confirm that magnetically-excited MNPs may be considered as a potentially appealing tool to mediate molecular transport phenomena at the nanoscale such as in nano/microfluidic systems.

4.2 Introduction

Stable colloidal suspensions of single-domain magnetic nanoparticles (MNP) in aqueous or organic nonmagnetic liquid carriers, commonly known as ferrofluids [1], exhibit fascinating

rheological properties under the effect of external magnetic fields [2]. A magnetic field exerts a magnetic torque on the magnetic moment of MNPs suspended in the liquid in an attempt to orient them toward its own dominant direction [1]. For rigid dipole MNPs (rdMNPs), featuring a magnetic moment locked to the particle solid crystal structure, the magnetic torque is felt bodily thereby transferring concomitantly momentum to the adjacent liquid phase [1,2]. This magnetic body torque is always opposed by Brownian collisions from solvent molecules and by flow-field frictional torque when the liquid is out of rest [1,2]. In a ferrofluid shear flow, it is known that an external magnetic field forces rdMNPs to spin asynchronously relative to the local vorticity of the fluid, resulting in a directional modification of viscosity. This behavior, known as rotational viscosity, was first observed by McTague [3] and then by Rosensweig et al. [4]

Since then, rotational viscosity has been studied vastly under three types of magnetic fields, i.e., static (or DC) magnetic field, (SMF), oscillating magnetic field (OMF) and rotating magnetic field (RMF) [1, 2, 5]. SMF rotational viscosity arises when the external magnetic field is not parallel to local fluid vorticity. While the fluid viscid nature forces rdMNPs to rotate in shear flows, the normal-to-vorticity component of magnetic field vector hinders the dipoles free rotation, thus leading to a greater rate of hydrodynamic energy dissipation around the MNPs [1]. This results in an inflated apparent viscosity as observed by McTague [3] and Rosensweig et al. [4] and explained theoretically by Shliomis [6].

Rotational viscosity under OMF was investigated experimentally by Bacri et al. [7] after it was conceived theoretically by Shliomis and Morozov [8]. Under OMF, rdMNPs try to chase the magnetic field via synchronized rotation due to periodic alternation of the magnetic field. Subjecting a ferrofluid laminar Poiseuille flow to low-frequency coaxial OMF (oscillating at frequency Ω_{OMF}) such that $\Omega_{OMF}\tau_B < 1$($\tau_B=3\eta_0V_h/k_BT$ is Brownian relaxation time) partially impedes the azimuthal spin of MNPs under fluid vorticity and results in a positive rotational viscosity manifesting as pressure drop augmentation [9]. Conversely, under high-frequency OMF such that $\Omega_{OMF}\tau_B >1$ the magnetic field amplifies azimuthal MNP spin. Accordingly, electromagnetic energy is transferred to the fluid flow as kinetic energy, thereby enhancing flow nearby MNPs and lessening pressure drop. This effect may be viewed as if the apparent ferrofluid viscosity has decreased tantamount to

negative rotational viscosity [7, 9, 10]. Gauzeau et al. [11] studied rotational viscosity in concentrated ferrofluids with large τ_B ($\tau_B \approx 0.01$ s) under OMF and determined that rotational viscosity depends also on flow vorticity.

Rotational viscosity under RMF was first observed experimentally by Moskowitz and Rosensweig [12] in the form of ferrofluid entrainment by the field originating from the average rotation of MNPs relative to their embedding matricial fluid. The velocity profile of this macroscopic motion in RMF was studied experimentally and theoretically by Chaves et al. [13, 14]. The ferrofluid rheological properties under RMF have been obtained from measurement of torques of a submerged spindle. Based on this method, Rosenthal et al. [15] and later, Rinaldi et al.[16] detected negative and positive rotational viscosity with co-rotating and counter-rotating magnetic fields with respect to spindle resistive torques. Interestingly, under RMF, no minimum field frequency is required to achieve negative rotational viscosity in contrast with Bacri et al. [7] experiments reported under OMF.

Except for research works on macroscopic momentum transfer in liquids (concealed in apparent viscosity alterations), [13, 17] other ferrofluid transport properties under constant or time-varying magnetic fields have thus far not received sufficient attention. Chilton-Colburn analogy [18] states that heat, mass and momentum transfer phenomena are subtended by the same basic mechanisms. Inspired by such analogy, together with rotational viscosity effects showcasing positive, zero and negative apparent viscosity in liquid, the quest of this study is to investigate how magnetically-excited MNPs, seeded in liquids, could manipulate other molecular transport properties, in particular liquid mass transfer. Notably, dilute ferrofluids (magnetic core volume fraction ϕ below 0.01) [11] are of particular interest in this study, as they may lead to potential applications in chemical reaction engineering where MNPs are already used as support-shuttles for recovery of costly catalyst complexes [19-24].

Aiming at the same objective, Suresh and Bhalerao [25] attempted to enhance mass transfer at the gas–liquid interface of two-phase flow systems. Ferrofluids were added to alkaline aqueous solutions in wetted-wall falling-film contactor and bubble column to sense the effect of MNP addition on CO_2 absorption under OMF for a diffusion-limited reaction. A

50-Hz longitudinal OMF (^{L}OMF) generated by two coils (mounted one on top of the other) led to 50% enhancement of mass transfer. More recently, Komati and Suresh [26] used a 50% v/v blend of ferrofluid (ϕ = 0.004) and MDEA solution to study CO_2 absorption in a falling-film contactor exposed to ^{L}OMF. MNPs excited by ^{L}OMF from 100 to 1000 Gauß and from 500 Hz to 100 kHz led to almost doubled volumetric mass transfer coefficient.

In this contribution, we perform Taylor dispersion tests in a capillary tube and determine the axial dispersion coefficient (K) as a means to investigate liquid-phase mass transfer in the presence of magnetically excited MNPs interacting with shear flow. Taylor dispersion is a phenomenon originating from combination between axial convective displacement of a tracer slab under laminar Poiseuille flow and its diffusive migration in radial direction [27]. Hence in a given experimental condition, any phenomenon that alters molecular diffusion could be detected indirectly through its effect on K [27]. Residence time distribution (RTD) measurements are thus performed using a Taylor dispersion capillary cell from which axial dispersion coefficients are obtained. MNPs in our Poiseuille experiments were excited successively by RMF, OMF and SMF to probe their influence on the lateral molecular transport mechanism in the capillary flows. Also, we put forward an approach to correlate (and infer from impulse RTD) the shape of laminar velocity profile under magnetic fields from the minimum residence (or breakthrough) time of the capillary tube.

4.3 Experimental section

4.3.1 Magnet

A tubular two-pole three-phase magnet was designed and built in collaboration with MotionTech LLC and Windings Inc. with bore dimensions as 55 mm height and 45 mm inner diameter. The magnet assembly consists of three identical coil pairs, spatially shifted from each other by 120° in azimuthal direction as depicted in figure 4-1.a,b. Each coil can be energized separately or coupled to other coils in various configurations. Therefore, the magnet can be used to generate different magnetic field types including RMF, OMF and SMF (figure 4-2) with moderate intensity at the center axis (up to 50 mT). In absence of any magnetic object, each ampere rms generates a RMF of nearly 186 Gauß at bore center. The resistance and inductance of the stator windings were measured as 14.6 ohms per coil (single winding) and 150 mH per coil at 200 Hz.

To generate a RMF transverse to capillary flow such as in figure 4-2.a, coils are fed by three balanced AC currents, 120° out of phase from a variable frequency drive (ABB, ACS150, 2.2kW), providing z-directed surface current distribution, Ψ_z, given by

$$\Psi_z(\theta,t) = \mathrm{Re}\left\{\Psi e^{j(\Omega_{cur}t - n_p\theta)}\right\} \tag{1}$$

where Ω_{cur} is the electrical current frequency and n_p is a positive integer parameter representing the number of pole pairs in stator (here, $n_p = 3$). In figure 4-2.b, two adjacent coils are energized with an AC current from an AC variable frequency drive (Invertek Drives, Optidrive E2) to generate an OMF of $H_x = H\cos(\omega_{cur}t)$ transverse to capillary flow. Figure 4-2.c illustrates two adjacent coils connected to a DC current from a DC source (Agilent Tech, N8739A) to provide an SMF parallel to capillary flow. The magnetic field strength and frequency is adjusted directly by power supplies. The temperature of the magnet solid part is controlled by a water cooling jacket that encompasses the outer shell of the stator and filled with a coolant circulated in and out from a constant-temperature thermostated bath (Lauda, Model RKT20).

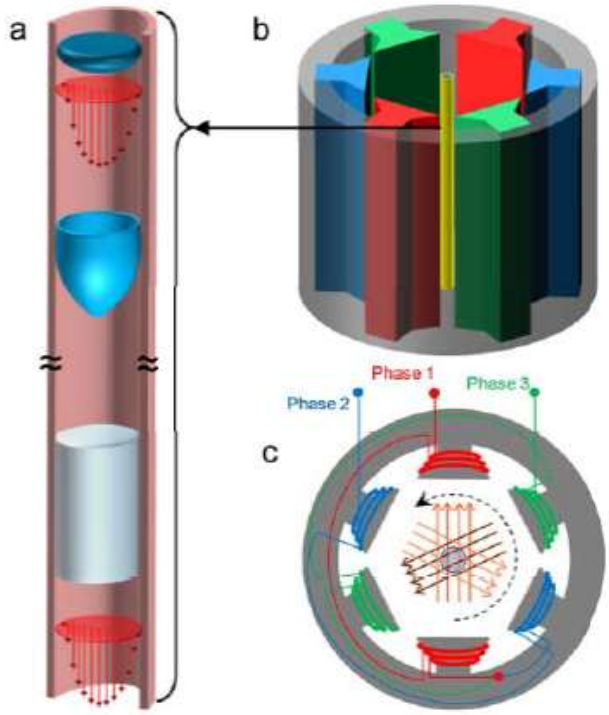

Figure 4-1 : Taylor dispersion in capillary tube exposed to magnetic field. a) Schematic drawing depicts dispersion of a tracer blob in Poiseuille flow with parabolic laminar velocity profile. b) Schematic of the experimental setup including two-pole three-phase magnet and glass-made capillary tube at the center. c) Upfront view of magnet with a capillary set vertically and coaxially with magnet bore, a uniform *horizontal* magnetic field imposed across capillary tube hosting a flow of MNP-laden suspension.

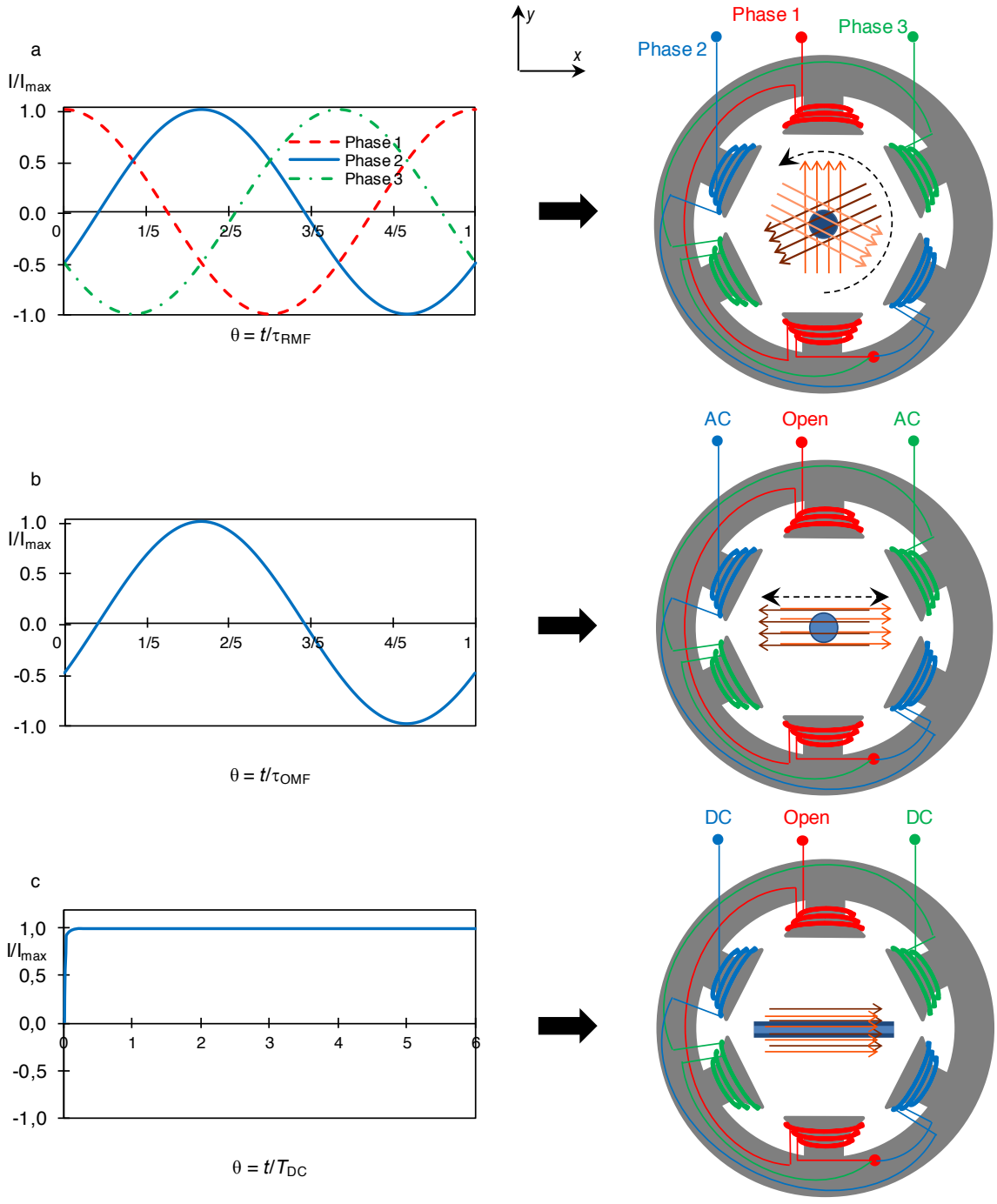

Figure 4-2 : Taylor dispersion capillary tube submitted to three magnetic field scenarios. Two-pole three-phase magnet generates a) uniform rotating magnetic field (RMF) when energized by a three-phase power supply, b) oscillating magnetic field (OMF) when energized by a single-phase power supply, c) uniform static magnetic field (SMF) when energized by a DC current. Perpendicular to (y,x) plane is z-direction.

4.3.2 Taylor dispersion in capillary

A Taylor dispersion test as first elaborated by Taylor [28,29] uses a thin band of solute injected in a capillary tube in which a laminar non-zero velocity field $u(r) = 2U(1-(r/R)^2)$ is dominant. At time equal to zero, the tracer band starts to be stretched by the convective flow to evolve into a paraboloidal shell. The liquid velocity on the capillary wall is zero and hence, tracer molecules close to centerline outpace those closer or adjacent to wall (figure 4-1.a). Consequently, a radial concentration gradient forms over the expanded stripe and tracer molecules diffuse radially to fade out the paraboloidal shape of the stretched band. Molecular diffusion frees tracer molecules from being trapped in the wall vicinity by moving them crosswise toward channel centerline. Accordingly, the back side of the stretched tracer band starts displacing in the direction of the convective flow as molecular diffusion restricts the extent of tracer convective broadening. This axial dispersion phenomenon refers to Taylor dispersion [27]. We reexamine the axial dispersion variations in presence of excited MNPs under different magnetic field types to assess their influence on liquid-phase molecular transport. Axial dispersion coefficients are measured by performing impulse residence time distribution (RTD) tests in capillary.

4.3.3 Impulse RTD test

The axial dispersion coefficient in a vessel can be estimated through impulse RTD tests which, due to their simplicity and effectiveness, are powerful to diagnose flow anomalies especially with the aid of a relatively simple model [30]. This approach uses detectable ions or molecules as tracer particles which are small enough to be influenced by the Brownian motion of liquid to mimic liquid diffusional behavior at the microscale [31].

A 1 mm I.D. glass capillary tube, equipped with a T-shaped injection site and two conductivity electrodes, 3-cm apart, is introduced either vertically (for RMF and OMF tests, figure 4-2.a, b), or horizontally (for SMF, figure 4-2.c) at the bore center of a vertically aligned magnet. The flow of a dilute ferrofluid is maintained using a syringe pump (Cole-Parmer® single-syringe infusion pump).

With regard to ferrofluids opaqueness even in the low concentration range, non-intrusive optical techniques are not applicable neither for tracer injection [32] nor for tracer detection

[33, 34]. Hence, we employed a conductometric technique that uses electrolytes (NaCl solution) at low concentration (i.e., 0.05 M) mixed with the dilute ferrofluids as a tracer. Great care was exercised in the preparation of the tracer solutions so that after dilution the MNP concentration in the tracer solution must be identical to that of the ferrofluids flowing in the capillary. This manner prevented magnetic Kelvin force [1] interference resulting from magnetic susceptibility jump at the injection of the tracer into the capillary. At $t = 0$, a small volume of tracer (i.e., 0.5 μl) was injected almost instantly into the flow by applying a side channel pressure, while cross-sectional average electrical conductivity was probed by two sets of wire electrodes 3 cm apart (figure 4-3.a). The electrodes were set in the capillary wall in a way to cause minimal perturbation of laminar flow pattern. The conductivity meter (Omega CDTX-90) generates a signal in mV reflecting the electrical conductivity of the fluid passing by each electrode set. Holding Kohlrausch's law, transient behavior of the signal intensities is associated with electrolyte concentration change in the liquid (figure 4-3b).

Hydrodynamic test conditions, i.e., liquid flow rate and capillary diameter, d, were chosen to have small Reynolds ($Re = Ud/\nu \sim O(1)$) and large Péclet ($Pe = Ud/D \sim O(10^3)$, where $U = 0.001$ m/s, $D \sim 10^{-9}$ m^2/s) numbers to make sure viscous forces are not dwarfed by inertial forces. However, convective transport outweighs molecular diffusion in the longitudinal direction. Each experiment was conducted for four Re numbers (0.50, 0.75, 1.25, and 1.50) with three repetitions for each flow rate. The axial dispersion coefficient was estimated using an axial dispersion model with open-open boundary conditions for laminar flow [31,35].

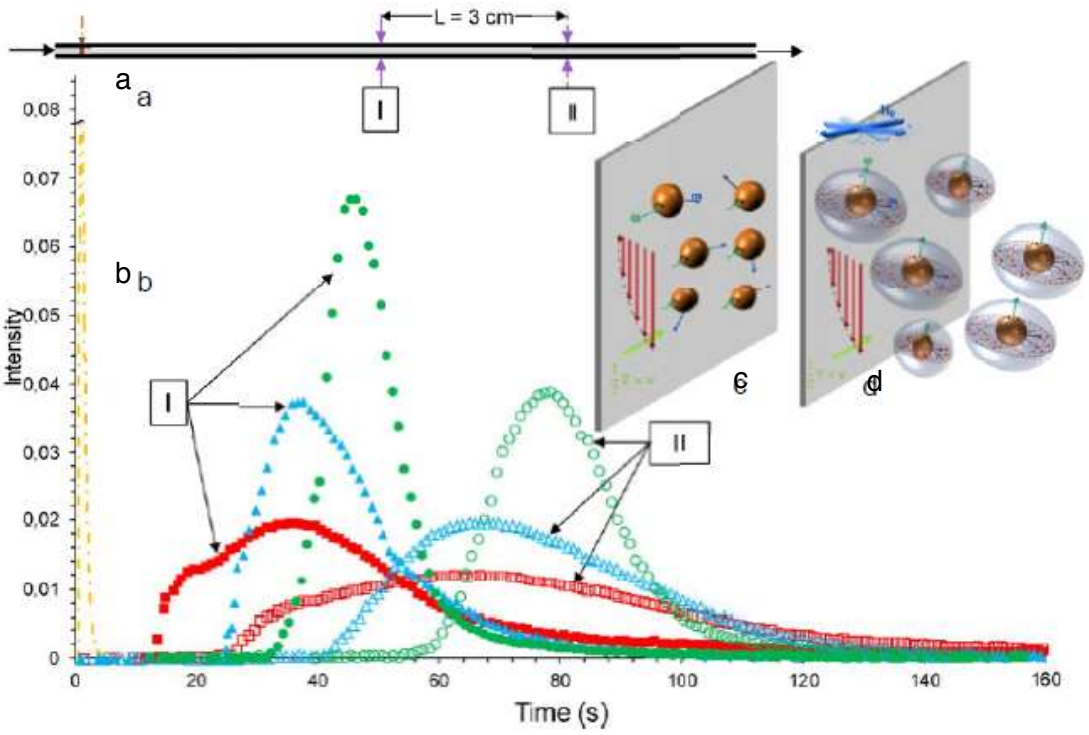

Figure 4-3 : Impulse test of a Taylor dispersion capillary with and without RMF. a) Schematic drawing of Taylor dispersion capillary tube with two sets of detectors five and eight cm down the injection point. b) RTD responses from first (full marks) and second (empty marks) electrode. Trends represent time evolution of tracer impulse responses, respectively, of first and second electrodes (intensity in arbitrary units): (■,□) for magnetic-field-free Poiseuille flow, (▲,Δ) for Poiseuille flow laterally stirred by nano-mixing ($\phi = 0.0025$, $H_0 = 10.4$ kA/m, $f = 50$ Hz), (●,○)for Poiseuille flow laterally stirred by nano-mixing ($\phi = 0.0025$, $H_0 = 36.5$ kA/m, $f = 50$ Hz). Peak narrowing indicates lateral mixing under rotating magnetic field. c, d) Schematic diagram of MNPs spin in shear flow with and without RMF. c) In the absence of magnetic field, MNP spins, $\boldsymbol{\omega}$, gyrate collinear to fluid vorticity and MNP magnetic moments ($\mathbf{m}$) are randomized in all directions. d) Under transverse RMF ($\mathbf{H}_0$), $\boldsymbol{\omega}$ becomes perpendicular to azimuthal fluid vorticity and hence, mixing is lateral. It is expected that a mixed zone forms around MNP when magnetic torque, $\mathbf{m}\times\mathbf{H}$ overcomes Brownian thermal agitation and viscous shear forces.

4.3.4 Capillary tube and magnetic field relative alignment

The magnetic field is generated horizontally perpendicular to magnet bore longitudinal axis. Theoretically, a dynamic magnetic field (i.e., RMF and OMF) drag rdMNPs to spin asynchronously with respect to fluid vorticity [1]. Therefore, the Taylor dispersion capillary was positioned coaxially with respect to the tubular magnet in transverse RMF (^{T}RMF) and transverse OMF (^{T}OMF) experiments to set the particle spin plane crosswise to the flow direction to promote lateral mixing (figure 4-2a,b). In contrast, SMF pins MNPs in the capillary making them to resist fluid vorticity when the magnetic field direction is perpendicular to fluid vorticity ($1/2\nabla V$). Since fluid vorticity lies in capillary azimuthal

direction and the magnetic field is transverse to magnet longitudinal axis, the only configuration in which all MNPs oppose fluid vorticity is by adjusting the capillary horizontally and parallel to the magnetic field direction (figure 4-2c).

4.3.5 Colloidal suspension

Dilute concentrations of ferrite (Fe_3O_4) MNPs (ϕ = 0.0005 – 0.01 v/v magnetic content) dispersed in water were prepared from a commercial ferrofluid, EMG705 (FerroTec). The magnetic properties of EMG 705 were measured by an alternating gradient magnetometer, MicroMag model 2900 (Princeton Instrument Co.) at 298 K in low-field (for initial susceptibility, χ_0) and high-field (for saturation magnetization, M_s) asymptote of magnetization curve. Using these values, particle core diameter was estimated following a method proposed by Chantrell [36]. Table 5 summarizes the magnetic properties of EMG-705 ferrofluid. Particle size distribution of dilute ferrofluid with different concentrations was measured by magnetometry and dynamic light scattering techniques (Zetasizer Nano 6, Malvern Instruments Ltd) before and after of sample exposure to magnetic field. The results assured us of no cluster or chain formation during the course of experiment.

Table 4-1 : Magnetic properties of EMG 705 from magnetometry measurement

Saturation magnetization, M_s (kA/m)	18.7
Initial susceptibility, χ_0	2.9
MNP volume fraction, ϕ (v/v)	0.042
Estimated median magnetic core diameter, d_p (nm)	16.0

4.4 Results and discussion

4.4.1 Taylor dispersion under ^{T}RMF and ^{T}OMF

Figure 4-3b presents capillary RTD responses to impulse tests with and without rotating magnetic field. Magnetically-excited spinning MNPs generate lateral mixing in capillaries as demonstrated by the attenuation of tracer band broadening relative to that in magnetic-field-free Poiseuille flow. More symmetric trends and shorter tails availed by two RMF

excitation levels imply that diffusive migration of electrolyte ions across streamlines is assisted by spinning MNPs as a secondary mixing mechanism.

The fact that the average MNP particle-particle distance is about 6 times the MNP diameter ($d_{p\text{-}p} \sim 95$ nm for $\phi = 0.0025$ [1]), particle interactions may be neglected [37,38] and the mixing phenomenon can be interpreted as resulting from the individual particle behavior under magnetic field. Figure 4-3c shows MNPs gyrate synchronously with fluid vorticity under shear flow when there is no magnetic field. Accordingly, the particle spin vector ($\boldsymbol{\omega}$) is equal to half of fluid vorticity ($1/2\nabla\times\mathbf{v}$) and MNP magnetic moments ($\mathbf{m}$) are randomized in all directions due to thermal agitation. Provided ^{T}RMF yields strong enough a magnetic torque, ($\mathbf{m}\times\mathbf{H}$), on individual MNPs, to overcome Brownian thermal agitation and hydrodynamic torque, a rotational reorientation undergone by MNPs lead them to spin almost parallel to flow direction (figure 4-3d). We hypothesize that at the MNP level, a mixed fluid zone is formed around individual spinning MNP particles wherein molecular transport phenomenon is assisted significantly with kinetic energy spread out from particle spin.

These RTD experiments in Poiseuille flows can be viewed as the flip side of the negative-viscosity studies evidenced by ferrofluid torque measurements subject to RMF [16]. Torque macroscopic observations were then explicated by momentum dissipation in a cylindrical cell under RMF. Likewise, spinning MNPs, while travelling downstream the capillary by the pressure-driven laminar flow, dissipate kinetic energy in an anisotropic manner by preferentially prompting effective *lateral* mixing at the nanoscale.

The lateral mixing mechanism, just evidenced above, cannot originate from azimuthal bulk flow of ferrofluid in ^{T}RMF (spin-up flow). Primarily, as measured by ultrasound velocimetry [13], spin-up flow is not observed to lead to the emergence of any radial velocity component which is a necessary condition for inducing lateral mixing in a capillary. Moreover, Khushrushahi and Zahn [39] recently confirmed experimentally that if RMF is truly uniform over the ferrofluid volume, spin-up flow cannot arise. The fact that our RMF is generated over a pretty narrow spatial region –a 1 mm diameter capillary precisely centered at the magnet bore without any free surface- supports the hypothesis of a

genuinely *uniform* RMF with zero demagnetizing effects. It is worthy to mention that the mixing mechanism investigated in this study occurs within a single-phase *homogeneous* dilute ferrofluid. As such, it is different from mixing of ferrofluids with nonmagnetic liquids under the effect of a time-varying magnetic field [40]. A distinguishable feature of this latter system is that it is the Kelvin magnetic force which drives mixing due to MNP concentration gradients. Accordingly, the mixing phenomenon per se vanishes once uniform MNP concentration throughout the suspension is achieved. In contrast, the nano-mixing mechanism highlighted in our study is not tied to magnetic-force mixing effects and occurs regardless of whether MNP concentration gradients exist or not.

Impulse RTD tests were also performed under ^{T}OMF to investigate the effect of magnetic field type on excited MNP behavior at low-*Re* laminar flow. For the sake of comparability, ^{T}OMF was generated using the same magnet (figure 4-2b) and imposed to the same capillary configuration in identical flow condition. OMF had rms field intensity equal to ^{T}RMF strength and same frequency. The axial dispersion coefficients for a range of liquid flow rates were estimated from moment analysis of convoluted data [31] acquired from conductivity electrodes' responses. Figure 4-4 presents the capillary axial dispersion coefficient of dilute ferrofluid (ϕ = 0.001) as dimensionless number (UL/K) versus *Re* number under equal strength of ^{T}OMF and ^{T}RMF (H_0 = 31.4 kA/m) and three different frequencies, i.e., 10, 50 and 100 Hz. Subject to various ^{T}OMF frequencies, UL/K does not change significantly relative to magnetic field-free tests. This is unlike under ^{T}RMF where axial dispersion decreases substantially. Figure 4-5 illustrates relative axial dispersion coefficient under ^{T}OMF and ^{T}RMF versus field frequency. K/K_0 is almost constant under ^{T}OMF indicating no pronounced lateral mixing effect in the capillary. In contrast, K/K_0 is notably attenuated under ^{T}RMF until a plateau is reached.

Figures 4-4 and 4-5 evidence that excited MNPs under ^{T}RMF induce lateral mixing by overcoming Brownian collisions at the molecular level and frictional torque in the studied range of *Re* numbers. In contrast, the very same MNPs will not give rise to lateral mixing under equally strong ^{T}OMF. This observation raises the question of OMF ability to bring MNPs in gyration similar to what occurs under RMF. To address this question, the MNP response mechanism under OMF must be scrutinized further.

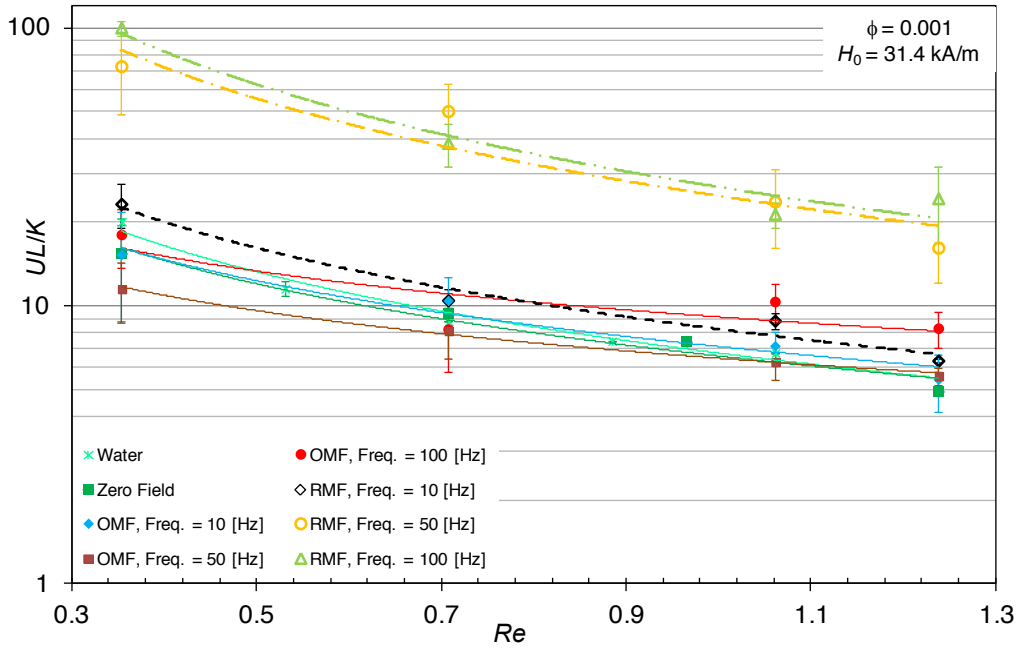

Figure 4-4 : Axial dispersion coefficient in capillary with low *Re* number subjected to transverse OMF and RMF. Axial dispersion coefficient, compacted in dimensionless number *UL/D,* estimated from impulse RTD tests. Experiments performed at $\phi = 0.001$, $d/\nu = 1.0$, $H_0 = 31.4$ kA/m for ^{T}RMF and $H_{0rms} = 31.4$ kA/m for ^{T}OMF. Axial dispersion attenuation under ^{T}RMF implies that it changes orientation of MNP spin vectors thus inducing lateral mixing in capillary whilst under ^{T}OMF, MNP behavior does not show significant change relative to no magnetic field tests. Error bars indicate standard deviation (triplicate tests).

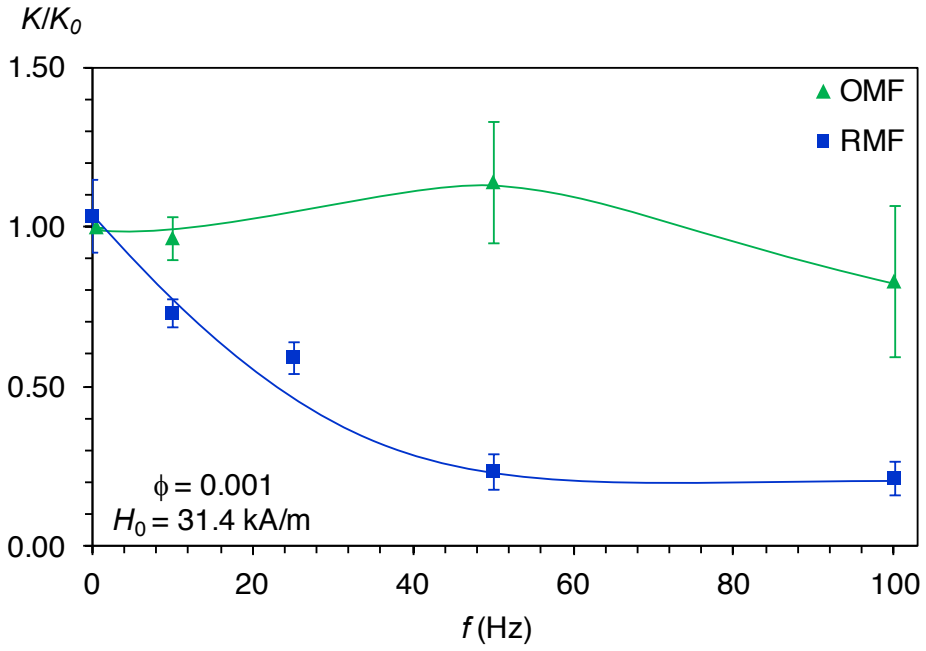

Figure 4-5 : Relative axial dispersion coefficient in capillary under ^{T}OMF and ^{T}RMF. $K_0 = 3.47\times10^{-6}$ m^2/s is axial dispersion coefficient of dilute ferrofluid ($\phi = 0.001$) without magnetic field excitation. Moderate-strength ^{T}OMF at low frequency cannot excite MNPs to reflect in notable effects on axial dispersion. Axial dispersion attenuation

under ^{T}RMF occurs and reaches a plateau after a certain frequency. Error bars indicate standard deviation (n = 12).

Figure 4-6 portrays MNP motions near capillary wall during one cycle period of transverse OMF. By exerting a torque at the very first part of the cycle (figure 4-6a), the magnetic field maintains the nanoparticle magnetic moment almost perpendicular to both wall and capillary longitudinal axis. When coil electrical current and resultant OMF pass through zero prior to changing direction (figure 4-6b), a brief time lapse prevails with a magnetic field almost zero. During this moment, relaxed rdMNPs are free either to rotate under the shear flow field, or to rotationally diffuse by random Brownian collisions with the solvent molecules. The time scale, upon magnetic field removal, during which rdMNPs get disoriented by 180° from magnetic field direction due to Brownian collisions is called Brownian relaxation time constant, τ_B [41]. It is of the order of 10^{-5} s for the MNPs used in our experiments [13]. Following the same concept, a hydrodynamic relaxation time constant, τ_h, can be defined as the time scale during which a nanoparticle is rotated by 180° under a shear flow field in the absence of magnetic field. Referring to the physical view of fluid vorticity as the shear flow tendency to gyrate an infinitesimally small suspended mass, τ_h ($= 2/|\nabla\times\mathbf{u}|$) amounts in average to $R/(2U) = 0.25$ s in our experiments ($U = 10^{-3}$ m/s, $R = 5\times10^{-3}$ m). Introducing the OMF half-period, τ_{OMF}, another key characteristic time coming into play (τ_{OMF} = 0.005 to 0.05 s for experiments presented in figure 4-5), we have $\tau_B << \tau_{OMF} < \tau_h$. Fluid vorticity is definitely too slow a mechanism to control MNPs rotational motion while **H** transitions across zero ($\tau_{OMF} < \tau_h$). However, directional randomization of MNP magnetic moments due to much faster Brownian agitation certainly occurs as such reshuffling requires less time compared to OMF period ($\tau_B<<\tau_{OMF}$). When the magnetic field strengthens again near the cycle end (figure 4-6c) it can resume an orientational coherence of the randomized MNP magnetic moments but in the opposite direction. Randomness of MNPs magnetic moment directions when ***H*** passes through zero (figure 4-6b) also guarantees randomized nanoparticle *spin* directions during magnetic reorientation ($\tau_B << \tau_h$) hence resulting in *zero* average-spin velocity per unit volume.

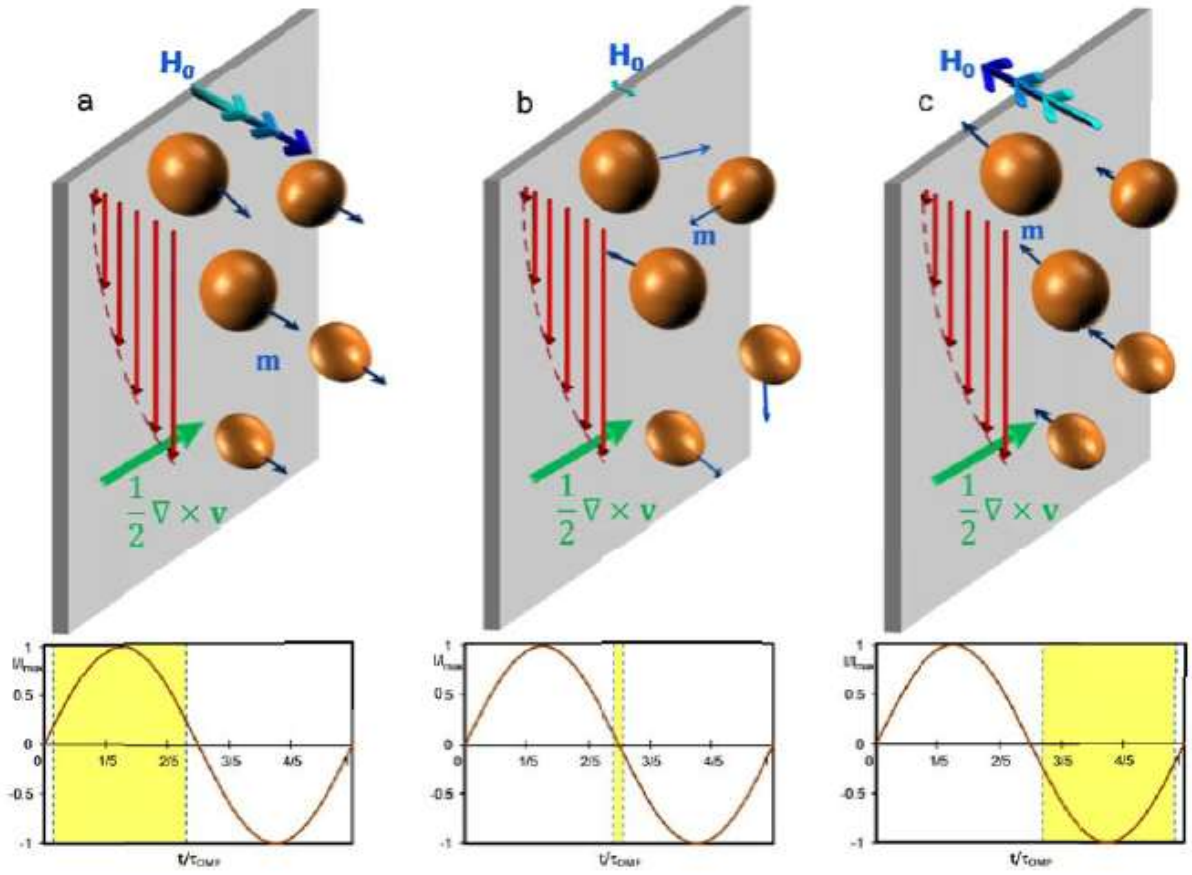

Figure 4-6 : MNP response to ^{T}OMF in a position where magnetic field direction is perpendicular to fluid vorticity, a) Magnetic field is strong enough to orient MNPs to its dominant direction, b) ^{T}OMF passes briefly through zero while changing direction leaving MNP magnetic moments shortly unassisted to lose, due to randomization effect of Brownian collisions, their coherent direction, c) Magnetic field on the rise until peak and MNP magnetic moments to resume orientational coherence. Synchronous particle rotation driven by ^{T}OMF is prohibited by midway Brownian reshuffling of MNPs.

In RMF, superposition of three oscillating magnetic fields shifted by 120° out of phase (figure 4-2a) provides a resultant magnetic field that never drops to zero. Consequently, neither Brownian collisions nor shear flow will have sufficiently wide opportunity time window to control MNP motion during a magnetic field cycle. Nevertheless, frequent reorientation of MNPs by ^{T}OMF and Brownian agitation may generate a slight lateral mixing effect particularly for a higher-frequency field as observed on the right side of figure 4-5. Due to the repeated Brownian reshuffling once in each period, exposure to ^{T}OMF of MNPs is not able to sustain the synchronized parallel spin seen with ^{T}RMF (figure 4-3d). This phenomenon may account for the fact that zero or a negative rotational viscosity under OMF does not occur until the magnetic field frequency will exceed MNP relaxation

time constant ($\tau_B/\tau_{OMF} > 1$) [7,9]. This is what had likely happened with the slight improvements in gas-liquid mass transfer reported by Suresh and Bhalerao [25] and Komati and Suresh [26] under high-frequency OMF. Recently, Sanchez and Rinaldi [42] studied rotational viscosity of dilute ferrofluids under oscillating and rotating magnetic fields through Brownian dynamic simulations. In conclusion, they stated that MNPs spin faster in RMF compared to in OMF, which explains the RMF higher magnitude of negative rotational viscosity. Our experimental finding is in agreement with this statement, as we detected a nanoscale mixing effect stronger in ^{T}RMF than in ^{T}OMF.

Figure 4-6 portrays part of the capillary wall on the side where ^{T}OMF is perpendicular to azimuthal fluid vorticity. Complementarily, figure 4-7 shows capillary wall at 90°-degree shifted angle from figure 4-6 where ^{T}OMF is parallel to fluid vorticity. In this position, the magnetic torque does not oppose frictional torque and MNPs can rotate freely under the shear flow field while magnetic moment directions are fully directed by ^{T}OMF. In this condition, no significant momentum exchange occurs between MNPs and liquid phase nearby the ^{T}OMF peaks. Since nanoparticle magnetic moments are randomized in the middle of each oscillation cycle, the only interlude where momentum exchanges are allowed between MNPs and liquid is during MNP reorientation after ^{T}OMF rises from zero to its maximum strength. Such nanoparticle *intermittent* spin is isotropic and may not significantly affect lateral mixing. MNPs lie between these two extreme positions conform to one of the mechanisms discussed above may not rotate continuously vis-à-vis the surrounding fluid under ^{T}OMF.

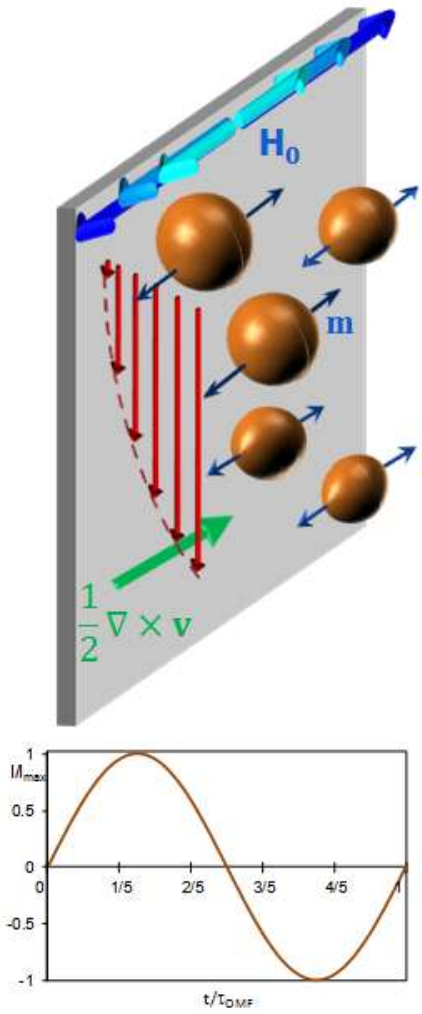

Figure 4-7 : MNP response to OMF in a position where magnetic field direction is parallel to fluid vorticity. MNP gyration under shear flow is not opposed by magnetic torque. As a result, there is no momentum transfer between MNP and fluid due to OMF-nanoparticle interactions.

4.4.2 Taylor dispersion under SMF

It has been demonstrated that SMF can lock rdMNPs from viscid rotation when magnetic field is perpendicular to fluid vorticity [3,4]. Inflation of apparent viscosity in capillaries, i.e., rotational viscosity, is a well-known consequence of such MNP hindrance [2]. Although there have been numerous studies on laminar and turbulent flow of ferrofluids under a coaxial SMF, [10,43-50] the transport properties of low-*Re* capillary flows has not received enough attention to date. Thus, we performed Taylor dispersion tests in capillaries to clarify in which manner interactions under SMF between excited MNPs and laminar flow fields may influence lateral mass transfer.

As discussed earlier in reference with figure 4-7, excited MNPs are unable to exchange momentum with the flow if their magnetic moments are aligned with fluid vorticity. To prevent this instance from happening, the capillary tube was positioned horizontally in the magnet where the magnetic field is coaxial with the capillary longitudinal axis (figure 4-2c). In this configuration, the magnetic field is perpendicular to the azimuthal fluid vorticity over the entire capillary cross-section.

Figure 4-8 shows RTD impulse responses with (●,○) and without (▲,Δ) axial SMF (^{A}SMF). Signals from upstream electrodes (●,▲) are very similar whilst, downstream signals (○,Δ) show marked deviations from each other. The resemblance of inlet signals in presence and absence of ^{A}SMF can be attributed to the short distance (1 cm) between tracer injection and first electrode. Therefore, the tracer residence time before reaching the first electrode is not sufficient to reflect the effect of excited MNPs on axial dispersion. The 1st-electrode skewed tracer responses are ascribed to imperfect tracer injections that are well accounted for in the convolution integral for the estimation of axial diffusion coefficients. The outlet signal under ^{A}SMF (○) is wider and its breakthrough time occurs earlier than without magnetic field (figure 4-8). Unlike in ^{T}RMF, this observation demonstrates that axial dispersion has been inflated even further by ^{A}SMF-excited MNPs interacting with shear flow.

Axial dispersion is caused by the stretching effect of convective flow while molecular diffusion restricts it by ensuring lateral transport over capillary cross-section [27]. At the same liquid flow rate lateral molecular diffusion of tracer appears to have been prohibited by the pinned MNPs which reflects in inflated axial dispersions under ^{A}SMF. Stokes-Einstein law for diffusion in solutions (eq.2) relates molecular diffusivity (D) to the reciprocal of liquid dynamic viscosity (η) [51]. Viewing diffusion through Stokes-Einstein law; we expect that *apparent* molecular diffusivity reduces as apparent viscosity augments with ^{A}SMF.

$$D = \frac{k_B T}{6\pi\eta_0 R_P} \qquad (2)$$

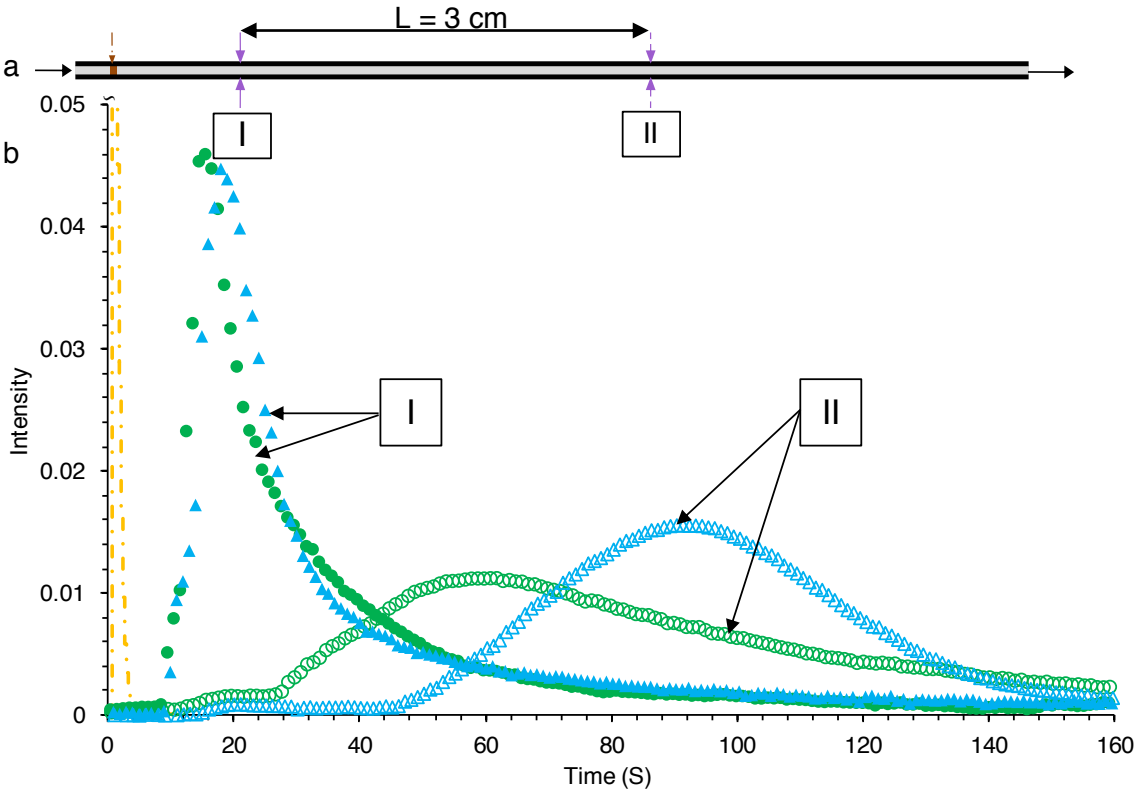

Figure 4-8 : Impulse test of a Taylor dispersion capillary with and without SMF. a) Schematic drawing of Taylor dispersion capillary tube with two sets of detectors one and four cm down the injection point, b) RTD responses from first (full marks) and second electrode (empty marks). Trends represent the time evolution of tracer intensity from first and second electrodes, respectively, (▲,△) with unexcited MNPs flowing in laminar Poiseuille flow, (●,○) with excited MNPs (ϕ = 0.0025, H_0 = 31.4 kA/m). Axial dispersion increases in capillary when magnetic torque prevents MNPs gyration under shear flow.

To explain this observation, we propose a mechanism to describe changes in velocity profile and tracer concentration gradient at nanometric scale in the presence of excited MNPs. Magnetic torque locks MNPs to prevent their rotation under viscous torque. The locked particles prevent liquid layers of laminar flow from sliding on top of each other, as compared to those in the absence of magnetic field (figure 4-9). Thus, laminar velocity profile may change from a smooth parabolic shape to a rugged form in nanoscale with some local zero-velocity-gradient segments (figure 4-9b). In Taylor dispersion test, radial tracer concentration gradient is induced originally by velocity gradient. This concentration gradient may drop to zero in certain positions over several contiguous stream layers wherein axial velocity is almost uniform. Consequently, radial mass transfer due to molecular diffusion declines over these narrow regions, as there is less driving force when

some neighboring streamlines are pinned by excited MNPs. Compensation imposed by the continuity equation suggests there must be other segments where linear velocity jumps between liquid layers (high velocity gradient) result in large tracer concentration gradient (figure 4-9b). However, faster transfer rate over these segments may not compensate for the global mass transfer decline; since molecular transport between streamlines occurs in-series and thus overall mass transfer rate is limited by the slowest slice. A consequence to this view dictated by continuity equation is that the maximum linear velocity on capillary's longitudinal axis must be higher than that in magnetic-free condition (figure 4-9b). This evidence will be thoroughly analyzed later based on minimum (or breakthrough) residence time (t_{min}) determinations.

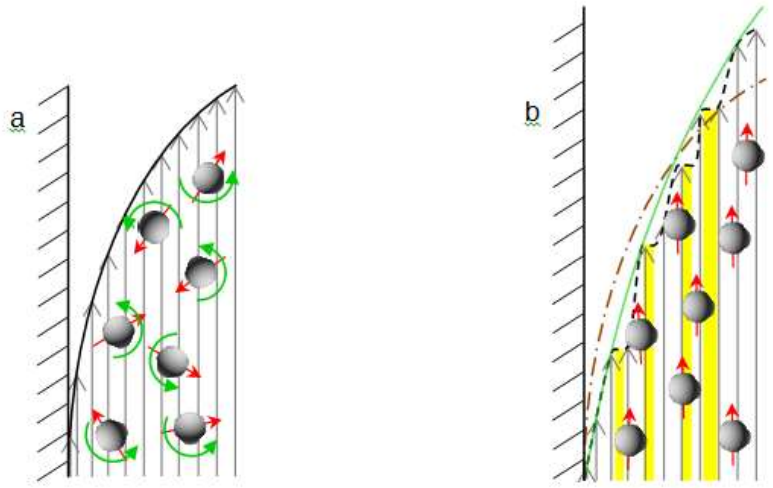

Figure 4-9 : Schematic of MNPs motion under shear flow in capillary tube. a) Magnetic field free, particles gyrate by friction torque and their magnetic moments directions are randomized. b) Under ^{A}SMF, hard dipoles are locked by the coaxially applied external magnetic field. Nanometrically, the velocity gradient has been removed in some regions (where highlighted) and augmented in the rest to satisfy continuity (black dotted line). That may result in mimetic shear thickening behaviour of liquid under ^{A}SMF. The brown dash-dotted line represents the original parabolic velocity profile as it occurs in a).

To gain more insights into the overall diffusion inhibition, we have further compared K dependency on H_0 (0 to 35 kA/m) and ϕ (0 to 0.01) under ^{T}RMF and ^{A}SMF. K/K_0 is plotted as a function of H_0 (figure 4-10a) and ϕ (figure 4-10b) where K_0 refers to axial dispersion coefficient at $H_0 = 0$ (figure 4-10a) and $\phi = 0$ (figure 4-10b). Since axial spinning or hindrance of MNPs is magnetic-torque driven, K/K_0 rises under ^{A}SMF and its decline under ^{T}RMF is intensified by H_0 magnitude. The other factor promoting both phenomena was

found to be MNP concentration (figure 4-10b). For magnetic core volume fractions ranging from 10^{-3} to 10^{-2}, the average MNP interparticle distance varies from 129 nm to 60 nm for d_p = 16.0 nm [1]. At such dilution levels, the relative vortex and shear viscosities are close to 0 and 1, respectively [52], and magnetic interactions between rigid dipole MNPs may be neglected. At such concentration levels, particle-flow field interaction may result only from the behavior of individual MNPs as conjectured in this study. The plateauing trend observed with increasing MNP concentration in ^{A}SMF (figure 4-10b) may imply two features. First, it confirms that MNPs are unlikely to obstruct tracer diffusion bodily, otherwise that would have resulted in steadily increasing trend of K/K_0 when MNPs interparticle distance shortens by factor 1.5 ($0.0025 < \phi < 0.01$). Second, the plateau suggests that uniform velocity segments grow among non-uniform segments to an extent whereby hydrodynamic torque dominates magnetic torque and controls MNP gyration in slimed steepened non-uniform segments.

Ferrofluid positive rotational viscosity under ^{A}SMF in a tube has been reported in the literature from rheometry measurement [3,4]. In this study, we measured lesser lateral mass transfer rate or equivalently inferior apparent liquid diffusivity in capillary as compared to that driven solely by molecular diffusion in magnetic field-free tests. These results together with those under ^{T}RMF suggest that extension of Stokes-Einstein law (eq.2) to apparent viscosity and apparent diffusivity of ferrofluid under ^{T}RMF and ^{A}SMF is valid *qualitatively*. Many applications in microfluidics require a tool to control axial dispersion coefficient in microchannels [53], such as reactant homogenization in chemical reactions [54] and protein folding [55].

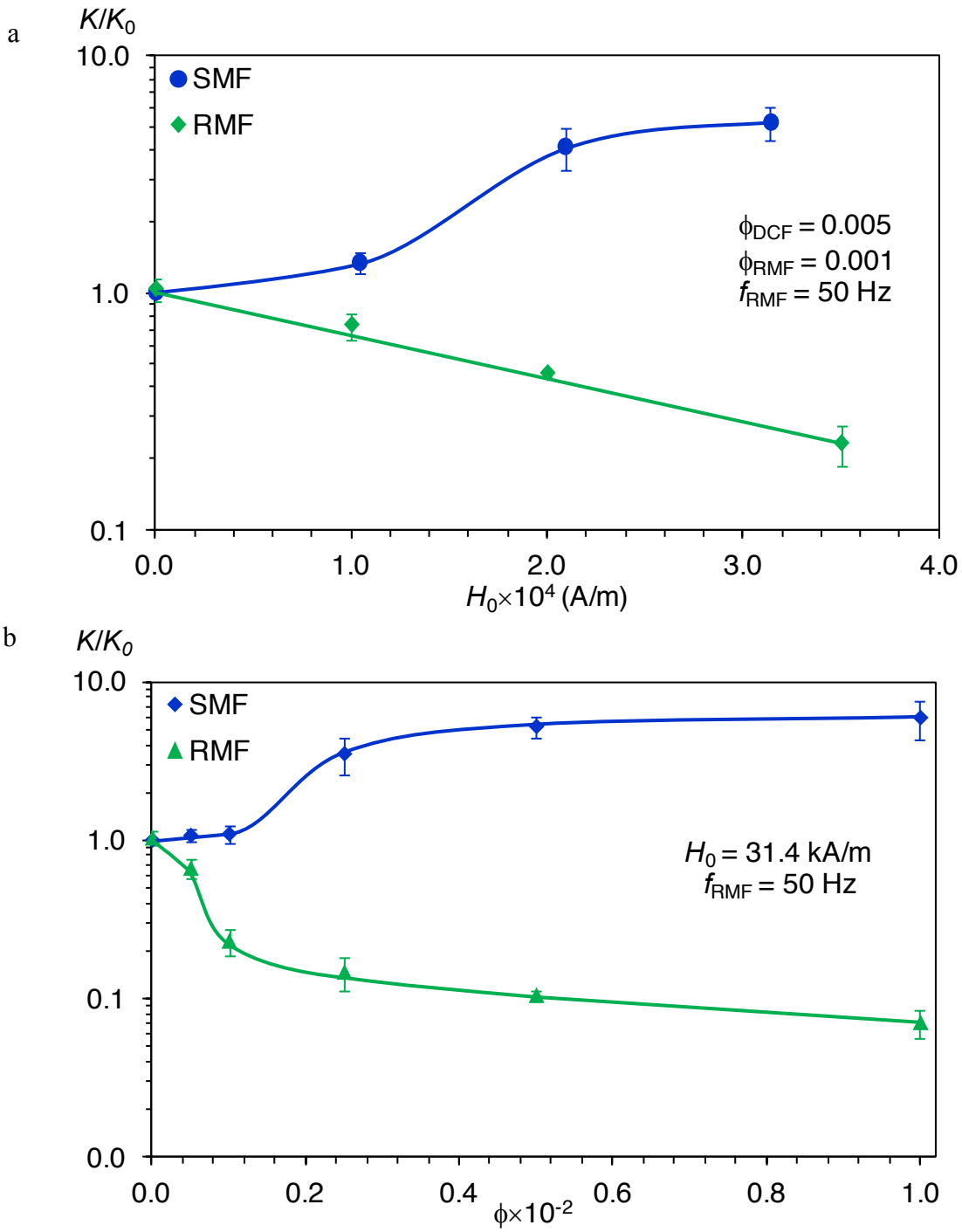

Figure 4-10 : Axial dispersion perturbations under ^{T}RMF and ^{A}SMF versus a) magnetic field strength and b) MNP concentration. a, b) ^{A}SMF promotes axial dispersion (●,♦) whilst ^{T}RMF attenuates K/K_0 (♦,▲). Error bars indicate standard deviation (number of repeat runs = 6). Magnetically locked MNPs under ^{A}SMF reduce lateral mass transfer rate in capillary whereas magnetically spinning MNPs under ^{T}RMF promote lateral mass transfer through nanoconvective mixing. In a) $K_0(\phi=0.001, {}^{T}\text{RMF}) = 3.47\times10^{-6}$ m^2/s and $K_0(\phi=0.005, {}^{A}\text{SMF}) = 1.13\times10^{-6}$ m^2/s. In b) $K_0(\phi=0, {}^{T}\text{RMF}) = 5.08\times10^{-6}$ m^2/s and $K_0(\phi=0, {}^{A}\text{SMF}) = 1.11\times10^{-6}$ m^2/s.

4.4.3 Excited MNPs alter laminar velocity profile in capillary flow

We further investigated how excited MNPs may affect the parabolic velocity profile of a laminar Poiseuille flow. We expect that axially spinning MNPs as depicted in figure 4-3d for ^{T}RMF attenuate radial velocity gradients and result in more flattened velocity profiles compared to magnetic-field-free parabolic shape. Locked MNPs under ^{A}SMF in contrast augment radial velocity gradient resulting in a magneto-thickening fluid behavior.

Figure 4-3b and 4-8.b provide a crucial clue as the time lag between breakthrough times changes with nano-mixing and nano-hindrance despite an identical mean residence time ($\bar{t} = L/U$) for both tests. Breakthrough time features the fastest centerline tracer blob passing by the electrodes with minimum residence time (t_{min}). Hence, $\bar{t}/t_{min}$ ratio can be used as a quantitative index to infer how velocity profiles change due to the presence of excited MNPs. This can be accomplished by drawing an analogy with non-Newtonian power-law radial velocity profiles [56], u(r):

$$u(r) = \frac{3n+1}{1+n} U \left(1 - \left(\frac{r}{R} \right)^{1+1/n} \right) \tag{3}$$

where the power-law index, n, is in the range of 0 (flat profile) to 1 (parabolic profile) and expressed as a function of $t_{min}/\bar{t}$ according to [56]:

$$n = \frac{1 - t_{min}/\bar{t}}{3t_{min}/\bar{t} - 1} \tag{4}$$

Power-law index, n, declines from 1 to 0 for a velocity profile evolving from parabolic to flat but increases over 1 for velocity profiles more fusiform than parabolic.

Figure 4-11a,b plots $\bar{t}/t_{min}$ versus H_0 and ϕ for Figure 4-10a,b experiments. Magnetic field strength and particle concentration promote flattening and protruding effects of excited MNPs on laminar velocity profile. Plateaued trends of Figure 4-11.b suggest that occurrence of local uniform velocity segments due to inter-streamline nanometric radial momentum transfer under ^{A}SMF will be limited by wall-induced shear stress. This

mechanism prevents uniform segments in capillary to grow and merge to lead to a whole flattened velocity profile (figure 4-9b). Hence, lateral momentum transfer in capillary in terms of homogenization of linear velocity may not be assisted effectively by excited MNPs except under ^{T}RMF. MNP-mediated hydrodynamic effects on velocity profile is illustrated in Figure 4-11c which shows computed, flattened or protruded, velocity profiles as $\bar{t}/t_{min}$ ratio deviate from 2 to echo nano-mixing or nano-hindrance intensities.

a

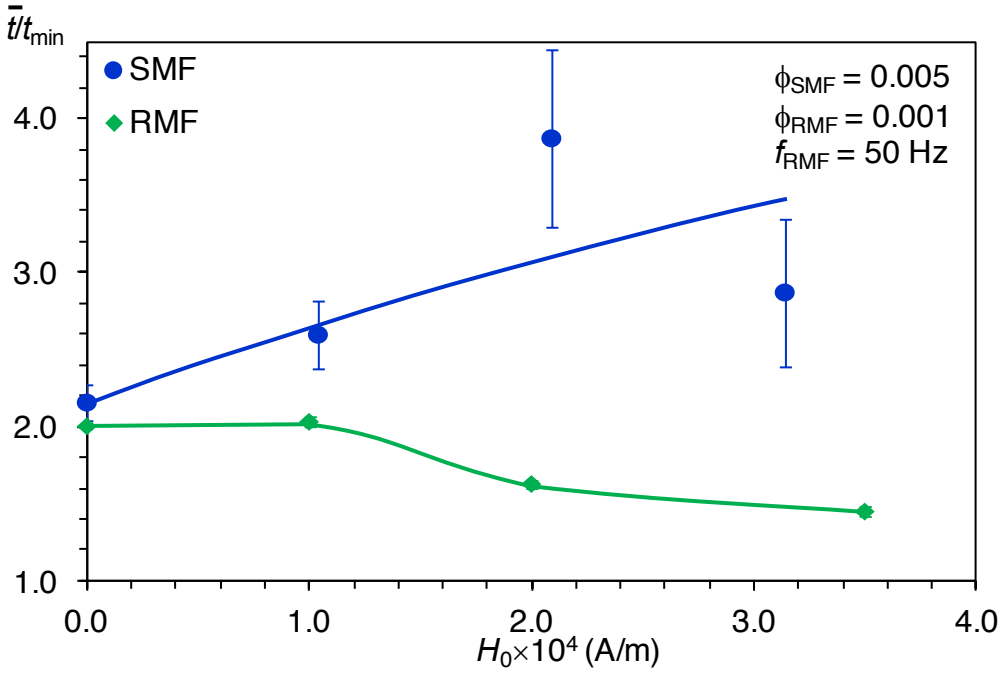

b

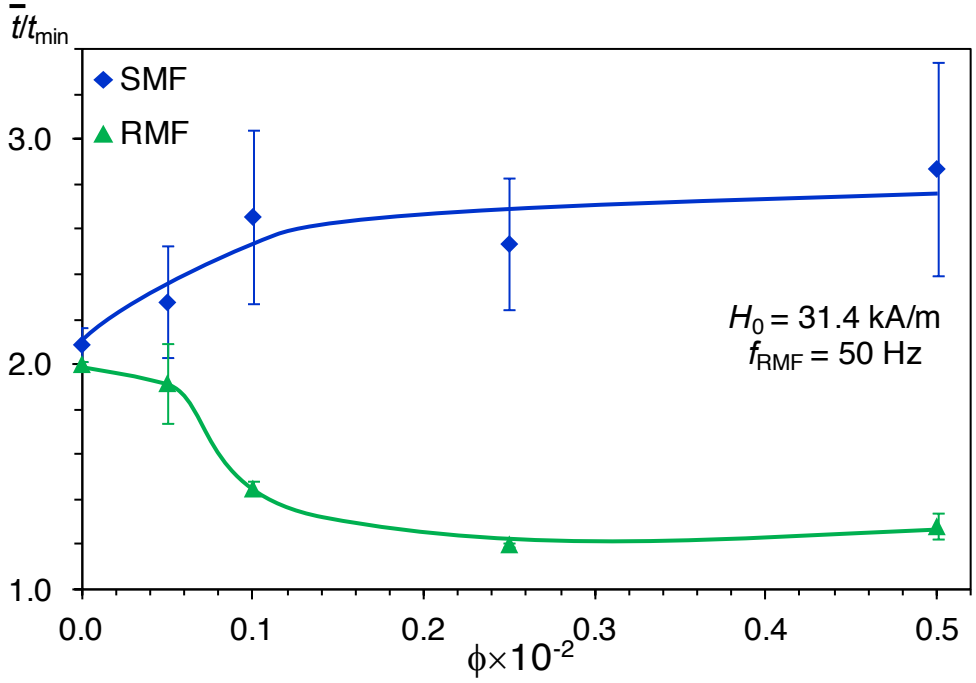

c

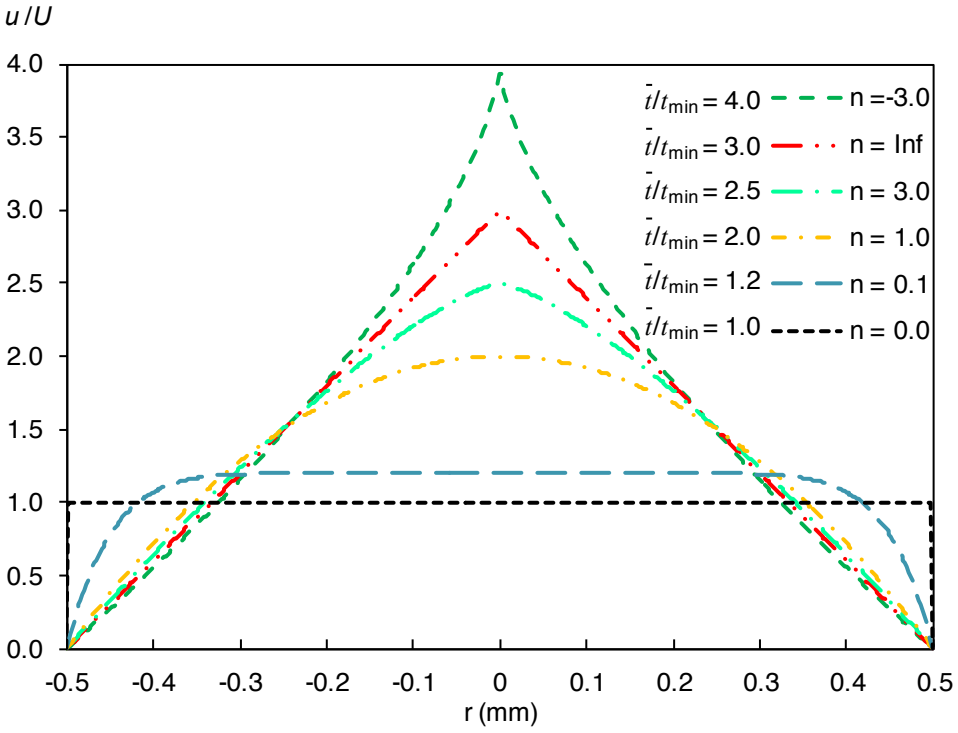

Figure 4-11 : Excited MNPs effect on laminar velocity profile under [T]RMF and [A]SMF. Power-law index *n* and $\bar{t}/t_{min}$ ratio as a function of a) magnetic field strength, b) MNP volume fraction. Error bars indicate standard deviation (number of repeat runs = 6). c) Expected laminar flow velocity profile in a capillary as a function of power-law index.

Except ultrasound velocimetry [13,39,48,57], no other technique has been proposed in the literature to measure ferrofluid velocity profiles. This technique is not reliable in regions closer than several millimeters to the wall due to echo interference [58] and therefore, may not be applicable in 1 mm micro-channel as well. Furthermore, velocity profile reconstruction confirmed magneto-thickening and magneto-thinning behavior of dilute ferrofluid under ^{A}SMF and ^{T}RMF in capillary. Although both effects would be perceived from positive [3,4,15,16] or negative [7,9,15,16] rotational viscosity, they have never been spotted experimentally from the perspective of manipulating laminar velocity profiles in capillaries.

Taylor [59] expressed the dispersion coefficient (K) of a solute flowing slowly through a tube in terms of U, d and D for a parabolic velocity profile as:

$$K = \frac{R^2U^2}{48D} \tag{5}$$

Later, this equation was adapted and extended to a power-law velocity profile [60]:

$$K = \frac{R^2U^2}{D}\frac{n^2}{2(3n+1)(5n+1)} \tag{6}$$

These two equations assume that lateral (radial) transfer of solute depends only on radial variation of tracer concentration and as such mass transfer is only driven by molecular diffusion. Thus, D appears in the denominator of eqs.5,6. This assumption is violated in our study as the nanoconvective effect by MNPs enhances or retards lateral mixing. Keeping other assumptions of the model still valid, the molecular diffusivity must be replaced by an effective diffusivity (D_{eff}) in the modified Taylor model of axial dispersion:

$$K = \frac{R^2U^2}{D_{\text{eff}}}\frac{n^2}{2(3n+1)(5n+1)} \tag{7}$$

For a parabolic profile (n = 1) and no magnetic field effects, eq. 7 becomes:

$$K_0 = \frac{R^2U^2}{48D} \tag{8}$$

Thus,

$$\frac{D_{\text{eff}}}{D} = \frac{K_0}{K}\frac{48n^2}{2(3n+1)(5n+1)} \tag{9}$$

Figure 4-12 is a plot of D_{eff}/D as a function of magnetic field strength (figure 4-12a) and MNP volume fraction (figure 4-12b). The D_{eff}/D ratios were estimated from the K/K_0 values shown in figure 4-10a,b and their corresponding $\bar{t}/t_{\min}$ values of figures 4-11a,b. In agreement with previous discussion of figures 4-10, 4-11 and figure 4-12 demonstrates a systematic augmentation of effective diffusivity by up to a factor three in the presence of spinning MNPs in rotating magnetic fields. The same factor also reflects in terms of reduction of effective diffusivity under a static magnetic field. Hence magnetically pinned MNPs even incapacitated molecular diffusivity in smoothing the radial concentration gradient in capillary. Reduction of micro-scale radial concentration gradient around pinned MNPs has been accounted for D_{eff} reduction as explained with respect to figure 4-9.

a

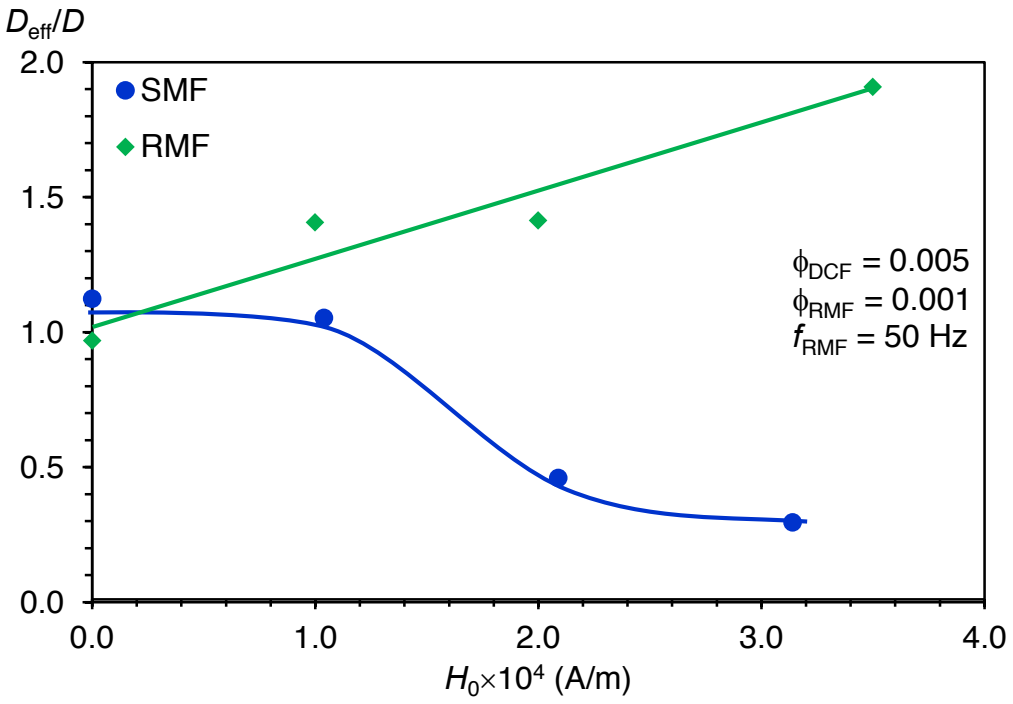

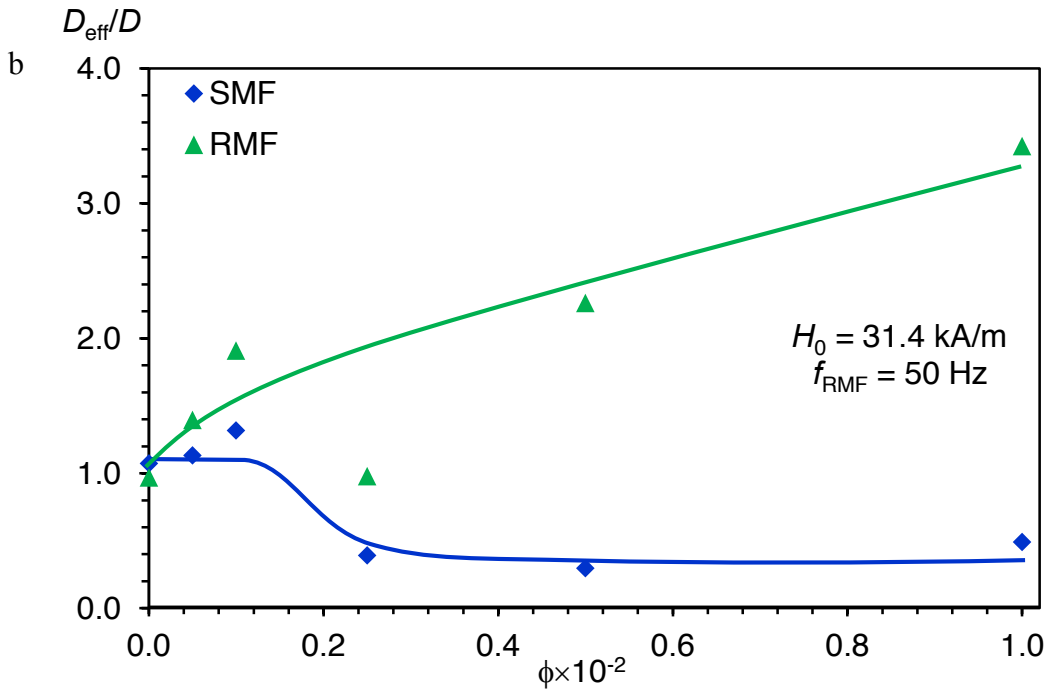

Figure 4-12 : Effective diffusivity in laminar flow under ^{T}RMF and ^{A}SMF. D_{eff}/D ratio as a function of a) magnetic field strength, b) MNP volume fraction.

4.5 Conclusion

Experimental works to elucidate the effect of magnetically-excited MNPs on molecular transport mechanism in ferrofluids is lacking. By studying axial dispersion in dilute ferrofluids flowing through a Taylor capillary cell under moderate strength and low frequency ^{T}RMF, ^{T}OMF and ^{A}SMF, we investigated the mass transfer phenomena induced by the interactions of excited MNPs with Poiseuille flow fields. Although any type of magnetic field gives rise to a bodily magnetic torque on rdMNPs, our study demonstrates that the nature of the imposed magnetic field must be accounted for as a crucial factor in determining the particle-field interactions. The experimental results point out that rdMNPs in ^{T}RMF and ^{A}SMF manipulate tracer lateral diffusion rate in capillary whilst particle excitation by ^{T}OMF has no significant impact on it.

Furthermore, we correlated the shape of ferrofluid laminar velocity profile in capillary to the breakthrough (minimum) residence time from impulse RTD test data. Using a single parameter model in this technique, we evidenced that ferrofluid laminar velocity profiles may change in ^{A}SMF or ^{T}RMF. More investigations are required on the shape of velocity profile by an optical velocimetry technique to verify the reported results.

In conclusion, we found that rdMNP rotational motion relative to contiguous liquid serves as a valuable molecular mixing tool for intensification or retardation of diffusion in liquids, especially in sub-micronic thin regions. Control of the dispersion phenomenon in a microfluidic context may be considered as a prime example. The fact that suspended functionalized MNPs find extensive applications in a variety of disciplines will broaden the scope of potential application of this technique. Moreover, this approach opens up a new trend in experimental methods to shed light on the interaction between magnetically excited MNPs and flow field at the nanoscale.

4.6 Nomenclature

d Capillary tube diameter, m

d_p Volume median particle diameter, m

$d_{p\text{-}p}$ Average particle-particle distance, m

D Molecular diffusivity, m^2/s

D_{eff} Effective diffusivity in presence of magnetically excited MNPs, m^2/s

V_h MNP hydrodynamic volume, m^3

$\mathbf{H}_0$ External magnetic field vector, A/m

H Magnetic field intensity, A/m

I Current intensity, A

I_{max} Peak current intensity, A

k_B Boltzmann's constant, J/K

K Axial dispersion coefficient, (m^2/s)

L Distance between two electrodes, m

$\mathbf{m}$ Magnetic dipole moment of single domain nanoparticles, Am^2

M_s Saturation magnetization, A/m

n_p The number of pole pairs in the stator windings

n Power low index in non-Newtonian power-law radial velocity profile

Pe Péclet number, Ud/D

r Radial position in cylindrical coordinate, m

R Capillary tube radius, m

R_p Diffusing particle radius in Stoks-Einstein law for diffusion in solution

Re Reynolds' number, Ud/ν

RTD Residence time distribution

t Time, s

$\bar{t}$ Capillary mean residence time, s

t_{min} Capillary minimum residence time, s

T Absolute temperature, K

u Local linear velocity in capillary, m/s

U Average linear velocity, m/s

Greek

η_0 Dynamic viscosity (shear viscosity), Pa s

θ Dimensionless time, t/τ

ν Kinematic viscosity, m^2/s

τ_B Brownian relaxation time constant, s

τ_{OMF} Oscillating magnetic field period = $1/\Omega_{OMF}$, s

τ_{RMF} Rotating magnetic field period = $1/\Omega_{RMF}$, s

ϕ MNP core volume fraction

χ_0 Initial susceptibility

Ψ Surface current distribution, A/m^2

ω MNP spin velocity per unit volume, rad/s

Ω Frequency, Hz

Subscripts

cur Electrical current

MNP In presence of MNPs

x Directional component

z Directional component

Acronyms

MNP Magnetic nanoparticle

OMF Oscillating magnetic field

SMF Static (DC) magnetic field

ID Inner diameter

rms Root mean square

RTD Residence time distribution

VFD Variable frequency derive

4.7 References

[1] R. E. Rosensweig, *Ferrohydrodynamics* (Dover Publications, Mineola, N.Y., 1997).

[2] S. Odenbach, *Magnetoviscous effects in ferrofluids* (Springer, Berlin, 2002).

[3] J. P. McTague, Magnetoviscosity of magnetic colloids, *J. Chem. Phys.* 51 (1969) 133.

[4] R. E. Rosensweig, R. Kaiser, G. Miskolcz, Viscosity of magnetic fluid in a magnetic field, *J. Colloid Interface Sci*. 29 (1969) 680.

[5] S. Rhodes, X. W. He, S. Elborai, S. H. Lee, M. Zahn, Magnetic fluid behavior in uniform DC, AC, and rotating magnetic fields, *J. Electrostat*. 64 (2006) 513.

[6] M. I. Shliomis, Effective viscosity of magnetic suspensions, *Sov. Phys. Jetp-Ussr* 34 (1972) 1291.

[7] J. C. Bacri, R. Perzynski, M. I. Shliomis, G. I. Burde, Negative-viscosity effect in a magnetic fluid, *Phys. Rev. Lett*. 75 (1995) 2128.

[8] M. I. Shliomis, K. I. Morozov, Negative viscosity of ferrofluid under alternating magnetic-field, *Phys. Fluids*. 6 (1994) 2855.

[9] A. Zeuner, R. Richter, I. Rehberg, Experiments on negative and positive magnetoviscosity in an alternating magnetic field, *Phys. Rev. E*. 58 (1998) 6287.

[10] K. R. Schumacher, I. Sellien, G. S. Knoke, T. Cader, B. A. Finlayson, Experiment and simulation of laminar and turbulent ferrofluid pipe flow in an oscillating magnetic field, *Phys. Rev. E*. 67 (2003) 026308.

[11] F. Gazeau, C. Baravian, J. C. Bacri, R. Perzynski, M. I. Shliomis, Energy conversion in ferrofluids: Magnetic nanoparticles as motors or generators, *Phys. Rev. E*. 56 (1997) 614.

[12] R. Moskowitz, Re. Rosensweig, Nonmechanical Torque-Driven Flow of a Ferromagnetic Fluid by an Electromagnetic Field, *Appl*. *Phys*. *Lett*. 11 (1967) 301.

[13] A. Chaves, C. Rinaldi, S. Elborai, X. He, M. Zahn, Bulk flow in ferrofluids in a uniform rotating magnetic field, *Phys*. *Rev*. *Lett*. 96 (2006) 194501.

[14] A. Chaves, M. Zahn, C. Rinaldi, Spin-up flow of ferrofluids: Asymptotic theory and experimental measurements, *Phys*. *Fluids*. 20 (2008) 053102.

[15] A. D. Rosenthal, C. Rinaldi, T. Franklin, M. Zahn, Torque measurements in spin-up flow of ferrofluids, *J*. *Fluid Eng*-*T Asme* 126 (2004) 198.

[16] C. Rinaldi, F. Gutman, X. W. He, A. D. Rosenthal, M. Zahn, Torque measurements on ferrofluid cylinders in rotating magnetic fields, *J*. *Magn*. *Magn*. *Mater*. 289 (2005) 307.

[17] L. D. Mao, S. Elborai, X. W. He, M. Zahn, H. Koser, Direct observation of closed-loop ferrohydrodynamic pumping under traveling magnetic fields, *Phys*. *Rev*. *B*. 84 (2011) 104431.

[18] T. H. Chilton A. P. Colburn, Mass transfer (absorption) coefficients - Prediction from data on great transfer and fluid friction, *Ind*. *Eng*. *Chem*. 26 (1934) 1183.

[19] S. Shylesh, V. Schunemann, W. R. Thiel, Magnetically separable nanocatalysts: Bridges between homogeneous and heterogeneous catalysis, *Angew*. *Chem*.-*Int*. *Edit*. 49 (2010) 3428.

[20] P. D. Stevens, G. F. Li, J. D. Fan, M. Yen, Y. Gao, Recycling of homogeneous Pd catalysts using superparamagnetic nanoparticles as novel soluble supports for Suzuki, Heck, and Sonogashira cross-coupling reactions, *Chem*. *Commun*. 35 (2005) 4435.

[21] M. Shokouhimehr, Y. Piao, J. Kim, Y. Jang, T. Hyeon, A magnetically recyclable nanocomposite catalyst for olefin epoxidation, *Angew*. *Chem*.-*Int*. *Ed*. 46 (2007) 7039.

[22] C. Che, W. Li, S. Lin, J. Chen, J. Zheng, J.-c. Wu, Q. Zheng, G. Zhang, Z. Yang, B. Jiang, Magnetic nanoparticle-supported Hoveyda-Grubbs catalysts for ring-closing metathesis reactions, *Chem*. *Commun*. 40 (2009) 5990.

[23] X. X. Zheng, S. Z. Luo, L. Zhang, J. P. Cheng, Magnetic nanoparticle supported ionic liquid catalysts for $CO_{(2)}$ cycloaddition reactions, *Green Chem*. 11 (2009) 455.

[24] V. Polshettiwar, R. Luque, A. Fihri, H. Zhu, M. Bouhrara, J.-M. Bassett, Magnetically recoverable nanocatalysts, *Chem*. *Rev*. 111 (2011) 3036.

[25] A. K. Suresh, S. Bhalerao, Rate intensification of mass transfer process using ferrofluids, *Indian J. Pure Appl*. *Phys*. 40 (2001) 172.

[26] S. Komati, A. K. Suresh, CO_2 absorption into amine solutions: a novel strategy for intensification based on the addition of ferrofluids, *J. Chem*. *Technol*. *Biotechnol*. 83 (2008) 1094.

[27] H. Brenner, D. A. Edwards, *Macrotransport Processes* (Butterworth-Heinemann, Boston, 1993).

[28] G. Taylor, Dispersion of soluble matter in solvent flowing slowly through a tube, *Proc*. *R*. *Soc*. *London*, *Ser*. *A* 219 (1953) 186.

[29] G. I. Taylor, Diffusion and mass transport in tubes, *Proc*. *Phys*. *Soc*. *B* 67 (1954) 857.

[30] O. Levenspiel, Modeling in chemical engineering, *Chem*. *Eng*. *Sci*. 57, 4691 (2002).

[31] O. Levenspiel, *Chemical Reaction Engineering* (John Wiley & Sons, New York, 1999).

[32] S. Lohse, B. T. Kohnen, D. Janasek, P. S. Dittrich, J. Franzke, D. W. Agar, A novel method for determining residence time distribution in intricately structured microreactors, *Lab Chip* 8 (2008) 431.

[33] F. Trachsel, A. Gunther, S. Khan, K. F. Jensen, Measurement of residence time distribution in microfluidic systems, *Chem*. *Eng*. *Sci*. 60 (2005) 5729.

[34] M. Gunther, S. Schneider, J. Wagner, R. Gorges, T. Henkel, M. Kielpinski, J. Albert, R. Bierbaum, J. M. Kohler, Characterisation of residence time and residence time distribution in chip reactors with modular arrangements by integrated optical detection, *Chem*. *Eng*. *J*. 101 (2004) 373.

[35] O. Levenspiel, W. K. Smith, Notes on the diffusion-type model for the longitudinal mixing of fluids in flow, *Chem*. *Eng*. *Sci*. 6 (1957) 227.

[36] R. W. Chantrell, J. Popplewell, S. W. Charles, Measurements of particle-size distribution parameters in ferrofluids, *IEEE*. *Trans*. *Magn*. 14 (1978) 975.

[37] S. P. Gubin, Y. A. Koksharov, G. B. Khomutov, G. Y. Yurkov, Magnetic nanoparticles: Preparation methods, structure and properties, *Usp*. *Khim*. 74 (2005) 539.

[38] H. T. Yang, H. L. Liu, N. N. Song, H. F. Du, X. Q. Zhang, Z. H. Cheng, J. Shen, L. F. Li, Determination of the critical interspacing for the noninteracting magnetic nanoparticle system, *Appl*. *Phys*. *Lett*. 98 (2011) 3.

[39] S. Khushrushahi, M. Zahn, Ultrasound velocimetry of ferrofluid spin-up flow measurements using a spherical coil assembly to impose a uniform rotating magnetic field, *J*. *Magn*. *Magn*. *Mater*. 323 (2011) 1302.

[40] L. Mao, H. Koser, Overcoming the diffusion barrier: ultra-fast micro-scale mixing via ferrofluids, in *Proceedings of the 14th International Conference on Solid-State Sensors, Actuators and Microsystems*, (IEEE, Lyon, 2007), p. 1829.

[41] A. H. Morrish, *The physical principles of magnetism* (IEEE Press, New York, 2001).

[42] J. H. Sanchez, C. Rinaldi, Magnetoviscosity of dilute magnetic fluids in oscillating and rotating magnetic fields, *Phys*. *Fluids*. 22 (2010) 043304.

[43] R. Patel, R. Upadhyay, R. V. Mehta, Viscosity measurements of a ferrofluid: comparison with various hydrodynamic equations, *J. Colloid Interface Sci*. 263 (2003) 661.

[44] N. Andhariya, B. Chudasama, R. Patel, R. V. Upadhyay, R. V. Mehta, Field induced rotational viscosity of ferrofluid: Effect of capillary size and magnetic field direction, *J. Colloid Interface Sci*. 323 (2008) 153.

[45] L. M. Pop, S. Odenbach, Capillary viscosimetry on ferrofluids, *J. Phys*. *Condens Matter* 20 (2008) 204139.

[46] M. Reindl, A. Leschhorn, M. Luecke, S. Odenbach, in *12th International Conference on Magnetic Fluids Icmf12*; *Vol. 9*, edited by H. Yamaguchi (2010), p. 121.

[47] M. Reindl, S. Odenbach, Effect of axial and transverse magnetic fields on the flow behavior of ferrofluids featuring different levels of interparticle interaction, *Phys*. *Fluids*. 23 (2011) 093102.

[48] M. Reindl, S. Odenbach, Influence of a homogeneous axial magnetic field on Taylor-Couette flow of ferrofluids with low particle-particle interaction, *Exp*. *Fluids* 50 (2011) 375.

[49] K. R. Schumacher, J. J. Riley, B. A. Finlayson, Effects of an oscillating magnetic field on homogeneous ferrofluid turbulence, *Phys*. *Rev*. *E*. 81 (2010) 016317.

[50] K. R. Schumacher, J. J. Riley, B. A. Finlayson, Turbulence in ferrofluids in channel flow with steady and oscillating magnetic fields, *Phys*. *Rev*. *E*. 83 (2011) 016307.

[51] C. C. Miller, The Stokes Einstein law for diffusion in solution, *P*. *R*. *Soc*. *Lond*. *a-Conta*. 106 (1924) 724.

[52] S. Feng, A. L. Graham, J. R. Abbott, H. Brenner, Antisymmetric stresses in suspensions: vortex viscosity and energy dissipation, *J. Fluid Mech*. 563 (2006) 97.

[53] S. W. Jones, W. R. Young, Shear dispersion and anomalous diffusion by chaotic advection, *J. Fluid Mech*. 280 (1994) 149.

[54] A. J. deMello, Control, detection of chemical reactions in microfluidic systems, *Nature* 442 (2006) 394.

[55] S. S. Varghese, Y. G. Zhu, T. J. Davis, S. C. Trowell, FRET for lab-on-a-chip devices - current trends and future prospects, *Lab Chip* 10 (2010) 1355.

[56] R. B. Bird, W. E. Stewart, E. N. Lightfoot, *Transport Phenomena* (J. Wiley, New York, 2002), p. 232.

[57] I. Torres-Díaz, C. Rinaldi, S. Khushrushahi, M. Zahn, Observations of ferrofluid flow under a uniform rotating magnetic field in a spherical cavity, *J*. *Appl*. *Phys*. 111 (2012) 07B313.

[58] I. Torres-Diaz, C. Rinaldi, Ferrofluid flow in the annular gap of a multipole rotating magnetic field, *Phys*. *Fluids*. 23 (2011) 082001.

[59] G. Taylor, Dispersion of soluble matter in solvent flowing slowly through a tube, *Proc*. *R*. *Soc*. *London*, *Ser*. *A* 219 (1953) 186.

[60] A. Dutta, R. A. Mashelkar, Taylor dispersion in the presence of slip effect, *Appl*. *Poly*. *Sci*. 27 (1982) 2739.

5 Remotely excited magnetic nanoparticles promote gas-liquid mass transfer in capillary Taylor flow regime

5.1 Abstract

Gas-liquid mass transfer from oxygen Taylor bubbles to liquid in capillaries was studied using dilute colloidal suspensions of magnetic nanoparticles (MNPs) as the liquid phase. The capillary was hosted inside the bore of a tubular two-pole three-phase magnet and the MNPs were remotely excited by subjecting them to different types of magnetic fields. The influence of magnetic field on the liquid side volumetric mass transfer coefficient ($k_L a$) was cast as an enhancement factor with respect to the magnetic field free base case. The repercussions of magnetic field frequency, MNP concentration, capillary tube and gas velocity on this enhancement factor were measured experimentally. Experimental results suggested that spinning nanoparticles under transverse rotating magnetic fields (^{T}RMF) improved mixing in the lubricating film that surrounds Taylor bubbles which reflected in a measurable enhancement of $k_L a$. On the contrary, axial stationary magnetic fields (^{A}SMF) pinned MNPs translating in systematically degraded gas-liquid mass transfer rates whereas axial oscillating magnetic field had no detectable effects on the mass transfer coefficient.

5.2 Introduction

Taylor flow in a single capillary or in microchannels is identified as the alternating movement of equally long Taylor bubbles separated by liquid slugs [1]. Taylor flow could be regarded as a top priority to study *in lieu* of other gas-liquid flow patterns prevailing in microchannels [2] owing to its interesting features. For instance, the axial dispersion in the liquid phase is significantly decreased as the only means for material exchange between two adjacent liquid slugs is through the thin liquid film between bubbles and the capillary wall "lubricating film" [3]. Moreover, the recirculation motion induced in the liquid slug, which is trapped between two consecutive bubbles, improves radial mass transfer [4, 5]. The remarkably high gas-liquid mass transfer rates observed in Taylor flow regime is one additional feature which attracts attentions towards multiphase microchannel systems. Consequently, gas-liquid microreactors have been utilized in a variety of chemical and

physical applications including, direct formation of hydrogen peroxide [6, 7], Pd-catalyzed carbonylation [8], direct fluorination [9, 10], and gas absorption [11, 12].

On the other hand, magnetic nanoparticles (MNPs) have found extensive applications in a broad range of scientific disciplines. In the realm of chemistry and chemical engineering, for example, they have been used vastly in homogeneous-heterogeneous (bio)catalysis and (bio)separations [13-22]. Recently, suspended MNPs in aqueous media have been shown to constitute a novel mixing agent in capillary flows upon excitation by magnetic fields. This effect was demonstrated by promoting or retarding lateral mixing in laminar Poiseuille flows [23]. By delivering their magnetic energy cargo via MNP stimulation anywhere into the liquid, a new portfolio of process intensification applications in chemical reaction engineering is foreseen to open up.

For this new class of nano-mixing stimulation, an external magnetic field exerts a magnetic torque on the magnetic moment of MNPs suspended in a liquid in order to orient the nanoparticles to align with the magnetic field direction [24]. For MNPs, whose magnetic moment is locked in the particle solid crystal lattice (rdMNPs), the magnetic torque is felt bodily leading to a momentum transfer from nanoparticle to the adjacent liquid phase [24]. This magnetic body torque is opposed by Brownian collisions from solvent molecules and flow-field hydrodynamic torque particularly when the liquid suspension and the magnetic field are in relative motion [24]. Interestingly, the nature of mechanical interactions between magnetically excited MNPs and the liquid depends on the characteristics of applied magnetic field. For instance, when a stationary magnetic field (SMF) is imposed over MNP suspensions in convective motion while fluid vorticity vector ($1/2\nabla\times\mathbf{V}$) is not parallel with MNP spin vector, rdMNPs, pinned by the magnetic field, resist against gyration under hydrodynamic torque that originates from fluid vorticity. This phenomenon, first observed by [25] and [26] gives rise to an inflated apparent viscosity called magnetoviscosity [24].

Alternatively, when the magnetic angular torque is exerted on MNPs by a time varying magnetic field, such as a rotating magnetic field (RMF), it causes the suspended rdMNPs to gyrate individually inside the contiguous liquid. A uniform RMF, which emerges from

superposition of three, 120° out of phase OMFs, has a constant intensity over time while it changes its direction continuously at any point of the domain. In a quest to catch-up with RMF direction, suspended rdMNPs spin in a direction primarily imposed by RMF [24].

Another type of time varying magnetic field is the oscillating magnetic field (OMF) characterized by an external magnetic field vector ($\mathbf{H}_0$) which changes as a sine-wave with time at each point of the space. Variable magnetic field strength and reversal of **H** direction at each wave cycle are two main features that distinguish OMF from RMF. Consequently, OMF and RMF MNP spin mechanisms are expected to be quite different. For instance, in restless MNP suspension ($1/2\nabla\times\mathbf{V} \neq \mathbf{0}$) subject to OMF, the nanoparticle spin direction under magnetic field is imposed in part by the direction of local fluid vorticity surrounding the particle [27]. This process may *per se* affect both characteristics and quality of mixing induced in OMF conditions.

In this contribution, we attempt to broaden the scope of MNP-mediated mixing toward the Taylor flow regime as the most commonly observed gas-liquid regime in microchannels [28]. Although in such contactors radial mixing is improved in the vortex region due to the recirculation patterns within liquid slug, molecular diffusion seems to play a prominent role in the micron-size thin lubricating film which encloses the bubbles [29]. The goal of this work is to unveil how magnetic nanoparticles (seeded in liquids at quite dilute levels), stimulated by different moderate-strength magnetic field types, while interacting with shear flow may affect the gas-liquid mass transfer phenomenon in the thin liquid film in Taylor flow regime. In this study, we carried out oxygen absorption from rising Taylor bubbles of pure oxygen into MNP suspensions as a model for gas-liquid mass transfer experiments in a capillary tube. Varying concentrations of nanoparticles in presence/absence of external magnetic field effects were studied. By positioning the capillary inside the magnet bore so as to provide the desired MNP spin plane, the magnetic nanoparticles were excited with three different types of magnetic fields, i.e., rotating magnetic field (RMF), oscillating magnetic field (OMF) and static magnetic field (SMF). The capillary diameter, gas and liquid flow rates were chosen such that saturation of lubricating film (evaluated from literature correlation of Vandu et al. [29]) was avoided.

5.3 Experimental

5.3.1 Magnet

A tubular two-pole three-phase magnet with bore dimensions of 55 mm height and 45 mm inner diameter was designed and fabricated in collaboration with MotionTech LLC and Windings Inc (Figure 5-1a,b). It was used to generate different magnetic field types including RMF, OMF and SMF with moderate magnetic field intensity at the center axis (up to 50 mT). Three identical coil pairs that constitute the magnet assembly can be energized separately or jointly in various configurations as depicted in Figures 5-3a, 5-4c and 5-5a. Since RMF emerges from superposition of three OMFs that are 120° out of phase, the coils were fed by three balanced AC currents from a variable frequency drive (ABB, ACS150, 2.2kW) to generate RMF (Figure 5-3a). To impose an OMF, two adjacent coils were energized with an AC current from an AC variable frequency drive (Invertek Drives, Optidrive E2) as shown in figure 5-4c. The coils having the same configuration were connected to a DC current from a DC source (Agilent Tech, N8739A) to provide a SMF as illustrated in figure 5-5a. The magnetic field strength and frequency was adjustable directly by power supplies. The temperature of the magnet solid part was controlled by a water cooling jacket encompassing the outer shell of the stator and filled with a coolant circulated in and out from a constant-temperature thermostated bath (Lauda, Model RKT20). Hajiani and Larachi [23] can be referred to for further information on the magnet design and specifications.

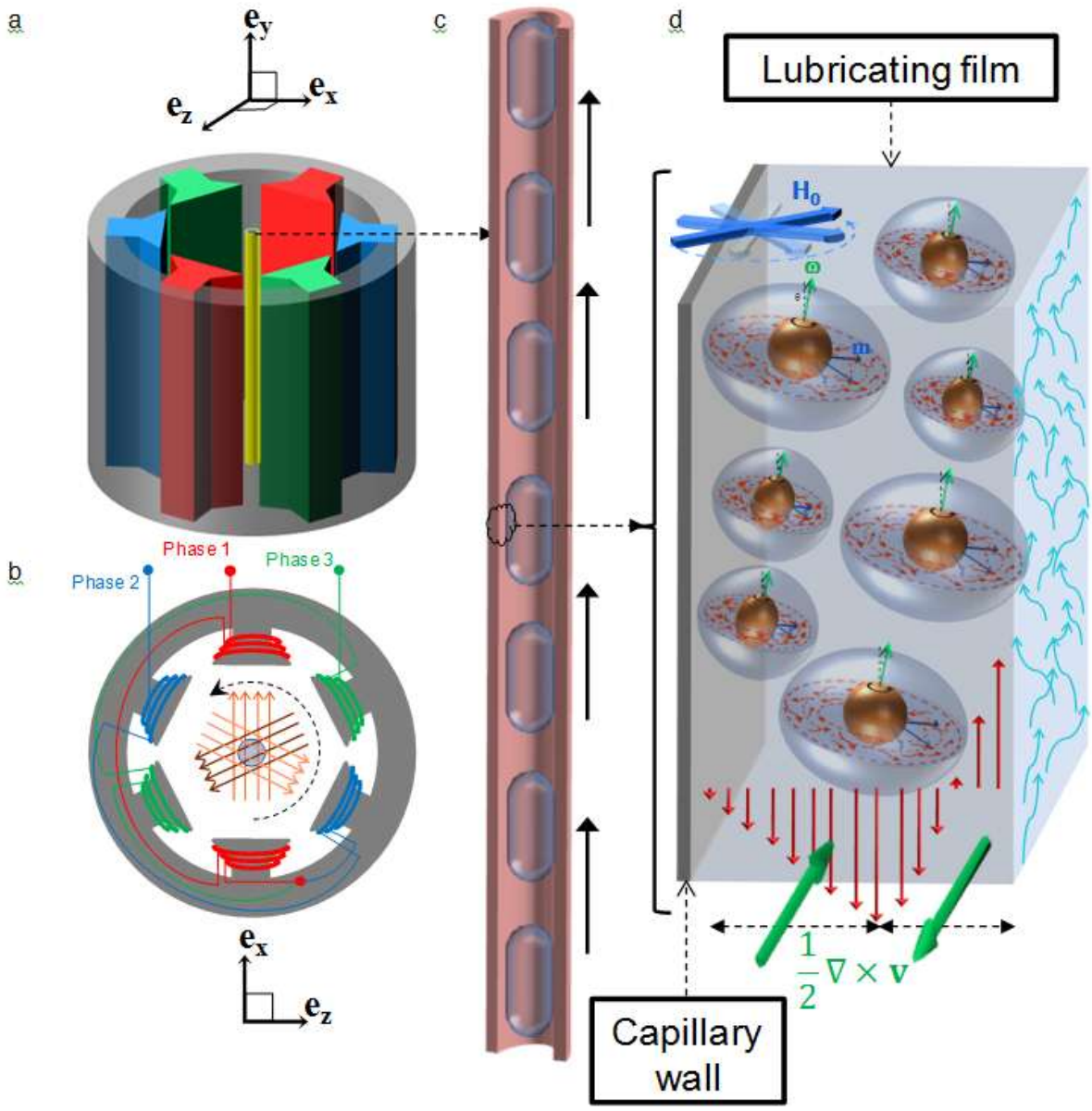

Figure 5-1 : Taylor bubbles in capillary tube exposed to magnetic field: a) experimental set-up including two-pole three-phase magnet and glass-made capillary tube at the center; b) upfront view of magnet with capillary set vertically and coaxially with magnet bore, and uniform *horizontal* magnetic field imposed across capillary tube hosting a flow of MNP-laden suspension; c) rising Taylor bubbles in capillary; d) expanded area of lubricating film where MNP spin plane is perpendicular to capillary wall.

5.3.2 Colloidal suspension

Dilute concentrations of colloidal ferrite (Fe_3O_4) MNPs (ϕ = 0.0005 – 0.005 v/v magnetic content) dispersed in water were prepared from commercial ferrofluid, EMG705 (FerroTec). The magnetic properties of EMG705 were measured by an alternating gradient magnetometer, MicroMag model 2900 (Princeton Instrument Co.) at 298 K in low-field (for initial susceptibility, χ_0) and high-field (for saturation magnetization, M_s) asymptote of magnetization curve [23]. Using these values, particle core diameter was estimated following a method proposed by Chantrell et al. [30]. Table 6 summarizes the magnetic properties of EMG-705 ferrofluid. The original ferrofluid supplied from the company was diluted in deionized water to reach our prescribed concentrations.

Table 5-1 : Magnetic properties of EMG 705 from magnetometry measurement

Saturation magnetization, M_s (kA/m)	18.7
Initial susceptibility, χ_0	2.9
MNP volume fraction, ϕ (v/v)	0.042
Estimated median magnetic core diameter, d_p (nm)	16.0

5.3.3 Capillary tube and magnetic field relative alignment

Theoretically, spinning rdMNPs dragged by a dynamic magnetic field (i.e., RMF and OMF) exchange angular momentum with liquid when particles spin *asynchronously* with respect to fluid vorticity ($1/2\nabla\times\mathbf{V}$) [24]. The fluid vorticity in the lubricating film of bubbles in Taylor flow regime is azimuthal while gas-liquid mass transfer occurs radially. Therefore, the capillary tube was positioned coaxially with respect to the tubular magnet in transverse RMF (^{T}RMF) to set the particle spin plane crosswise to the flow direction which is expected in turn to promote lateral mixing in the lubricating liquid film (Figure 5-1c). Regarding the work of Shliomis and Morozov [27], another conceivable configuration to enhance mass transfer in capillary is when magnetically excited rdMNPs outpace fluid vorticity while they spin in parallel with it. They exemplified an OMF applied in parallel with a tube as a case and grounded the theoretical framework of MNPs dynamic behavior in

such a system. Hence, the tube was also adjusted vertically and collinear with the magnetic field direction in the horizontal magnet (Figure 5-4a). In contrast, SMF in the same tube-magnet configuration is postulated to pin all rdMNPs in the capillary, making them resist against fluid vorticity (Figure 5-5a). This configuration was used to explore the effect of MNP hindrance on gas-liquid mass transfer in the lubricating film.

5.3.4 Experimental setup

Taylor flow gas-liquid mass transfer experiments were carried out by means of oxygen absorption into MNP-water suspensions in two distinct glass capillaries with circular cross-sections. The 4 mm I.D.-tube (L = 7 cm) was positioned coaxially at the center of the magnet bore whereas the other with 2 mm I.D. (L = 4.5 cm) was located transverse at the middle height of the magnet bore. The capillary length was limited by the size of the magnet bore in both cases. A schematic diagram of the experimental set-up is shown in Figure 5-2. Oxygen flow supplied from a gas cylinder was regulated through mass flow controller (Omega FMA14P). The designated flow of oxygen was directly fed into a T-shape plastic contactor inside the magnetic field where gas bubbles and liquid slugs form. Each batch of colloidal liquid phase was stripped out with pure nitrogen for at least three hours prior to each experiment to reach negligible initial oxygen concentration (i.e., less than 1 ppm). The magnetic properties of the suspension were verified to be unaltered by this pretreatment. A syringe pump with a range of 0-77.4 mL/min (Orion SAGE, Model 365) was used to deliver metered amounts of flow to the capillary. The accurate liquid flow rate under each run was measured by weighting method. For each capillary diameter, the gas and liquid flow were selected such that the flow regime in the capillary turned into a sustainable Taylor flow regime with partially oxygen-saturated lubricating films [29]. After passing the main capillary, the multiphase mixture was directed immediately to a disengagement chamber connected to capillary end for phase separation. This phase separator was equipped with an outlet weir and downcomer tube which was itself connected to a peristaltic pump (Cole Palmer MasterFlex, Console Drive, Model 7521-50) for keeping the volume of the liquid constant at 1 mL during the course of experiment, corresponding to a liquid height of 5 mm as shown in Figure 5-2a. Interferences between the magnetic field and the oxygen probe obligated installing this latter outside the disengagement chamber as shown in Figure 5-2a. Therefore, a programmable inverted syringe pump was taking a

sample from the bottom of disengagement cell once a minute and the dissolved oxygen content therein was analyzed by the oxygen probe (FOXY-R Stainless-steel, Fiber Optic Probe from Ocean Optics) on its passage. The oxygen content of the inlet suspension was measured prior to each run with a similar analysis without passing through the disengagement cell. All experiments were conducted under ambient conditions (101 kPa, 23-25°C). Figure 5-2b illustrates schematically the spinning MNPs around a single bubble when the system is subjected to the ^{T}RMF.

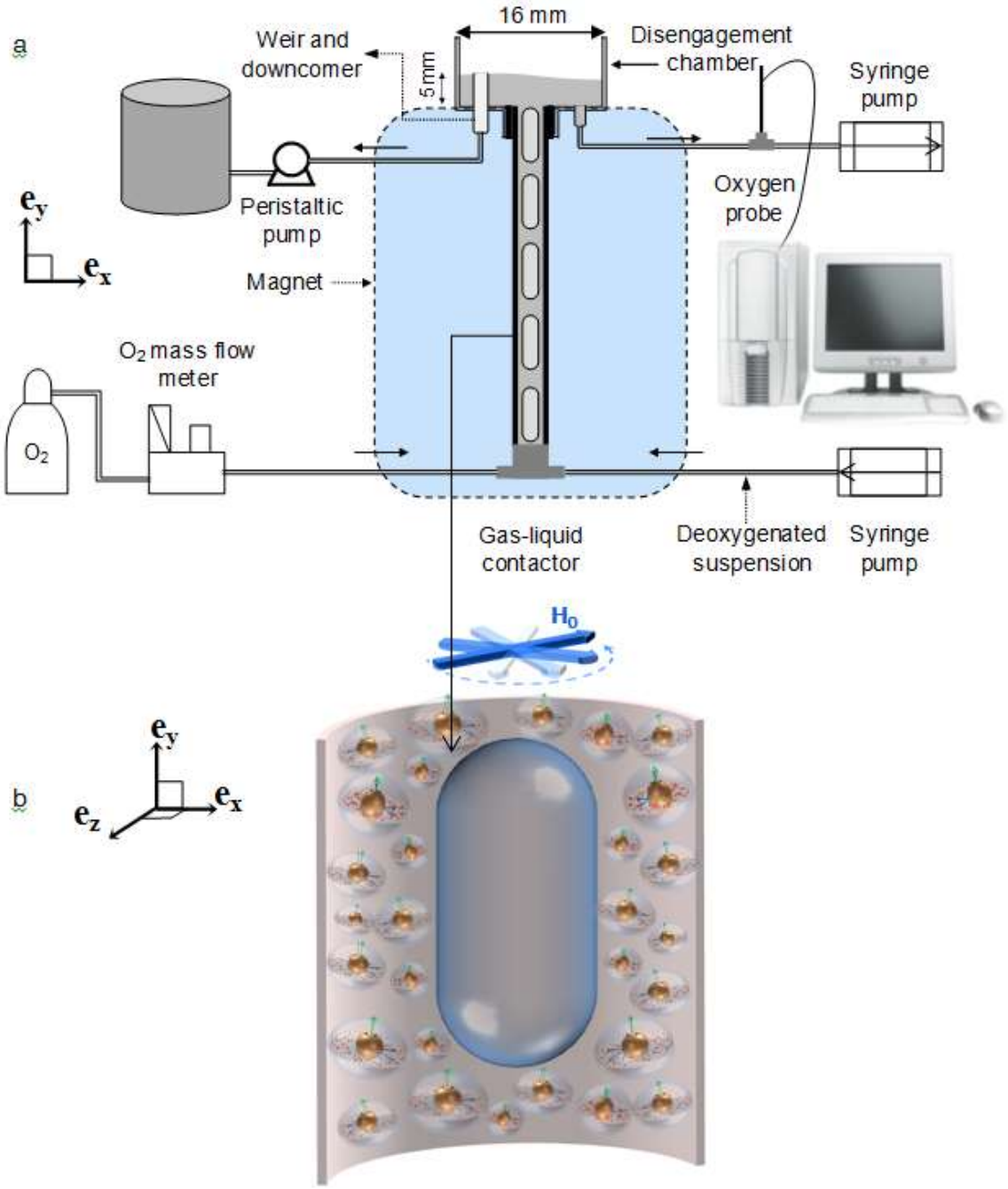

Figure 5-2 : a) Experimental set-up for gas-liquid mass transfer study in capillary; b) single Taylor bubble surrounded by spinning MNPs in a ^{T}RMF

5.4 Results and discussion

Liquid side volumetric mass transfer ($k_L a$) measurements were performed under three types of magnetic fields, i.e. transverse rotating magnetic field (^{T}RMF), axial oscillating magnetic field (^{A}OMF) and axial static magnetic field (^{A}SMF). As explained above, the capillary

configuration was adapted with the desired spin direction of MNPs for each magnetic field type.

5.4.1 Mass transfer enhancement in rotating magnetic field

Figure 5-3a shows the configuration in which k_La measurements were made for dilute ferrofluids flowing through a vertical coaxial capillary at the magnet bore center under ^{T}RMF. k_La enhancement factors versus magnetic field frequency (Ω_{RMF}) for several particle concentrations are shown in Figure 5-3b. The figure demonstrates that for low field frequencies ($\Omega_{RMF} < 50$), the magnetic field tendency to spin MNPs is slower than the hydrodynamic propensity, due to fluid vorticity, to gyrate the MNPs. Consequently, the magnetic torque exerted on MNP slows down the fluid vorticity and partially retards the hydrodynamic mixing mechanism in the lubricating film. At higher frequencies, the faster particles spin intensifies liquid phase mixing and improves the mass transfer rate through a nanoconvective effect [23]. Moreover, the MNP concentration exacerbates both above-mentioned mechanisms (see Figure 5-3b, ϕ = 0.0025, 0.0050). As such, a more concentrated suspension leads to stronger mass transfer retardation in low frequencies and higher k_La enhancement in the high frequency region.

Complementarily, k_La enhancement under magnetic field effect was compared to k_La increase results merely from gas flow rate augmentation for $\phi = 0$ and $H_0 = 0$ kA/m (see Figure 5-3b) while keeping the other operational conditions the same. The results indicate that the maximum mass transfer improvement achieved with the nano-mixing mechanism (i.e., 16.5%) is attainable as well without any magnetic effect with three fold higher gas flow rate at the same liquid flow. Note that at the highest volume fraction $\phi = 0.0050$, an increase neither in gas flow rate nor in frequency were able to stimulate k_La under rotating magnetic field conditions ($H_0 = 31.4$ kA/m, Figure 5-3b).

Figure 5-3c gives another evidence of how the spinning magnetic nanoparticles interact with fluid vorticity to control mixing in the lubricating film. On the left side of the graph (U_g < 1cm/s), the MNP spin dominates fluid vorticity which gives rise to an enhancement of k_La. By increasing the gas flow rate, the shear rate on the gas-liquid interface results in higher fluid vorticity that surpasses MNP spin and thus undermines the transverse

nanoconvective effect. On the right side of Figure 5-3c, fluid vorticity outweighs nanoparticle spin and results in downgrading the gas-liquid mass transfer compared to its magnetic field free counterpart. Both spin-dominant (lower U_g) and vorticity-dominant (higher U_g) effects are likely magnified at higher MNP concentration (Figure 5-3c).

The aggregate of observations discussed under Figure 5-3 implies that there is an intrinsic disadvantage of having the MNPs spin in a plane perpendicular to the fluid vorticity in the liquid film. From either stagnant film theory [31] or penetration theory [32, 33] it may be concluded that apart from molecular diffusion, fluid vorticity is the only mixing mechanism of the liquid bulk in gas-liquid contactor. Hence, the fact that ^{T}RMF opposes fluid vorticity is in contradiction with the ultimate goal of k_La enhancement. This notion is conceivable from figure 5-3c and is reinforced from figure 5-3b results as at low frequencies, k_La decreases in presence of particle spin. Increasing the field frequency will strengthen the restrictive effect of spinning MNPs on vorticity. However, strong nano-stirring in higher frequencies compensates the lack of vorticity-based mixing and slightly modifies k_La.

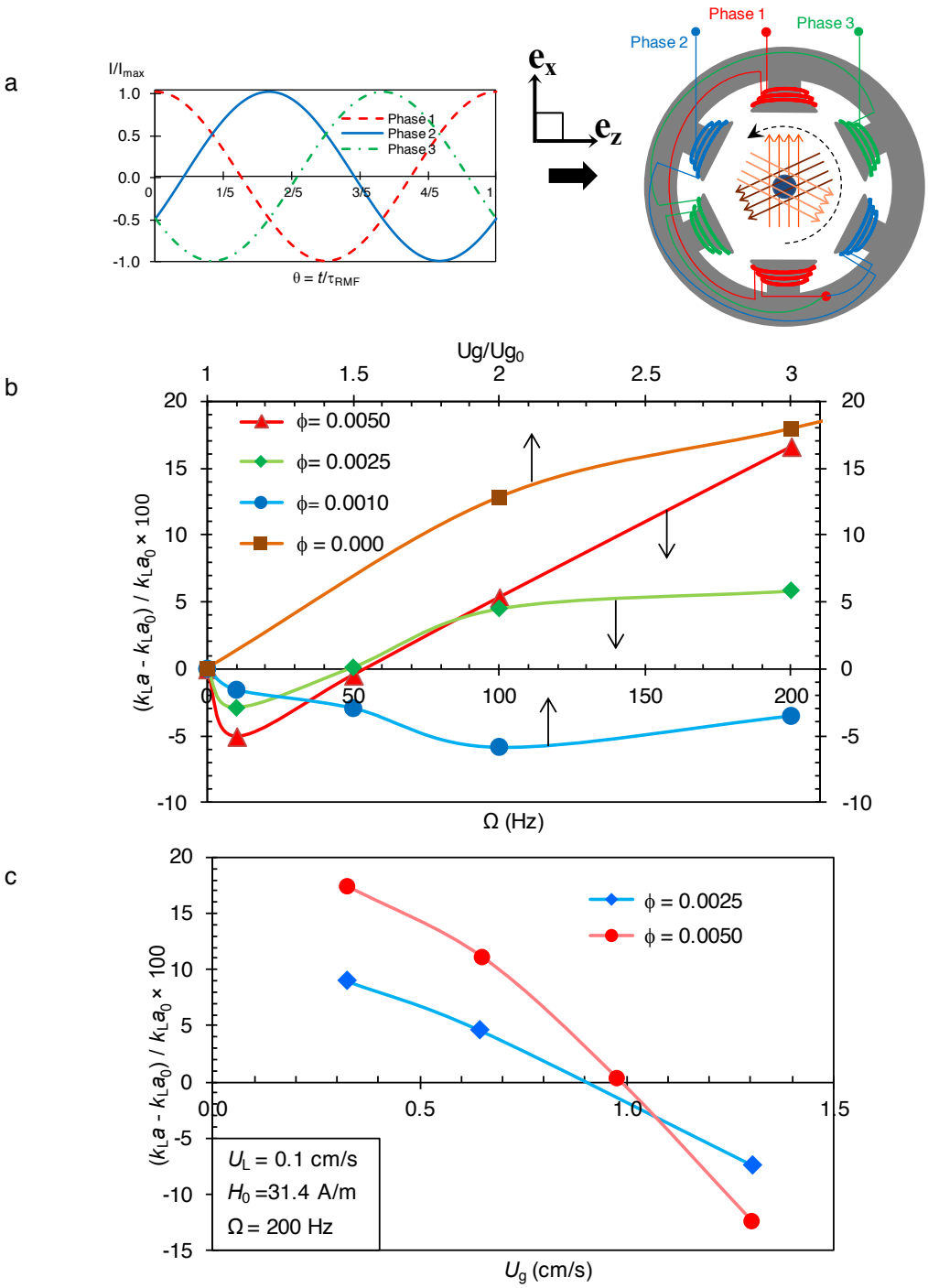

Figure 5-3 : a) Capillary tube located coaxially in the bore of a two-pole three-phase magnet (top view). Magnet generates a uniform rotating magnetic field (RMF) when energized by a three-phase power supply; b) k_La enhancement factor as a function of ^{T}RMF frequency: For experiments under magnetic field (♦, ▲, ●), enhancement was due to ^{T}RMF and k_La_0 is mass transfer coefficient in absence of magnetic field for each particle concentration, U_L = 0.1 cm/s, U_g = 0.3 cm/s and H_0 = 31.4 kA/m. For k_La versus gas flow rate without magnetic field (■), enhancement originated from gas flow augmentation and k_La_0 corresponds to U_g = 0.3 cm/s. Other parameters are the same (i.e., ϕ = 0 and U_L = 0.1 cm/s); c) k_La enhancement factor under ^{T}RMF as a function of U_g for two MNP concentrations while U_L, H_0 and Ω were kept constant.

5.4.2 Mass transfer enhancement in oscillating magnetic field

A substitution approach would be to force MNPs to spin in parallel with fluid vorticity. Such particles spin, ω, when becoming fast enough, i.e., $\omega > 1/2|\nabla\times\mathbf{V}|$, may intensify mixing without restraining fluid vorticity. In this case, nano-convective effect does not necessarily inhibit the vorticity in order to play a role in liquid film agitation, as it does under ^{T}RMF. According to the azimuthal direction of fluid vorticity in liquid film within the capillary, the particle spin vector should be azimuthal as well. Furthermore, the vorticity vector changes sign over film thickness where the liquid film velocity reaches maximum as illustrated in Figure 5-4b. Therefore, the direction of particle spin vector must be reversed locally over that hypothetical hydrodynamic boundary which is set by the direction of fluid vorticity. In this view, the advantages obtained by applying an ^{A}OMF would be twofold. Particle spin vector ($\boldsymbol{\omega}$) is favorably azimuthal under ^{A}OMF in cylindrical geometry [27, 34]. Moreover, since the sign of $\boldsymbol{\omega}$ is at discretion of the fluid vorticity [27], the particle spin is entirely synchronous with fluid vorticity over entire liquid film.

To establish ^{A}OMF conditions, we used a capillary (d = 2 mm, L = 4.5 cm) which was set vertically at the center of horizontal magnet bore (Figure 5-4a). Four coils, which were connected in series, were energized with an AC electrical current from a variable frequency drive (ABB, ACS150, 2.2kW) to generate ^{A}OMF (Figure 5-4c). Figure 5-4d shows $k_L a$ enhancement factor of three MNP concentrations versus field frequencies with H_{0rms} of 31.4 kA/m. As seen, insignificant mass transfer enhancement under ^{A}OMF did not comply with our expectation in the framework explained in Figure 5-4b. According to the small particle size (d_p = 16.0 nm) and extremely low field frequency ($\Omega < 300$ Hz), the underlying cause of this result would be the intrinsic inability of low frequency OMF to bring rdMNP into consistent full rotation. Brownian agitation interference or the effect of strong hydrodynamic torque at the very brief moment when OMF pass through zero intensity during each wave cycle may have inhibited the synchronized rotation of MNPs under OMF in our experiments. Larger MNPs [35] or much higher frequencies ($\Omega > 10^5$ Hz) are perceived to be required [34, 36, 37]. Such a high frequency does not match with the design of our present magnet setup. However, having larger MNPs would be regarded as a rational solution to this challenge.

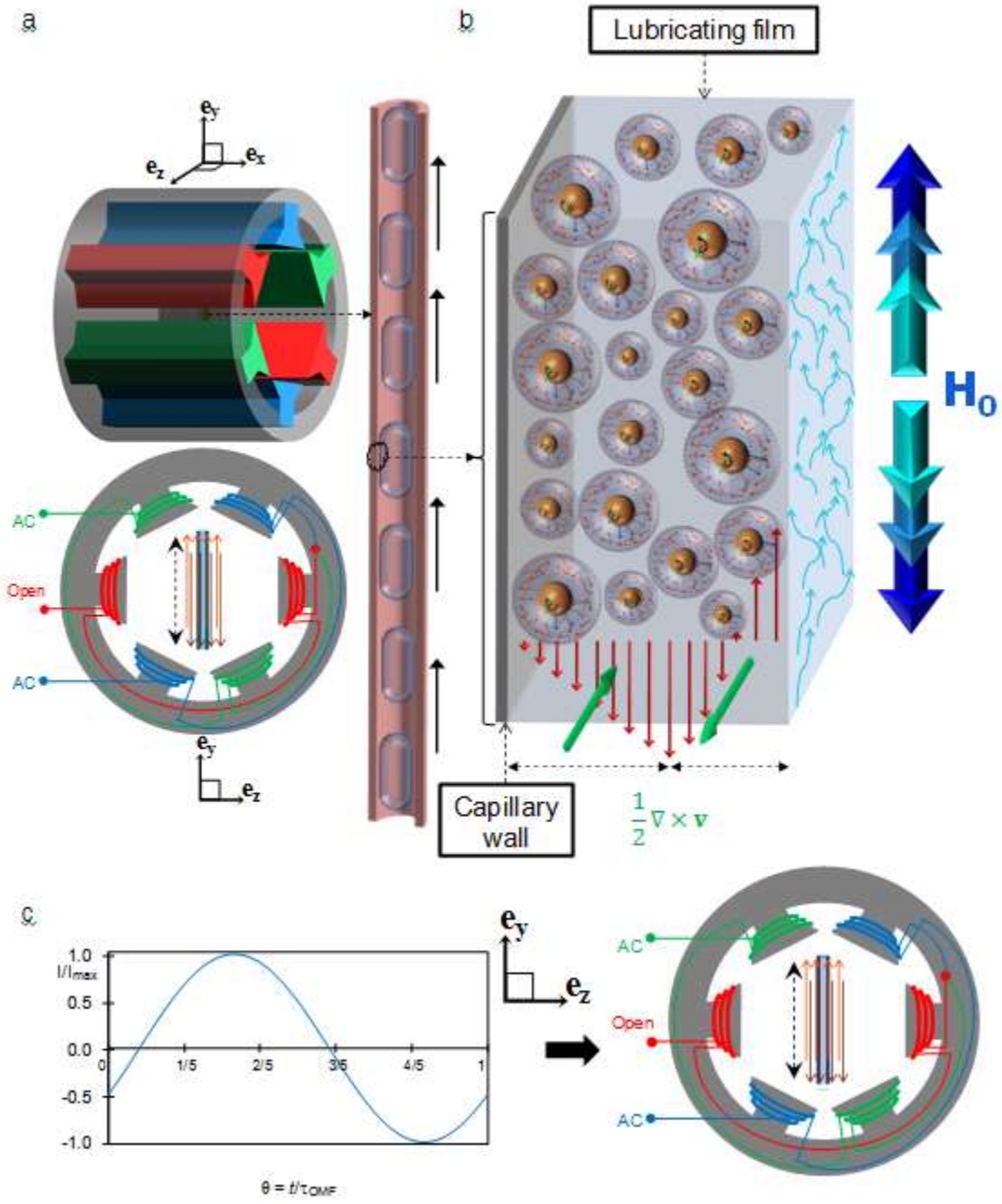
a
b
Lubricating film
e_y
e_x
e_z
AC
Open
AC
H_0
Capillary wall
$\frac{1}{2}\nabla \times \mathbf{v}$
c
1.0
I/I_{max}
0.5
0.0
-0.5
-1.0
0
1/5
2/5
3/5
4/5
1
$\theta = t/\tau_{OMF}$
e_y
e_z
AC
Open
AC

d

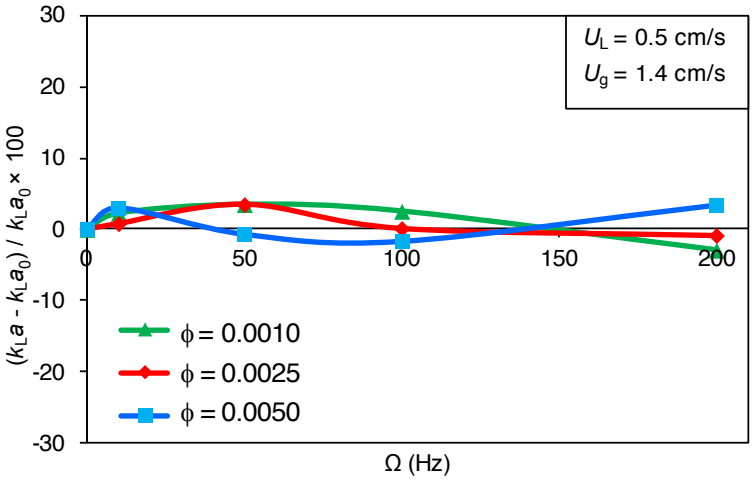

Figure 5-4 : a) Side view of the magnet with a capillary tube which was set vertically and transverse with magnet bore, a uniform *vertical* magnetic field imposed along capillary tube; b) rising Taylor bubbles surrounded with azimuthally spinning MNPs are shown. Fluid vorticity and consequently, particle spin vector inverted over film thickness; c) the magnet generates a uniform oscillating magnetic field (OMF) when energized by an AC power supply; d) k_La enhancement factor versus field frequency for three particle concentrations exposed to $H_{0\ rms}$ = 31.4 kA/m. k_La_0 is mass transfer coefficient for each particle concentration without magnetic field effect.

5.4.3 Mass transfer enhancement in static magnetic field

Finally, we investigated the effect of magnetically locked MNPs (magnetoviscosity) on k_La in the Taylor flow regime. The capillary in the same configuration as in Figure 5-4a was subjected to a uniform static magnetic field (SMF) which was generated by four coils energized by a DC power supply (Figure 5-5a). As k_La declines versus H_0 and MNP concentration in Figure 5-5b, the results indicate that magnetically pinned MNPs incapacitate gas-liquid mass transfer systematically. In fact, pinned MNPs prevent liquid layers from free sliding on top of each other under viscid flow. This phenomenon impairs mixing or surface renewal in liquid film around the rising bubble to a certain extent. Besides, it may lessen liquid recirculation in the slug due to inflated viscosity. Therefore, k_La reduction observed in Figure 5-5b may be attributed to the aggregate effects of magnetically locked MNPs around the bubbles and in the liquid slugs.

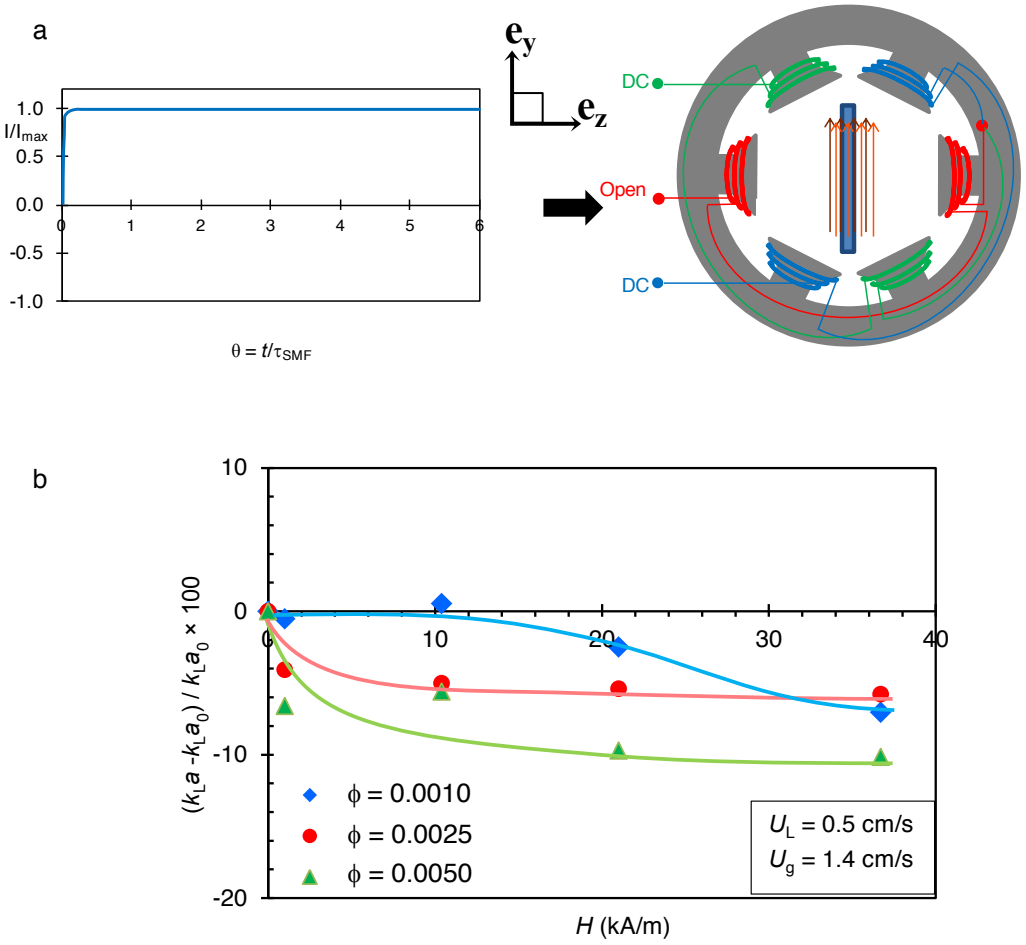

Figure 5-5 : a) Capillary tube was located vertically in horizontal magnet (side view). The magnet generates a uniform stationary magnetic field (SMF) when energized by a DC power supply; b) k_La enhancement factor versus field intensity for three particle concentrations. k_La_0 is suspension mass transfer coefficient for each particle concentration without magnetic field effect.

5.5 Conclusion

By studying k_La in a Taylor flow system comprising dilute aqueous colloidal suspension of MNPs and oxygen bubbles under moderate strength ^{T}RMF, ^{A}OMF and ^{A}SMF, we investigated the effects resulting from nanoparticle magnetic torque exchange with liquid phase on the gas-liquid mass transfer. The nature of these effects in a two-phase system was found to be similar to that in single-phase systems. Our results demonstrated k_La enhancement due to nanoconvective stirring induced by excited MNPs under ^{T}RMF. Moreover, it provided clear evidence of the interaction between magnetic torque and fluid

vorticity as contributing to two distinctive competing mixing mechanisms while indicating the conditions in which either of them prevails.

By contrast, no significant mass transfer enhancement could be seen under low frequency ^{A}OMF, probably due to the small particle size or extremely low field frequency. Further studies are required to identify the optimal particle size or field frequency that sustains full synchronized spin of MNPs driven by ^{A}OMF. Finally, reductions in $k_L a$ were also observed while the capillary was subjected to ^{A}SMF. This observation confirms earlier reports on inhibitive role of magnetically pinned MNPs on mass transfer phenomenon in diluted colloidal systems [23]. In sum, our experimental results point out further evidences that MNPs, excited by appropriate magnetic field, manipulate liquid transport properties in a variety of flowing systems. However, nano-mixing application for liquid mass transfer enhancement would be limited to those systems in which hydrodynamic torque, originating from fluid vorticity, has the same magnitude relative to magnetic torque on MNP which is imposed by time varying magnetic fields.

5.6 Nomenclature

d	Capillary tube diameter, mm
d_p	Volume median particle diameter, m
H_0	External (imposed) magnetic field intensity (A/m)
$k_L a$	Liquid side volumetric mass transfer (1/s)
L	Capillary length, cm
rdMNP	Rigid dipole magnetic nanoparticle
U_g	Gas superficial velocity, cm/s
U_L	Liquid superficial velocity, cm/s
Greek	
$\boldsymbol{\omega}$	MNP spin velocity vector per unit volume, rad/s

Ω	Magnetic field frequency, Hz
τ_{RMF}	Rotating magnetic field time constant = $1/\Omega_{RMF}$, s
τ_{OMF}	Oscillating magnetic field time constant = $1/\Omega_{OMF}$, s
τ_{SMF}	Static magnetic field time constant = 1 s
ϕ	MNP core volume fraction
$1/2\nabla\times\mathbf{V}$	Fluid vorticity vector = s^{-1}

Acronyms

MNP	Magnetic nanoparticle
OMF	Oscillating magnetic field
RMF	Rotating magnetic field
SMF	Static (DC) magnetic field

5.7 References

[1] V. Hessel, P. Angeli, A. Gavriilidis, H. Lowe, Gas-liquid and gas-liquid-solid microstructured reactors: Contacting principles and applications, *Ind. Eng. Chem. Res.* 44 (2005) 9750-9769.

[2] J. Yue, G. W. Chen, Q. Yuan, L. G. Luo, Y. Gonthier, Hydrodynamics and mass transfer characteristics in gas-liquid flow through a rectangular microchannel, *Chem. Eng. Sci.* 62 (2007) 2096-2108.

[3] F. Trachsel, A. Gunther, S. Khan, K. F. Jensen, Measurement of residence time distribution in microfluidic systems, *Chem. Eng. Sci.* 60 (2005) 5729-5737.

[4] P. Zaloha, J. Kristal, V. Jiricny, N. Volkel, C. Xuereb, J. Aubin, Characteristics of liquid slugs in gas-liquid Taylor flow in microchannels, *Chem. Eng. Sci.* 68 (2012) 640-649.

[5] A. Gunther, S. A. Khan, M. Thalmann, F. Trachsel, K. F. Jensen, Transport and reaction in microscale segmented gas-liquid flow, *Lab Chip* 4 (2004) 278-286.

[6] X. Wang, Y. T. Nie, J. L. C. Lee, S. Jaenicke, Evaluation of multiphase microreactors for the direct formation of hydrogen peroxide, *Appl. Catal., A* 317 (2007) 258-265.

[7] J. F. Ng, Y. Nie, G. K. Chuah, S. Jaenicke, A wall-coated catalytic capillary microreactor for the direct formation of hydrogen peroxide, *J. Catal.* 269 (2010) 302-308.

[8] X. Q. Gong, P. W. Miller, A. D. Gee, N. J. Long, A. J. de Mello, R. Vilar, Gas-Liquid Segmented Flow Microfluidics for Screening Pd-Catalyzed Carbonylation Reactions, *Chem.-Eur. J.* 18 (2012) 2768-2772.

[9] N. de Mas, A. Gunther, M. A. Schmidt, K. F. Jensen, Increasing Productivity of Microreactors for Fast Gas-Liquid Reactions: The Case of Direct Fluorination of Toluene, *Ind. Eng. Chem. Res.* 48 (2009) 1428-1434.

[10] P. Lang, M. Hill, I. Krossing, P. Woias, Multiphase minireactor system for direct fluorination of ethylene carbonate, *Chem. Eng. J.* 179 (2012) 330-337.

[11] M. Sato, M. Goto, Gas absorption in water with microchannel devices, *Sep. Sci. Technol.* 39 (2004) 3163-3167.

[12] W. E. TeGrotenhuis, R. J. Cameron, V. V. Viswanathan, R. S. Wegeng, Solvent extraction and gas absorption using microchannel contactors, *Microreaction Technology: 3rd International Conference on Microreaction Technology; Topical Conference Preprints; Springer-Verlag: Berlin,* (2000) 541-549.

[13] Q. Zhang, H. Su, J. Luo, Y. Y. Wei, A magnetic nanoparticle supported dual acidic ionic liquid: a "quasi-homogeneous" catalyst for the one-pot synthesis of benzoxanthenes, *Green Chem*. 14 (2012) 201-208.

[14] R. Hudson, C. J. Li, A. Moores, Magnetic copper-iron nanoparticles as simple heterogeneous catalysts for the azide-alkyne click reaction in water, *Green Chem*. 14 (2012) 622-624.

[15] T. P. N. Ngo, W. Zhang, W. Wang, Z. Li, Reversible clustering of magnetic nanobiocatalysts for high-performance biocatalysis and easy catalyst recycling, *Chem. Commun*. 48 (2012) 4585-4587.

[16] Y. S. Fu, H. Q. Chen, X. Q. Sun, X. Wang, Combination of cobalt ferrite and graphene: High-performance and recyclable visible-light photocatalysis, *Applied Catalysis, B: Environmental* 111 (2012) 280-287.

[17] X. Y. Du, J. He, J. Zhu, L. J. Sun, S. S. An, Ag-deposited silica-coated Fe3O4 magnetic nanoparticles catalyzed reduction of p-nitrophenol, *Appl. Surf. Sci.* 258 (2012) 2717-2723.

[18] F. W. Zhang, J. R. Niu, H. B. Wang, H. L. Yang, J. Jin, N. Liu, Y. B. Zhang, R. Li, J. T. Ma, Palladium was supported on superparamagnetic nanoparticles: A magnetically recoverable catalyst for Heck reaction, *Mater. Res. Bull.* 47 (2012) 504-507.

[19] Y. H. Liu, J. Deng, J. W. Gao, Z. H. Zhang, Triflic Acid-Functionalized Silica-Coated Magnetic Nanoparticles as a Magnetically Separable Catalyst for Synthesis of gem-Dihydroperoxides, *Adv. Synth. Catal.* 354 (2012) 441-447.

[20] C. J. Zhu, Y. Y. Wei, Facile Preparation and Reactivity of Magnetic Nanoparticle-Supported Hypervalent Iodine Reagent: A Convenient Recyclable Reagent for Oxidation, *Adv. Synth. Catal.* 345 (2012) 313-320.

[21] A. G. Kong, P. Wang, H. G. Zhang, F. Yang, S. P. Huang, Y. K. Shan, One-pot fabrication of magnetically recoverable acid nanocatalyst, heteropolyacids/chitosan/Fe3O4, and its catalytic performance, *Appl. Catal., A* 417 (2012) 183-189.

[22] H. J. Xu, X. Wan, Y. Y. Shen, S. Xu, Y. S. Feng, Magnetic Nano-Fe3O4-Supported 1-Benzyl-1,4-dihydronicotinamide (BNAH): Synthesis and Application in the Catalytic Reduction of alpha,beta-Epoxy Ketones, *Org. Lett.* 14 (2012) 1210-1213.

[23] P. Hajiani, F. Larachi, Reducing Taylor dispersion in capillary laminar flows using magnetically excited nanoparticles: Nano-mixing mechanism for micro/nanoscale applications, *Chem. Eng. J.* 203 (2012) 492-498.

[24] R. E. Rosensweig, *Ferrohydrodynamics*. Dover Publications: Mineola, N.Y., 1997.

[25] R. E. Rosensweig, R. Kaiser, G. Miskolcz, Viscosity of magnetic fluid in a magnetic field, *J. Colloid Interface Sci.* 29 (1969) 680-686.

[26] J. P. McTague, Magnetoviscosity of magnetic colloids, *J. Chem. Phys*. 51 (1969) 133-136.

[27] M. I. Shliomis, K. I. Morozov, Negative viscosity of ferrofluid under alternating magnetic-field, *Phys. Fluids* 6 (1994) 2855-2861.

[28] M. N. Kashid, A. Renken, L. Kiwi-Minsker, Gas-liquid and liquid-liquid mass transfer in microstructured reactors, *Chem. Eng. Sci.* 66 (2011) 3876-3897.

[29] C. O. Vandu, H. Liu, R. Krishna, Mass transfer from Taylor bubbles rising in single capillaries, *Chem. Eng. Sci.* 60 (2005) 6430-6437.

[30] R. W. Chantrell, J. Popplewell, S. W. Charles, Measurements of particle-size distribution parameters in ferrofluids, *IEEE Trans*. *Magn*. 14 (1978) 975-977.

[31] W. G. Whitman, A Preliminary Experimental Confirmation of the Two-Film Theory of Gas Absorption, *Chem*. *Metall*. *Eng*. 29 (1923) 146-148.

[32] R. Higbie, The rate of absorption of a pure gas into a still liquid during short periods of exposure, *Trans. Am. Inst. Chem. Eng.* 31 (1935) 365-389.

[33] P. V. Danckwerts, A. M. Kennedy, Kinetics of liquid-film process in gas absorption. part 1: Models of the absorption process, *Trans. Am. Inst. Chem. Eng.* 32 (1954) S101-S104.

[34] J. C. Bacri, R. Perzynski, M. I. Shliomis, G. I. Burde, Negative-viscosity effect in a magnetic fluid, *Phys. Rev. Lett.* 75 (1995) 2128-2131.

[35] F. Gazeau, C. Baravian, J. C. Bacri, R. Perzynski, M. I. Shliomis, Energy conversion in ferrofluids: Magnetic nanoparticles as motors or generators, *Phys. Rev. E* 56 (1997) 614-618.

[36] A. Zeuner, R. Richter, I. Rehberg, Experiments on negative and positive magnetoviscosity in an alternating magnetic field, *Phys. Rev. E* 58 (1998) 6287-6293.

[37] K. R. Schumacher, I. Sellien, G. S. Knoke, T. Cader, B. A. Finlayson, Experiment and simulation of laminar and turbulent ferrofluid pipe flow in an oscillating magnetic field, *Phys*. *Rev*. *E* 67 (2003) 026308.

6 Conclusion and future work

6.1 Key contributions

Chapter 2 showed that a rotating magnetic field (RMF) delivers electromagnetic energy into the liquid phase through spinning MNPs. We speculate that a nano-convective zone forms around each MNP in which mixing mechanism is enhanced by particle motion. Thus, at the distance between two neighboring MNPs, the length scale within which molecular diffusion is the dominate transport mechanism decreases and mass transfer rate increases. The enhancement factor can be increased or decreased with respect to magnetic field amplitude, frequency and MNP concentration. These experiments are believed to be the first measurements of self-diffusion coefficient with MNPs under the effect of uniform RMF. During the measurements, we also found that linear non-uniform rotating magnetic field with identical average field amplitude relative to uniform field will not increase the enhancement factor of self-diffusivity. This implies that the magnetic force which is exerted on single particle in the non-uniform magnetic field is not strong enough to overcome stokes drag force and cannot induce a translational motion of MNPs under rotating gradient of magnetic field. In conclusion, the enhancement seems to be originated only from MNPs spin.

In Chapter 3 it is demonstrated that nano-mixing in controlled direction gives rise to lateral mixing in presence of low *Re* convective flow in capillary. By studying axial dispersion in a dilute liquid suspension containing MNPs and flowing through a Taylor capillary cell under moderate strength low frequency transverse rotating magnetic fields (^{T}RMF), we found that spinning MNPs produce nano-sized vortices that objectively enhance lateral mixing beyond the capability of molecular diffusion. In these experiments, magnetic torque overcomes hydrodynamic torque which tends to gyrate MNPs perpendicular to the MNP spin plane. During systematic study of system parameters, plateauing effect was observed in axial dispersion reduction versus MNP concentration and field frequency. This effect was explained and attributed to the size of mixed-cup zones around single MNPs. Using the RTD data, the laminar velocity profile was reconstructed in the presence (absence) of magnetic field. Under ^{T}RMF, slight shear-thinning behavior of suspension was detected that flattened the originally parabolic velocity profile toward plug flow like profile.

Chapter 4 studied the effect of different magnetic field scenarios on the axial dispersion variation and laminar velocity profile in capillaries, which were investigated in chapter 4. Oscillating magnetic field (OMF) did not have significant effect on lateral mixing in capillary. A detailed discussion was included to explain this observation. Axial stationary magnetic field (^{A}SMF) locked the particles and made them resist against gyration with fluid vorticity. We speculated that locked MNPs remove radial tracer concentration locally which will in turn reduce mass transfer rate. Shear-thickening behavior was also detected under ^{A}SMF since reconstructed laminar velocity profile protruded from no-field parabolic profile.

In chapter 5, mixing and blockage effects of MNPs were incorporated into a gas-liquid mass transfer system in Taylor flow regime. Since the hydrodynamic shear rate around Taylor bubbles is extremely stronger compared to that of low *Re* single phase flow in capillaries, the mixing effect of spinning MNPs and mass transfer enhancement in lubricating file was marginal. Larger MNPs, stronger magnetic field and higher field frequencies are required to produce significant mass transfer augmentation in Taylor flow regime. Gas-liquid mass transfer rate also decreased up to 10 percent by magnetically locked MNPs under ^{A}SMF. This effect is also expected to be emphasized with stronger magnetic field and larger nanoparticles.

6.2 Suggested future work

In closing, the following directions for future work are suggested to extend and build upon the results presented in this thesis:

1) Quite recently, we prepared magnetic colloidal suspensions of magnetic micron-size particles (i.e. 1 μm median average diameter). This suspension is not stable per se and significant particle sedimentation occurs after an hour. However, we observed that under the effect of RMF, MMPs spin vigorously and agitate the solution strong enough to keep them afloat as long as they stay inside the magnet. Particle size measurement after the stability test shows that the particle-particle interaction did not agglomerate MMPs under the RMF. Using this suspension, self-diffusion measurement was performed under RMF as explained in chapter 2. Preliminary results shows 200 folds enhancement using over ten

times less particle content in the liquid. Such a low particle concentration makes the nano-mixing technique even more versatile for process intensification applications.

2) One important step in future work will be to apply MMPs in two-phase Taylor experiments as presented in chapter 5. Larger particles can absorb more magnetic energy into the liquid phase and may enhance mass transfer rate significantly, particularly when hydrodynamic torque is strong. MMPs will also be applied to Taylor dispersion tests in order to generate strong lateral mixing in capillary and to diminish axial dispersion to reach to plug flow regime in low *Re* laminar flow.

3) Very recently, a colloidal suspension of MNPs (50 nm median average diameter) mixed with MMPs (1 μm particle) is prepared and showed to be stable without significant sedimentation and agglomeration under RMF. Polydisperse mixture of MNPs and MMPs may be exploited to generate mixing in different length scales in suspension. An experimental frame work is required in which multi-scale mixing can enhance distinguishable properties of the system.

4) Future experiments will also be performed with MMPs under rotating gradient of magnetic field. Drag force on particle increases with the square of particle diameter while magnetic moment of particle increases with the third power of particle diameter. Mathematical model of suspended MMPs in non-uniform magnetic field confirms the magnetic force can maneuver MMPs in a circular motion while they spin. This secondary orbital motion of MMPs under non-uniform RMF may increase the mixing beyond what has been obtained so far under uniform RMF.

5) An appropriate visualization technique should also be integrated in order to illuminate nano-mixing phenomenon. For instance, direct velocity profile measurement in capillary will clarify shear-thinning and shear-thickening behavior of suspension under ^{T}RMF and ^{A}SMF. Another example would be self-diffusion coefficient measurement of a florescent dye under the effect of RMF in a static cell visualized by microscope. The major challenge in such experiments is that MNP suspension is opaque and cannot be illuminated in depth for optical visualization. However, using very thin micro channels or larger MNPs/MMPs in suspension providing less particle concentration may resolve this problem.

6) Applying nano-mixing technique to other chemical engineering systems will help to identify its advantages and limitations. For example, a small packed bed reactor has been fabricated in order to be fed by colloidal suspension of MNPs. This reactor has been equipped with two sets of conductivity electrodes to measure tracer concentration during RTD tests. The ability of nano-mixing technique in promoting mixing in pores and liquid film under ^{T}RMF would be examined as it may affect the RTD of the reactor. This experiment would also be repeated in a 3-phase reactor including gas.

7) Another important aspect which is left to be investigated is to develop the mathematical model to compare with experimental results of nano-mixing for better understanding of this phenomenon. First, current ferrohydrodynamic formulation should be applied to predict our experimental results. By fitting theoretical predictions to the current measurements, many physical parameters can be determined such as the vortex viscosity, spin viscosity, ferrofluid spin velocity, and spin velocity boundary conditions. However, since ferrohydrodynamic theory considers ferrofluid as a uniform continuum in which angular momentum can be exchanged with an external magnetic field, nano-mixing between particles may not be fully reflected.

7 Appendix A

7.1 Properties of magnetic nanoparticles (MNP)

Dilute concentrations of ferrite (Fe_3O_4) MNPs (0.1%vol to 1%vol magnet content) dispersed in water are prepared using as a source of MNPs, a commercially available ferrofluid (EMG705, FerroTec, USA). Thanks to the small particle sizes (*ca*. 16-nm magnetic core), MNPs can be easily dispersed by thermal agitation while surfactants prevent them from sticking to each other under short-range Van der Waals attraction forces.

The magnetic properties of suspended MNPs are measured using an alternating gradient magnetometer (MicroMag model 2900, Princeton Instrument) at 298 K in low-field (about zero A/m) and high-field (near saturation magnetization, M_s) asymptote of magnetization curve with particle core diameter estimated thereof. In as-received ferrofluids, saturation magnetization amounts to M_s = 18.7 kA/m (Figure 6-1). The magnetic volume content of suspension is estimated to be φ = 4.2 % vol using $\phi = M_s/M_d$ where magnetite domain magnetization is M_d = 446 kA/m [1]. The initial susceptibility is determined to be 2.94 using the magnetization-curve low-field zone (i.e., 0 to 765 A/m) lay on a straight line (Figure 6-2). Then, both low-field and high-field asymptotes of the Langevin equation are fitted to the magnetization measurements using a log-normal particle size distribution following a method proposed by Chantrell [2]. The magnetic-core volume median particle diameter, d_c, and its standard deviation are estimated as 16.0 nm and 0.3, respectively.

The hydrodynamic diameter of MNP suspension is also measured based on dynamic light scattering technique on a Zetasizer Nano 6 (Malvern Instruments Ltd). Figure 6-3 shows the particle size distribution with number average diameter and standard deviation, respectively, of 24.8 nm and 7.25. The particle hydrodynamic diameter measured by DLS technique was found to be larger than core MNP diameter and is consistent with literature findings [3,4].

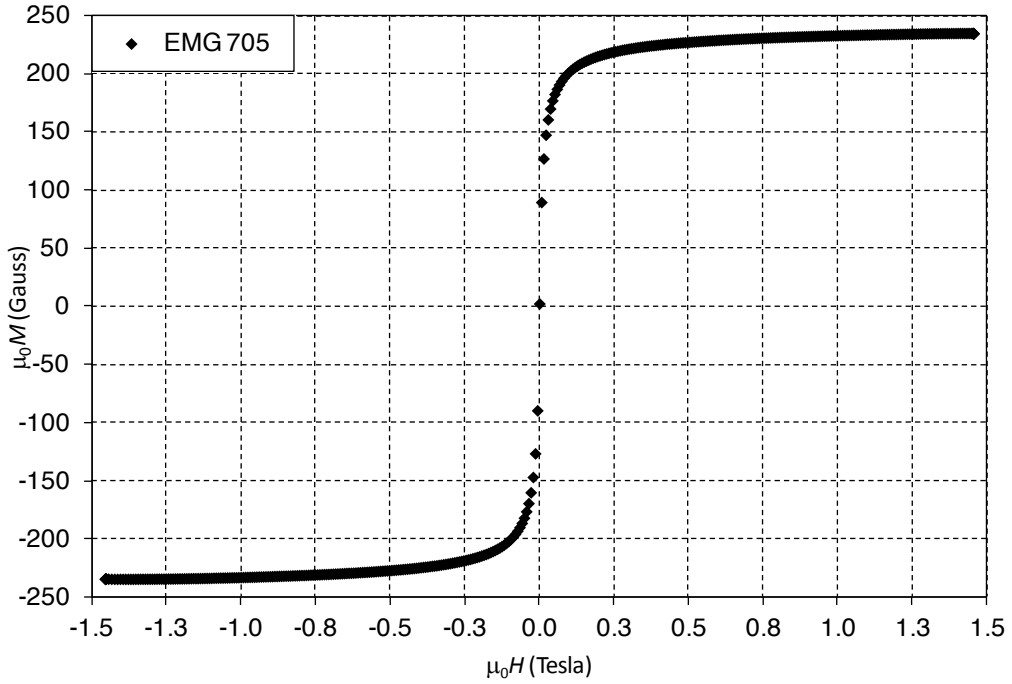

Figure 7-1: Magnetization curve of EMG705 water-based ferrofluid (M_s = 18.7 kA/m)

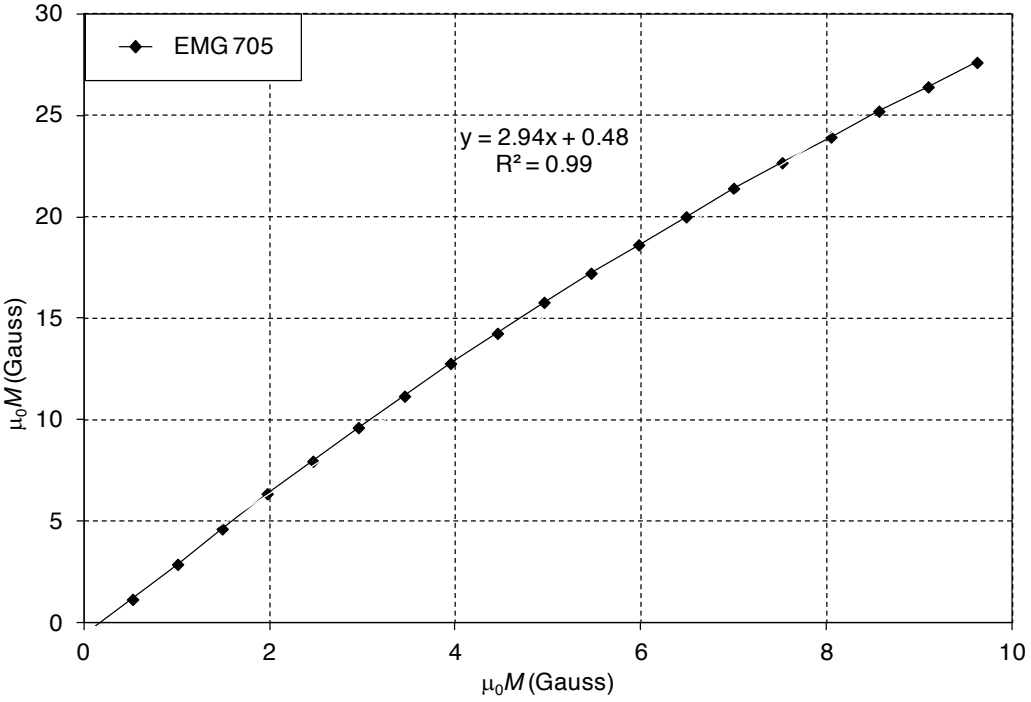

Figure 7-2 : Magnetization linear region for EMG705 water-based ferrofluid (χ_0 = 2.94)

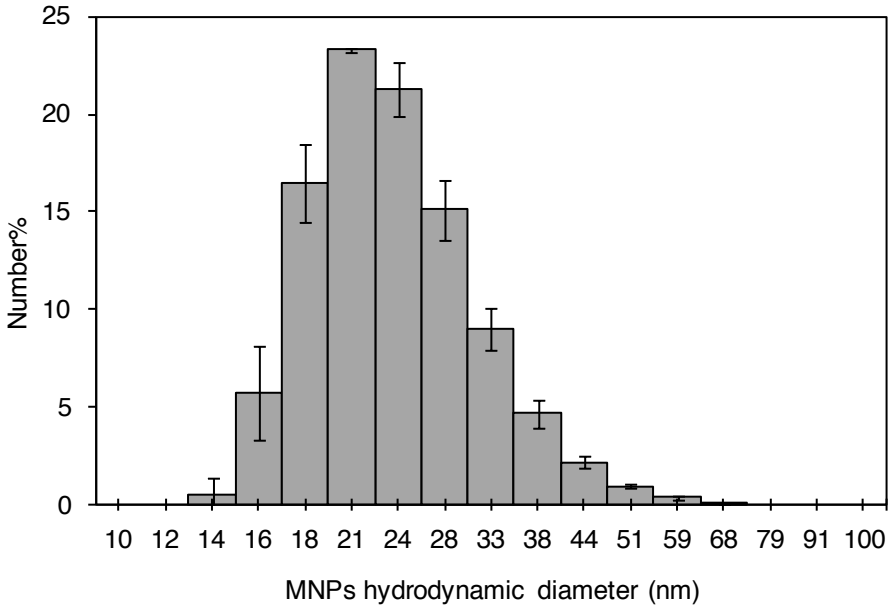

Figure 7-3 : Particle size distribution measurement for EMG705 by DLS technique (number average diameter = 24.8 nm), error bars indicate standard deviation with 3 runs.

7.2 Section II: magnet

The uniform rotating magnetic field is generated by a three-phase, 6-coil and 2-pole stator winding. Rotating magnetic is a resultant of three 120° out-of-phase balanced AC currents passing through each pair of stator coils. As a three-phase power supply, a variable frequency drive is connected to the stator to provide the currents (ABB ACS150, 2.2kW variable frequency drive).

To validate the relationship between applied current and resulting magnetic field strength as a function of position inside magnet bore, a DC current (Agilent Tech, N8739A) through each pair of three-phase stator coils equal to AC peak current is used. In addition, the magnetic field pattern is computed in COMSOL 3.5 using a 2-D finite element simulation of the stator for both DC and rotating modalities. The direction and strength of simulated DC field is found to agree with measurements and the simulation made reliable prediction of magnetic field vector in the case of ^{T}RMF.

The magnet bore has 45 mm inner diameter and 55 mm height. The magnetic field intensity mid-height and at the center of the magnet bore is reported in Table S.1 for a range of three-phase currents. In absence of any magnetic object, each Ampere rms generates a rotating magnetic field about 186 Gauss at the bore center as an external magnetic field. The

resistance and inductance of the stator windings are measured as 14.6 Ohm per (single-winding) coil and 150 mH per coil at 200 Hz.

Table 7-1 : RMF strength generated by 3-phase current intensity at center of magnet bore

I_{peak} [A]	I_{rms} [A]	$B_0 = \mu_0 \times H_0$ [Gauss]
1.0	0.71	131
1.5	1.06	197
2.0	1.41	263
2.5	1.77	328
3.0	2.12	394
3.5	2.47	459
4.0	2.83	525

7.3 Section III: RTD test & data reduction

Tracer impulse tests provide useful information about residence time distribution of a fluid flowing in a vessel. This experiment is easy to perform and has been considered as an effective method to characterize and interpret the mixing behavior in chemical reactors using simple mixing models [5,6]. One approach is to use (molecular or ion) tracers that are prone to liquid Brownian motion to mimic the diffusional flow behavior at the microscale [7].

Tracer experiments are performed using a simple glass-made capillary (1 mm i.d.) connected upstream to a T-shaped injector. After a steady-state flow is established through the capillary using a syringe pump (Cole-Parmer® single-syringe infusion pump), a small volume of tracer (ca. 0.5 μL), consisting of dilute NaCl (ca. 0.05 M) MNP suspension, is injected briefly into the flow by applying a side channel pressure. The transient flow response is thence monitored using a conductimetric technique whereby the increase in electrical conductivity is detected with two wall-wrapping electrodes –to avoid flow distortions– placed 3 cm apart along the capillary. The cross-sectionally averaged conductivities are measured with a two-channel conductivity meter (Omega CDTX-90).

The probes are calibrated to render concentration from the measured electrical conductivity using dilute-electrolyte Kohlrausch-inspired linear calibration relationships. Electrical conductivity measurements are performed at subsequent downstream distances from tracer injection point: L_1 = 50.0 mm, L_2 = 80.0 mm. Transient conductivity signals associated with electrodes at positions L_1 and L_2 are recorded over the course of experiment (Figure 6-4).

The mean residence time, $\bar{t}$, within the L_2 - L_1 segment is estimated from the 1st-order moments of inlet (I) and outlet (II) signals [5]:

$$\bar{t} = \frac{\sum_i t_i I_{IIi} \Delta t}{\sum_i I_{IIi} \Delta t} - \frac{\sum_i t_i I_{Ii} \Delta t}{\sum_i I_{Ii} \Delta t} \qquad i = 1 \text{ to n \& I, II stand for inlet \& outlet probes} \qquad \text{(S.1)}$$

where n is the number of time recordings, I_{Ii} and I_{IIi} are the instantaneous conductivity (or electrolyte concentration) signal intensities for probes I and II at time instant t_i. The time step, Δt (= 1 s), is constant for all measurements.

Assuming linear dynamic theory is valid [5], convolution of the inlet signal, I_I, to the system's residence time distribution density function, E, which accounts for the flow intrinsic behavior over L_2 - L_1 segment, restores the outlet signal I_{II} according to the convolution integral:

$$I_{II}(t) = \frac{1}{\bar{t}} \int_0^t I_I(t') E(t - t') \, dt' \qquad \text{(S.2)}$$

Analytical solutions for the residence time distribution (RTD) density function in axially dispersed flows are available and have been used to predict the evolution of tracer concentration in Taylor dispersion experiments [8]. Equation S.3 refers to the RTD axial dispersion model with open-open boundary conditions such as the one depicted in Figure 6-4 [5,9]:

$$E(t/\bar{t}) = \frac{UL}{4\pi D} \frac{\bar{t}}{t} \exp\left[\frac{UL}{4\pi D} \frac{\bar{t}}{t} \left(1 - t/\bar{t}\right)^2 \right] \qquad \text{(S.3)}$$

The axial dispersion coefficient, D, in (S.3) characterizes the degree of mixing during flow. A classical frequency-domain parameter estimation method [10] is used to estimate D for each of the present RTD experiments with and without magnetic field excitation. The method consists of a least-squares curve fitting between the discrete Fourier transform of measured outlet signal, $I_{II}(t)$, and the discrete Fourier transform of simulated outlet signal, $I_2(t)$, computed as the convolution integral (equation S.2) of measured inlet signal, $I_I(t)$, and the axial dispersion RTD model from equation S.3. It is implemented in Matlab (MathWorks) using a fast Fourier transform algorithm.

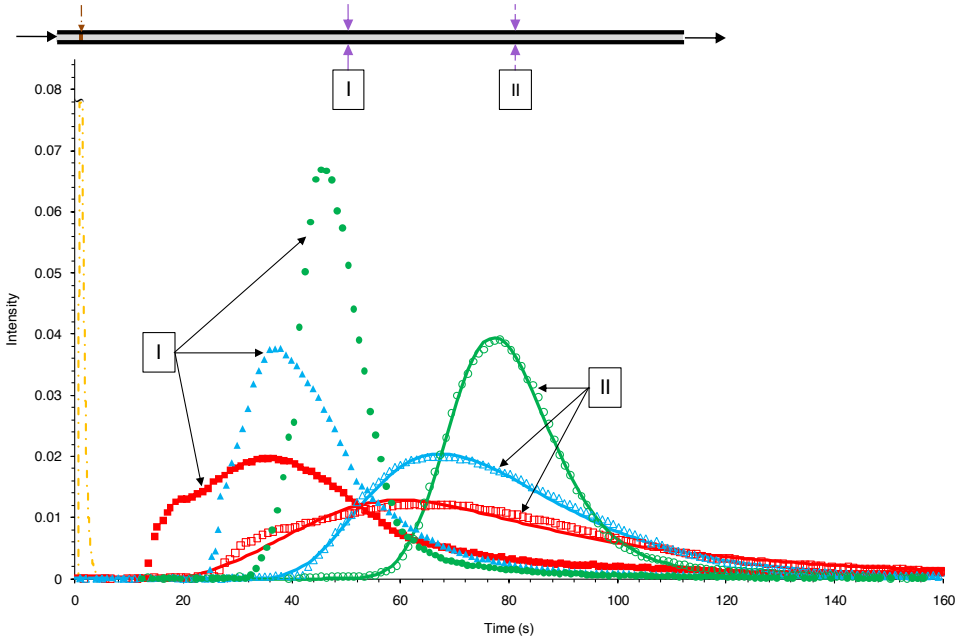

Figure 7-4 : Goodness of fit between measured I_{II} and simulated I_2 outlet signals using axial dispersion model.

Three sets of experiments are presented for no magnetic field and two magnetic field strengths in a capillary tube, d = 1mm with laminar Poiseuille flow, $Pe \sim 10^3$, $Re \sim 1$ and mean residence time of 30 s. All curves are fitted with axial dispersion model (equations S2, S3) with axial dispersion coefficient, D, as fitting the parameter. (■,□) impulse response with $\phi = 0.0025$, $H_0 = 0$ kA/m, $f = 0$ Hz, $UL/D = 3.48$. (▲,Δ) impulse response with $\phi = 0.0025$, $H_0 = 10.4$ kA/m, $f = 50$ Hz, $UL/D = 7.96$. (●,○) impulse response with $\phi = 0.0025$, $H_0 = 36.5$ kA/m, $f = 50$ Hz, $UL/D = 39.4$.

Figure 6-4 illustrates the quality of fit by means of the axial dispersion model (equation S.3) of the Taylor capillary flows with and without magnetic field excitation. The variance of both inlet and outlet signals is narrowed owing to magnetic nano-mixing as compared to off-magnetic field tests at similar flow rate, i.e., identical mean residence time. This results, *per se*, from the narrowing of the RTD density function because of a likewise reduction in the axial dispersion coefficient, D, under magnetic field conditions. The fitting quality of axial dispersion coefficients from equation S.3 can be judged from the goodness of fits in Figure 6-4 which illustrates closeness between measured $I_{II}(t)$ signals together with their corresponding fitted siblings, $I_2(t)$, (solid lines) for various experiments.

7.4 References

[1] R.E. Rosensweig, Ferrohydrodynamics, Dover Publications, Mineola, 1997.

[2] R.W. Chantrell, J. Popplewell, S.W. Charles, Measurements of particle-size distribution parameters in ferrofluids, *IEEE Trans*. *Magn*., 14 (1978) 975-977.

[3] R.A. Wassel, B.P. Grady, R.D. Kopke, K.D. Dormer, Dispersion of super paramagnetic iron oxide nanoparticles in poly(D,L-lactide-co-glycolide) microparticles, *Abstr*. *Papers Am*. *Chem*. *Soc*. 233 (2007).

[4] A. Tomitaka, T. Koshi, S. Hatsugai, T. Yamada, Y. Takemura, Magnetic characterization of surface-coated magnetic nanoparticles for biomedical application, *J*. *Magn*. *Magn*. *Mater*. 323 (2011) 1398-1403.

[5] O. Levenspiel, Chemical Reaction Engineering, John Wiley & Sons, New York, 1999.

[6] O. Levenspiel, Modeling in chemical engineering, *Chem*. *Eng*. *Sci*. 57 (2002) 4691-4696.

[7] K. Tanaka, Self-diffusion coefficients of water in pure water and in aqueous-solutions of several electrolytes with O-18 and H-2 as tracers, *J*. *Chem*. *Soc*. *Farad*. *T*. 1, 74 (1978) 1879-1881.

[8] G. Taylor, Dispersion of soluble matter in solvent flowing slowly through a tube, *Proc*. *R*. *Soc*. *London*, *Ser*. *A* 219 (1953) 186-203.

[9] O. Levenspiel, W.K. Smith, Notes on the diffusion-type model for the longitudinal mixing of fluids in flow, *Chem*. *Eng*. *Sci*. 6 (1957) 227-233.

[10] N. Wakao, S. Kaguei, Heat and Mass Transfer in Packed Beds, Gordon and Breach Science Publisher, New York, 1982.